Experimental and Numerical Investigations into Laser-Induced Plasma Assisted Ablation (LIPAA) of Transparent Polycarbonate for Fabrication of Microchannels

A Thesis

Submitted in partial fulfilment of the requirements for the degree of

DOCTOR OF PHILOSOPHY

by

Upasana Sarma

(Roll No. 166103017)

Department of Mechanical Engineering
Indian Institute of Technology Guwahati
Guwahati, Assam, India
2021

Indian Institute of Technology Guwahati
Department of Mechanical Engineering
Guwahati – 781039

STATEMENT

The present thesis entitled, **"Experimental and Numerical Investigations into Laser-Induced Plasma Assisted Ablation (LIPAA) of Transparent Polycarbonate for the Fabrication of Microchannels"** has been carried out by me under the supervision of Prof. Shrikrishna N. Joshi, Department of Mechanical Engineering, Indian Institute of Technology Guwahati. This work has not been submitted elsewhere for the award of any degree.

Upasana Sarma

Date: December, 2021

(Upasana Sarma)
Roll. No. 166103017
Department of Mechanical Engineering
Indian Institute of Technology Guwahati,
Guwahati – 781039, India

Indian Institute of Technology Guwahati
Department of Mechanical Engineering
Guwahati – 781039

CERTIFICATE

It is certified that the work described in this thesis, entitled **"Experimental and Numerical Investigations into Laser-Induced Plasma Assisted Ablation (LIPAA) of Transparent Polycarbonate for the Fabrication of Microchannels"** done by **Upasana Sarma (Roll No. 166103017),** a Ph.D. student in the Department of Mechanical Engineering, Indian Institute of Technology Guwahati, for the award of degree of **Doctor of Philosophy** has been carried out under my supervision. This work has not been submitted elsewhere for the award of any degree.

Date: December, 2021

(Prof. Shrikrishna N. Joshi)
Professor
Department of Mechanical Engineering
Indian Institute of Technology Guwahati,
Guwahati – 781039, India

DEDICATION

I dedicate this to my family for their advice, patience and faith in me

Abstract

Microchannel-based devices are widely used in microelectronic devices, turbine blade cooling, microfluidics for drug delivery devices, etc. Therefore, microchannel-based devices require the use of materials with high optical, chemical, and mechanical properties, and thus, transparent materials have become a significant material for the production of microchannels.

Transparent polycarbonate (PC) is a highly durable material, making it resistant to impacts and fracture, providing safety and comfort in applications that demand reliability and high performance. As such, PC can be considered as an ideal material for the biomedical and optical industries.

PC-based microchannels can be fabricated using a variety of processes such as lithography, wire moulding, micro-milling, laser micro-machining etc. Nonetheless, the mentioned techniques have limited applicability. Further, the high transmissivity of PC over a wide range of wavelength makes the laser based fabrication of microchannels on it a challenging task. However, with Laser-Induced Plasma Assisted Ablation (LIPAA), lasers may have the potential to process transparent PC. In view of this, in the present research work, systematic and extensive experimental as well as numerical studies have been carried out to assess the feasibility, productivity and product quality during LIPAA for microchannel fabrication on PC.

LIPAA is a technique, by which transparent materials can be ablated on its rear side with the aid of laser-induced plasma. The first phase of the research work presents the successful fabrication of microchannels on transparent PC using the LIPAA technique. Besides, the effect of properties of metal targets on microchannel fabrication was also investigated. Three different metal targets utilized during the process are namely aluminium, copper and stainless steel. Evaluation was then performed to investigate the influence of metal target properties such as thermal conductivity and specific heat on the geometrical characteristics of the microchannels. The study concludes by stating that the higher thermal conductivity value of the metal target leads to the formation of a narrow microchannel, while the higher specific heat value leads to a deeper microchannel fabrication. In addition, the metal target resulting in the highest microchannel aspect ratio was recommended for further study in our research.

In second phase of research work, experiments are carried out based on a full factorial 3^4 experiments on PC by the appropriate selection of the laser parameters viz.

pulse power density, pulse repetition rate, pulse duration and laser scanning speed. The influence of the laser parameters on channel width, channel depth and the channel roughness has been studied. Analysis of Variance (ANOVA) is also carried out to determine the most influential parameters. Second order mathematical relations among the input laser parameters, their interactions and the responses were developed. To analyse the accuracy of the developed mathematical model, confirmation experiments are performed and is found to be in good agreement. Based on the confidence gained from the confirmation experiments performed, multiple objective (response) optimization of the input parameters to predict a better quality channel geometry and channel roughness is carried out. For a width of 250 µm, depth of 150 µm and minimum roughness on a single pass, the optimized condition of laser parameters is found to be 40 Hz repetition rate, 2 ms pulse duration and 4.79 MW/cm^2 pulse power density. Using the optimal laser parameters, open microchannels are fabricated and were closed by using a thermal bonding process. Further, a fluid flow test carried out on the closed microchannel to prove its potentiality to be used as a microfluidic device has also been described in the chapter. Different configuration channels on PC have also been fabricated using the optimal laser parameters.

The third phase of the work represents a two-dimensional transient numerical model to understand the physics of material removal during the LIPAA process. A realistic model is developed concerning the effect of plasma along with the effect of input laser irradiation. The channel dimensions, i.e., the width and the depth of the channel, were computed from the numerical study. The computed results have been duly verified with our experimental results and found in good agreement. Also, considering the effect of moving heat flux, it is witnessed that the peak temperature attains a constant value on reaching a certain distance, thus assuring a channel of uniform dimension.

A three-dimensional nonlinear transient modelling was also developed to simulate the LIPAA process for microchannel fabrication on transparent polycarbonate. The merit of the approach lies in simulating simultaneous ablation of both transparent polycarbonate and aluminium metal target during the process. The developed model has the potential of estimating spatial-temperature distribution along the traverse direction and direction perpendicular to it. The spatial distribution lent a hand in predicting the width and depth of the microchannel. Temporal-temperature distribution for pulse-on and pulse-off time was also explored. A channel index (CI) has also been estimated which determines channel formation in or out of the micron-scale (1-999 μm) for a selected set of process conditions.


भारतीय प्रौद्योगिकी संस्थान गुवाहाटी
Indian Institute of Technology Guwahati

Acknowledgements

Years of hard work and the countless help and support from the people around me has made it possible for me to complete the thesis work and it is my heartfelt desire to acknowledge their immense goodwill and valuable support.

I wish to express my sincere and deep appreciation to my supervisor, Prof. Shrikrishna N. Joshi for his encouragement, insightful guidance, all the patience and enthusiastic support throughout my studies, including the writing of this dissertation. I must acknowledge him for providing the unconditional freedom to work, think and express on whatever I have done in my research work by having faith in my capabilities. I am also thankful to my supervisor for providing me the opportunity to work on this research project. I owe him a lot for the valuable advice he have given whenever I needed.

I am highly thankful to my doctoral committee members, Prof. Swarup Bag, Prof. Sukhomay Pal and Prof. Ashwini Kumar Sharma for their continuous academic guidance and checking my work progress and seminars during my Ph.D. work. Their valuable discussions and suggestions were truly encouraging for me. I am also very thankful to the anonymous reviewers of our journal and conference papers for their valuable suggestions which enhanced the course of this work.

I would like to express my sincere gratitude to Prof. K. S. R. Krishna Murthy, Prof. S. Senthilvelan, Prof. Santosha K. Dwivedy and Prof. Anoop K. Dass, present and former Heads, Department of Mechanical Engineering, Indian Institute of Technology Guwahati, for providing various laboratory facilities and sanctioning funds without which completion of the work would not have been possible. I am also grateful to all the faculty members of the Mechanical Engineering department.

I would also like to thank Ministry of Education (MoE), Government of India for providing financial support. I sincerely thank Indian Institute of Technology Guwahati for providing all sort of infrastructural facilities to carry out this doctoral research work. I would also like to acknowledge Advanced Manufacturing Laboratory, Material Science Laboratory, Central Workshop and Central Instruments Facility of Indian Institute of Technology Guwahati and all scientific officers and staff members for providing instruments and helping me to carry out the research work.

I highly appreciate the technical cooperation given by Mr. Jiten Basumatary, Mr. Pranjol Paul, Mr. Saiffuddin Ahmed, Mr. Nandan Kanan Das and Mr. Chandan Banikya.

I deeply acknowledge the unabated support and counselling provided by my colleagues Dr. Ravikant, Dr. Borad M. Barkachary, Dr. Gururaj Bolar, Dr. Sanasam Sunderlal Singh, Ms. Ngangkham Devarani, Ms. Sanghamitra Das, Mr. Brijesh K. Singh, Mr. Ritam Sarma, Mr. Evenmore Mylleium, Mr. Antash K. Sinha and Ms. Swati Singh throughout my studies. I am also grateful to my friends Dr. Rashmi Ranjan Behera, Dr. Rajkumar Shufen, Dr. Bikash Kumar, Ms. Priyanka Duarah and Mr. Sasanka Kakati, for their constant support.

My most sincere gratitude and appreciation go to my father Mr. Rudreswar Sarma, my mother Mrs. Santa Sarma, my sister Dr. Aradhana Sarma, my in-laws Mr. Dimbeswar Talukdar and Mrs. Rina Talukdar and finally my dear husband Mr. Nabajyoti Talukdar for their patience, continuous encouragement and moral support over the past difficult years. I am deeply indebted to all the other members of my family who gave me continuous support and encouragement throughout my life.

There are many more persons who helped me in many more ways and whose names elude me at this moment of time. I extend my gratitude to them.

Last, but not the least, I shall always be grateful to God for providing me such an awesome aura for research work.

Date: December, 2021

Upasana Sarma
(Roll No. 166103017)

Contents

List of figures

List of tables

List of abbreviations

2D	Two-dimensional
3D	Three-dimensional
ANOVA	Analysis of variance
CI	Channel index
CNC	Computer numerical control
CO_2	Carbon dioxide
DF	Degree of Freedom
DoE	Design of experiments
DNA	Deoxyribonucleic acid
EDX	Energy-Dispersive X-ray spectroscopy
EHT	Extra high tension
eV	Electronvolt
FEM	Finite element method
FESEM	Field Emission Scanning Electron Microscope
FWHM	Full width half maximum
LESAL	Laser Etching at a Surfaced-Adsorbed Layer
LIBDE	Laser Induced Backside Dry Etching
LIBWE	Laser Induced Backside Wet Etching
LIPAA	Laser-Induced Plasma Assisted Ablation
MS	Mean square
Nd: YAG	Neodymium-doped yttrium aluminium garnet
PC	Polycarbonate
PD	Pulse duration
PDMS	Polydimethylsiloxane
PI	Polyimide
PMMA	Polymethylmethacrylate
PPD	Pulse power density
PRR	Pulse repetition rate
RBCs	Red blood cells
RSM	Response surface methodology
SS	Sum of square

Nomenclature

A	Focal spot area (mm^2)
$[B]$	General geometric matrix
$[C]$	Global heat capacity matrix
C_{depth}	Channel depth
$C_{\mathrm{roughness}}$	Channel roughness
C_{width}	Channel width
c	Specific heat (J/kgK)
D_{L}	Overlap distance (µm)
d	Microchannel depth (µm)
E	Laser pulse energy (J)
E_{plasma}	Plasma Energy Density (J/m^3)
f	Pulse repetition rate (Hz)
h	Convective coefficient of heat transfer (W/m^{2}K)
h_r	Combined coefficient of heat transfer (W/m^{2}K)
I	Laser pulse intensity (W/mm^2)
I_{P}	Pulse power density (MW/cm^2)
I_{o}	Peak laser pulse intensity (W/mm^2)
K	Average Kinematic Energy (J)
$[K_{\mathrm{T}}]$	Global conductivity matrix
k	Thermal conductivity (W/mK)
O	Percentage overlap of pulses
$[N]$	Interpolation or shape function matrix
N_{e}	Electron Density (cm^{-3})
P	Pulse power
P_{peak}	Peak laser power (W)
R	Laser spot radius (µm)
R_{a}	Reflectivity of metal target
R_{t}	Reflectivity of transparent material
T	Temperature (K)
T_{∞}	Ambient temperature (K)
$\{T_{\mathrm{e}}\}$	Element nodal temperature matrix
T_{g}	Glass transition temperature (K)
T_{s}	Surface temperature (K)

t	Time (s)
t_{on}	Pulse-on time (ms)
$\{Q\}$	Heat flux vector
q	Laser heat flux (W/mm^3)
q_1	Plasma Power Density (W/mm^3)
v	Scanning speed (mm/s)
w	Microchannel width (µm)
x,y,z	Cartesian coordinates

Greek Letters

α	Absorption coefficient
ΔE	Ionisation energy (eV)
ε	Emissivity
ρ	Density (kg/m^3)
σ	Stefan Boltzmann constant (W/m^{2}K^4)
ω	Laser spot diameter (µm)

List of publications

International Journals

1. Sarma, U. and Joshi, S.N., 2020. Machining of micro-channels on polycarbonate by using Laser-Induced Plasma Assisted Ablation (LIPAA). Optics & Laser Technology, 128, p.106257. doi.org/10.1016/j.optlastec.2020.106257. Elsevier (Impact factor: 3.867, Citation: 14, SCI) *(Related to the reported work in thesis)*

2. Sarma, U. and Joshi, S.N., 2020. Numerical modelling and simulation of microchannel fabrication on polycarbonate using Laser-Induced Plasma Assisted Ablation (LIPAA). Optik, 223, p. 165379. doi.org/10.1016/j.ijleo.2020.165379. Elsevier (Impact factor: 2.443, Citation: 4, SCI) *(Related to the reported work in thesis)*

3. Sarma, U. and Joshi, S.N., 2021. Geometric and Surface Analysis of Microchannels Fabricated Using Laser-induced Plasma Assisted Ablation (LIPAA). Lasers in Engineering, 49, pp. 119-143. Old City Publishing (Impact factor: 0.665, SCI) *(Related to the reported work in thesis)*

4. Kore M., **Sarma U.**, Joshi, S.N., and Kuriachen B., 2021. Processing Parameter Influence for Dimple Fabrication on WC Tool Inserts Using Laser Surface Texturing (LST). Lasers in Engineering, 49, pp. 49-66. Old City Publishing (Impact factor: 0.665, SCI) *(Not related to the reported work in thesis)*

5. Kant R., Gurung H., **Sarma U.** and Joshi, S.N., 2021. Development and Analysis of Laser-assisted Bending with Moving Pre-Displacement Load. Lasers in Engineering, 49, pp. 21-47. Old City Publishing (Impact factor: 0.665, Citation: 1, SCI) *(Not related the reported work in to thesis)*

6. **Sarma, U.** and Joshi, S.N., 2022 Spatial and Temporal Thermo-Physical Analysis of Laser-Induced Plasma Assisted Ablation (LIPAA) of polycarbonate. Optics & Laser Technology, 150, p. 107908. doi.org/10.1016/j.optlastec.2022.107908. Elsevier (Impact factor: 3.867, SCI) *(Related to the reported work in thesis)*

In-progress Journal Publications

1. Sarma, U. and Joshi, S.N. Comparative assessment on the effect of material properties of different metal targets during Laser-Induced Plasma Assisted Ablation (LIPAA) of Polycarbonate *(To be submitted)* *(Related to the reported work in thesis)*

2. **Sarma, U.** and Joshi, S.N. Microchannel Fabrication on Polycarbonate using Laser-Induced Plasma Assisted Ablation (LIPAA) with Copper Metal Target *(To be submitted)* *(Related to the reported work in thesis)*

International Conferences

1. Sarma U. and Joshi S. N. Two-Dimensional Numerical Investigation on the Effect of Laser Parameters on Laser Indirect Machining of Glass, Proceedings of

International Conference on Recent Innovations and Developments in Mechanical Engineering (IC-RIDME-2018) National Institute of Technology Meghalaya, Shillong, Meghalaya, INDIA, November 8-10, 2018, pp. 347-357*(Related to the reported work in thesis)*

2. Sarma U. and Joshi S. N. Effect of Laser Parameters on Laser-Induced Plasma-Assisted Ablation (LIPAA) of Glass, Proceedings of 7th International & 28th All India Manufacturing Technology Design and Research Conference (AIMTDR-2018) College of Engineering Guindy, Anna University, Chennai, Tamil Nadu, INDIA, December 13-15, 2018, pp. 67-76 *(Related to the reported work in thesis)*

3. Sarma U. and Joshi S. N. Computation of microchannel width during Laser Induced Plasma Assisted Ablation of Polycarbonate, 7th International Conference on Advancements and Futuristic Trends in Mechanical and Materials Engineering (AFTMME-2019) Indian Institute of Technology Ropar, Rupnagar, Punjab, INDIA, December 5-7, 2019 *(Related to the reported work in thesis)*

4. Sarma U. and Joshi S. N. Computation of Microchannel Dimensions during Laser-Induced Plasma Assisted Ablation (LIPAA) of Polycarbonate with Copper Metal Target, 8th International & 29th All India Manufacturing Technology Design and Research Conference (AIMTDR-2021) Departments of Mechanical Engineering of PSG College of Technology, Coimbatore and PSG Institute of Technology and Applied Research, Coimbatore, Tamil Nadu, INDIA, December 9-11, 2021 *(Related to the reported work in thesis)*

5. Singh B.K., **Sarma U.,** Kapil S. and Joshi S. N. Numerical Modelling and Simulation of Laser-Based Micro-Drilling of Titanium Alloy, 8th International & 29th All India Manufacturing Technology Design and Research Conference (AIMTDR-2021) Departments of Mechanical Engineering of PSG College of Technology, Coimbatore and PSG Institute of Technology and Applied Research, Coimbatore, Tamil Nadu, INDIA, December 9-11, 2021 *(Not-related to the reported work in thesis)*

Book Chapters

1. Sarma U. and Joshi S.N., 2020. Two-Dimensional Numerical Investigation on the Effect of Laser Parameters on Laser Indirect Machining of Glass. In: Biswal B., Sarkar B., Mahanta P. (eds.) Advances in Mechanical Engineering. Lecture Notes in Mechanical Engineering. Springer, Singapore. pp 347-357, ISBN No. 978-981-15-0124-1 *(Published)* *(Related to the reported work in thesis)*

2. Sarma U. and Joshi S.N., 2020. Effect of Laser Parameters on Laser-Induced Plasma-Assisted Ablation (LIPAA) of Glass. In: Shunmugam M., Kanthababu M. (eds.) Advances in Unconventional Machining and Composites. Lecture Notes on Multidisciplinary Industrial Engineering. Springer, Singapore. pp 67-76, ISBN No. 978-981-32-9471-4 *(Published)* *(Related to the reported work in thesis)*

3. Sarma U., Joshi S.N. and Chandra P., 2021. Advanced Microchannel Fabrication Technologies for Bio-medical Devices. In: Joshi S.N. and Chandra P. (eds.) Advances in Micro and Nano Manufacturing Technologies. Springer. Singapore. pp 127-143, ISBN No. 978-981-16-3645-5 *(Published)* *(Related to the reported work in thesis)*

Chapter 1

Introduction

Microchannels are simple and distinct patterns engineered to allow a controlled flow of fluids through them. The passages usually with a diameter below 1 mm are referred to as microchannels. Microchannels have widespread applications in the development of biomedical devices. The microchannel-based lab-on-a-chip (Pan *et al.*, 2017), electro-fluidic devices (Xu *et al.*, 2017), printed circuit patterns (Kim and Park, 2017), micro-reactors (Suryawanshi *et al.*, 2018), etc. are some of the emerging onsite clinical applications that can be used as personalized diagnostic devices. Figure 1.1 shows some microchannel-based applications in real life.

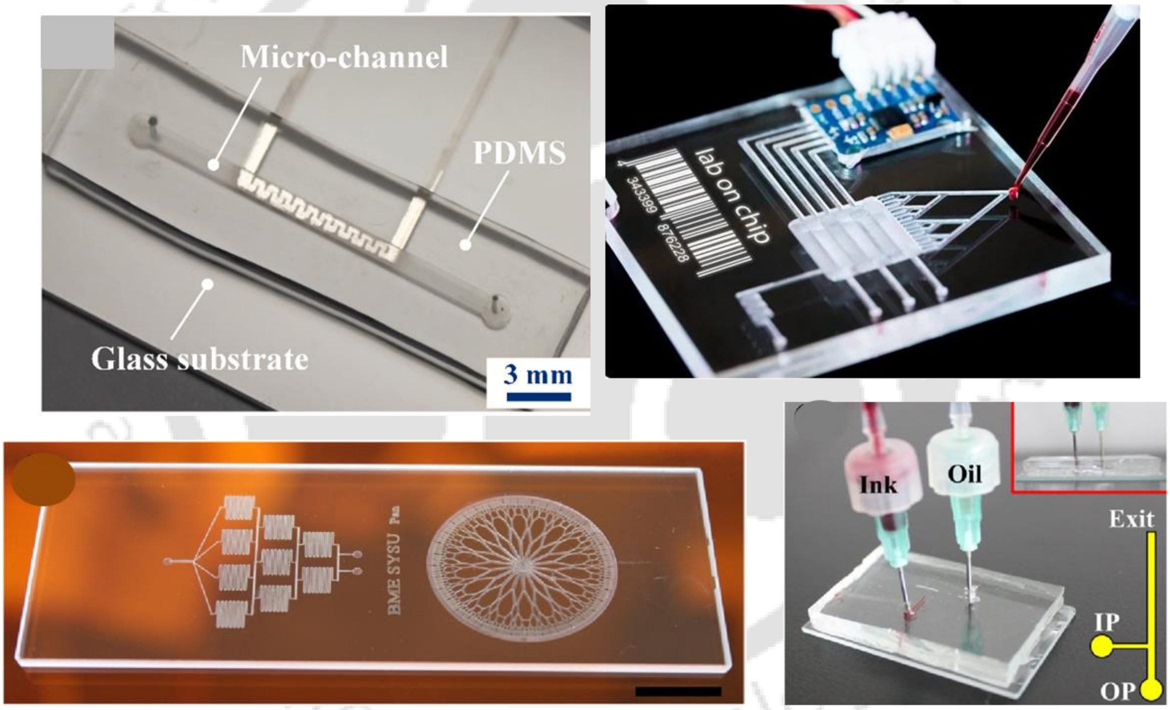

Figure 1.1 Microchannel-based lab-on-a-chip setups (Pan *et al.*, 2017; Xu *et al.*, 2017) (Reproduced with permission from Elsevier)

Microchannels are fabricated on a variety of materials like glass (Nieto *et al.*, 2014), metals like stainless steel (Singh *et al.*, 2018), polymers like polycarbonate (PC) (Kim et al., 2015), polydimethylsiloxane (PDMS) (Li and Xu, 2015) and polymethylmethacrylate (PMMA) (Prakash and Kumar, 2017). Yet, polycarbonates low weight, inherent impact strength, high dimensional stability and eco-friendly nature attract their wide applications in medical devices, optical instrumentation and sensors.

1.0 Microchannel Fabrication Technologies

Microchannels can be generated on substrates by using conventional as well as unconventional manufacturing processes viz. microwire molding, imprinting, lithography, micro-milling, abrasive jet machining, chemical etching, plasma etching, and laser-based machining. These techniques are capable of machining microchannels on a variety of materials, however, some of these have certain limitations. Micro-wire molding, despite being a flexible method, has a higher volume of waste due to the overflow of the degassed polymer from the mold. Also, the mold complexity and its maintenance make it an expensive and time–consuming process. While the disadvantage of using lithography for microchannel fabrication is that the substrate usually absorbs the development solution. Moreover, its requirement of a room preventing UV radiation makes it an expensive process. Limitations in the imprinting technique also arise due to the slow mass transport and permanent entrapment of the material into the metal blocks, leading to the heterogeneous distribution of material and also inadequate properties. Laser direct machining has however been found as a promising tool if it is applied with proper setting of laser parameters such as wavelength, laser power, pulse duration, etc. Laser processing has proved its capability in fabricating clean and uniform channels on opaque materials (Majumdar and Manna, 2003).

1.1 Laser-based micromachining

During laser-based micromachining, the thermal energy converted from the light energy of a highly coherent beam of photons is used to remove the material from the substrate. A laser beam irradiates the substrate. A fraction of the laser energy (light energy) gets absorbed, while the remaining part gets reflected. The absorbed portion of the energy gets converted into heat energy instantaneously and increases the temperature in the irradiated zone. When the laser energy is sufficiently high enough, it leads to the melting and vaporization of the material. The vapor thus formed from the vaporization induces a recoil pressure at the surface of the melt pool, which results in melt ejection, and hence, the material removal is obtained. This process works effectively with materials that are capable of absorbing laser energy.

1.2 The motivation of the present work

For microchannel fabrication using lasers, the laser must be highly absorbed by the material. But on the other hand, most microchannels demand the use of transparent materials. High transparency of the transparent material does not allow laser energy to be absorbed and hence, it is difficult to machine transparent material by a laser. Nevertheless, ultrashort lasers are capable of processing transparent materials as it produces a highly localized light field that is absorbed into the transparent material by non-linear absorption and is sufficient enough to ionize any atom. Similar to ultrashort lasers, short-wavelength lasers also can process transparent materials. It is due to the low transmissibility of most of the transparent materials at short wavelengths. Laser processing of transparent materials with long-pulsed and long-wavelength lasers is thus quite difficult to achieve. It can however be noted from the reported literature that the method of Laser-Induced Plasma Assisted Ablation (LIPAA) may have the potential to process transparent materials with longer pulses and longer wavelength lasers. Thus it was thought to be worth having in-depth, comprehensive experimental and numerical investigations into the LIPAA for microchannel fabrication on transparent materials. An investigation into the effect of thermal properties of the metal target and obtaining the optimal levels of important process parameters would certainly improve the product quality and process efficiency of the LIPAA process.

1.3 Laser-Induced Plasma Assisted Ablation (LIPAA)

In the LIPAA process, the transparent material gets ablated on its rear side with the aid of laser-induced plasma Figure 1.2 shows the schematic of the arrangement of LIPAA. A transparent material is placed above a thin sheet of metal without the application of any external pressure between the two materials.

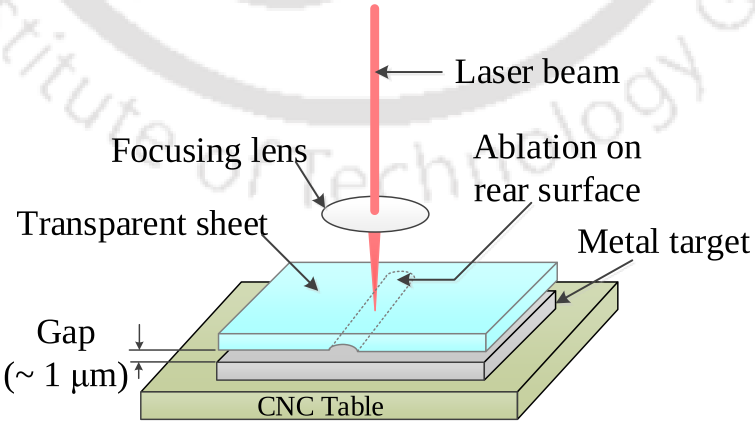

Figure 1.2 Schematic of the LIPAA setup

The laser beam passes through the material and is focussed on the upper surface of the metal target sheet. Figure 1.3 illustrates the mechanism of the LIPAA process. A fraction of the laser energy is absorbed by the absorbing metal target sheet, while the rest gets reflected from the surface. The absorbed energy results in the excitation of the free electrons, which instantaneously in time duration of about 10^{-13} s gets converted into heat energy (Dahotre and Hamirkar, 2008). This heat energy then gets dissipated through various modes of heat transfer viz. conduction, convection, and radiation, however, conduction plays the most significant role. The thermal energy of the plasma dissipates into the target metal, thereby increasing the temperature of the surface. Once the laser intensity is fairly high (more than 10^5 to 10^8 W/cm^2), the temperature exceeds the melting and boiling temperature of the metal target sheet. The vapors generated during the ablation process contain molecules, atoms, ions, and electrons. The incoming laser beam interacts with the vapors and ionizes the vapor molecules. It results in the formation of opaque and dense plasma. The plasma generated flies towards the transparent sheet at a high speed of approximately 10^4 m/s (Hong *et al.*, 2001). The plasma generated, yet again interacts with the incoming laser beam and Inverse Bremsstrahlung absorption takes place, causing isothermal expansion of the plasma perpendicular to the metal surface (Pan *et al.*, 2017). The expanded plasma has a greater thermal effect on both the transparent and the absorbing metal, thereby ablating both the materials. The generation of the plasma at the interface is confirmed by the simultaneous ablation on the upper surface of the metal target and the rear surface of the transparent sheet.

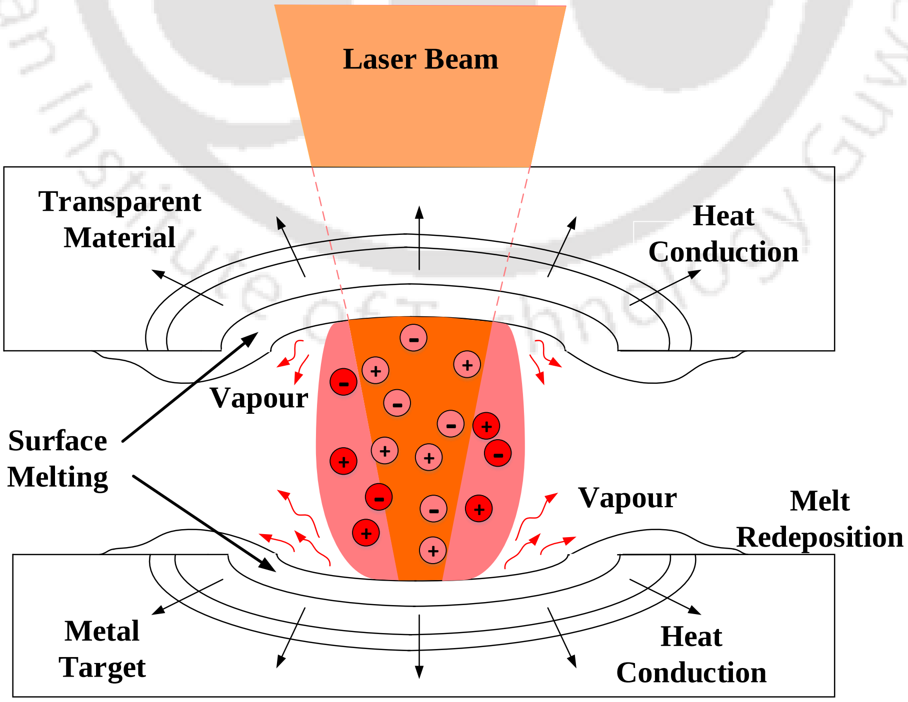

Figure 1.3 Mechanism of LIPAA process

The LIPAA process has certain advantages over the other fabrication technologies of microchannels. It can machine transparent materials even at longer wavelengths and with longer pulse width. Moreover, irrespective of the hardness, brittleness, and transparency of the material, LIPAA can process any transparent materials. The process is can easily be operated by using CNC-based controllers. However, the process has certain limitations as well. Deposits may be formed on the channel surface from the metal target sheet used on its rear side. Besides, it requires an additional fixture to maintain the gap between the transparent material and the metal target sheet.

Literature reports eminent research work on various aspects of the LIPAA process, such as fabrication of microstructures like microfluidic devices and electro-fluidic devices, use of different absorbing media on the rear side of the transparent material and comparative assessment of LIPAA and direct laser ablation process (Pallav *et al.*, 2014; Pan *et al.*, 2017; Xu *et al.*, 2017; Rahman *et al.*, 2019). Most of the reported work is mainly focused on employing the short and ultra-short wavelengths of laser pulses. Limited research has been carried out on the application of LIPAA process for the fabrication of microchannels on polycarbonate (PC) using high wavelength pulses. Scant work has been reported on the effect of the material properties of the metal target on the geometrical characteristics of the microchannels produced during the LIPAA process. Moreover, very scant work is noted on the numerical modeling, simulation, and parametric study of the LIPAA process. Systematic experimental investigations into the fabrication of microchannels on PC by using LIPAA process may thus be worth carrying out. It may be useful studying the influence of laser parameters viz. pulse repetition rate, pulse duration, scanning speed, and pulse power density on the channel geometry and roughness. Also, developing a realistic numerical model may provide useful insights in understanding the underlying physics of the LIPAA process.

1.4 Scope of the present research work

The present work primarily focuses upon the enhancement of the product quality and process efficiency during the laser-induced plasma-assisted ablation (LIPAA) of polycarbonate. For this purpose, comprehensive experimental and numerical investigations have been carried out. During the LIPAA process, ablation on both the transparent material and the metal target is achieved. Our current study is mainly focused on the ablation of the transparent material. Studies on the ablation of the metal target are not in the scope of the present research work.

Experiments were carried out on microchannel fabrication on transparent PC using LIPAA with different metal targets such as aluminum, copper, and stainless steel. The effect of material properties of different metal targets on microchannel fabrication during the LIPAA has been studied. Experiments were conducted considering the effective range of process parameters viz. pulse power density, pulse repetition rate, pulse duration, and scanning speed. The dimensions and the surface roughness of the fabricated microchannels were then determined. A comprehensive parametric study on the effect of the process parameters on the responses like channel geometry (channel width and channel depth) and channel quality (channel roughness) has been performed. Further, statistical analysis is carried out to find the significance of the factors on the responses and to develop mathematical relations among the input laser parameters, their interactions, and the responses. Optimal levels of the laser parameters have been determined to predict better quality channel geometry and channel roughness. Furthermore, finite element method (FEM) based two-dimensional as well as three-dimensional thermo-physical models of the LIPAA process have been developed. The width and the depth of the microchannels were computed by using the numerical models and the results were validated with the experimental results.

1.5 Organization of the thesis

The thesis work is presented in seven chapters.

Chapter 1 presents an overview of the Laser-Induced Plasma Assisted Ablation (LIPAA) of transparent materials, its advantages and limitations, and applications. The motivation for carrying out the research work on LIPAA of PC has also been explained at the end of the chapter.

Chapter 2 presents an extensive literature survey on the fundamentals of laser-based processing of transparent materials. The current status on related aspects such as laser micromachining, surface texturing, micro-drilling, forming, etc. has been presented. Literature about available experimental studies and numerical work related to LIPAA as well as laser machining has been presented. Accordingly, the research gaps identified have been discussed and subsequently, a brief insight into the experimental and numerical investigation on the LIPAA process for microchannel fabrication on transparent PC has been presented.

Chapter 3 presents the feasibility of laser processing of transparent PC using the LIPAA process. The effect of properties of metal targets like aluminum, copper, and stainless steel on microchannel fabrication was also investigated. The width and depth of the microchannels were carefully examined and recorded. Then, the effect of the material properties like thermal conductivity and the specific heat capacity on the channel width and channel depth has been presented in the chapter.

Chapter 4 presents the comprehensive full factorial experimental investigation on microchannel fabrication on polycarbonate using LIPAA and aluminium metal target. The effect of laser process parameters viz. pulse power density, pulse repetition rate, pulse duration, and scanning speed on the responses like channel geometry (channel width and channel depth) and channel quality (channel roughness) have been extensively studied. Further, a fluid flow test carried out on the closed microchannel to prove its potentiality to be used as a microfluidic device has also been described in the chapter. Fabrication of different configuration channels on PC has also been described in the chapter.

Chapter 5 presents the development of a two-dimensional thermo-physical model of Laser-Induced Plasma Assisted Ablation (LIPAA) using the finite element method (FEM). The details of process continuum, geometric modelling, governing equation, boundary conditions, laser heat source model and solution methodology have been presented. The validation of the predicted results from the model with the experimental results has also been presented in the chapter. A systematic parametric study was performed to study the LIPAA process.

Chapter 6 reports a three-dimensional nonlinear transient model of the LIPAA process for microchannel fabrication on transparent materials. The effect of plasma energy along with the input laser irradiation has been considered to make the model more realistic. The spatial and temporal analyses on the LIPAA process have been illustrated and consequently, the ablation width and depth on the rear side of polycarbonate have been computed. The predicted results were duly validated with the in-house experimental results. The chapter concludes with important insights with the help of a detailed parametric study.

Chapter 7 summarizes the findings of the research work and presents the conclusions from the present research work. The scope for carrying out future work in this area has also been presented towards the end of the chapter.

Chapter 2

Literature review on laser machining of transparent materials

2.0 Scope

This chapter presents a critical review on research carried out in the area of laser machining of transparent materials. Initially, the importance of transparent materials in various scientific and industrial applications is presented, followed by a detailed description of different transparent material processing techniques. Details on laser-induced plasma assisted ablation (LIPAA) process in terms of its types, laser process parameters and workpiece materials have also been presented. Published literatures on experimental investigations into the process mechanism, process parameters, process planning and process optimization of the LIPAA process are covered extensively. Numerical approach of laser-induced plasma process has been critically studied. The chapter concludes by summarizing important observations from the literature review and identifying the grey areas in the LIPAA process. In the end, the research objectives are derived. The overview of the present chapter has been depicted schematically in figure 2.1.

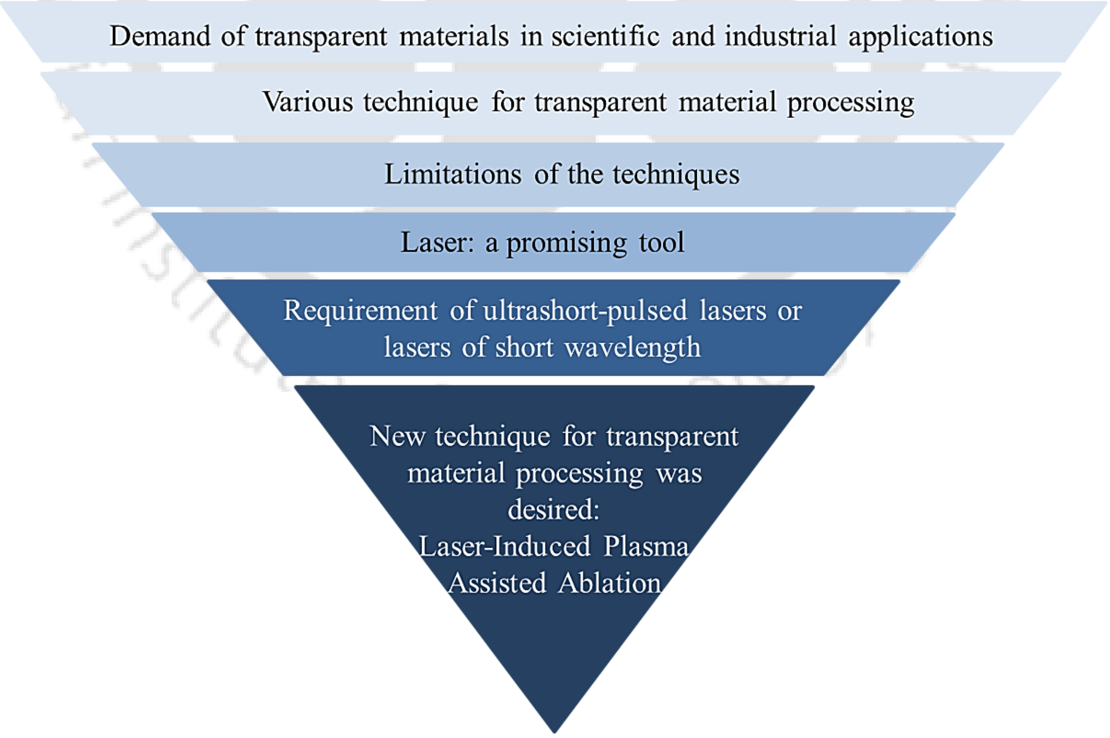

Figure 2.1 Overview of the present chapter

2.1 Transparent materials in scientific and industrial applications

Micro-channel based devices find wide applications in microelectronic devices (Wei *et al.*, 2007), cooling turbine blades (Stevens and Baelmans, 2008), waste heat recovery (Yih and Wang, 2019); micro-fluidics for drug delivery devices (Sanjay *et al.*, 2018; Ahn *et al.*, 2018), bio-optical sensors (Jin *et al.*, 2018), micro reactors (Shi *et al.*, 2019); automotive (Wegeng *et al.*, 2001), etc. In a microfluidic devices, the microchannels are connected together in an organized network that enables proper mixing and control of the biochemical reactions. In a biomedical device, the concentration of a sample solution has direct effect on the chemical reactions and also on the ability to detect sample molecules such as proteins and DNA. The use of a microfluidic device enables concentrating of the samples in one specific area and hence, it became the key to the success of many biomedical devices (Daghighi, 2015). Another important characteristic of a microfluidic device is that, it enables the mixing of several solutions to obtain a uniform mixture, which otherwise is not easy to achieve. An electrofluidic device is also an integration of metallic patterned or coated microchannels. A microchannel based circuit pattern is a conductive narrow path that connects electrically conducting sample solutions or components. They play an important role in the screen display technologies of the bio-sensing medical devices. Indeed, the use of such wireless patterns make a device light weight, economic and flexible. Again, micro reactors are devices that involve biochemical reactions in microstructures like microchannels with dimensions below 1 mm. Such devices are used in laboratories for development of new catalysts. Also, diagnostic devices use micro reactors for various biomedical applications like cell generation, separation and its detection too. It has the advantage of high efficiency, low-volume utilization and repeatability of processes. Thus, quality of these microchannel based devices is thus a main concern due to their functional necessities. The dimensional precision and surface quality of these micro devices represent the vital quality facets. Thus, microchannel based devices call for the use of materials with high optical, chemical and mechanical properties and accordingly, transparent materials have become a significant material for microchannels fabrication.

Transparent materials like glass, polycarbonate (PC), polyimide (PI), polydimethylsiloxane (PDMS), polymethylmethacrylate (PMMA) etc. are the most trending transparent material. It is due to their eco-friendly nature and high transparency in the visible and near infrared spectral range (Singh *et al.*, 2018). Most transparent materials have a very good resistance to chemical reactions, high thermal stability, and high hardness.

Glass microfluidic devices provide exceptional chemical resistance, biocompatibility and optical properties, in addition to mechanical stability, which prevents swelling and deformation. Glass is the material selected to build microfluidic chips after the early focus on silicon which is relatively expensive and optically opaque to certain electromagnetic wavelengths, limiting its applications in optical detection (Hwang *et al.*, 2019). Hnatovsky *et al.* (2006) fabricated high quality microchannels on fused silica and BK7 glass using the combination of femtosecond laser dielectric modification and selective chemical etching. Also, Rodriguez *et al.* (2003) described two rapid and economic methods for fabricating microfluidic systems in glass. These glass microchannels were then applied in analytical separations, such as capillary electrophoresis where the robust surface characteristics of glass proves it to be a convenient device. However, the high cost and time-consuming labour for fabricating microchannels on glass due to its brittleness limit the development of glass-based microfluidic devices, especially for point-of-care test devices.

PC's inherent impact strength, dimensional stability, optical clarity and eco-friendly nature makes it an ideal material in the medical device industries. Many researchers have reported the fabrication of microchannels in PC (Chen and Hu, 2017; Qi *et al.*, 2009; Singh *et al.*, 2020). PCs dimensional stability makes them valuable for tube connectors. Its ability to transmit light in a large range of wavelength makes it as effective in visual monitoring of blood or other biological fluids. PC plate is used in the manufacturing of microfluidic device that can capture colorectal cancer cells from one of the most common types of human malignant tumours (Kim *et al.*, 2015). It is also used in developing urethane (Polycarbonate Urethane, PCU) that acts as the bearing material in orthopaedic prosthesis, knee prosthesis (Kanca *et al.*, 2018) etc. Such urethane has higher resistance and stability compared to polyester and polyether urethanes.

PDMS's distinguished properties also make it an important material for micro channels. It is optically transparent, electrically and thermally insulating and additionally, it is impermeable to water and organic solvents (Li and Xu, 2015). PDMS-based microfluidic devices enable us to realize microchips for biomedical applications in a relatively easy and cost effective way. Fujii (2002) worked on PDMS-based microfluidic devices for biomedical applications, where micro reactors, microchips for capillary gel electrophoresis and hydrophobic vent valves are successfully integrated into the microchannels. Further, properties of PDMS make it a suitable platform for miniaturized biological devices by fabricating PDMS microstructures (Sia and Whitesides, 2003). Biological procedures that have been miniaturized into PDMS-based micro devices include immunoassays, separation of proteins and DNA, sorting and manipulation of cells, studies of cells in microchannels exposed to laminar flows of fluids, and large-scale, combinatorial screening.

PMMA, also known as acrylic or acrylic glass, is a transparent and rigid thermoplastic material widely used as a shatterproof replacement for glass. It is used in biomaterial applications such as bone cement, lenses, bone substitutes, and drug delivery systems. Smooth walled cylindrical microchannels with diameters in the range of 8-20 μm were fabricated on PMMA substrate by Day and Gu (2005). Dudala *et al.,* (2020) and Prakash and Kumar (2015a) also fabricated microchannels on PMMA substrate using the CO_2 laser for microfluidic applications. Further, PMMA microfluidic device with filtration features was used to separate RBCs (red blood cells) from blood (Li *et al.*, 2008). Microchannels in PMMA substrates bonded to porous PETE track-etched membranes are also utilized for the cytotoxicity testing of anticancer drugs in a microfluidic device (Nguyen *et al.*, 2019).

Observations

PC has high strength making it resistant to impact and fracture, providing safety and comfort in applications that demand high reliability and performance. Further, it maintains toughness upto 140°C and down to –20°C. Also, PC is a clear plastic that can transmit over 90% of light and exhibits good chemical resistance against diluted acids, aliphatic hydrocarbons and alcohols. Offering good heat resistance, PCs are thermally stable up to 135°C. Thus, comprising such unique set of chemical and physical properties makes PC suitable over most transparent materials like glass, PMMA and PDMS.

2.2 Overview of various microchannel fabrication technologies

The fabrication technologies of the microchannels have a strong impact on the ability to implant the microchannels into a small-sized biomedical device. Consequently, the different technologies used for microchannel fabrication on a variety of materials and various applications have been studied by many researchers all over the world and the list is ceaseless. Microchannels are fabricated by both conventional and non-conventional techniques like micro-milling, dry and wet etching, micro-wire molding, lithography, injection molding, electrospinning, imprinting, laser processing, laser-induced plasma-assisted ablation (LIPAA) etc. A graphical representation of the overview of the various technologies used for the fabrication of microchannels on a variety of materials and their applications is shown in figure 2.2.

Although there are many processes, certain processes are predominantly being used, mainly micro-wire molding, lithography, imprinting, direct laser micromachining and laser-induced plasma-assisted ablation (LIPAA) in the industry. These processes have been discussed in in the following sections.

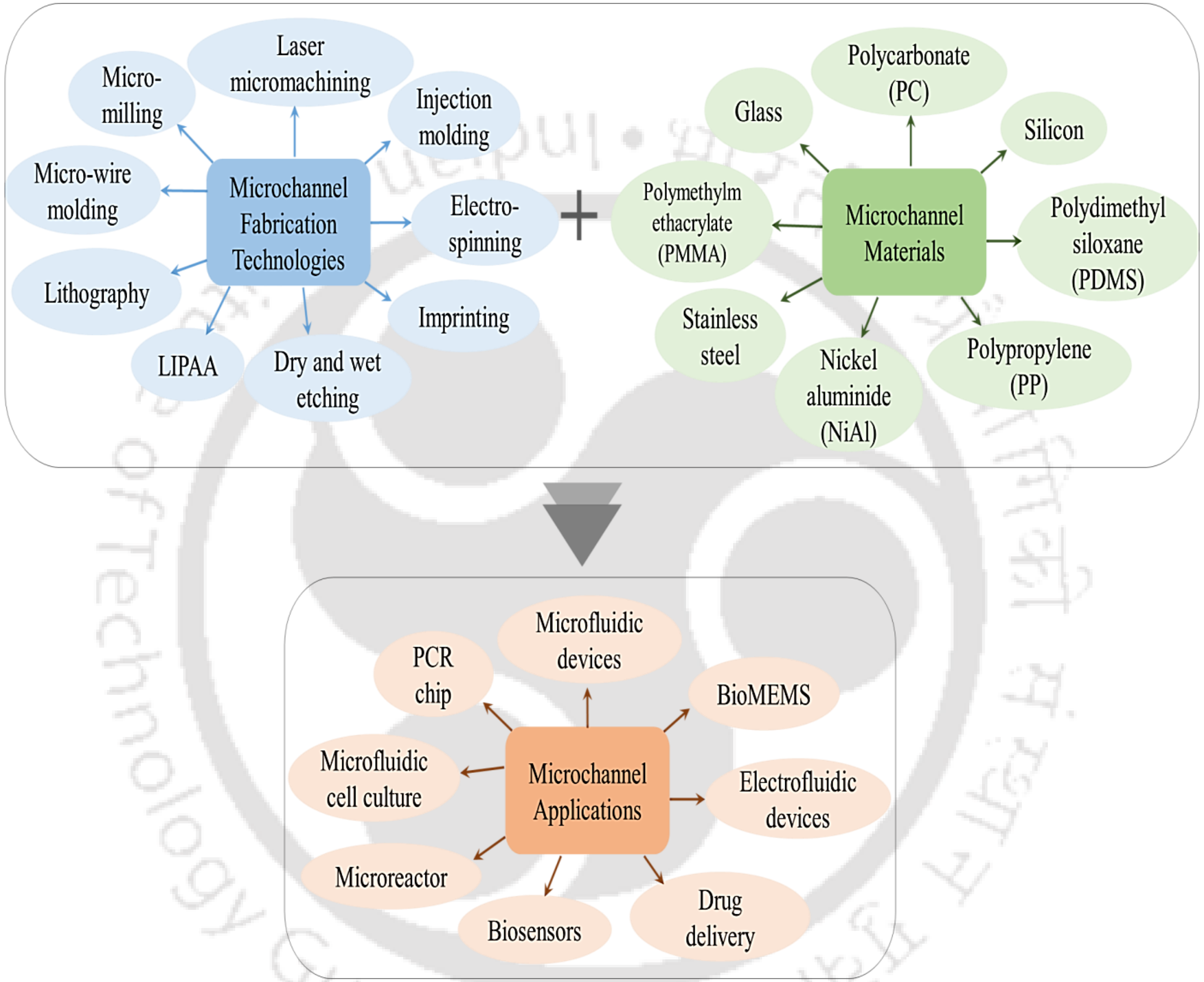

Figure 2.2 Overview of microchannel fabrication technologies, materials and applications

2.2.1 Micro-wire molding

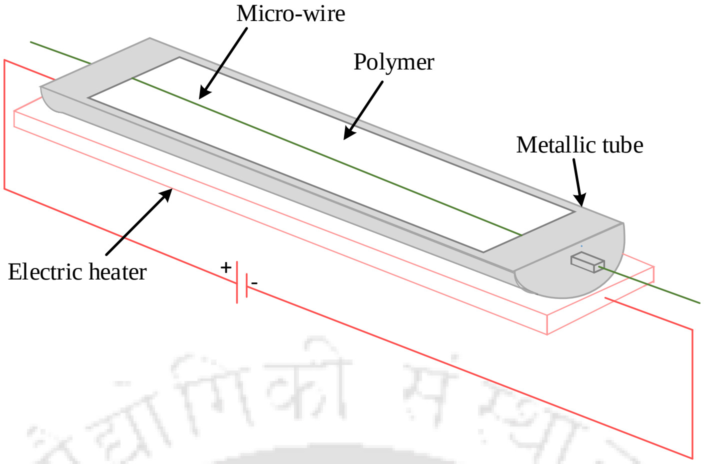

Figure 2.3 Schematic of wire molding

Micro-wire molding is a simple and flexible technique for microchannel fabrication. It utilizes the concept of embedding a micro wire into a degassed polymer and later, removing the wire after the curing of the polymer. Depending on the strategy of the process, the key resources required in this technique are polymers (on which the microchannel is intended to be fabricated), micro wires, a mold of metallic tube and a heating source (Jia *et al.*, 2008). Here, the mold of metallic tube is taken to be of internal diameter approximately 5 mm. The tube is attached with an electric heater to the bottom of it for heating and temperature control. The temperature is maintained depending on the melting point temperature of the polymer. Wires of varying diameter and shape are fixed to both the end of the mold. The degassed polymer mixture is poured into the molding cavity where the wire acts as the axis of the mold. The mold is then closed under hydraulic pressure and the excess degassed polymer material is removed. The mold is held closed until the polymer is cured. Later, on curing the polymer, the mold is opened and the wire is pulled of the polymer and hence the micro channel is obtained. Figure 2.3 shows a schematic representation of the wire molding process.

Several literatures have reported the use of this wire molding technique for microchannel fabrication. Effati and Pourabbas (2018) explained a quick method for the design and fabrication of 3D microchannel by the technique of micro-wire molding. Microchannels on PDMS was fabricated using Nylon and metallic wires of diameter ranging from 150-800 µm. The technique provides the possibility to fabricate microchannels with different cross-sections. The same technique of wire molding has also been utilised by Kumar *et al.* (2018) for fabricating microchannels in PDMS casting using copper wire of 0.21mm diameter. Two different types of inlet sections (L and T types) have been constructed by the technique. Further, YueFei et al. (Jia *et al.*, 2008) utilised the conventional molding capability of PDMS for microchannel fabrication by the wire molding process. It was possible to generate different types of topological structures of the microchannels due to the smooth surface, high-intensity, and high flexibility of the wires. Zou *et al.* (2015) fabricated a new economical microfluidic viscometer to measure the viscosity of biological fluids using the micro-wire molding technique, thereby making the fabrication process easier and cheaper.

2.2.2 Lithography based technology

Lithography is mainly a printing process that is based on the idea of the immiscibility of oil or grease with water. It is simple technique and is the most widely used fabrication technique for microchannels. The key steps involved in the process are coating, baking, exposing and development (Yao *et al.*, 2005). In most of the cases, surface conditioning precedes the step of the surface coating. It prepares the substrate surface to accept the photoresist by providing a clean surface. The substrate is then placed on a vacuum chuck and the resist is applied by the method of spin coating. The speed of the chuck determines the thickness of the resist applied. The thickness of the spin coated layer is usually kept equal to the height of the microchannel. Two types of resists are available, namely positive resist and negative resist. In the positive resist, the portion exposed to the light becomes more soluble, while in the negative resist the portion exposed to the light gets hardened. It is then soft-baked to remove the excess solvents and later cooled to room temperature. The coated substrate is then covered with a mask that has the required pattern on it. Then, it is exposed to a wavelength (light) travelling through the mask, that the resist is designed for. In the region exposed, the resist undergoes a chemical reaction with the light. The substrate is then etched in a suitable solution and thus, the microchannel is finally formed. A simple description of the method is shown in figure 2.4.

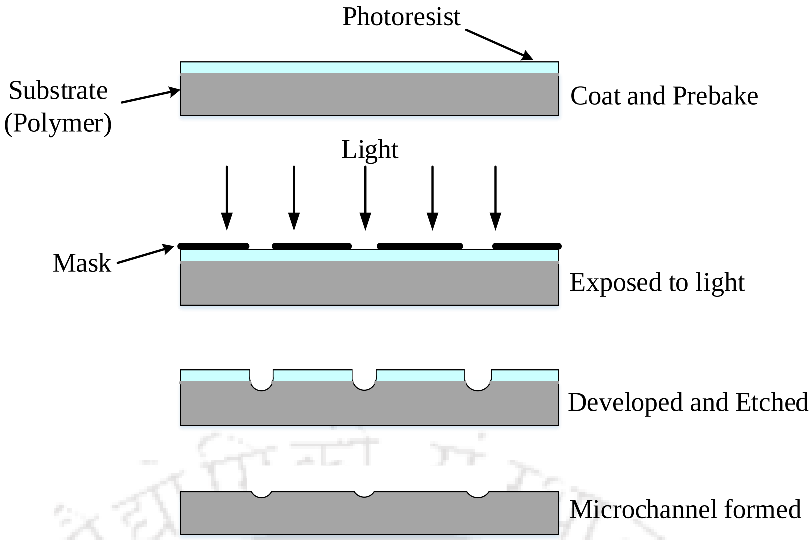

Figure 2.4 Stepwise lithographic process

Literature reports various applications of the lithography technique for microchannel fabrication. Yao *et al.* (2005) performed the lithography process based on an inconsistent combination of resists and standard lithography facilities. They fabricated microchannels using both one resist layer and multiple resist layers and also demonstrated fluid delivery through the channel. McUsic *et al.* (2012) also reported the use of lithography process for the fabrication of bio-inspired pattern microchannel scaffolds. The authors used patterned silicon master and PDMS negative mold casting. The fabricated channels were used for directing the morphogenesis and differentiating the retinal cells derived from mice and human embryonic stem cells. Also, Laviano *et al.* (2010) presented the same technique of lithography to produce an inclined array of microchannel. Further, it was demonstrated how it could be utilised to produce a precise vortex flow in a well-controlled environment. Wang *et al.* (2018) used two cycles of photolithographic and chemical wet etching for the fabrication of micro channel arrays and also capillary connecting channels on glass substrate. The channels after the completion of the fabrication process, were treated with plasma using a plasma cleaner for surface cleaning. The channels were then bonded with a cover plate by dropping ultrapure water at the edge of the substrates. Thus, channels on various materials and of different dimensions can be made utilizing the lithographic technique.

2.2.3 Embossing or imprinting technology

Embossing or imprinting is a technique of creating different structures like microchannel in polymeric matrices, which are complementary to a template in size and shape. It is a simple and cost-effective process that takes into consideration the versatility of the materials to be imprinted (Chen *et al.*, 2015). In this method, a template is first prepared on a silicon substrate mostly by the photolithography method. They are characterized using an optical microscope to determine the effect of the imprinting procedure. The template is then coated with a solution containing biomolecules. It is one of the simplest methods where the template is brought in contact with the plastic or polymer substrate. The plastic or the polymer material is however cleaned and dried before bringing to contact with the silicon template. The whole arrangement of this polymer substrate and the silicon template is then sandwiched between two metallic blocks (Pimpin and Srituravanich, 2012). The imprinting time depends on the material to be imprinted and also on the temperature and pressure applied between the two metallic blocks. The process when carried out at room temperature, the pressure and time required are high, while performing the process at a high temperature requires less time and pressure. The metallic blocks are subjected to a hydraulic press, varying the pressure between 450 to 2700 psi at room temperature (Xu *et al.*, 2000). On releasing the pressure, open microchannels are formed on the substrate. The difference in the dimension of the template before and after the imprinting process is generally less than 1%, which indicates the absence of detrimental effect on the fabricated microchannels. Figure 2.5 shows the schematic of the imprinting technique.

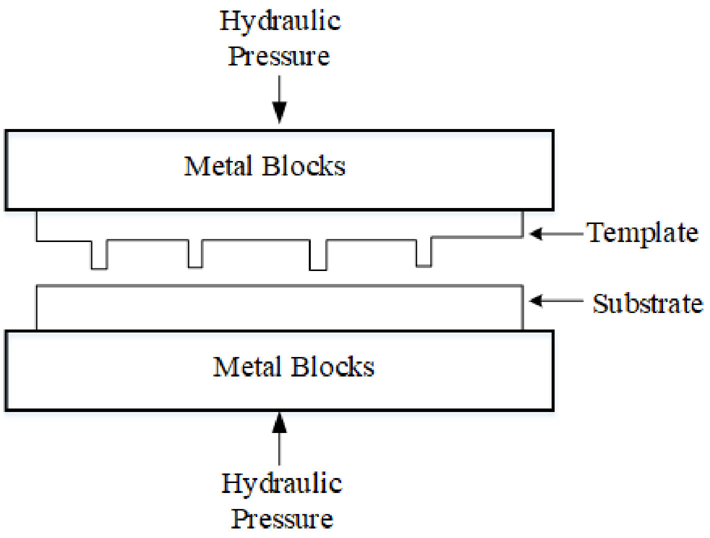

Figure 2.5 Schematic of the imprinting technique

Researchers carried out several experiments on fabricating microchannels by the technique of embossing or imprinting. Xu *et al.* (2000) adopted the room-temperature imprinting method for microchannel fabrication on a variety of plastic substrates. They showed that this method improved the device yield from approximately ten devices to above 100 devices per template. Indeed, the number of devices produced by the single template showed a variation of less than even 2 %. Zhai *et al.* (2014) presented the fabrication thin glass/PDMS microfluidic coupled with a monolithic capillary column. In the fabrication process, a copper mold with a microchannel network imprinted on it was utilised. Lei and Tong (2005) also employed the technique of imprinting, however instead of utilizing a conventional mold with microchannel embedded on it as the template, authors used a stainless steel wire mold of outer diameter 105 μm. This makes the technique more flexible.

2.3 Laser based fabrication technologies

In laser machining, the material removal takes place due to the application of thermal energy converted from the light energy of a highly coherent beam of photons. When a laser beam irradiates a material, a fraction of the laser energy (light energy) gets absorbed, while the remaining part gets reflected. The absorbed portion of the energy gets converted to heat energy instantaneously and leads to a rise in temperature in the irradiated zone (Dahotre and Hamirkar, 2008). When the laser energy is sufficiently high enough, it further leads to the melting and vaporization of the material. The vapour thus formed from the vaporization induces a recoil pressure at the surface of the melt pool, which results in melt ejection and hence, lastly the material removal is obtained (Vora *et al.*, 2013). A laser based technology is generally suitable for materials that are capable of absorbing laser energy. However, most microchannels demand the use of transparent materials due to its high visibility. High transparency of the transparent material does not allow laser energy to be absorbed and hence, it is difficult to process the transparent materials by using lasers. Nevertheless, ultrashort lasers are capable of processing transparent materials as they produce highly localized light field that is absorbed into the transparent material by non-linear absorption, which is sufficient enough to ionize any atom. Similar to ultrashort lasers, short wavelength lasers have shown the ability to process transparent materials, provided this lasers have to be applied repeatedly at optimum process conditions (Singh *et al.*, 2018).

McCann fabricated micro-channels on cyclic olefin polymer using an industrial 1064 nm Nd: YAG laser (McCann *et al.*, 2016). The ability to vary the channel width and channel depth by varying the laser fluence was demonstrated. Prakash and Kumar (2017) obtained rectangular cross-section micro-channels on PMMA by CO_2 laser.

Authors described how with the application of a mask, micro-channels with U-shape cross-section and rectangular cross-section can be machined by a CO_2 laser. The technique was found to provide better control of channel dimensions and also, better surface quality of the micro-channels. Wu *et al.* (2019) also tried to overcome the difficulty of fabricating trapezoidal cross-section micro-channels by CO_2 laser. Multi-pass translational method was utilized and was observed that the technique was able to produce clean bottom micro-channels. Micro-channel fabrication on alumina using Nd: YAG laser writing was presented by Mohammed *et al.* (2019). The best inputs of process parameters for fabricating micro-channels by optimization using RSM and Lipschitz sampling were selected. It was found that laser intensity and pulse overlap are the major controlling parameters in micro-channel fabrication. Likewise, Singh *et al.* (2018) reported the fabrication of microchannels on transparent PC by using nanosecond Nd: YAG laser and further, produced closed channels by the method of thermal bonding. The effect of the laser fluence and the number of laser scans on the channel width, depth and its cross-section was studied. It was observed that laser fluence below the ablation threshold resulted in bulging and bubble formation. However, due to the incubation effect, ablation on the PC material was induced by repeated laser shots. Zhou *et al.* (2014) presented the technique of laser micro-milling for fabricating micro-channels with different geometry and dimensions on copper. Bulushev *et al.* (2016) employed high speed femtosecond laser to process BK7 glass. It was found that crack free reticles and micro-fluidic structures fabrication were possible without the requirement of additional post-processing. Further, Hammadi (2020) used third harmonic radiation of Nd:YAG laser to fabricate micro-channels on UV photoresistive material.

Observations

Though the mentioned techniques like micro-wire molding, lithography, embossing, laser direct machining etc. are capable of machining microchannels on a variety of materials, there are certain limitations too. Micro-wire molding, despite being a flexible method, has a higher volume of waste due to the overflow of the degassed polymer from the mold. Also, the mold complexity and its maintenance make it an expensive and time-consuming process. While the disadvantage of using lithography for microchannel fabrication is that the substrate usually absorbs the development solution. Moreover, its requirement of a room preventing UV radiation make it an expensive process. Limitations in the imprinting technique also arise due to the slow mass transport and permanent entrapment of the material into the metal blocks, leading to the heterogeneous distribution of material and also inadequate properties. Laser direct machining has however been found as a promising tool if it is applied with proper setting of laser parameters such as laser power, pulse repetition rate, pulse duration and laser scanning speed. It is known that laser beam must be highly absorbed to achieve ablation. For high absorption, short wavelength (high energy photons) and short pulse width in the sub-picosecond range were first attempted, but such laser faced difficulties due to its high capital cost. Also, small beam diameter results in low material removal rate and slow scanning process. For research and other applications, the development of a new fabrication technique of glass was desired and hence, in 1998 a group of Japanese scientists invented laser-induced plasma-assisted mechanism, which may have the potential to process transparent materials.

2.4 Laser-Induced Plasma Assisted Ablation (LIPAA)

For microchannel fabrication using lasers, it is essential that the laser must be highly absorbed by the material. On the other hand, materials preferred for microchannels are mostly transparent materials like glass, PC, PMMA and PDMS. Due to the high transparency of such material, laser beam energy does not get absorbed in the material and as such, it passes through the material leading to no thermal effect. However, such materials are absorptive at very low wavelength and also at shorter pulse. Consequently, laser processing of transparent materials with long pulsed and long wavelength lasers is quite difficult to achieve. It is reported that, during Laser Induced Plasma Assisted Ablation (LIPAA), both longer and shorter laser pulses of wavelength may be applied to process the transparent materials. In the LIPAA process, an additional absorbing layer is placed beneath the transparent material. Based on the medium of the absorbing layer, the LIPAA process can be classified into three categories (i) LIBWE (Laser Induced Backside Wet Etching), (ii) LIBDE (Laser Induced Backside Dry Etching) and (iii) LESAL (Laser Etching at a Surfaced-Adsorbed Layer). In LIBWE, a highly absorbing solvent for the used laser wavelength is applied beneath the transparent material. It is characterized by low etching rate, low surface roughness and incubation effect (Zimmer and Böhme, 2008). In LESAL, a thin absorbing layer is continuously formed on the rear side of the transparent material by adsorbing hydrocarbon products from a gaseous organic medium. It is characterized by very low etching rate, low surface roughness, and incubation effects (Ehrhardt *et al.*, 2012). And in LIBDE, a thin metal is placed underneath the transparent material. It is characterized by high etching rate and no incubation effects are found (Hopp *et al.*, 2007). Incubation effect characterizes the laser ablation process when using trains of pulses and strongly influences the ablation threshold, leading to the reduction of the threshold fluence as a function of the number of impinging pulses. Figure 2.6 shows the principal experimental setup for the three categories of LIPAA.

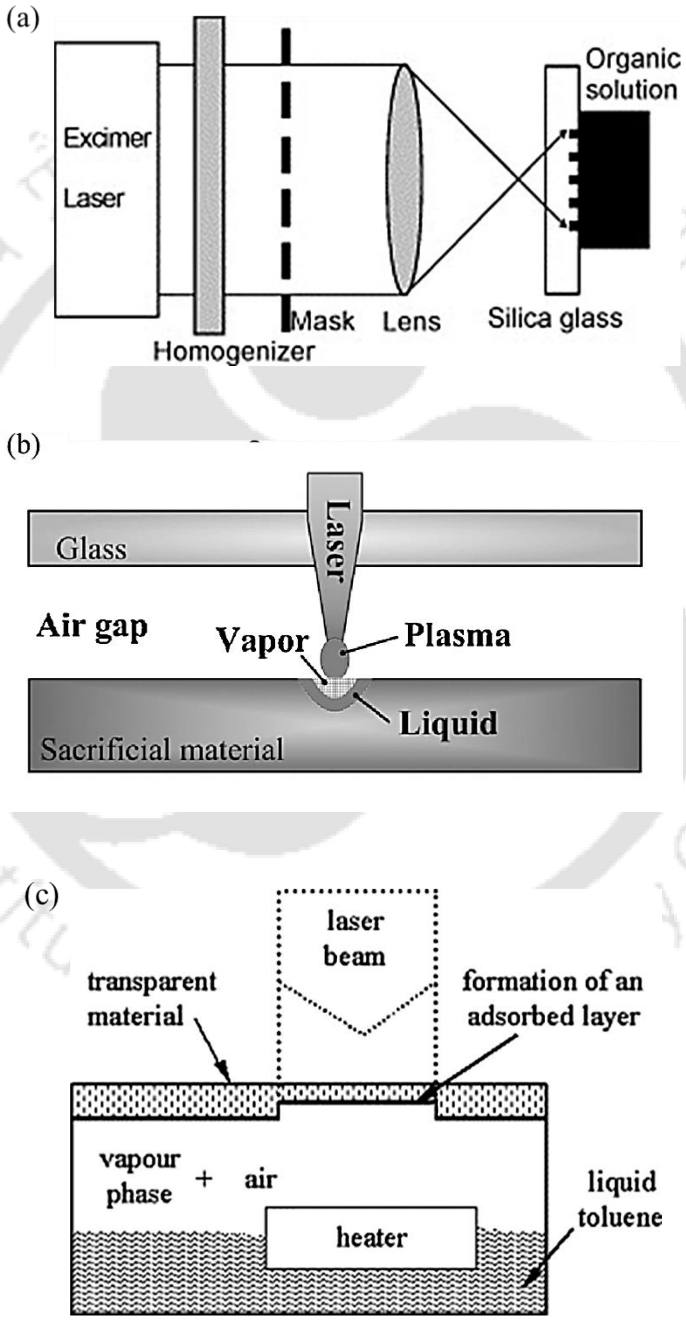

Figure 2.6 Principal experimental setup for (a)LIBWE, (b)LIBDE and (c)LESAL (Ding *et al.*, 2004; Pan *et al.*, 2017; Böhme and Zimmer, 2004) (Reproduced with permission from Elsevier)

Kopitkovas *et al.* (2007) adopted LIBWE for the fabrication of three-dimensional structures, such as micro lens arrays on UV transparent materials like quartz using an organic solution as an absorbing layer on the rear side of the quartz. Also, Kim and Park (2017) reported successful generation of circuit patterns on glass using the LIBWE process. Further, Zimmer and Böhme (2008) performed high quality etching of transparent materials by LIBWE approach using hydrocarbon and metallic liquid absorbers. Authors observed that the processing parameters, the achievable patterns, and the surface morphology have a strong dependance on the used absorber. Again, Ehrhardt *et al.* (2012) studied the alterations of the optical properties of LESAL-etched fused silica samples. It was reported that such changes are important for the etching process, because they cause the laser energy absorption in a very small near-surface volume, resulting in extremely high energy densities. The same group further investigaed the influence of the processing parameters like laser wavelength and laser fluence on the etch rate and the surface roughness for etching of fused silica, quartz, sapphire, andmagnesium fluoride (MgF_2) during the LESAL process (Böhme *et al.*, 2006).

LIBDE on the other hand is often denoted by the general term LIPAA. Pan *et al.* (2017) and Xu *et al.* (2017) employed LIPAA to fabricate microchannels for microfluidic and electrofluidic devices respectively. A research group from Nothwestern University compared the machining capability of laser direct machining and laser-induced plasma machining (Pallav *et al.*, 2014). It was revealed that laser-induced plasma machining provides better machining with improved geometrical characteristics, high aspect ratio, minimal built-up edge, etc. Similar observations were reported by Bhandari *et al.* (2019). Laser induced plasma can also be utilised for micro-drilling as reported by Paul *et al.* (2007) and Bulgakova *et al.* (2011). Both the research groups used nanosecond lasers to generate the plasma plume and carried out micro-drilling of opaque and transparent solids. Further, a research group from Russia carried out surface modification of amorphous and crystalline materials with the aid of the laser induced plasma (Zakoldaev *et al.*, 2015; Shkuratova *et al.*, 2018).

2.4.1 Experimental investigation on LIPAA

Literature reports several investigations carried out on the experimental studies on LIPAA of various materials. Zhang *et al.* (1998) reported the novel method of LIPAA for micromachining fused quartz using the fourth harmonic of Nd:YAG laser. A series of experiments were performed to find the dependence of ablation rate and threshold laser fluence on parameters such as laser fluence, the number of pulses and the distance between the fused quartz and the metal target. Zhang *et al.* (1999) also fabricated high quality micro-grating structures and holes in fused quartz and pyrex glass and reported the dependence of ablation depth on laser fluence and distance between the target and the substrate material. Increasing the distance between the target and the substrate and also the laser fluence, results in decrease and increase in ablation depth respectively. They indicated that either energetic species in the plasma or thin metal film deposited is responsible for glass ablation. Hong *et al.* (2001) focused at the various applications of LIPAA such as different colour and tones of laser printing by varying the target metal and the gap distance, picture printing, non-crack surface printing and metallization on glass substrate. Hanada *et al.* (2004) reported an improvement in the selective metallization with the use of an encapsulated film of oil based black ink. The same research group further utilised the LIPAA process for scribing of sapphire substrate (Hanada *et al.*, 2005).

Pan *et al.* (2017) reported a combined process of LIPAA with chemical corrosion to fabricate micro-channels with micro-texture surface on glass. They investigated the effect of chemical corrosion parameters on the micromorphology of micro-texture. Also the effect of scanning cycles, scanning speed, pulse power density and the gap distance between the glass and the target metal on the channel geometry and chemical corrosive rate was investigated. Recently, Xu *et al.* (2017) also proposed a combined process of LIPAA with successive electroplating to fabricate an electrofluidic device. They fabricated microchannel on the glass by the laser plasma plume using graphite as the target metal. A graphite film thus sputter coated on the rear side of the glass results in strong adhesion of Ni pattern after being electro plated. The electroplating was found to be helpful in enhancing the conductivity of the metallized pattern. Lorenz *et al.* (2014) reported a laser-induced front side etching process for fabrication of sub-µm structures on glass fibre surfaces using a thin absorbing metal layer of high absorbing co-efficient. The analysis of the surface structures presented that the laser-induced front side etching method allowed successful fabrication of well-defined periodic sub-µm structures. Furthermore, the structuring process was simulated by a thermodynamic equation including an approach of the laser–plasma interaction.

Investigations were also carried out for backside wet etching where the metal targets are replaced by strong absorbing aqueous solution. Kopitkovas *et al.* (2007) fabricated complex structures on UV transparent materials like quartz using conventional

XeCl excimer laser and an organic solution. They reported that roughness of the etched surface varied between 10 to 200 nm and depends on the laser fluence and pulse duration. Also the influence on the etching mechanism due to the formation of carbon deposits was discussed. Niino *et al.* (2006) fabricated well-defined deep trenches without crack on fused silica plates. Kim and Park (2017) fabricated circuit patterned glass by backside wet etching followed by electroless plating. Further, Vass *et al.* (2015) carried out comparative study on grating fabrication by backside wet etching and direct ablation by ultrashort laser pulses. Tsvetkov *et al.* (2017) investigated the mechanism involved in single-pulse laser-induced backside wet etching of silicate glass. The study showed significant differences in the mechanism of crater formation in the “soft” mode (laser fluence < 150-170 J/cm^2) and in the “hard” mode (at higher laser fluencies). Accurate craters with good pulse to pulse reproducibility of their shape and smooth walls were obtained in “soft” mode which was not obtained in “hard” mode. Hopp *et al.* (2009) carried out a comparative study for laser-induced backside dry and wet etching of transparent material using solid and molten tin as absorbers. It showed that etch rate was same for both the method for the first pulse. However for successive laser pulses, etch rate was seen decreasing for dry etching while for wet etching it was maintained constant. It was found that decreasing etch rate was due to residual tin incorporation near the fused silica surface. Ehrhardt *et al.* (2017) studied the confinement effect of thin liquid and solid hydrocarbon absorber films with different thickness at the laser induced backside etching. It was noted that the phase of the absorber (solid or liquid) does not influence the principle backside etching characteristics, whereas the thickness of the absorber at the interface influences the etching rate.

Observations

From the available literature, it can be noted that most of the research related to laser processing of transparent materials employ ultrashort pulsed lasers or lasers of short wavelength. Though, the ultrashort lasers produce clean and quality micro-channels, they are expensive and provide low material removal rate. Moreover, their ablation capability is also restricted to a few hundreds of nano meter. Very scant work has been reported on the use of LIPAA process in the fabrication of microchannels on PC. Also, it has been obsevered that limited work on the study of the effect of the laser process parameters on the channel dimensions and surface quality during LIPAA process has been reported. Moreover, the application of millisecond pulsed lasers during LIPAA for the fabrication of microchannels on PC was also found to be very limited. It can also be observed that there has been limited research on the investigation of the effect of the metal target properties on the geometrical characteristics of the microchannels produced during the LIPAA process.

2.4.2 Numerical investigation on LIPAA

After reviewing the literature on experimental studies of LIPAA, a literature survey on numerical studies of LIPAA was also carried out. But there was scant work reported on numerical study of LIPAA. As per the mechanism of LIPAA, the ablation of the transparent material is mainly governed by the thermal energy generated by laser–induced plasma. Thus, some important literature related to numerical investigation on laser direct machining and literature relevant to the principle of LIPAA have been studied.

Literature reports various numerical studies on the laser machining process using finite element method (FEM) and finite difference method (FDM). Zhao and Shin (2013) extablished a 2D axisymmetric hydrodynamic model to study the ablation mechanism of of silicon by a femtosecond (fs) laser at both low and high laser fluence. They calculated the ablation depth of the silicon wafer ablated in air at different laser fluence and carried out the corresponding experimental measurements for validation. It was observed that, while two-photon absorption dominates in the low fluence regime (<2 J/cm^2), electron heat diffusion is a major energy transport mechanism at higher laser fluences (>2 J/cm^2). Tani *et al.* (2008) developed a 3D numerical model to predict the physical phenomena involved in laser ablation of metals taking into account the heat distribution in the work piece, the velocity of the vapor/liquid front and the physical state of the plasma plume. The simulations made it possible to predict the ablated workpiece volume and the shape of the resulting craters for a single laser pulse or multiple pulses and also for any path of the laser spot.

Again, Linsen and Guoquan (2012) have built a laser drilling thermodynamic model based on the characteristics of the laser drilling and processing environment. The temperature field is simulated by using the finite element analysis software ANSYS. The influence of the different drilling parameters on the laser drilled hole quality are analyzed and predicted from the temperature field distribution, which provides a basis for selecting the optimal parameters of the laser drilling. They assumed a Gaussian heat flux and also took into consideration the phase change. The temperature field is determined by solving the two dimensional nonlinear transient heat balance taken as:

$$\rho c \frac{\partial T(x,y,t)}{\partial t} = k\frac{\partial^2 T(x,y,t)}{\partial x^2} + k\frac{\partial^2 T(x,y,t)}{\partial y^2} \tag{2.1}$$

where k is the thermal conductivity, ρ is the density and c is the specific heat capacity

In the boundary conditions, the phase change interface and peripheral change interfaces are described as:

Phase change interface: $$k\frac{\partial T(x,y,t)}{\partial t} = -\alpha I(x) - \rho L_v v_r \tag{2.2}$$

where α is the absorption coefficient, L_v is the latent heat of vaporization, v_r is the speed of the vapour molecules during phase change.

and, peripheral interfaces: $$-k\frac{\partial T}{\delta n} = h\left(T - T_0\right) + e\sigma\left(T^4 - T_0{}^4\right) \tag{2.3}$$

where, $\frac{\delta T}{\delta n}$ is the rate of change of temperature along outside the normal, h is the convective heat transfer coefficient, e is sample surface emission coefficient and σ is the Blackbody radiation constant.

Further, Yang *et al.* (2010) developed a 3D transient finite element model for a moving Gaussian laser beam to predict the temperature, depth and the width of the heat affected zone on the Ti6Al4V alloy. Authors considered the heat generation per unit volume and also the velocity of the workpiece assuming Gaussian mode of laser beam. The three-dimensional heat conduction equation that governed the heat generation during the process has been described as:

$$\rho c\left(\frac{\partial T}{\partial t} + U\frac{\partial T}{\partial y}\right) = \frac{\partial}{\partial x}\left(k\frac{\partial T}{\partial x}\right) + \frac{\partial}{\partial y}\left(k\frac{\partial T}{\partial y}\right) + \frac{\partial}{\partial z}\left(k\frac{\partial T}{\partial z}\right) + Q \tag{2.4}$$

where, ρ, c, k, Q,U are the density, specific heat, thermal conductivity, heat generation per unit volume and the velocity of the workpiece respectively.

Acherjee *et al.* (2012) reported numerical analysis on the laser transmission welding of PC. The impact of the laser parameters on temperature distribution and weld bead dimensions via finite element (FE) modeling of the process was studied. The thermal field has been simulated by solving a three dimensional transient heat diffusion equation with temperature dependent material properties:

$$\rho . c \frac{\partial T}{\partial t} = \vec{\nabla}\left(k \vec{\nabla} T\right) + q_v \tag{2.5}$$

where ρ is the material density (kg/m^3), c is the specific heat (J/kgK), T is the temperature (K), t is the time (s), k is the thermal conductivity (W/mK), q_v is the rate of internal heat generation (W/m^3) and ∇ is the gradient operator. Further, the combination of convection and radiation boundary conditions into a single boundary condition was considered as:

$$-k\left(T\right)\vec{\nabla} T\, \vec{n} = h_r\left(T_s - T_0\right) \tag{2.6}$$

where h_r is the combined heat transfer coefficient that can be expressed as:

$$h_r = h + \varepsilon \sigma \left(T_s + T_0\right)\left(T^2_s + T_0^2\right) \tag{2.7}$$

Similarly, Ai *et al.* (2018) reported the development of a 3D transient numerical modeling of welding of polyethylene terephthalate and titanium alloy by laser transmission process. The melting and the fluid flow during the process was considered in the model to predict the weld geometry and porosity formation.

Literature also reveals several attempts on the numerical study of laser-induced plasma micromachining and the role of laser-induced plasma properties in its material removal behaviour. Saxena *et al.* (2014) established a 3D model to determine the spatial and temporal distribution of a Gaussian-pulsed laser–induced plasma for understanding the material removal procedure during laser-induced plasma micromachining. The simulation further predicted the distribution of plasma energy density, absorption coefficient and laser intensity within the focal region. The study revealed that laser-induced plasma in a condensed media exhibits unsymmetrical spatial distribution along the direction of beam propagation and shifts the plasma toward the direction of incidence. Also, Fabbro *et al.* (1990) analysed the different physical phenomena involved in laser-produced plasma in a confined geometry. They developed a model which described the various steps involved in this process and also compared it to the direct ablation regime. It was observed that during the laser heating, the generated pressure for laser induced plasma is typically 4–10 times greater than the corresponding one obtained in laser direct ablation. Further, Rajendran *et al.* (2007) developed a model for nanosecond pulse ablation of an aluminum target in vacuum for cases when the laser beam absorption by the plasma above the target is not significant. The model described the laser-solid interaction that results in target heating and vaporization leading to ablation. It was observed that, the laser solid interaction plays a dominant role in ablation for lower laser fluences whereas the plasma plume expansion above the target plays the major role for higher fluences. An end-to-end modeling procedure was formulated by Keidar *et al.* (2004) to predict the plasma plume structure generated by a micro laser-ablation plasma. The plasma formation model was based on a fluid approach and the plasma plume was modeled using a Particle-in-cell plus direct simulation Monte Carlo (PIC-DSMC) approach. Further, Lorenz *et al.* (2012) presented both front and back side etching of fused silica using a chromium absorbing layer. A 2–dimensional model was used to analyze the interaction of the laser radiation with the metal/fused silica system to estimate the etching depth and the dependence on the laser fluence by using finite element method (FEM). Authors described the laser heating of the solids as :

$$\rho C\frac{\delta T(x,z,t)}{\partial t}-\nabla\left(k.\nabla T\left(x,z,t\right)\right)=Q(x,z,t)=\frac{\phi_q(x,t)}{\Delta tp}.\alpha.\exp\left(\pm\alpha\left(z-z_0^{f,b}\right)\right) \tag{2.8}$$

where –ve is denoted for front side etching (*f*) and +ve for back side etching (*b*); T denotes temperature, Q is the laser-induced heat power, x and z are spatial coordinates, ρ is the density, C the heat capacity, k is the thermal conductivity, α the absorption coefficient and φ_q is the laser-induced heat fluence.

A three-dimensional thermal model was also established to simulate the material removal during the LIBWE process by considering the material data variations of temperature, enthalpy change and latent heat fusion by Xie *et al.* (2017). The developed model could predict the groove shape influenced by the laser processing parameters like laser fluence, scanning velocity and scanning pass. It was observed that the groove depth increases with decreasing scanning velocity and increasing laser fluence and number of scanning passes. Vass *et al.* (2004) studied numerically the micromachining process of transparent material fused silica by laser-induced backside wet etching (LIBWE) process. Authors calculated the maximal depth of melted fused silica layer by numerical solution of the one-dimension heat flow equation taking into account the phase transformations of the liquid reagents and the fused silica target. From the study, it was concluded that the thickness of the melted quartz layer depends linearly on both absorption coefficient of the liquid and laser fluence. Again, Jiao and Wang (2008) reported that in order to reduce the possibility of fracture in the process of cutting glass by lasers, the thermal stress has to be less than the critical rupture strength. For the purpose, a numerical model of machining glass by laser beam using a finite element analysis was developed. The distribution of the thermal stress and the temperature was simulated and the thermal stress was studied both when the glass sample was machined by a single CO_2–laser beam and by dual CO_2–laser beams. It was observed that the thermal stress can be reduced by means of the dual-laser-beam method. Similarly, the process of nano-drilling of fused silica was also simulated by finite element method using a thermodynamic model by Lorenz *et al.* (2015). Similarly, Moradi *et al.* (2021) developed a numerical simulation of the laser cutting of a 3.2 mm thickness PC sheet using finite element method. The developed analysis could predict the depth of kerf in a continuous mode for different values of laser power, speed and laser focal plane and as such, the effect of these parameters were investigated on the top and bottom kerf width, the ratio of upper kerf width to lower kerf width and taper kerf.

Observations

From the literature, it can be observed that several attempts on the numerical study of laser-induced plasma micromachining and the role of laser-induced plasma properties in its material removal behaviour have been reported. Further, numerical study on laser direct and laser transmission processes of various materials are also described in several pieces of literature. However, limited work in the simulation study of the LIPAA process have been reported. Scant 2D or 3D numerical study of the LIPAA process has been carried out embracing the influence of the plasma together with the incoming laser beam on both the transparent material and the metal target.

2.5 Process parameters

Laser machining or ablation is mainly controlled by lasers parameters and workpiece material properties. Figure 2.7 shows the parameters affecting the quality of the laser ablation. Effect of these parameters have been discussed in the following sections:

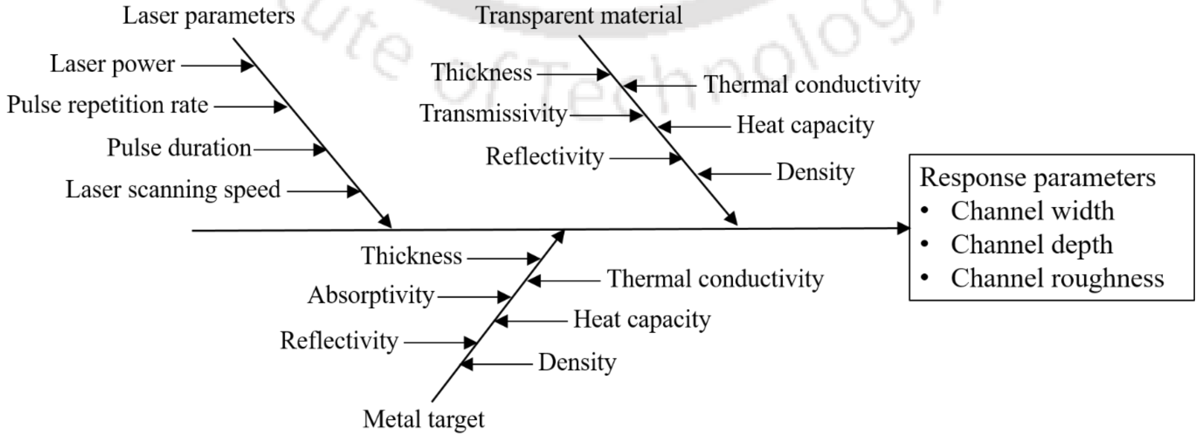

Figure 2.7 Parameters affecting the ablation quality

2.5.1 Laser parameters

In order to achieve maximum efficiency and best quality laser machining or ablation process, it is important to employ optimum laser parameters. Laser parameters that have an influence on the process involve laser power, pulse repetition rate, pulse duration, scanning speed and beam geometry. The effects of these parameters are discussed as follows:

(A) Laser power

The laser power is a parameter that has direct control on the laser heat flux density and laser energy input into the workpiece material. An increase in the laser power results in the increase in heat flux density and energy input. Salama *et al.* (2016) reported an investigation into the effect of laser power on HAZ and ablation depth during laser machining of carbon fibre-reinforced polymer (CFRP) composites. The experimental study shows that the HAZ and ablation depths reduce as the laser power reduces. Also, Bogaerts and Chen (2005) found that target heating, melting and vaporization, vapor and background gas density, plume expansion velocity and temperature, ionization degree and densities of ions and electrons in the plume, and hence also the plasma shielding, all increase with the increase in the laser power. Likewise, Samant and Dahotre (2008) reported that the temporally and spatially intense and restricted heat source of laser power provides an extremely efficient method to increase the temperature of the work piece making the machining process convenient.

(B) Pulse repetition rate

When a laser is running in pulsed mode, the number of pulses per second or frequency of pulses is known as the pulse repetition rate (PRR). The term PRR and pulse frequency are commonly used. The pulse repetition rate controls the heat input per unit time and plays a significant role in the size of the heat affected zone. With increasing pulse repetition rate, more effective number of pulses irradiate the workpiece surface, resulting in better overlap of pulses which leads to a smoother cutting edge or microchannel formation (Tan *et al.*, 2009). RAČIUKAITIS *et al.* (2009) reported that the ablation threshold of metals (aluminum, copper, stainless steel) and silicon depended on the number of pulses affecting the area. The reduction in the ablation threshold with increasing pulse repetition rate is found to be useful in application of the high repetition-rate lasers with the low pulse energy in order to increase the processing efficiency.

Further, Cheng *et al.* (2009) and Schille *et al.* (2010) also indicated that higher pulse repetition rate results in lower ablation thresholds accompanied with higher ablation rates due to the combined effects of plasma, residual thermal energy and phase transition.

(C) Pulse duration

Pulse duration is the measure of the time between the beginning and end of the pulse, typically based on the full width half maximum (FWHM) of the pulse shape. It directly controls the pulse energy and the average laser power. An increase in the pulse duration results in a decreased ablation rate and it is due to the decrease in laser peak intensity with increasing pulse width (Chien and Gupta, 2005). Le Harzic *et al.* (2005) reported that ablation thresholds and penetration depths are deduced as a function of pulse duration. Increasing pulse duration increases the threshold fluence and reduces the effective energy penetration depth. Moreover, the machined feature quality is improved as the pulse width becomes shorter and consequently, the peak intensity becomes higher (Chen and Liu, 1999). Pulse duration not only affects the ablation rate and penetration depth, but it also has control on heat-affected damage of the material. Shorter pulses reduce heat-affected damage of the material and opens new ways for nanometer accuracy (Meijer *et al.*, 2002).

(D) Scanning speed

Scanning speed controls the heat input per unit length and the time of interaction of the laser beam with the workpiece material. In other words, the laser energy per unit area is determined by the laser scanning speed. A higher scanning speed results in less irradiation of the laser beam in a specified area. Thus, there will be less thermal effect on the on the workpiece material, resulting in less laser beam penetration into the material. Also, the successive laser pulse moves far away from the former laser pulse. As such, there will be less overlapping of the laser pulses and smaller heat affected zone at higher scanning speed. Also, Salama *et al.* (2016) observed that scanning speed plays a dominating role in controlling the HAZ size and ablation depth.Authors showed that minimum HAZ and ablation depth was achieved at a very high scanning speed. The scanning speed not only affects the HAZ and penetration depth of the laser beam, but also plays an important role in the formation of a channel. For a channel to be formed, the pulse overlap must be greater than zero. For pulse overlap less than zero, discrete crater formation will occur. The effect of these pulse overlap is called the jump effect

(Pan *et al.*, 2017). The overlap distance or the distance between two laser pulses, D_L and the overlap, O are given by (Vora and Dahotre, 2015):

$$D_L = \frac{v}{f} \tag{2.9}$$

$$O = \left(\frac{\omega - D_L}{\omega}\right) \times 100\% \tag{2.10}$$

where, ω is the focussed beam diameter, D_L is the overlap distance, v is the scanning speed and f the pulse repetition rate.

Further, Schnell *et al.* (2020) demonstrated that ablation threshold depends on pulse overlap as well as on the fluence. Also, high pulse overlap cause extended phase explosion and heat accumulation which ultimately leads to a decrease of the ablation threshold.

Observations

Laser machining has been found as a promising tool if it is applied with proper setting of laser parameters such as laser power, pulse repetition rate, pulse duration and laser scanning speed. Laser parameters are the main controlling parameters, having non-linear interaction among themselves and with the workpiece material properties. The effect of combinations of laser parameters on the performance parameters such as ablation width, ablation depth and roughness of the ablated area is thus difficult to generalize. Besides, it can be observed that scant work has been carried out on the effect of these parameters for obtaining an optimal set of process parameters especially during the LIPAA process. This may thus be of interest to improve the productivity and product quality of the process.

2.5.2 Workpiece material properties

During laser based machining, the material ablation is a thermal process. The temperature distribution is mainly responsible for the desired process outcome. The thermal and optical properties of the workpiece materials have a major effect on the laser ablation process. The important materials properties are discussed below:

(A) Optical property

Absorptivity is an optical property of a material, which describes how much light can be absorbed in a material in relation to an amount of light incident on the material. Absorptivity depends on the wavelength and direction of the incident light, type of the material (metal, plastic, etc.), chemical composition and structure of the material, and state of the material and its surface (temperature, surface roughness, degree of oxidation and contamination). Absorptivity (A) can be calculated as:

$$A = 1 - R - T \tag{2.11}$$

where R is the reflectivity and T is the transmissivity of the material.

The laser beam does not get absorbed by the workpiece surface completely. A fraction of the beam is absorbed into the material, while the rest is reflected to the surrounding. Increase in absorptivity increases the laser energy input into the workpiece surface. The absorbed energy excites free electrons, which is instantaneously converted into heat in a time duration of about 10^{-13} s (Dahotre and Harimkar, 2008). The heat then dissipates through various heat transfer modes such as conduction, convection and radiation; however, the conduction plays the most significant role (Mishra e*t al.*, 2019). The heat conducted into the metal surface increases the temperature of the surface, thereby supporting the laser ablation process. Lawrence (2002) found that a high-power diode laser is more efficient than a CO_2 laser because the wavelength of the diode laser is small, which enhances the absorptivity as most materials are highly absorbing at low wavelength. In general, the metals have low absorptivity, however it increases due to the presence of rust, oxides, dust, contaminants, grease, oil or other foreign particles. Similarly, Li *et al.* (2007) investigated the effect of the absorptivity of metal on femtosecond pulsed laser ablation. It was observed that the absorptivity of the material increases with the temperature evolution with time and as such, an increase in the ablation is achieved.

On the other hand, transparent materials are highly transmissible to laser beams in the visible and near-infrared wavelength range. The laser beam transmits through the transparent material uninterrupted, thereby causing no thermal effect on the material. However, transparent materials like glass and polymers exhibit high absorptivity in UV and infrared wavelength range (Singh *et al.*, 2020). Researchers around the globe used CO_2, excimer and Nd:YAG lasers to machine microchannels on transparent materials such as glass (Chang *et al.* 2016) and polymers (Day and Gu, 2005; Darvishi *et al.*, 2012). Also, it was revealed that CO_2 and excimer laser could successfully machine the transparent polymer material because most of the polymers exhibit significant absorptivity at the far infrared spectrum and low UV wavelength (Prakash and Kumar, 2015b).

(B) Thermal property

Thermal properties control the temperature distribution in a workpiece. The significant thermal properties are namely thermal conductivity (k) and heat capacity (c). The thermal conductivity of metals is such a thermal property that signifies its ability to conduct heat into the material. In metals, the value of thermal conductivity varies in a wide range, from a value of approximately 8 W/mK to a value of about 400 W/mK. It determines the heat flow into the surrounding material, and therefore, the temperature gradient and peak temperature are affected by the thermal conductivity (Bejan and Kraus, 2003). The peak temperature and temperature gradient both decrease with the increase in thermal conductivity. It is due to quick heat dissipation in high conductivity material (Hu *et al.*, 2002). Benton *et al.* (2019) studied the effect of thermal conductivity on laser micromachining of microchannels and observed that the melted and vaporized volume in the metal target increases with the increase in the thermal conductivity value of the material.

Specific heat capacity on the other hand signifies the amount of heat required to be supplied per unit mass to raise the temperature by unit degree. In metals, its value range from a lowest value of about 120 J/kgK to a highest value of 3500 J/kgK. Similar to thermal conductivity, specific heat also governs the peak temperature obtained during the laser irradiation. In fact, when different materials absorb identical quantity of heat, it is the materials' specific heat that decides the generation of peak temperature. The smaller the specific heat is, the higher the peak temperature is obtained (Guan *et al.*, 2005). Benton *et al.* (2019) also investigated the effect of specific heat capacity on laser micromachining of microchannels and reported that, the higher the specific heat of a metal, the lower the depth of cut for a given laser power is obtained.

Observations

From the aforementioned studies, it can be observed that depending on the various factors such as wavelength of the incident laser beam; surface roughness of the material and the temperature evolution on the surface, the metals get highly absorbing thereby causing thermal ablation on its surface. Transparent materials exhibit significant absorptivity at the far infrared spectrum and low UV wavelength. No laser beam can be absorbed in the visible and near-infrared spectral range making the laser machining of transparent materials in such spectral range a challenging task. It may be worthy studying the laser machining process of transparent materials in the visible and near-infrared spectral range. While, concerning the thermal properties, it is observed that several literature reports the effect of the thermal conductivity and the specific heat capacity on the laser machining of metals. However, limited research on the investigation of the effect of the thermal properties of the metal target on the transparent material during the LIPAA process have been carried out. An investigation on the effect of thermal properties of metal target on the transparent material during the LIPAA process may thus be useful.

2.6 Optimum process condition for laser-micromachining of transparent materials

The optimum selection of process parameters has played an important role for increasing the machining ability, improving surface finish, increasing material removal rate and reducing machining time of any laser machining process. Umer *et al.* (2017) carried out multi-response optimization of machining parameters during laser micro-milling of alumina ceramic by Nd: YAG laser. Authors aimed at minimizing the surface roughness and maximizing the machining rate using MOGA-II. It was found that better surface finish was achieved at low pulse overlaps, high intensity of laser, low frequency and shorter pulse duration while, high laser beam intensity resulted in higher machining rate. Authors further machined micro-channels of different depths by varying three parameters, viz. intensity of laser beam, pulse overlap and scanning speed (Mohammed *et al.*, 2019). Response Surface Methodology (RSM) and Lipschitz sampling were used to optimize the parameters for different depth categories and was found that intensity of laser beam plays a major role for depth control. McCann *et al.* (2018) developed a model to predict the micro-channel depth and width during laser ablation of cyclic olefin polymer (COP) films by Nd: YAG laser. The group observed that the laser fluence is the primary factor affecting the micro-channel depth, in addition to which number of laser passes and substrate thickness were also found to be significant factors. Chen and Hu (2017) proposed an effective method to fabricate micro-channels on the PC using CO_2 laser. Orthogonal experimental method was successfully applied to investigate the effect of laser power, machining speed and length of the micro-channel on the channel width. It was observed that the degree of sensitivity of the laser parameters on the channel width was highest for laser power, followed by the length of micro-channel and laser moving velocity. Third-harmonic of an Nd: YAG laser was used by Hammadi (2020) to fabricate micro-channels for bio-medical applications. The author showed that the micro-channel width can be minimized to a value of 1 µm by precise control of laser power, beam radius and irradiation time. Further, Bulushev *et al.* (2016) investigated laser processing of BK7 glass using Design of Experiments and regression analysis. From the regression analysis, a regression model was obtained with the help of which micro-channels with predefined dimensions can be fabricated with an average accuracy of 5%. It was observed in the study that greater overlaps lead to higher material removal rate as the material is not fully cooled between the successive pulses.

Observations

Fabrication of micro-channels on transparent material by LIPAA require proper setting of laser parameters like pulse power density, pulse repetition rate and pulse duration to obtain desired channel width and depth. Generally, high pulse power density generates more plasma as a result of which burning of the transparent material may occur. Moreover, increasing number of pulses with increase in the pulse repetition rate may lead to large heat affected zone. Also, wider and deeper channels are produced at higher pulse duration. It is thus essential to study the influence of the process parameters like pulse power density, pulse repetition rate and pulse duration on the variation of the channel geometry and channel quality. From the literature survey, it is observed that several studies have been reported on micro-channel fabrication using different techniques and also on the variety of materials. However, scant work has been reported on the systematic and detailed analysis on the influence of laser parameters on the size and quality of the channels during Laser-Induced Plasma Assisted Ablation (LIPAA) process. Measurement and analysis of channel width, channel depth and channel roughness accurately would be significant to interpret the physics behind the LIPAA process.

2.7 Observations and conclusions

Literature reports research on various aspects of the laser machining process such as ablation mechanism, effect of process parameters and material properties on the process responses, process parameter optimization strategies, its various applications, etc. Significant research has also been reported on the demand of transparent materials in various scientific and industrial applications. Different transparent material processing techniques have also been discussed. Further, it has been described how laser among the other processing techniques proves itself a promising tool for transparent material processing. Details on laser-induced plasma assisted ablation (LIPAA) process in terms of its types, laser process parameters and workpiece materials have also been presented. Published literatures on experimental investigations into the process mechanism, process parameters, process planning and process optimization of the LIPAA process are covered extensively. Numerical approach of laser-induced plasma process has been critically studied. Overall, this chapter has provided an overview of the published research work on the laser machining process. The key observations from the literature review can be summarized as:

- Polycarbonate (PC) is highly transmissible to the laser beam at visible and near-infrared wavelength range. Most of the research related to laser processing of PC employ ultrashort pulsed lasers or lasers of short wavelength. Conversely, limited work has been reported on laser machining of PC using large pulsed lasers and at larger wavelength. Also, very scant work has been reported on the use of LIPAA process in the fabrication of microchannels on PC.
- The literature reports eminent articles on micro-channel fabrication by a number of different processes, experimental parametric analysis and also on the variety of materials used for its fabrication. However, very few studies have been reported on the systematic and detailed analysis of the effect of the laser parameters on the channel dimensions and quality during Laser Induced Plasma Assisted Ablation (LIPAA) process.
- Numerical modelling of laser micromachining of transparent material has been reported in various literatures. Laser-induced plasma micromachining and the role of laser-induced plasma properties in its material removal behaviour have been studied. Further, numerical study on laser direct and laser transmission processes of various materials are also described. However, a very limited work in the simulation of LIPAA process has been reported. No two-dimensional or three-dimensional numerical modelling and simulation of the LIPAA process on PC has been attempted.
- Research related to fabrication of microstructures like microfluidic devices and electrofluidic devices, micro drilling, use of different absorbing media on the rear side of the transparent material, comparative assessment of LIPAA and direct laser ablation process, parametric analysis of the laser process parameters, etc. have been reported. During direct laser machining, the effect of the thermal conductivity and the specific heat capacity on the workpiece material have also been reported in several literatures. However, very limited research pertaining to the effect of the thermal

properties of the metal target on the transparent material during the LIPAA process has been carried out.

2.8 Research objectives

Based on the research gaps identified during the literature review on various aspects of laser machining, the objectives of present research have been derived. The primary objective of the present work is to enhance the product quality and process efficiency during the laser-induced plasma assisted ablation of polycarbonate. To achieve this objective, the following are the specific objectives undertaken:

- To perform laser machining of transparent polycarbonate material which has high transmittance in the visible and near-infrared spectral range.
- To fabricate microchannels on polycarbonate using LIPAA.
- To study the influence of different metal targets on the geometrical characteristics of the microchannels.
- To study the effect of the process parameters viz. pulse power density, pulse repetition rate, pulse duration, and scanning speed on the microchannel geometry and quality.
- To develop a 2D and 3D non-linear thermo-physical model of LIPAA to compute the micro-channel width and depth.
- Based on the numerical model, to study the effect of the laser process parameters on the microchannel fabrication.

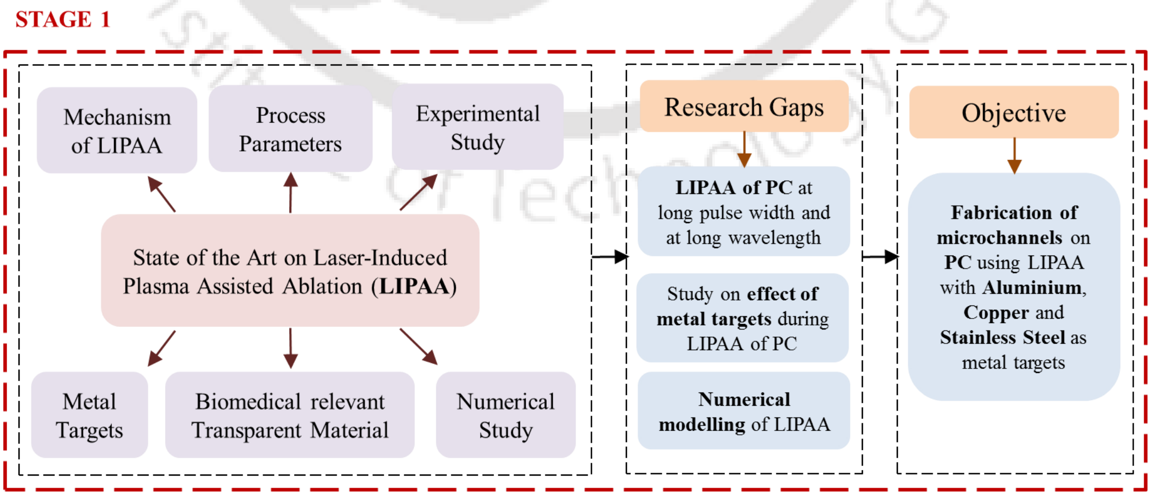

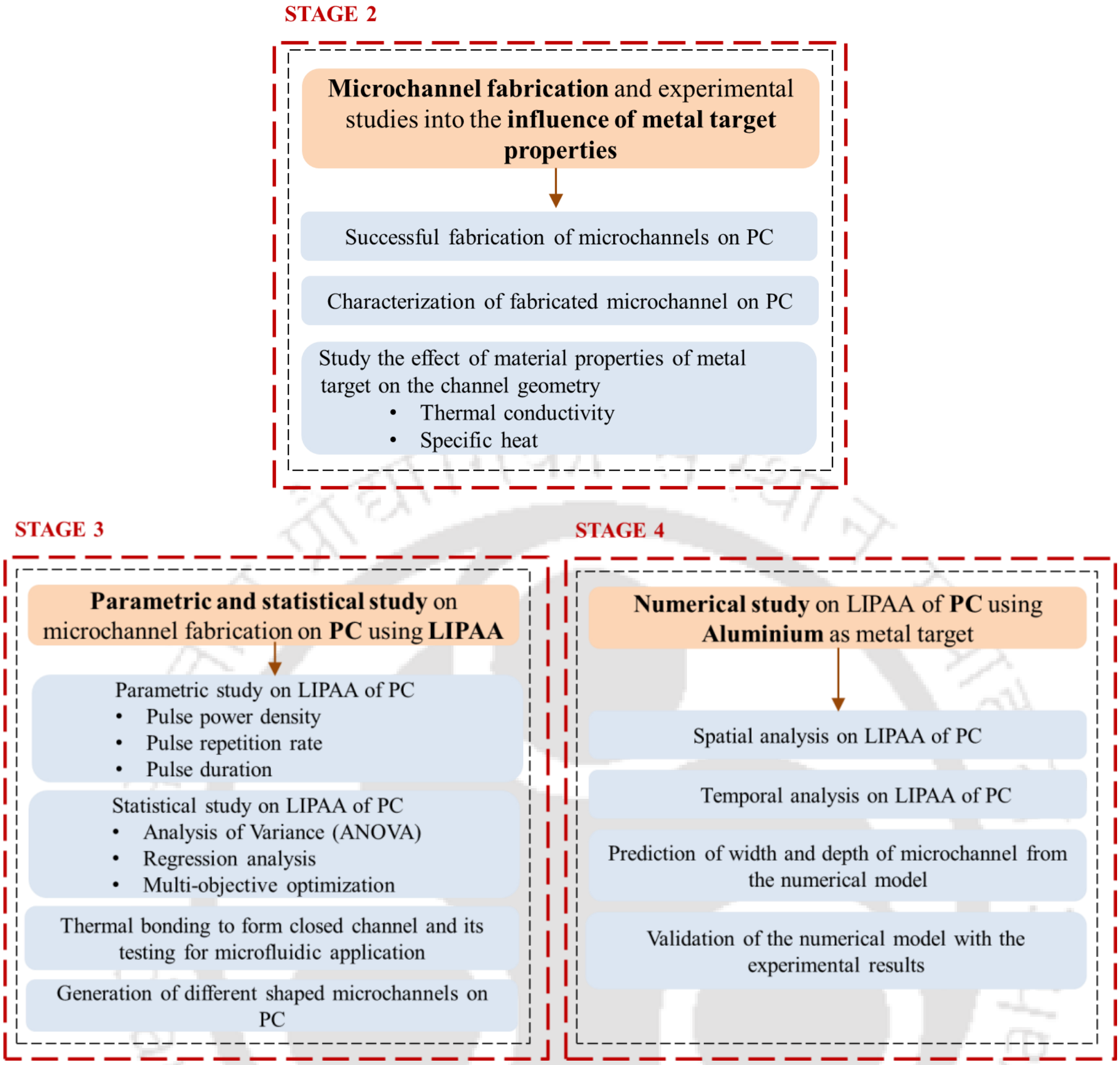

Figure 2.8 Methodology of the present research work

Figure 2.8 gives an overview of the methodology of the research carried out in the present work. The various stages of the work are as follows.

Stage 1: Initially, a literature survey relevant to laser machining of transparent materials has been thoroughly carried out. The study comprises of understanding the process mechanism of Laser-Induced Plasma Assisted Ablation (LIPAA), its process parameters, workpiece materials, and parametric analysis. The research gaps identified have been discussed and subsequently, a brief insight into the experimental and numerical investigation on the LIPAA process for microchannel fabrication on transparent PC has been presented.

Stage 2: In this module, experimental investigations have been carried out for successful fabrication of micro-channels on PC by using the LIPAA process. Besides, the effect of properties of metal targets such as aluminium, copper and stainless steel on microchannel fabrication was also investigated. The width and depth of the microchannels were observed at same condition of laser parameters for the three metal targets and based on the data, the effect of the material properties like thermal conductivity and the specific heat capacity on the channel width and channel depth has been presented.

Stage 3: This module reports the full-factorial experiments on microchannel fabrication on PC using LIPAA with aluminium metal target. Experiments were performed considering the effective ranges of process parameters viz. pulse power density, pulse repetition rate, pulse duration and scanning speed. The influence of laser parameters on the channel geometry and roughness have been extensively studied. A statistical analysis was carried out to analyse the significance of factors on the responses and to develop mathematical relations of the input laser parameters and process responses. An optimal condition of laser parameters has been determined and open microchannels were fabricated. The fabricated open micro-channels were then closed by using a thermal bonding process. A fluid flow test was carried out on the closed microchannel and its applicability as a microfluidic device was proved.

Stage 4: In this module, a non-linear transient finite element model of LIPAA process has been developed taking aluminium as the metal target and polycarbonate as the transparent material. The model was validated with the experimental findings of the present work. A systematic study was carried out to understand the physics of the ablation process. Parametric studies were performed by varying the levels of process parameters such as pulse power density, pulse repetition rate and pulse duration. The effect of these parameters onto the performance parameters such as channel width, channel depth and channel roughness was thoroughly studied.

Chapter 3

Microchannel fabrication using LIPAA and study on the influence of metal target properties

3.0 Scope

This chapter presents successful fabrication of microchannels on transparent polycarbonate (PC) using LIPAA. Initially the mechanism of LIPAA has been thoroughly studied. Details of the experimental setup, workpiece material, machining process and characterization of the fabricated microchannels have been elaborated in the chapter. LIPAA process is governed by factors such as laser parameters, process parameters and metal target properties. In the present chapter, the effect of the metal target properties like thermal conductivity and specific heat capacity on the microchannel geometrical characteristics has been studied. Three different metal targets viz. aluminium, copper and stainless steel have been utilized during the process. Microchannel aspect ratio was then determined for the three metal targets at the same condition of the laser parameters. The metal target leading to the highest microchannel aspect ratio is recommended for further study.

The parametric and statistical analysis of the laser process parameters has however been presented comprehensively in the subsequent chapter.

3.1 Motivation

The primary objective of the current research work is successful fabrication of microchannels on transparent materials. In general, techniques like microwire moulding, injection moulding, compression moulding, imprinting, lithography, micro-milling, etc., are used in creation of features on transparent materials. Nonetheless, the mentioned techniques have limited applicability due to their longer lead-time, complex process mechanisms, and poor geometric accuracy. On the other hand, ultrashort pulsed lasers or lasers of short wavelength prove themselves a promising tool for machining transparent materials. But, they are expensive and provide a low material removal rate. However, it was noted from the reported literature that LIPAA can be an alternate and efficient manufacturing process to create various features on transparent materials. A need was thus identified to carry out a systematic experimental study on microchannel fabrication using the LIPAA process.

3.2 Theoretical background of LIPAA

LIPAA is a versatile technique that has the potential to process transparent materials at longer laser pulses and with laser of longer wavelength. In the process, a sheet of transparent material is placed above metal target sheet with no external pressure being applied among the two materials. Thus, a micron level gap will be present in between the transparent and the metal target sheet. Both the sheets are placed over the computer controlled X–Y position stage. The schematic representation of the LIPAA experimental setup and its mechanism is shown in figure 3.1.

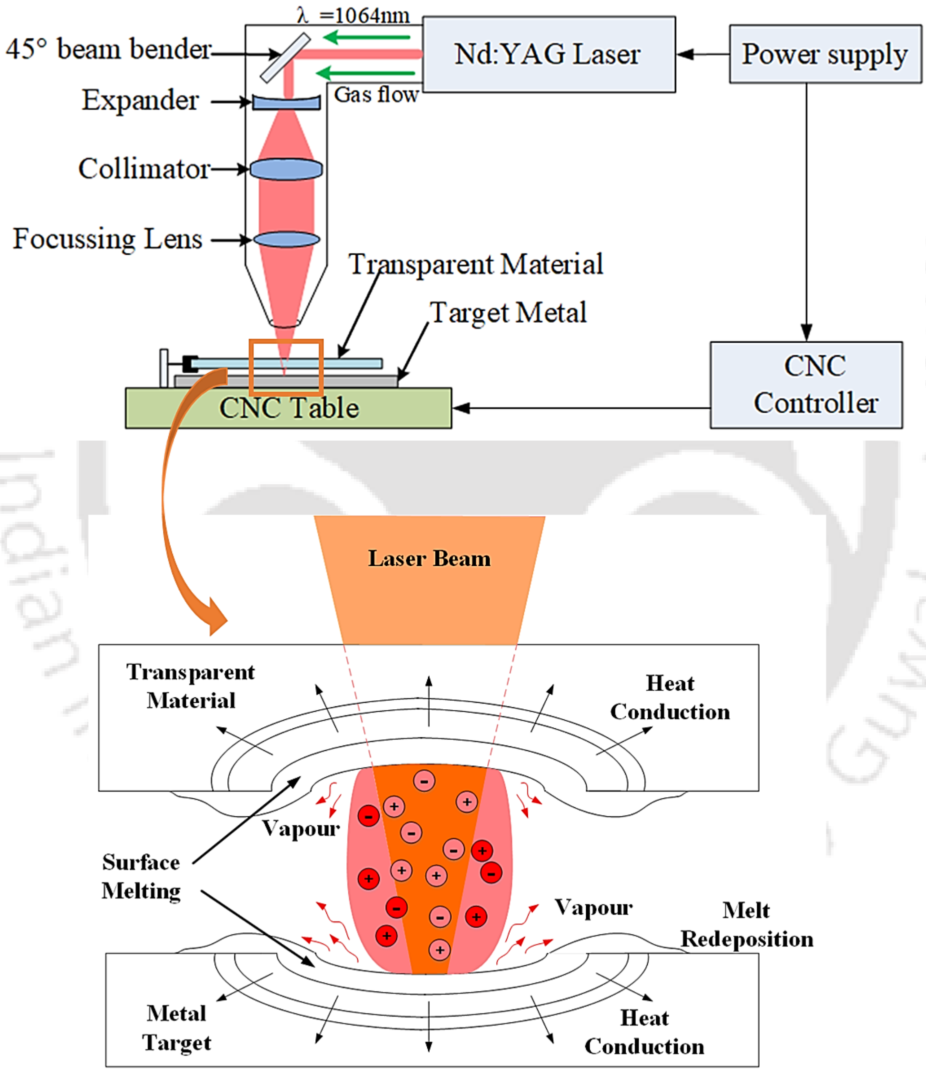

Figure 3.1 Schematic representation of the experimental setup and mechanism of LIPAA

Due to the transparency of the transparent material, as the laser passes through the transparent material, the laser beam is focussed on the upper surface of the metal target. The incident energy of photon at 1064 nm wavelength (1.2 eV) is comparable to the minimum bond energy of aluminium (1.38 eV). Thus, laser photo-absorption occurs and a few percentage of the energy gets absorbed while the remaining portion reflects from the work surface. The absorption of the laser incident energy in the substrate material can be expressed in terms of Beer-Lambert law as (Dahotre and Harimkar, 2008):

$$I(z) = I_o e^{-\mu z} \tag{3.1}$$

where, $I\,(z)$ is the laser intensity at depth z, I_o is the incident laser intensity and μ is the absorption coefficient of the substrate material. The percentage of the laser incident energy that is absorbed by the substrate material is expressed as:

$$A = 1 - R \tag{3.2}$$

where, A is the absorptivity of the material and R is the reflectivity of the material. The absorbed energy excites free electrons, which is instantaneously converted into heat in a time duration of about 10^{-13} s (Dahotre and Harimkar, 2008). The heat then dissipates through various heat transfer modes such as conduction, convection and radiation; however, the conduction plays the most significant role. The heat conducted into the metal surface increases the temperature of the surface. When the laser intensity is sufficiently high (10^5–10^8 W/cm^2) (Negarestani and Li, 2012), the temperature exceeds the melting and boiling temperature, which results in material removal. Some portion of the material transforms into vapour form. The liberated vapours contain molecules, atoms, ions and electrons. The interaction of vapours with the incoming laser beam results in the ionisation of the vapour leading to the formation of dense and opaque plasma which confines itself to the irradiated surface. The degree of ionisation $\lambdabar$ in a vapour is given by the Saha Equation as (Dahotre and Harimkar, 2008):

$$\frac{\lambdabar^2}{1-\lambdabar} = \frac{2g_\mathrm{i}}{g_\mathrm{a} N_\mathrm{g}} \left(\frac{2\pi m k_\mathrm{b} T_\mathrm{s}}{h^2} \right)^{3/2} \exp\left(-\frac{\Delta E}{k_\mathrm{b} T_\mathrm{s}} \right) \tag{3.3}$$

where, $\lambdabar = N_\mathrm{e} / N_\mathrm{g}$ and $N_\mathrm{g} = N_\mathrm{e} + N_\mathrm{a}$. N_e and N_a denote the number densities of electrons and atoms/molecules respectively; g_i and g_a denote the degeneracy states of ions and atoms/molecules; m is the mass of vapour molecule; k_b is the Boltzmann's constant; T_s is the surface temperature; h is the Planck's constant and ΔE is the ionisation energy.

It is considered that the plasma generation threshold is obtained when the number density of the electrons (N_e) reaches a value of about 10^{18}/cm^3 (Dahotre and Harimkar, 2008). The plasma energy density can thus be estimated from the electron density by the following equation (Saxena *et al.*, 2014):

$$E_{\text{plasma}} = N_{\text{e}} \left(\frac{\Delta E}{2} \right) \tag{3.4}$$

Also, the average plasma temperature is given by:

$$T = \frac{2K}{3k_{\text{b}}} \tag{3.5}$$

where K is the average kinetic energy of the electrons.

For an ionisation energy of 34 eV of air, the E_{plasma} can be calculated to be about 2.72×10^6 J/m^3. Also, the plasma can attain a temperature from approximately 2500 K to as high as 50000 K and with a pressure up to 500 MPa. The plasma generated flies towards the substrate at a high speed of approximately 10^4 m/s (Hong *et al.*, 2001). The generated plasma further interacts with the incoming laser and results in the Inverse Bremsstrahlung absorption which causes the isothermal expansion of the plasma (Pan *et al.*, 2017). The expanded plasma has increased energy intensity than the input laser irradiance. The plasma, thus, ablates both the transparent and the metal target sheets. Thus, the IB is considered to be the main heating mechanism for higher laser power irradiations, while for the lower range, photo-absorption plays still an important role. When the transparent sheet gets ablated, a few percentage of the molten material gets redeposited on the ablated zone itself and the major percentage of the molten material is acted upon by the shockwave produced by the plasma (Campanella *et al.*, 2019). This shockwave expels a major percentage of the molten material from the site of irradiation through the micron level gap present in between the transparent and the metal target sheet.

After the study of the mechanism of LIPAA process, the details about the experimental setup, workpiece material, characterization of the fabricated microchannels and study on the effect of metal target properties are presented in the subsequent sections.

3.3 Development of experimental setup

In the present work, Nd: YAG pulsed millisecond laser (Model: 500 W pulsed Nd: YAG CNC Laser, Make: Suresh Indu Lasers Pvt. Ltd) having a wavelength of 1064 nm has been utilized for the fabrication of micro-channels on PC. The laser workstation consists of the beam bending, expanding, collimating and focusing optical units and a computer-controlled X-Y position stage. The specification of the laser setup is given in table 3.1.

Table 3.1 Specifications of Nd: YAG Laser

Laser parameters	**Value**
Wavelength (λ)	1.06 μm
Average Power (P_{avg})	500 W
Pulse Width (τ)	0.5 – 20 ms
Pulse Repetition rate (F)	1 – 500 Hz
Laser Spot Radius (R)	100 μm

The image of the experimental setup is shown in figure 3.2. A PC sheet of 1 mm thickness is kept on the upper surface of a 1 mm thick metal target. No external pressure is being applied to them. This set of PC and metal target is placed on the computer-controlled X–Y position table. PC has a transmittance of about 89% in the infrared spectral range. Thus, the homogenized laser beam having a wavelength of 1.06 μm passes through the PC sheet and is focussed on the upper surface of the metal target sheet, leading to the plasma generation, thereby ablating both the PC and the metal target sheet. The profile or shape of the microchannel to be fabricated is designed by using the RD-Works V8 software.

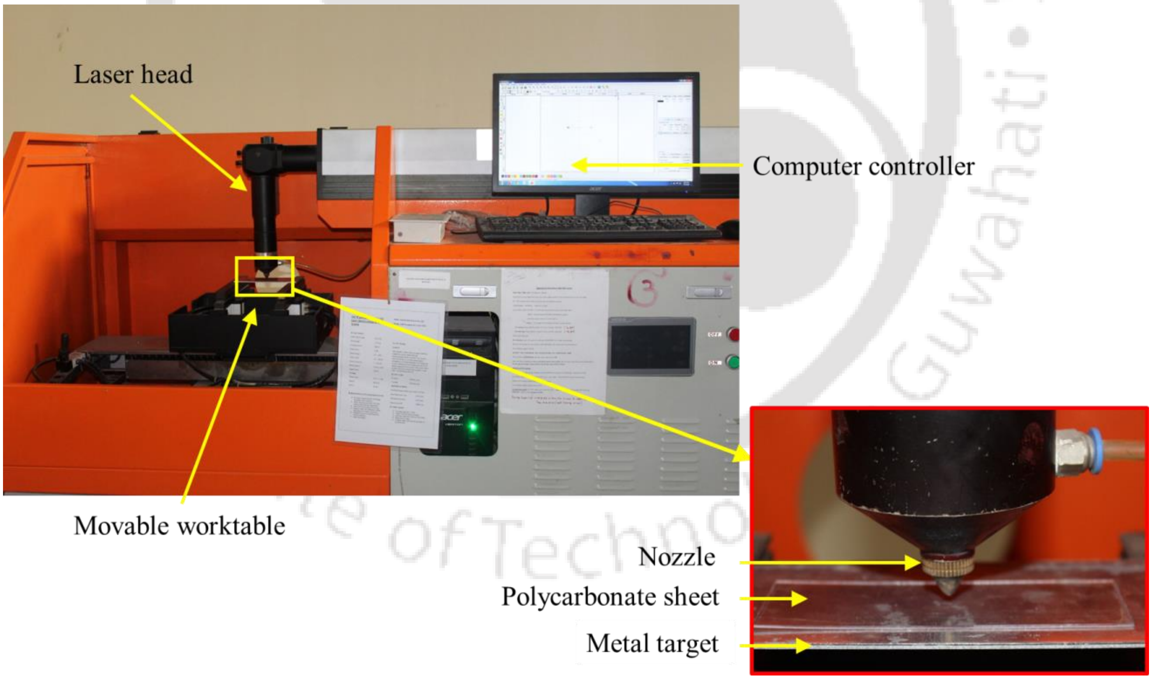

Figure 3.2 Nd:YAG laser experimental setup

3.4 Workpiece material

In the present research work, microchannels were fabricated on a transparent PC sheet. The reason for taking PC as the transparent sheet lies in its inherent high impact strength, high transparency, high dimensional stability, optical clarity and environment-friendly nature. PC has high value for microfluidic devices as it can be sealed, supplied with reagents and integrate electrical and microelectronic components (Temiz *et al.*, 2015). Further, they possess a glass transition temperature of 154 °C, which is higher than most of the other similar polymers like polymethyl methacrylate (PMMA), polystyrene or polydimethylsiloxane (PDMS). As such, PC can be considered as an ideal material for bio-medical as well as optics industries. While for the metal target sheet to be placed beneath the transparent sheet, a sheet of aluminium of thickness 1 mm was chosen for the initial experimental investigation. An important property of aluminium is that it is a good reflector of both visible light and radiated heat. Taking into consideration this property, aluminium was chosen as the metal target for well-defined ablation to take place at the rear side of the transparent material.

3.5 Laser based machining using LIPAA principle

After the study of the principle of operation of LIPAA, experiments were carried out to fabricate microchannels on PC. An overview of the laser based machining process using LIPAA principle is shown in figure 3.3. For fabrication of microchannels, the laser parameters like pulse power density, pulse repetition rate and pulse duration and laser scanning speed were utilized and varied initially in a wide range of values. They were varied in the range of 1.53-7.64 MW/cm^2 pulse power density, 20-100 Hz pulse repetition rate, 1-10 ms pulse duration and 1 ms to 10 ms scanning speed. Again, the above mentioned figure shows the generation of plasma image in between the transparent PC and the metal target sheet. The ablative plasma can clearly be noticed during the LIPAA process. Material removal was thus achieved on both the PC and the aluminium sheet due to the effect of the plasma. However, in our present study, the main focus was on the analysis of microchannel fabricated on a transparent PC using the LIPAA process.

Subsequently, the channel geometry (channel width and channel depth) and channel roughness of the fabricated microchannels on PC were measured and analysed, thereby establishing successful fabrication of quality microchannels by LIPAA on transparent PC. The successful creation of the microchannel on PC is shown in figure 3.4. After efficiently fabricating microchannels, the effect of the properties of metal target was also investigated.

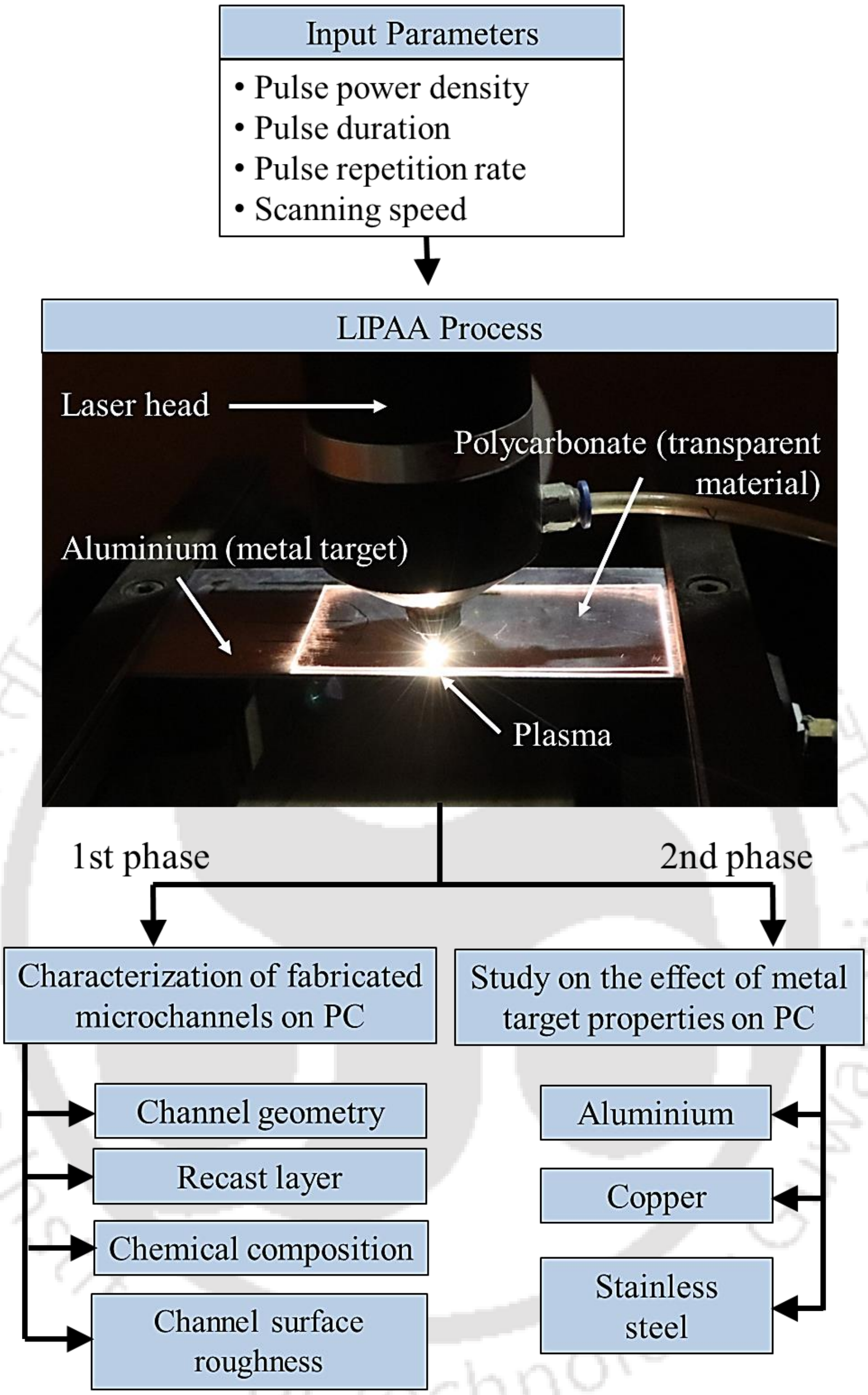

Figure 3.3 (a) Image of plasma generated near irradiated zone of aluminium sheet (b) PC placed above aluminium (c) no PC placed above aluminium

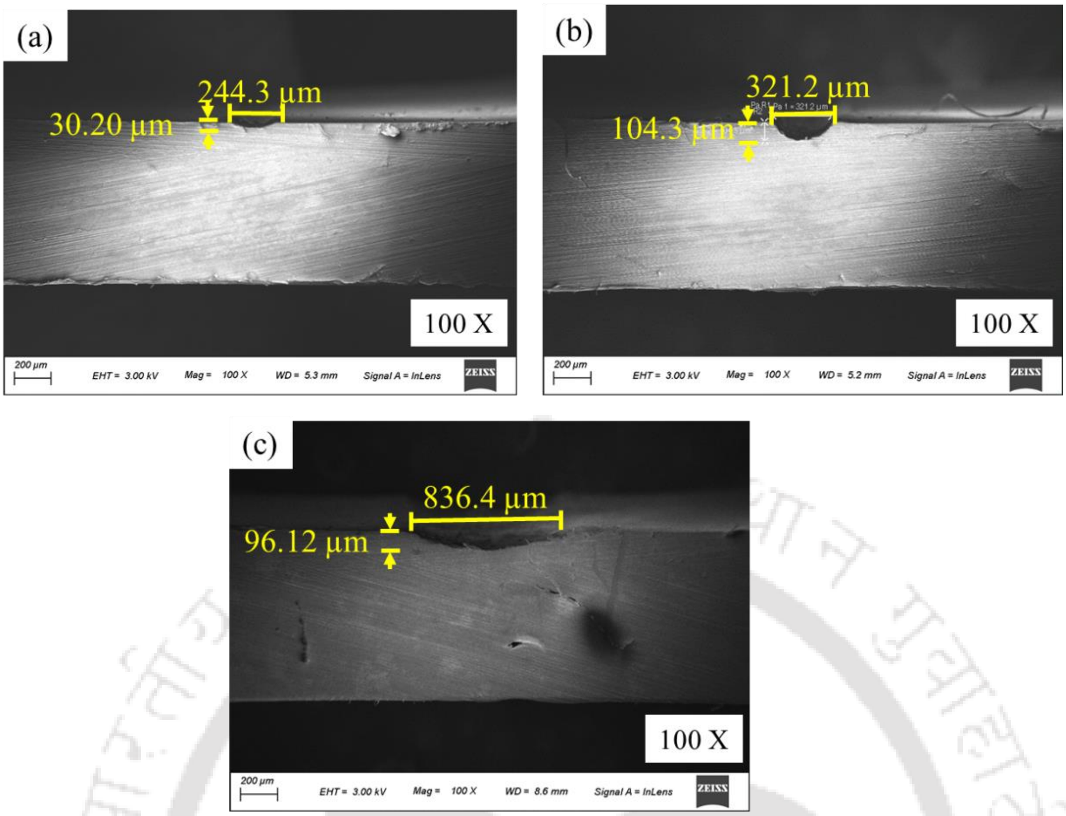

Figure 3.4 Microchannel fabrication on polycarbonate

3.6 Characterization of LIPAA fabricated microchannels

After fabricating microchannels, the measurement and characterization of the microchannels fabricated on PC have been carried out using Field Emission Scanning Electron Microscope (FESEM) and Energy Dispersive X-ray (EDX) spectroscopy available in the Central Instruments Facility (CIF) of IIT Guwahati and non-contact high precision surface profilometer available in the Advanced Manufacturing Laboratory of Mechanical Engineering Department, IIT Guwahati. The detail analysis on the above mentioned equipment have been presented in the following section.

3.6.1 Field Emission Scanning Electron Microscope (FESEM)

Field Emission Scanning Electron Microscope (FESEM) with magnification up to 200000× (Model: Gemini 300) has also been utilized to determine the channel dimensions and characterize the ablation area's morphology of the PC sample. To bring the PC sheet (with the micro-channel fabricated on it) to the size as per the requirement of the FESEM, the sheets were cut into squares of 1.3 cm and then polished on its edges to give it a smooth finish and bring it to a square of side 1 cm. The PC sheets were made conductive for the electrons by sputter coating with an extremely thin layer of 1.5 to 3.0

nm of Au. FESEM uses a beam of electrons to generate an image of the specimen and then to analyze it. For image visualization, analysis software SmartSEM was used. In our current study, the In-Lens detector of the FESEM was utilized to analyze the channels on the PC sheet. During the analysis, the extra high tension (EHT) accelerating voltage was kept at a value of 3 kV. Figure 3.5 shows the setup of the FESEM.

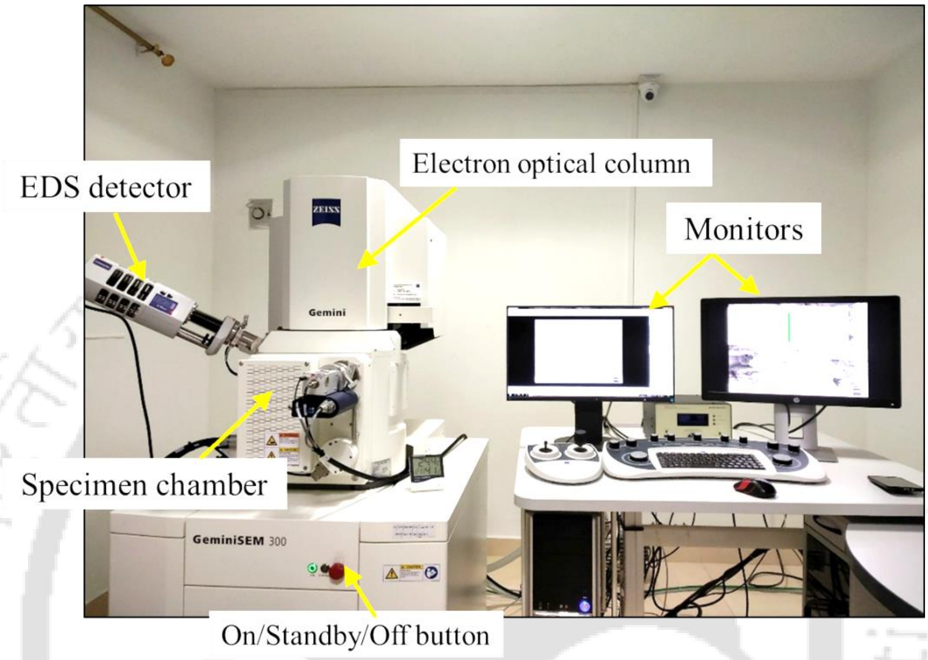

Figure 3.5 Field Emission Scanning Electron Microscope (FESEM) used to measure channel dimensions

Figure 3.6(a) and 3.6(b) shows the FESEM images of a typical microchannel fabricated on the PC by LIPAA at process condition of 40 Hz repetition rate, 4 ms pulse duration, 4 mm/s scanning speed and 3.06 MW/cm^2 pulse power density. The machined channel was cleaned with an ultrasonic bath. It can be seen that during the process, a prominent recast layer has been formed on the channel bed and channel edge. The recast layer can be noted from the enlarged view of the channel bed and channel edge respectively from figure 3.6(c) and 3.6(d). It is generally formed from the resolidification of molten material that was not ejected from the channel. During LIPAA, material removal occurs due to a combination of vaporization and melting as a consequence of plasma generation. Increasing the laser irradiation will further increase the plasma generation, promoting evaporation of the rear side of the PC and an associated recoil pressure. When the rate of evaporation or vaporization is high, the action of the recoil pressure on the molten surface can be sufficient to first form a depression in the melt pool and then to push molten material out of the hole. However, a small fraction of the molten material gets redeposited on the channel bed and edge, thereby forming a recast layer.

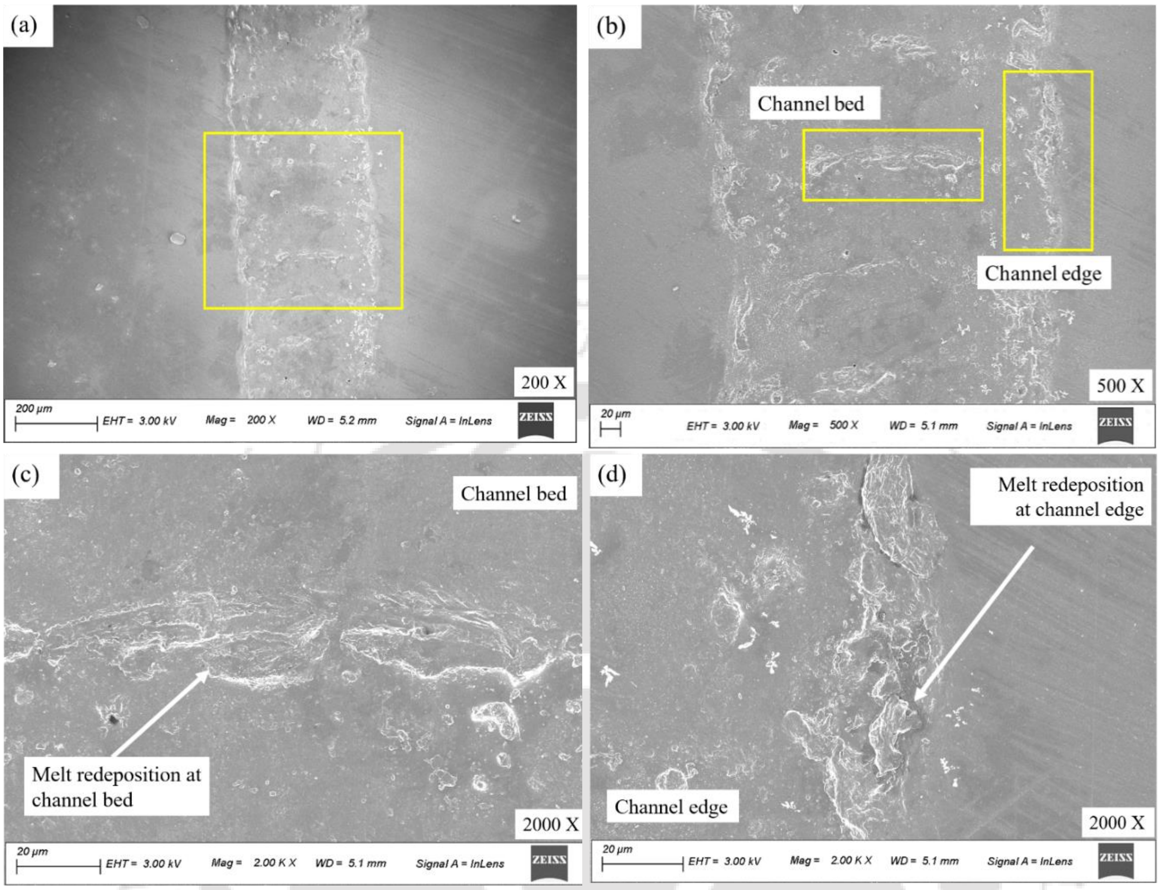

Figure 3.6 FESEM images showing (a-b) melted redeposits forming recast layer in the channel (c) melt redeposits at channel bed and (d) melt redeposits at channel edge.

3.6.2 Energy Dispersive X-ray (EDX) spectroscopy

Energy-Dispersive X-ray spectroscopy system (EDX) integrated with FESEM (Model: Gemini 300) was used to analyze the processed micro-channel. EDX analysis was performed to confirm the deposition of carbon and aluminium particles on the micro-channel bed and microchannel edge. The sample preparation for the analysis is the same as that for the FESEM analysis.

Figure 3.7 shows the elemental composition of the base PC material, micro-channel bed and micro-channel edge. Figure 3.7(a) shows the electron image of the micro-channel directly after the machining process. During the machining process, the temperature generated is higher than the vaporization temperature of both the PC and aluminium sheet. As a result, it was expected that carbon particles along with aluminium particles would be deposited on and around the fabricated micro-channel. Figure 3.7(b) confirms the deposition of carbon and aluminium particles on the base PC. Also, the deposition of carbon and aluminium particles on the micro-channel bed and micro-channel edge was confirmed by EDX analysis as shown in figures 3.7(c) and 3.7(d), respectively. It was observed that the percentage deposition of aluminium from the substrate material on the micro-channel bed is less compared to the micro-channel edge. This may be due to the shock wave generated during the evaporation at the irradiated zone of the PC and aluminium sheet. This results in explosive melt expansion and the sputtered melted material gets deposited on the channel edge. However, it was found that the deposits were not permanent in nature. The deposits were easily removed by subjecting the channels to ultrasonic bath for about 15 minutes in ethanol. This can be noticed in the EDX analysis of the cleaned-microchannel (see Figure 3.8). The deposits at the channel bed and channel edge are negligible. Thus, the LIPAA based fabricated microchannel on transparent PC will be safe to use in bio-medical applications.

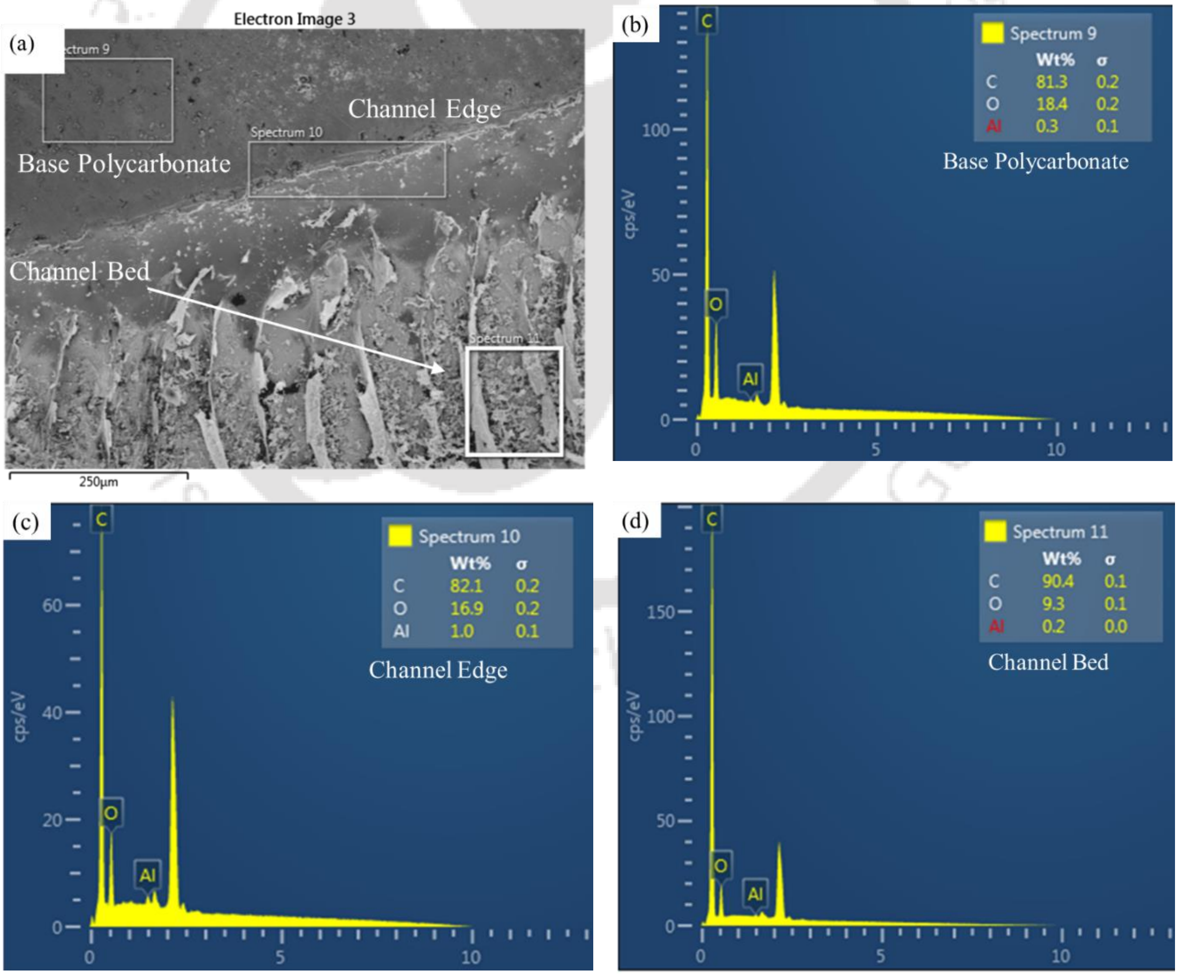

Figure 3.7 (a) Electron image of micro-channel before cleaning with the spectrums for elemental composition of (b) base PC, (c) micro-channel edge and (d) micro-channel bed.

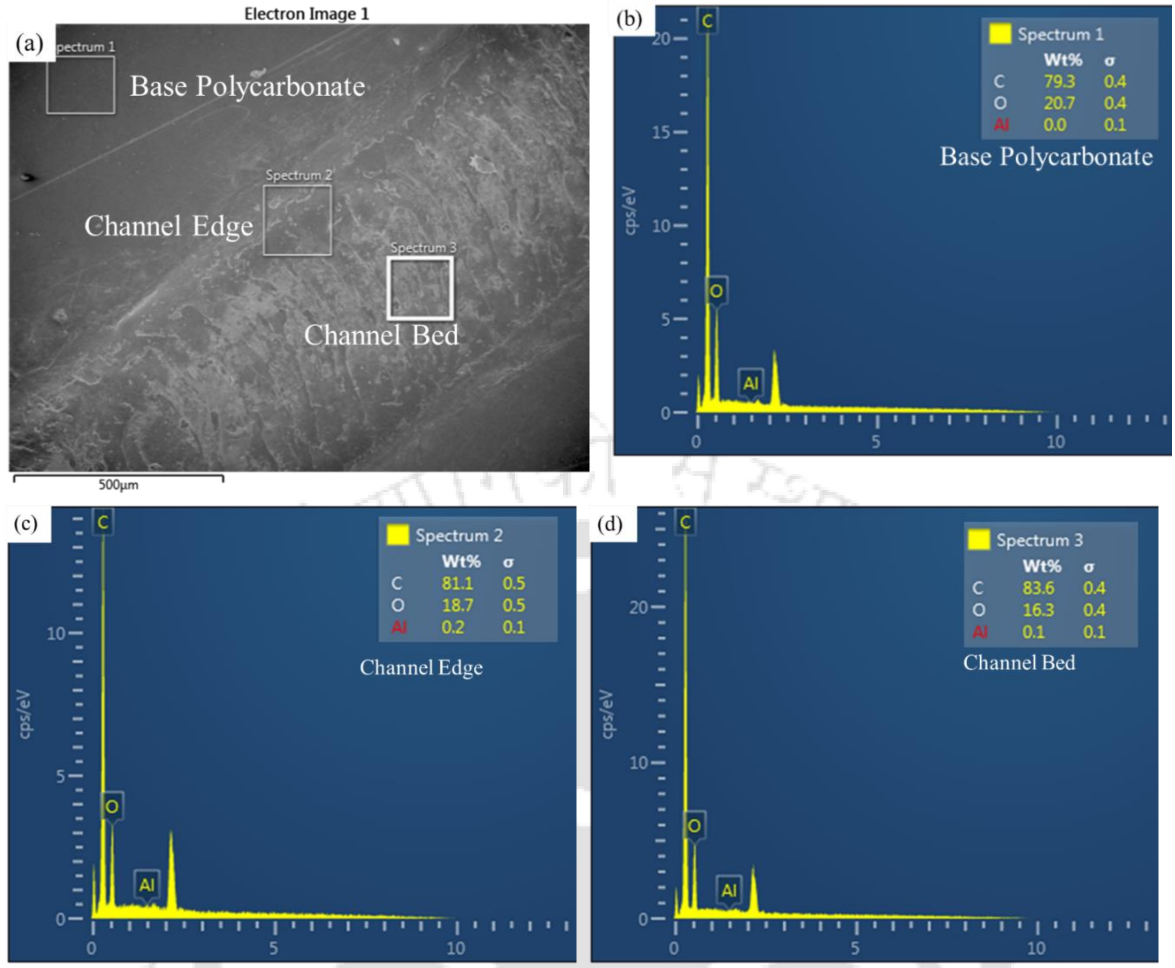

Figure 3.8 (a)Electron image of micro-channel after cleaning with the spectrums for elemental composition of (b) base PC, (c) micro-channel edge and (d) micro-channel bed.

3.6.3 Non-contact high precision surface profilometer

The surface roughness measurement was carried out with a high precision non-contact surface profilometer (Talysurf CCI; Taylor Hobson, Ltd.) as shown in figure 3.9. To prepare the channels for measurement, the specimen were first cleaned by using ultrasonic bathing for about 15 minutes in ethanol. The field of view of the profilometer is 0.825 × 0.825 mm^2 with a 20× magnification lens and a focal distance of 4.7 mm. The data of roughness measurement was analyzed using the software TalyMap.

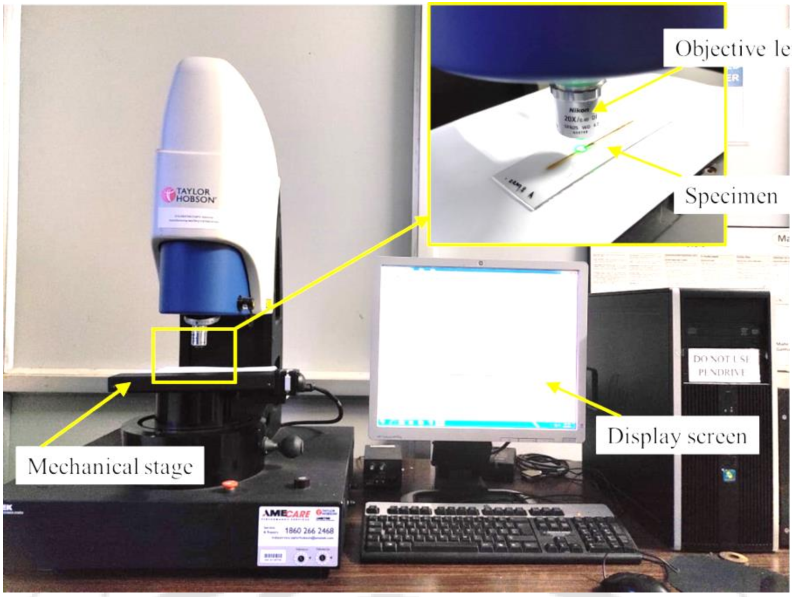

Figure 3.9 Non-contact high precision surface profilometer for channel roughness measurement

The roughness measurement was taken longitudinally along the feed direction. As shown in figure 3.10, roughness values at three different zones were recorded and their average value was taken into consideration for further analysis. The wavy roughness profile along the axis X-X′ and Y-Y′ are also shown in figure 3.11.

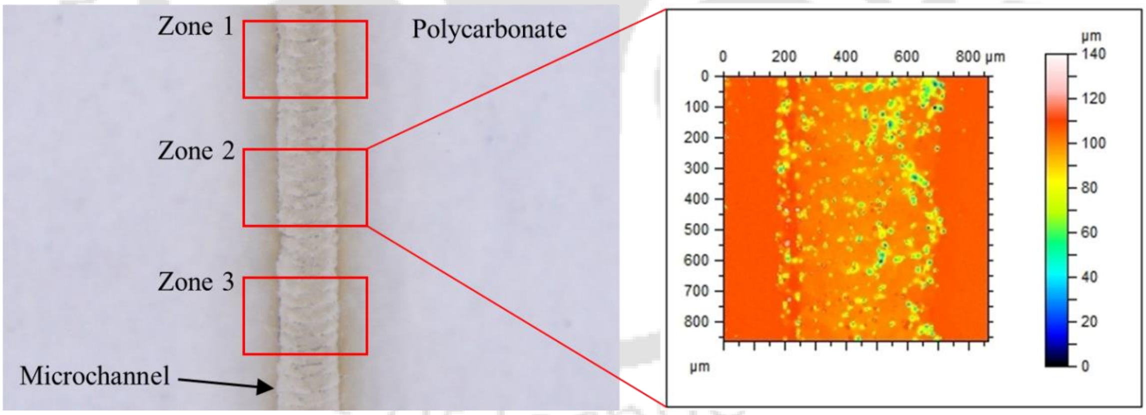

Figure 3.10 Channel roughness measurement zones

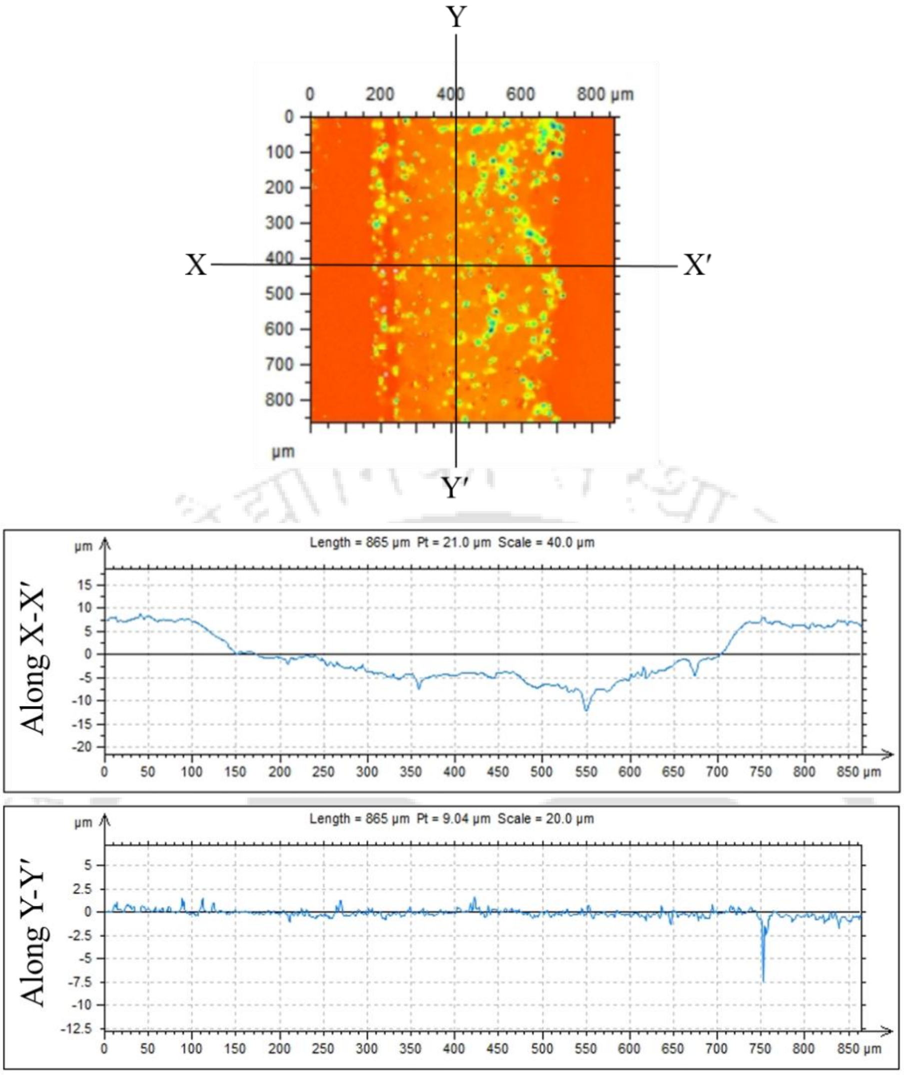

Figure 3.11 Roughness profile along the X-X′ and Y-Y′ axis

3.7 Effect of metal target properties on microchannel fabrication

Considering the flexibility of the LIPAA process, experiments were performed to fabricate microchannels on PC altering three different metal targets. It has been observed from the literature that in most of the reported studies on LIPAA, aluminium, copper and stainless steel were utilised as the metal target and as such, the three metal target sheets were chosen. Table 3.2 shows the properties of the metal targets.

Table 3.2 Material properties of the metal targets (Sharma *et al.*, 2014; Tadamalle *et al.*, 2014; Cheng *et al.*, 2016; Sharma et al. 2019; Li *et al.*, 2019; Zhao *et al.*, 2018)

Metal target	Reflectivity	Thermal conductivity (W/mK)	Specific heat capacity (J/kgK)
Aluminium	0.96	237	896
Copper	0.96	400	382
Stainless steel	0.98	26	602

The width and depth of fabricated microchannels were determined and are plotted graphically as shown in figure 3.12.

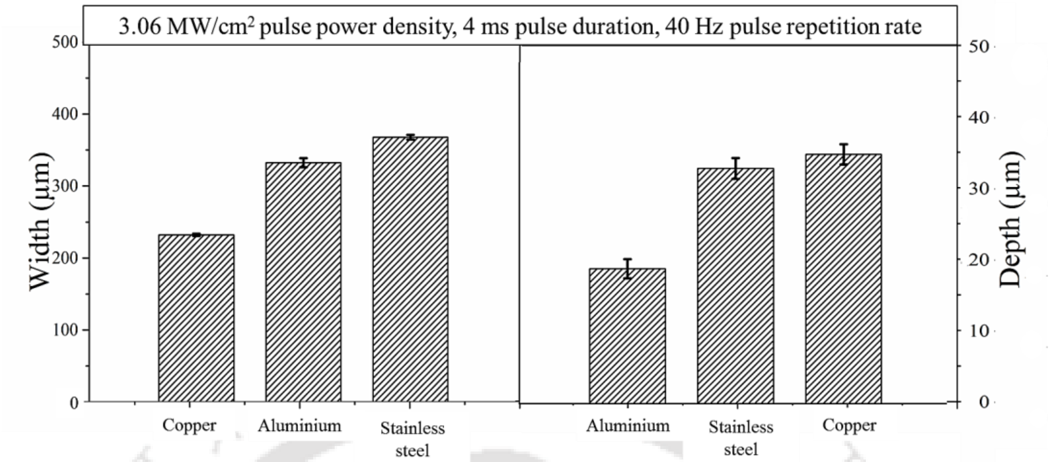

Figure 3.12 Width and depth of microchannels on PC for aluminium, copper and stainless steel as the metal targets

The FESEM images of the width and depth of fabricated microchannels is shown in figure 3.13. It is observed that at same condition of laser process parameters, microchannels of different widths and depths are obtained for the three metal targets. The dimensions of a microchannel fabricated during LIPAA must be governed by factors such as the medium between transparent and metal target material, laser parameters, the properties of transparent material and the properties of metal target. Since the medium between the materials is kept constant and microchannels were fabricated on PC at same laser parameters, it can be said that the metal target properties may have an influence on the microchannel formation during LIPAA.

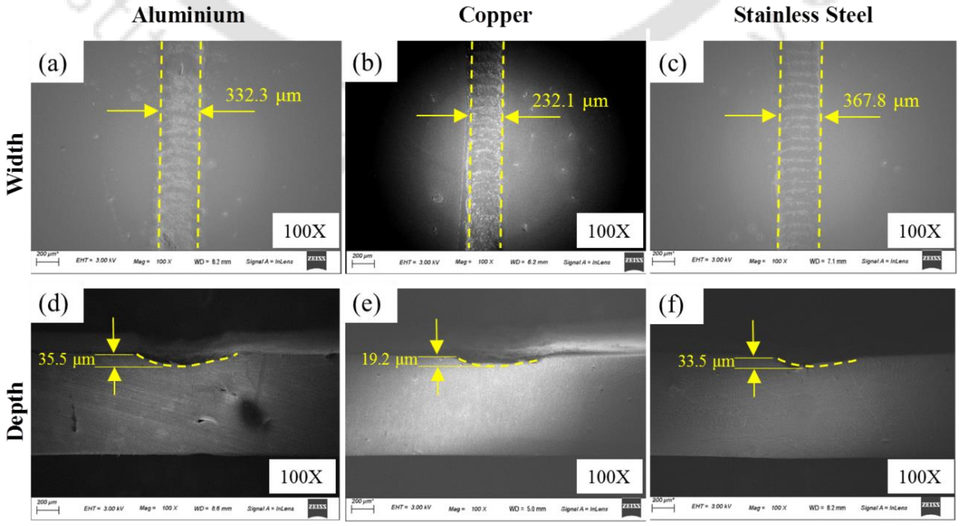

Figure 3.13 Width and depth of the cleaned microchannels for aluminium, copper and stainless steel as the metal targets observed under the FESEM

3.7.1 Effect of the thermal conductivity of the metal targets on the channel dimensions

The thermal conductivity of metals is a thermal property that signifies its ability to conduct heat into the material. In metals, the value of thermal conductivity varies in a wide range, from a value of approximately 8 W/mK to a value of about 400 W/mK. During laser machining, when a laser beam irradiates a metal surface, the heat generated at the initial stage remains localized in a small region near the irradiated zone. In metals with high thermal conductivity, the generated heat gets conducted deeper and wider onto the material, before it is lost by convection. A higher conductivity value consequence a wider transmission of heat into the metal sheet. While, in metals with low thermal conductivity, the heat remains accumulated at the irradiated zone. When this heat is sufficient enough, it increases the temperature of the metal surface and induces its melting and vaporization. Thus, on laser irradiation with the same power, the melted and vaporized volume in the metal target increases with the increase in the thermal conductivity value of the material (Benton *et al.*, 2019).

However, it can be witnessed that, though there is an increase in the volume of the melted and vaporized volume in the metal target, the time to reach the melting and boiling point temperature in metals with higher thermal conductivity is much longer. Greater is the time to reach the boiling point temperature of the metal sheets, greater will be the time for plasma generation. It is because, plasma generation initiates when the initial vapour particles interact with the incoming laser beam resulting in the ionisation of the vapour particles and leading in the formation of an opaque and dense plasma. As such, plasma generation will take longer duration in high thermal conductivity materials. With the laser source moving at a specific speed for channel formation, late plasma formation results in less melting and vaporization on the rear side of the transparent material. Thus, it can be understood from the above discussion that, with increasing thermal conductivity of metals, the dimension of the crater or channel formed increases in the metal targets, while that on the transparent material decreases. A schematic representation of the effect of high thermal conductivity of the metal target on microchannel fabrication on transparent material during LIPAA is shown in figure 3.14.

But again, it can be observed from the experimental analysis that, the above mentioned effect of the thermal conductivity on the transparent materials during LIPAA is more prominent on the width of the channel rather than on the depth of the channel. The variation of the channel width and the channel depth with thermal conductivity has been plotted graphically in figure 3.15. Such variation may be due the reason that, the plasma as it reaches the rear side of the PC gets expanded radially. Thus, more the plasma generation, the more radially the plasma gets expanded, resulting in an increased channel width. On the other hand, the plasma has no significant effect longitudinally with the variation in plasma generation. It may be because, when a deeper ablated volume is obtained on the metal surface with higher thermal conductivity, the generated plasma will be at a greater distance from the rear surface of the transparent material compared to plasma generated in metals with lower thermal conductivity and hence leads to no specific change in the depth of the channel.

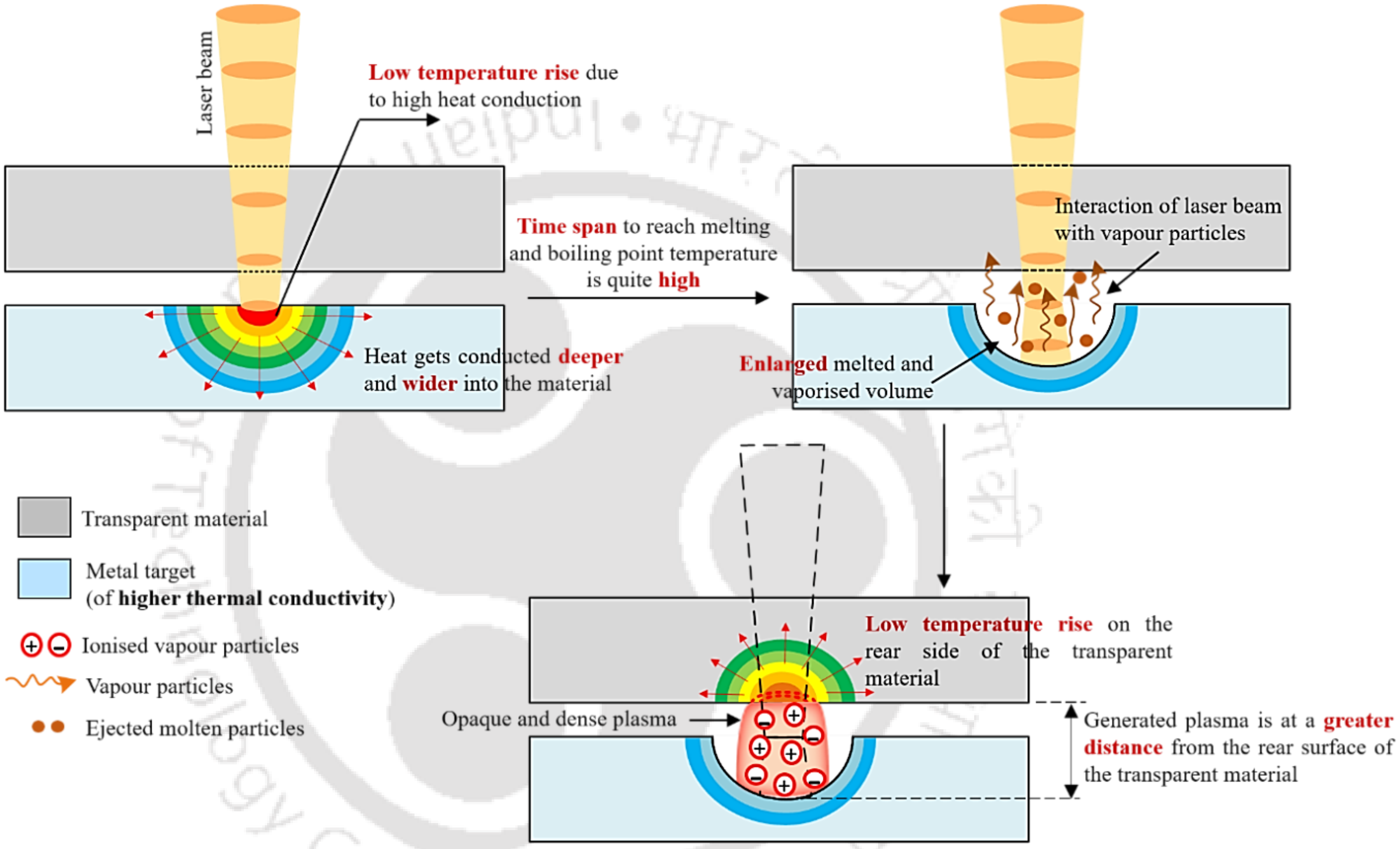

Figure 3.14 Schematic representation of the effect of high thermal conductivity of the metal target on microchannel fabrication on transparent material during the LIPAA process

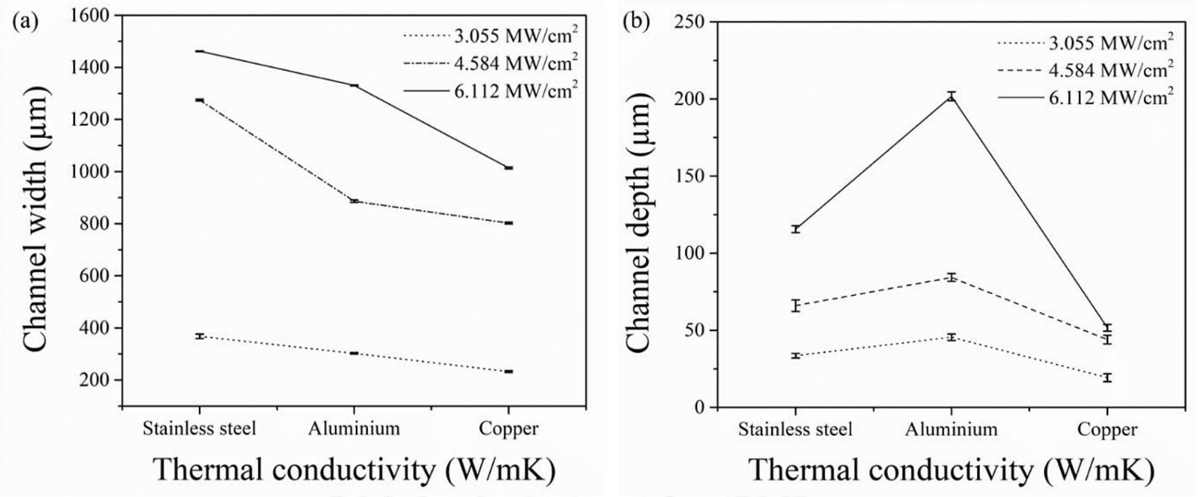

Figure 3.15 Effect of the thermal conductivity of the metal targets on (a) channel width and (b) channel depth

3.7.2 Effect of the specific heat capacity of the metal targets on the channel dimensions

Specific heat capacity on the other hand signifies the amount of heat required to be supplied per unit mass to raise the temperature by unit degree. In metals, its value range from a lowest value of about 120 J/kgK to a highest value of 3500 J/kgK. On laser beam irradiation on a metal surface, the peak temperature obtained on the surface is governed by the specific heat capacity of the material. Higher is the specific heat capacity; more is the amount of heat required to raise the temperature of the metal surface. Thus, the boiling point temperature of the material will be reached in a longer duration when compared to materials with low specific heat capacity. As a result, the melting and vaporization of the metal target sheet will be less for the same laser power in metals with higher specific heat capacity value (Benton *et al.*, 2019) and hence lead to lower melted and vaporized volume in such metal targets.

Thus, it can be understood that, the melting and vaporization will be less in metal targets with higher specific heat capacity for the same amount of laser power. Since the plasma generation depends on the vaporization of the material, it can be assumed that later the boiling point temperature is reached, late will be the plasma formation. But on the other hand, by the time the plasma is generated, laser irradiation on the metal surface also increases and consequently, more laser heat flux will be reflected from the metal surface towards the rear surface of the PC. Thus, there will be a combined effect of the generated plasma and the reflected laser heat flux on the rear side of the PC sheet and as such, an increased dimension of the crater or channel formed will be obtained on the PC sheet with metal targets of higher specific heat capacity. On the whole, it can be stated from the above discussion that, with increasing specific heat capacity of metals in a LIPAA process, the dimension of the crater or channel formed decreases in the metal targets, while that on the transparent material increases. A schematic representation of the effect of higher specific heat capacity of the metal surface on microchannel fabrication on transparent material during the LIPAA process is shown in figure 3.16.

Despite that, it can be witnessed from the experimental analysis that, the above mentioned effect of the specific heat capacity on the transparent materials during LIPAA is more notable on the depth of the channel rather than the width of the channel. It may be because, the reflected laser heat flux has a major impact with the variation of specific heat capacity and as such, has a significant longitudinal effect. Thus, higher the specific heat capacity of a metal target, more amount of reflected laser beam will reach the rear side of the PC and leads in the formation of a deeper crater or channel. Whereas, the reflected beam has no specific effect radially and hence leads to no specific variation in the width of the channel. The variation of the channel width and the channel depth with specific heat capacity has been generated graphically in figure 3.17.

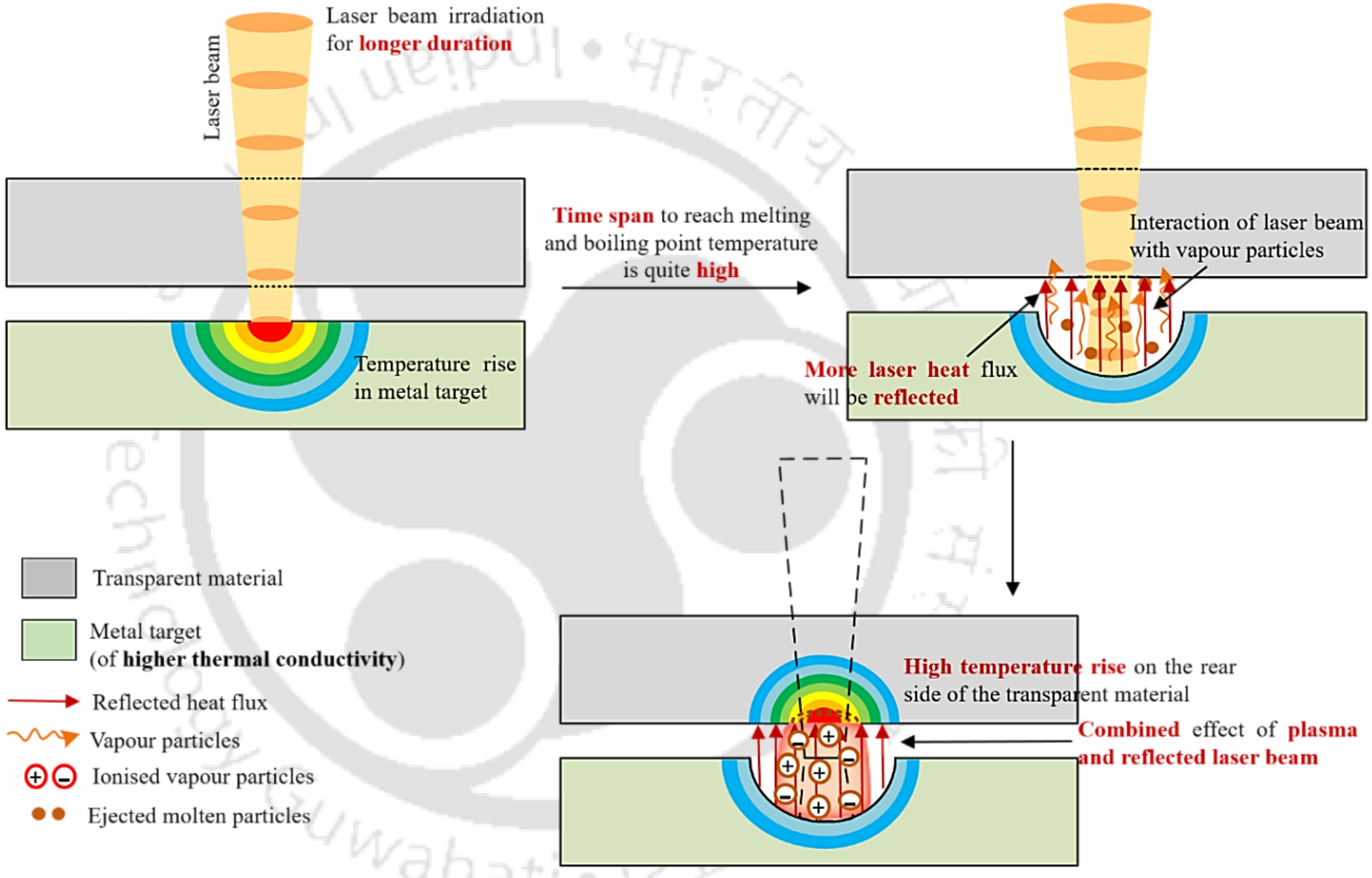

Figure 3.16 Schematic representation of the effect of high specific heat capacity of the metal target on microchannel fabrication on transparent material during the LIPAA process

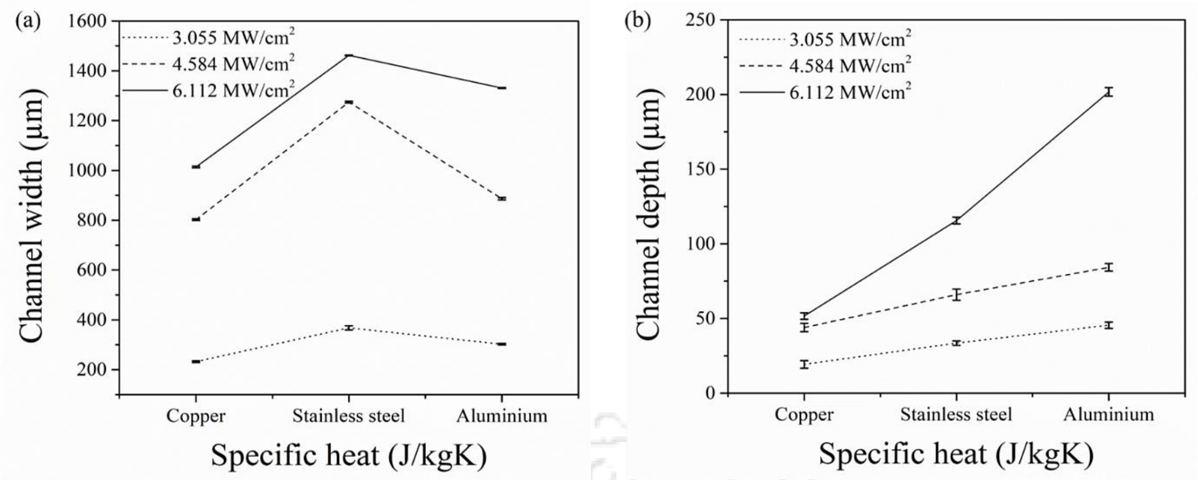

Figure 3.17 Effect of the specific heat capacity of the metal targets on (a) channel width and (b) channel depth

The above analysis on the effect of metal target properties on microchannel fabrication shows that microchannels formed with aluminium metal targets have a higher aspect ratio than those fabricated with copper and stainless steel as metal targets. The aspect ratio of microchannels fabricated at same condition of laser parameters (3.06 MW/cm^2 pulse power density, 4 ms pulse duration and 40 Hz pulse repetition rate) for the three metal targets have been shown in figure 3.18.

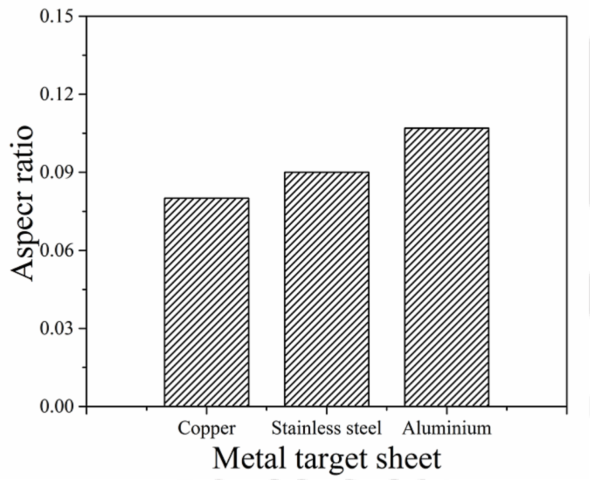

Figure 3.18 Aspect ratio of microchannels on PC for aluminium, copper and stainless steel as the metal targets

In most applications, the aspect ratio is defined as the depth of a structure over the width. Mathematically, it can be expressed as

$$aspect\,ratio = \frac{depth}{width} \tag{3.6}$$

Higher the aspect ratio, the more challenging it is to manufacture a microchannel. Further, higher aspect ratio microchannels leads to annular flow of fluid inside the micro-channel. Uniform fluid is thus obtained in such microchannels, which emphasizes its potential for use in microfluidics. Also, high aspect ratio microchannels lead to high rate of heat and mass transfer, making it an excellent microdevice for heat exchangers.

Thus, further investigation of our research was conducted considering aluminium as the metal target.

3.8 Summary

The chapter presented successful fabrication of microchannels on transparent PC using LIPAA. Subsequently, the channel geometry (channel width and channel depth) and channel roughness of the fabricated microchannels were measured and analysed. After successful fabrication of microchannels, the effect of the properties of metal target was also investigated. Three different metal targets viz. aluminium, copper and stainless steel have been utilized during the process. The important observations from the study can be summarized as follows:

- LIPAA can successfully fabricate high quality microchannels for various scientific and industrial applications.
- EDX analysis showed the presence of carbon, aluminium and oxygen deposits on the channel edge and channel bed. The deposits are temporary in nature and are easily removed, thereby having no specific influence of the deposits on the quality of the microchannel for bio-medical applications.
- An increase in the thermal conductivity of the metal targets results in the decrease in the dimension of the channels fabricated on the PC sheet, while an increased melted and vaporized volume is obtained in the metal target itself. However, this effect of the thermal conductivity is more distinctly visible on the channel width rather than on the channel depth.
- The time span for plasma generation and the distance of the generated plasma from the rear side of the PC sheet plays the major role in determining the channel width on considering the variation in thermal conductivity of the metal targets.
- Again, an increase in the dimension of the channels fabricated on the PC sheet was observed with the increase in the value of the specific heat of the metal target, whereas a decrease in the melted and vaporized volume in the metal target itself was obtained. On the other hand, this influence of the specific heat capacity is more prominent on the channel depth rather than on the channel width.

- The reflected laser beam that reaches the rear side of the PC sheet during the process plays the main role in determining the channel depth when the variation in specific heat capacity is considered.

Higher aspect ratio microchannels are fabricated with aluminium metal target compared to that fabricated with copper and stainless steel as metal target. As such, further investigation of our research has been performed considering aluminium as the metal target.

Chapter 4

Parametric and statistical investigation into microchannel fabrication on PC and fabrication of thermally bonded micro-channels

---

4.0 Scope

This chapter presents the results obtained during the full-factorial experiments on microchannel fabrication on polycarbonate (PC) using LIPAA with aluminium metal target. Experiments were conducted considering the effective range of process parameters viz. pulse power density, pulse repetition rate, pulse duration and scanning speed. A systematic study has been performed to analyze the effect of these process parameters on the responses like channel geometry (channel width and channel depth) and channel quality (channel roughness). Analysis of Variance (ANOVA) is carried out to find the significance of the factors on the responses viz. channel dimensions and channel roughness. Second order mathematical relations among the input laser parameters, their interactions and the responses were developed. To assess the prediction accuracy of the developed mathematical model, the confirmation experiments were planned and performed. Also, multiple objective (response) optimization of the input parameters to predict a better quality channel geometry and channel roughness was carried out. Further, the main effect plot and the surface plots are plotted to give a visual evaluation of the effect of the process parameters on the responses.

The fabricated open microchannels were closed by using a thermal bonding process. A fluid flow test was also carried out on the closed microchannel and its potentiality to be used as a microfluidic device has been proved. The study also demonstrates that LIPAA process can be utilized to fabricate channels of different shapes to achieve better performance of the microchannel based devices.

4.1 The need

The fabrication of microchannels on PC by LIPAA requires a proper setting of laser parameters like pulse power density, pulse repetition rate and pulse duration to obtain desired channel geometry and quality. Subsequently, it is essential to study the influence of the process parameters on the variation of the channel width, channel depth and channel roughness. Channel width is a crucial factor in microchannel based microfluidics as it affects the flow through the microfluidic; channel depth also plays an important role in the controlled flow of chemicals and solvents through the microchannel based microfluidics, while the roughness of the channel has a vital role in determining the fluid flow characteristics through the microchannel. A need was thus identified to carry out experiments, study the effect of process parameters on the responses and determine suitable parameters for microchannel fabrication as desired by different applications. Further, the need to form a closed channel and test its ability to be used as a microfluidic device was also identified, thereby verifying the sustainability of the LIPAA process. In addition, the effect of microchannel profiles on the flow resistance of the fluid passing through them has been identified. A need was thus also identified to fabricate different profile microchannels to achieve the best performance of the microfluidics or microchannel based heat sinks.

4.2 The present approach for parametric and statistical analysis of LIPAA

The key objective of the present experimental study was to investigate the impact of the laser parameters on channel geometry (channel width and channel depth) and channel quality (channel roughness) and to find the significance of the factors on the responses. For the purpose, comprehensive parametric and statistical analysis of the experimental results was carried out. An overview of the analysis is shown in figure 4.1.

Microchannels were fabricated on PC by LIPAA process by varying four process parameters viz. pulse repetition rate, pulse duration, scanning speed and pulse power density. The selected laser parameters were varied at three equal intervals. Table 4.1 presents the process parameters and their levels. Design of experiments (DoE) based on full-factorial (3^4) was made and experiments were carried out accordingly (with reference to Table 4.1). A repetition of three times were made for each set of experiments and three responses viz. channel width, channel depth and channel roughness were measured for each set. Details about the measurement procedure are presented in Chapter 3, Section 3.5.

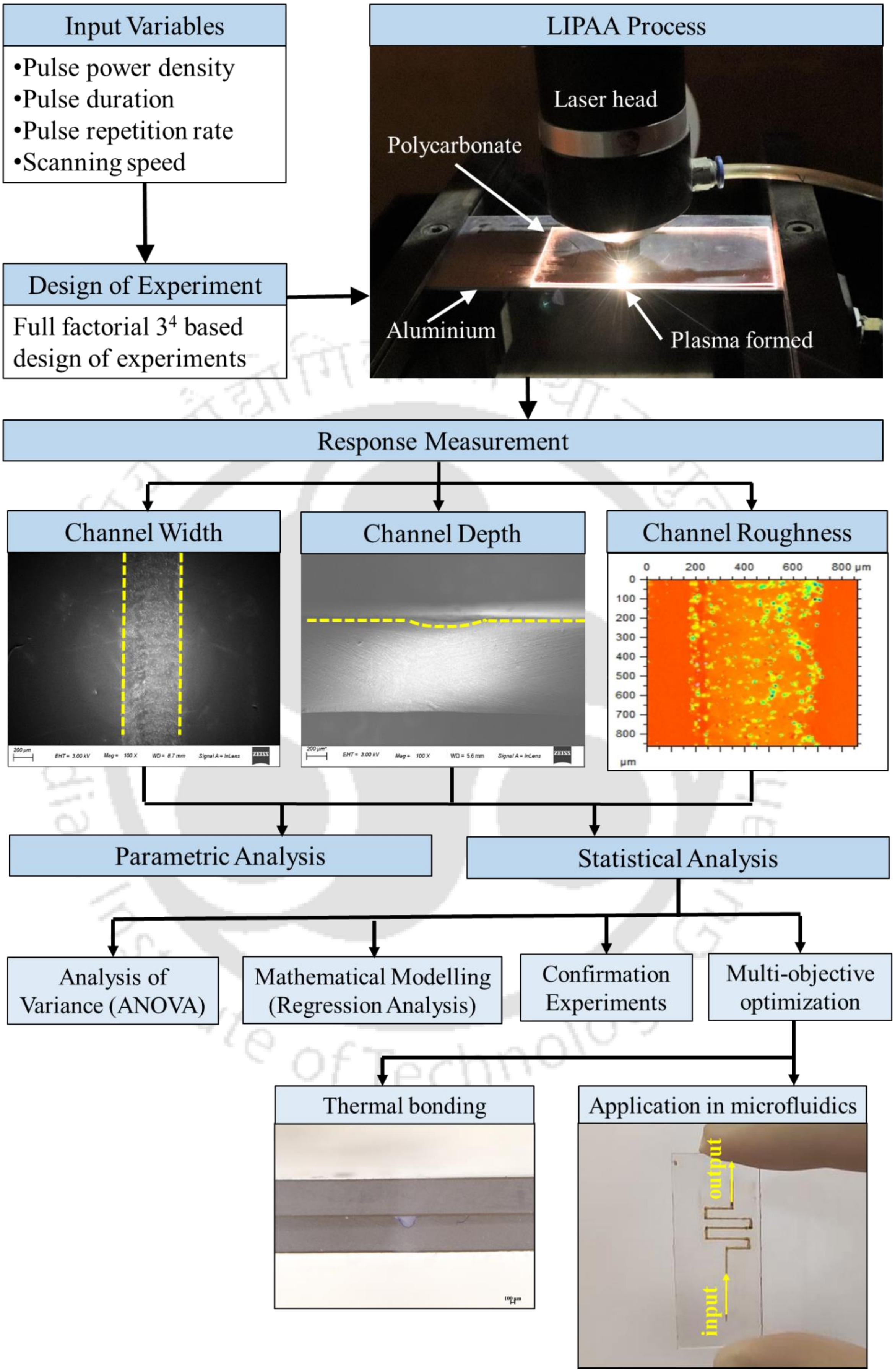

Figure 4.1 Approach for the parametric and statistical analysis

Table 4.1 Laser process parameters and their levels

Laser Parameters	**Levels**		
Pulse power density (MW/cm^2)	3.06	4.6	6.1
Pulse duration (ms)	2	4	8
Pulse repetition rate (Hz)	40	60	80
Scanning speed (mm/s)	4	7	10

4.3 Results and discussion

Experiments on microchannel fabrication on PC during LIPAA were performed as per the designed array and the responses were measured using the instruments. The complete set of experimental results is presented in Table 4.2. A detailed parametric analysis of process responses was then carried out and analysis of variance (ANOVA) was performed. ANOVA examines the main effects of independent laser process parameters and their interaction effects. It was conducted at 95% confidence level ($\alpha = 0.05$) for all the responses. The backward elimination method was used in the process of ANOVA. Statistical terms related to ANOVA are listed below:

- *P-value*: It denotes the probability that whether the results observed in the study could have occurred by chance. The P-*value* ranges from zero to one. If the P- *value* is greater than 0.1 for any parameter, then the parameter is deemed insignificant. If the P-*value* lies in between 0.05 to 0.1, then the parameter is considered mildly significant, and if the value is less than 0.05, then the parameter is considered highly significant.
- R^2: It is called the coefficient of determination. It provides a measure of variability in the response values which are under observation and can be explained by controllable factors and their interactions. The predicted model is considered sensitive if the R^2 is greater than 75%, else the model is considered as insignificant. Usually, *adjusted*-R^2 is used in statistical methods to compare the models with different numbers of independent variables. This is because; *adjusted*-R^2 increases only if the new term improves the model more than would be expected. The value of *adjusted*-R^2 is always smaller than or equal to R^2. Another term used during the analysis is *predicted*-R^2. It determines how well the model can predict the responses for any new observation. The larger the value of *predicted*-R^2 greater is the predictive capability of the model.

Table 4.2 3^4 full factorial experimental results for microchannel fabrication on Polycarbonate

PRR−Pulse repetition rate, **PD**− Pulse duration, **SS** −Scanning speed, **PPD**−Pulse power density, **SD**−Standard deviation

Sl No	PRR (Hz)	PD (ms)	SS (mm/s)	PPD (MW/cm^2)	Mean Width (µm)	SD of width	Mean Depth (µm)	SD of depth	Mean Roughness (µm)	SD of roughness
1	40	2	4	40	*					
2	40	2	4	60	228.24	5.47	12.01	2.07	2.53	0.61
3	40	2	4	80	588.37	5.87	14.39	4.01	2.90	1.11
4	40	2	7	40	*					
5	40	2	7	60	219.36	5.32	10.87	2.10	2.29	0.66
6	40	2	7	80	582.7	6.63	12.04	0.95	2.62	0.17
7	40	2	10	40	*					
8	40	2	10	60	205.58	5.28	7.43	0.50	2.19	0.16
9	40	2	10	80	425.04	9.55	10.54	1.38	2.32	1.35
10	40	4	4	40	232.28	10.41	35.48	2.62	2.72	0.32
11	40	4	4	60	836.42	10.81	74.88	2.52	17.79	4.90
12	40	4	4	80	1380.11	7.06	201.68	8.91	18.38	4.16
13	40	4	7	40	227.97	11.65	23.59	4.57	2.90	0.47
14	40	4	7	60	806.82	31.86	27.93	9.19	4.14	1.65
15	40	4	7	80	1277.53	6.20	180.75	5.74	16.93	1.67
16	40	4	10	40	194.91	6.17	17.92	2.27	1.56	0.22
17	40	4	10	60	896.01	6.72	26.78	3.39	4.33	0.51
18	40	4	10	80	1177.73	9.15	176.91	2.89	15.25	1.15
19	40	6	4	40	869.26	38.08	59.31	6.96	10.72	5.86
20	40	6	4	60	998.92	27.35	621.13	34.04	11.50	1.82
21	40	6	4	80	1386.31	7.57	332.49	3.35	18.14	0.60
22	40	6	7	40	731.07	34.33	42.74	4.20	10.43	1.44
23	40	6	7	60	916.16	4.66	497.12	3.52	10.74	0.80
24	40	6	7	80	1175.08	19.88	504.98	5.74	12.83	1.78
25	40	6	10	40	709.96	3.40	34.70	3.02	10.34	2.45
26	40	6	10	60	903.74	5.56	359.09	7.29	10.92	1.55
27	40	6	10	80	1021.63	5.54	467.59	4.44	11.73	0.32
28	60	2	4	40	225.88	2.66	*		1.78	0.20
29	60	2	4	60	603.76	6.82	21.67	2.00	6.64	0.43
30	60	2	4	80	1013.97	9.28	39.62	1.40	7.49	0.23
31	60	2	7	40	216.25	4.71	*		1.72	0.35
32	60	2	7	60	574.87	5.53	19.64	1.98	6.11	0.70
33	60	2	7	80	989.09	10.85	35.06	3.97	6.79	0.56
34	60	2	10	40	188.21	4.63	*		1.62	0.18
35	60	2	10	60	590.09	7.45	18.59	1.19	5.27	1.00
36	60	2	10	80	901.29	3.06	36.07	1.57	8.60	0.64
37	60	4	4	40	797.93	29.87	269.81	30.67	13.38	4.89
38	60	4	4	60	916.15	5.24	302.83	6.81	17.21	2.45
39	60	4	4	80	1492.98	12.74	355.49	6.40	18.29	0.41
40	60	4	7	40	702.11	13.38	47.48	8.24	7.48	1.17
41	60	4	7	60	886.43	5.71	270.15	3.71	8.04	0.98
42	60	4	7	80	1322.86	10.14	296.55	4.27	17.93	0.54
43	60	4	10	40	688.70	0.02	25.26	3.27	8.41	1.11

Sl No	PRR (Hz)	PD (ms)	SS (mm/s)	PPD (MW/cm^2)	Mean Width (µm)	SD of width	Mean Depth (µm)	SD of depth	Mean Roughness (µm)	SD of roughness
44	60	4	10	60	901.60	2.48	224.72	5.69	8.30	1.66
45	60	4	10	80	1260.19	6.18	287.74	4.02	16.27	0.73
46	60	6	4	40	888.17	27.24	363.28	8.69	12.00	1.30
47	60	6	4	60	1024.98	3.63	669.17	3.87	18.57	1.20
48	60	6	4	80	1577.18	2.64	712.15	4.19	19.02	0.24
49	60	6	7	40	761.39	6.10	340.19	4.31	11.63	0.40
50	60	6	7	60	959.29	2.31	587.47	3.99	13.21	0.33
51	60	6	7	80	1337.61	3.21	614.07	4.00	17.99	0.21
52	60	6	10	40	612.69	1.49	325.51	2.82	11.27	0.72
53	60	6	10	60	947.75	4.83	471.00	2.23	12.44	0.50
54	60	6	10	80	1149.26	1.67	599.47	6.04	16.50	0.61
55	80	2	4	40	320.02	4.80	18.08	2.59	4.58	2.38
56	80	2	4	60	1066.75	16.39	90.55	17.89	15.07	1.51
57	80	2	4	80	1429.51	3.66	95.10	3.91	16.19	0.36
58	80	2	7	40	366.19	7.29	15.81	0.56	8.49	0.51
59	80	2	7	60	1266.77	45.04	29.78	2.15	8.99	1.66
60	80	2	7	80	1366.14	7.23	47.43	4.42	9.09	0.29
61	80	2	10	40	319.15	9.12	10.98	0.83	2.55	1.84
62	80	2	10	60	1176.24	15.80	20.92	1.56	5.50	2.07
63	80	2	10	80	1200.43	7.16	37.93	3.48	8.86	0.35
64	80	4	4	40	821.12	3.75	329.43	3.73	14.66	0.14
65	80	4	4	60	1018.50	6.40	411.44	2.82	17.96	0.40
66	80	4	4	80	**					
67	80	4	7	40	767.18	4.11	82.02	2.98	8.95	0.22
68	80	4	7	60	953.98	4.96	225.76	1.50	9.19	1.23
69	80	4	7	80	**					
70	80	4	10	40	702.46	6.11	32.97	1.36	8.48	0.17
71	80	4	10	60	928.13	2.28	224.13	5.38	8.77	0.47
72	80	4	10	80	1429.42	8.53	311.73	3.48	17.34	0.30
73	80	6	4	40	901.63	3.59	424.97	4.54	15.28	0.40
74	80	6	4	60	1408.66	5.59	702.57	3.20	18.96	0.06
75	80	6	4	80	**					
76	80	6	7	40	798.42	2.07	258.28	4.72	10.21	0.62
77	80	6	7	60	1164.34	4.77	548.21	2.83	14.45	0.63
78	80	6	7	80	**					
79	80	6	10	40	659.48	1.64	268.89	3.71	11.11	0.43
80	80	6	10	60	1060.19	2.44	503.62	2.80	14.01	0.21
81	80	6	10	80	**					

*   No ablation occurred

** Unable to collect data due to burning of samples

4.3.1 Parametric study

Microchannel fabrication on PC using LIPAA requires a proper setting of laser parameters such as pulse power density, pulse repetition rate and pulse duration. Subsequently, the influence of the process parameters on the variation of the channel width, channel depth and channel roughness was studied and is presented in the following section.

(A) Effect of process parameters on channel geometry and channel roughness

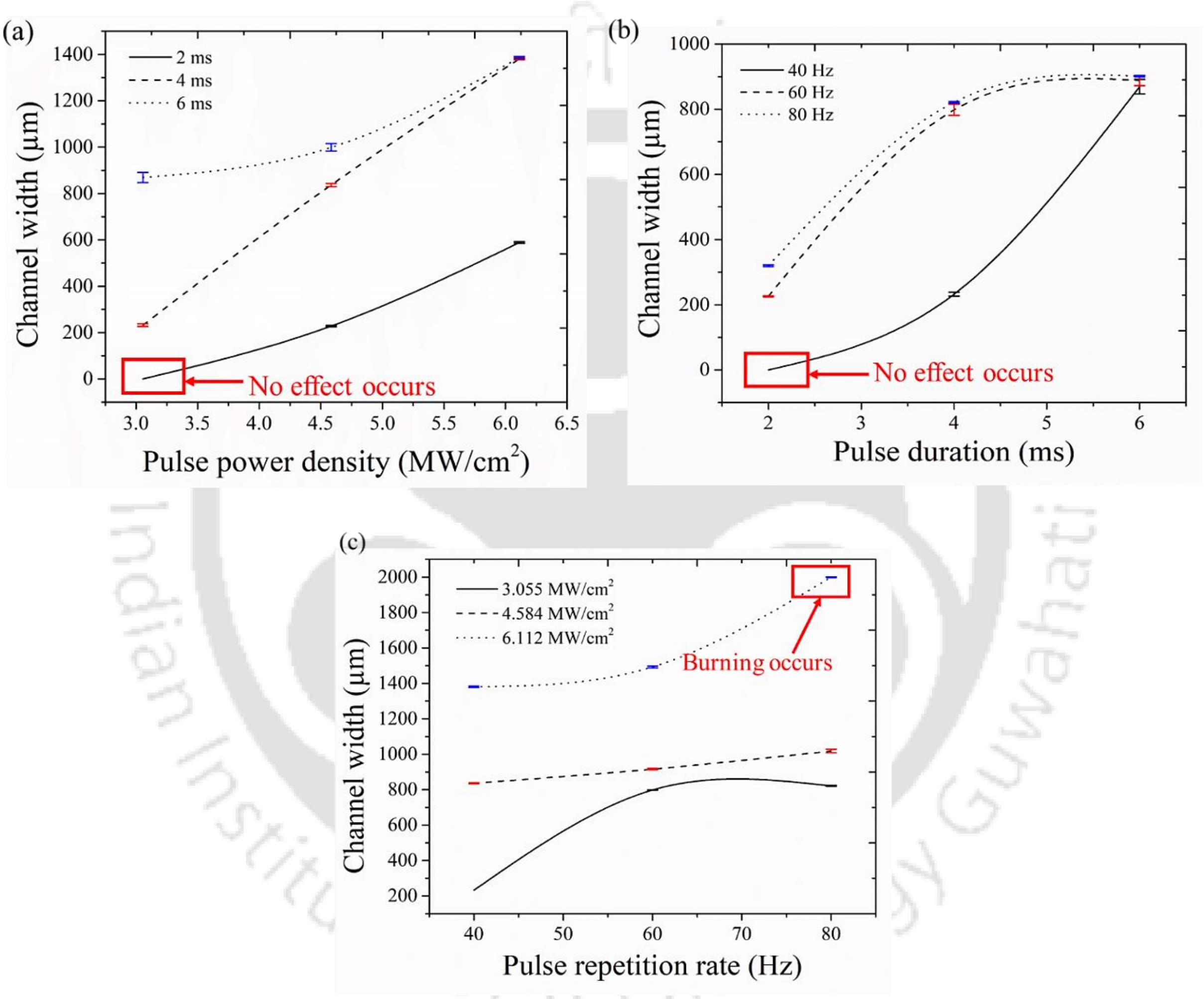

Figure 4.2 Effect of pulse power density, pulse duration and pulse repetition rate on channel width

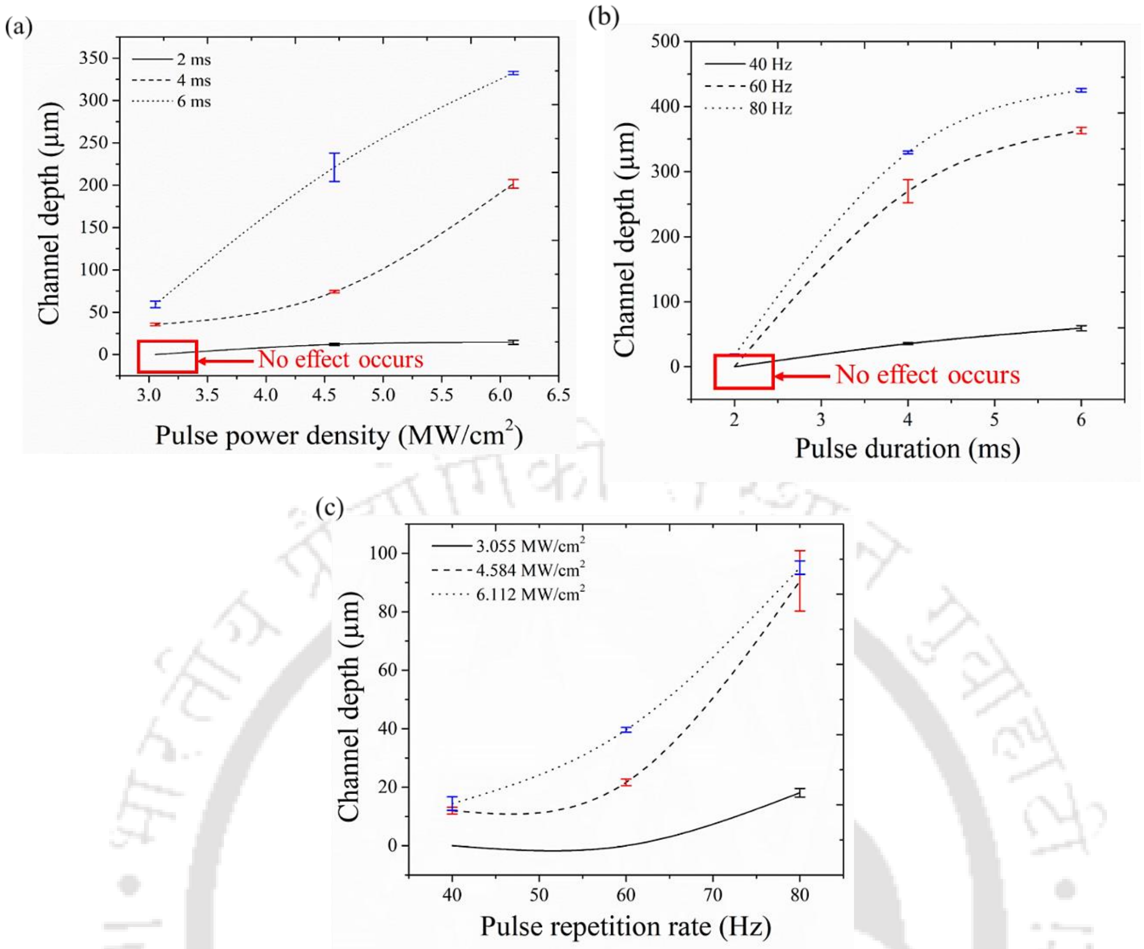

Figure 4.3 Effect of pulse power density, pulse duration and pulse repetition rate on channel depth

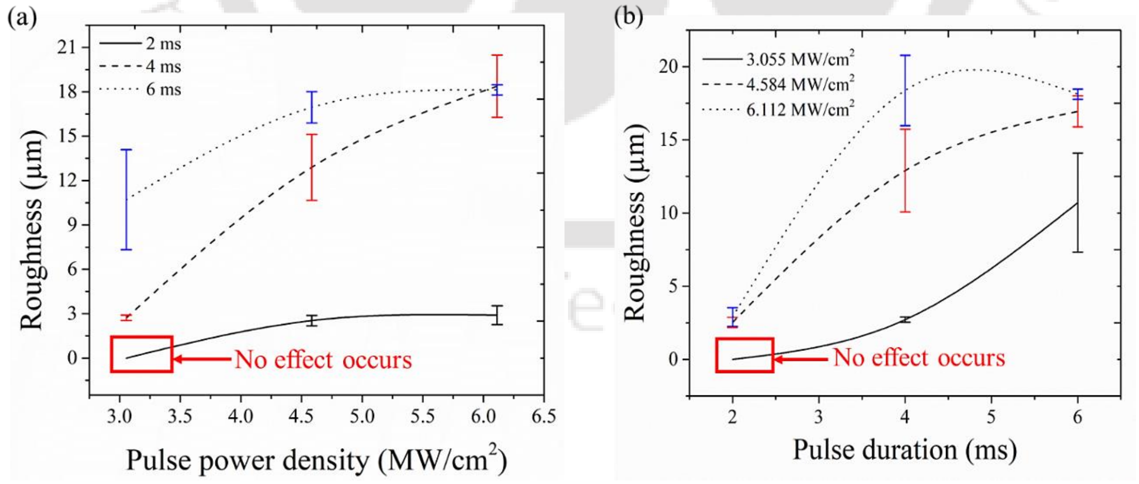

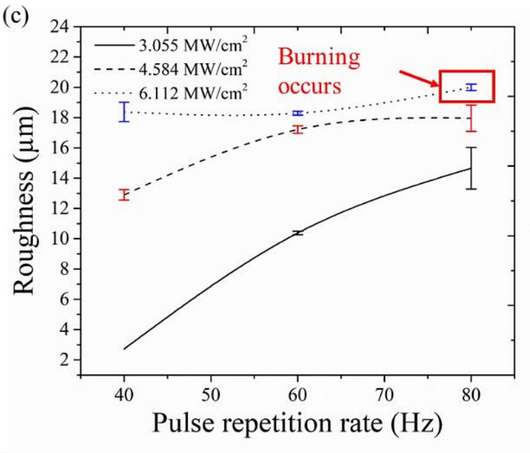

Figure 4.4 Effect of pulse power density, pulse duration and pulse repetition rate on channel roughness

The effect of the process parameters viz. pulse power density, pulse duration and pulse repetition rate on the responses like channel width, channel depth and channel roughness are shown graphically in figure 4.2, 4.3 and 4.4. It has been observed that, at a low pulse power density of 3.055 MW/cm^2 and low pulse duration of 2 ms, there was no thermal effect found on the PC sheet. However, very less effect on the PC is obtained when low pulse power density of 3.055 MW/cm^2 is applied with a low pulse repetition rate of 40 Hz. In general, it can be understood from the graphs that an increase in the process parameters causes an increase in the channel width, channel depth and channel roughness. The reason for the increase in the responses with the increase in the process parameters like pulse power density, pulse repetition rate and pulse duration mainly lies with the fact that the increase in the process parameters causes an enhanced generation of plasma.

As the pulse power density increases, it induces a higher population inversion, as a result of which greater stimulated emission takes place. Thus, there will be an enhanced irradiation of the photons on the aluminium sheet and increases the density of the electrons and ions. The plasma generation is again governed by the density of the electrons and ions. Therefore, the increase in the density of the electrons and ions enriches the generation of plasma. Similarly, when the pulse repetition rate increases, the number of laser pulses interacting with the aluminium sheet and with the vapour formed by the former laser pulses also increases. This causes more vaporization and more ionization of the vapour molecules and at last enhances the generation of plasma. Further, the rise in the pulse duration also corresponds to a rise in the plasma formation with high initial velocity. It is because; interaction of the laser beam for longer duration causes more vaporization and more ionization of the vapour molecules too.

Further, it can be observed from the plots that, the variation of the channel dimensions and its roughness value with increasing pulse power density is less sensitive with shorter pulse duration (~ 2 ms). There is no effect if both parameters, i.e. pulse power density and pulse duration, are kept low. However, the variation in responses with increasing pulse power density has been found to be more sensitive for pulse durations of more than 4 ms. It is because as the pulse power density is increased at higher pulse duration, it results in higher generation of plasma and the plasma affects wider and deeper into the PC, thus producing channels of larger dimensions. Moreover, the generated plasma gets accelerated and creates a higher thermal effect on the rear side of the PC. Thus, a non-linear variation of channel width with pulse power density is noticed at higher pulse duration.

It is also witnessed that as the pulse repetition rate increases at higher pulse power density (~ 6.112 MW/cm^2), there is an increase in the channel width and depth. Moreover, burning of the PC sheet occurs when the pulse repetition rate exceeds beyond a certain limit (80 Hz). It may be due to the reason that with increasing pulse repetition rate at higher pulse power density, the initial velocity of the generated plasma is very high, thereby causing a greater thermal effect on the rear side of the PC sheet. On the contrary, it is observed that at 40 Hz pulse repetition rate and 3.055 MW/cm^2 power density, though there was formation of channel, the depth of the channel formed was negligible. It may be due to the radial expansion of the plasma initially due to which channels of considerable width was produced. But the generated plasma did not have a deeper effect on the PC and thus channel with negligible depth was formed.

Again, it is observed that there is no formation of channel at pulse duration of 2 ms keeping pulse power density at its lowest considered values of 3.055 MW/cm^2. It is because, when the pulse duration together with pulse power density is less, the heat energy of the laser is not allowed to sink into the aluminium sheet. Hence, there will be no plasma formation, leading to no formation of channels. Moreover, increasing the pulse duration beyond a certain limit (≥ 4 ms) at higher values of pulse power density (≥ 6.112 MW/cm^2), the change in the channel width and roughness was very less. But the same was not observed for channel depth. Considerable change in the channel depth was obtained. The reason for such variation may be that, at higher pulse duration, as the laser interaction is longer, the longitudinal effect gets enhanced whereas the lateral impact of the plasma ceases. Thus, an increase in channel depth and nearly constant channel width is obtained with increasing pulse duration.

Thus, it can be said that the plasma generation gets enhanced with the increase in the pulse power density, pulse repetition rate and pulse duration. This enhanced plasma thermally affects the PC sheet resulting in an increased channel width, channel depth and channel roughness. However, it is difficult to have *in situ* measurement of the plasma energy density as the plasma is thermally coupled with the laser beam. But as reported by Saxena *et al.* (2014), above the plasma generation threshold, a linear increase in the input laser irradiance results in a linear increase in the energy transfer to the plasma. It is considered that the plasma generation threshold is obtained when the density of the electrons (N_e) reaches a value of about 10^{18}/cm^3 (Dahotre and Harimkar, 2008). The plasma energy density can thus be estimated from the electron density by the following equation (Saxena *et al.*, 2014):

$$E_{\text{plasma}} = N_e \left(\frac{\Delta E}{2} \right) \tag{4.1}$$

where ΔE is the ionisation energy. The average plasma temperature is given by:

$$T = \frac{2K}{3k_b} \tag{4.2}$$

where K is the average kinetic energy of the electrons and k_b is the Boltzmann's constant.

For an ionization energy of 34 eV of air, the E_{plasma} can be calculated to be about 2.72×10^6 J/m^3. Also, the plasma can attain a temperature from approximately 2500 K to as high as 50000 K and with a pressure up to 500 MPa. Thus the corresponding plasma properties has a large impact on the PC sheet. A temperature above the melting point temperature of the PC will be generated on its surface. The plasma induced pressure plays an important role in the material removal process. Major portion of the molten material will be expelled through the micron level gap present in between the PC and the aluminium sheet and a small portion gets redeposited.

The FESEM images of the channel width and the channel depth have been depicted in figure 4.5 and 4.6 respectively. It can also be seen from figure 4.5 that pits have been formed on the channel bed when a high pulse power density of 4.584 MW/cm^2 is applied. This may be due to the generation of high pressure plasma at high laser power density that results in explosive removal of the molten material. It is noted that at low power with a moderate pulse duration of 4 ms and pulse repetition rate of 40 Hz a clean and uniform channel is formed while higher power causes burning of the PC sample. Hence, low power with a moderate pulse duration and pulse repetition rate can be used to fabricate a clean and uniform micro-channel.

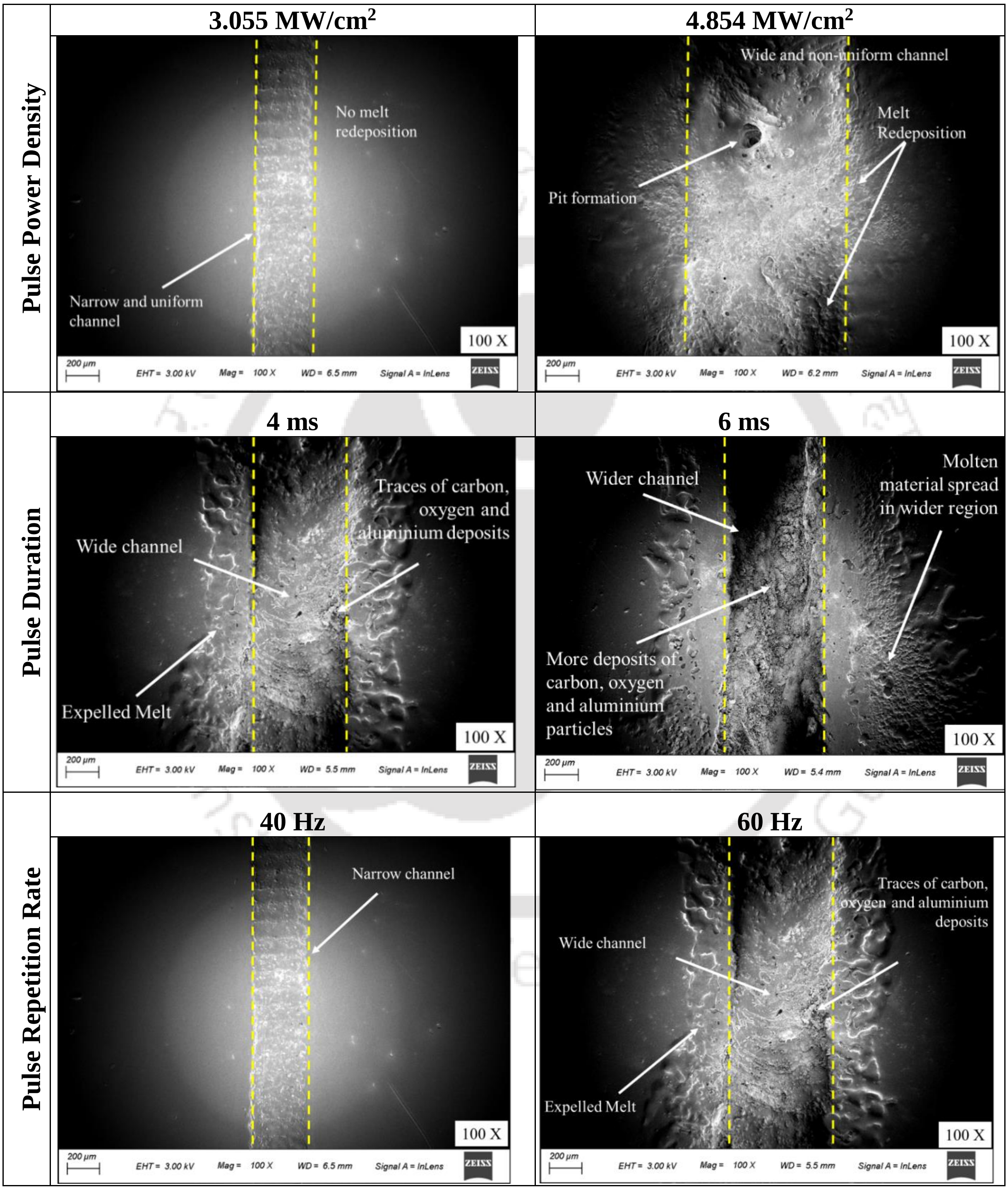

Figure 4.5 FESEM images of the effect of pulse power density, pulse duration and pulse repetition rate on channel width

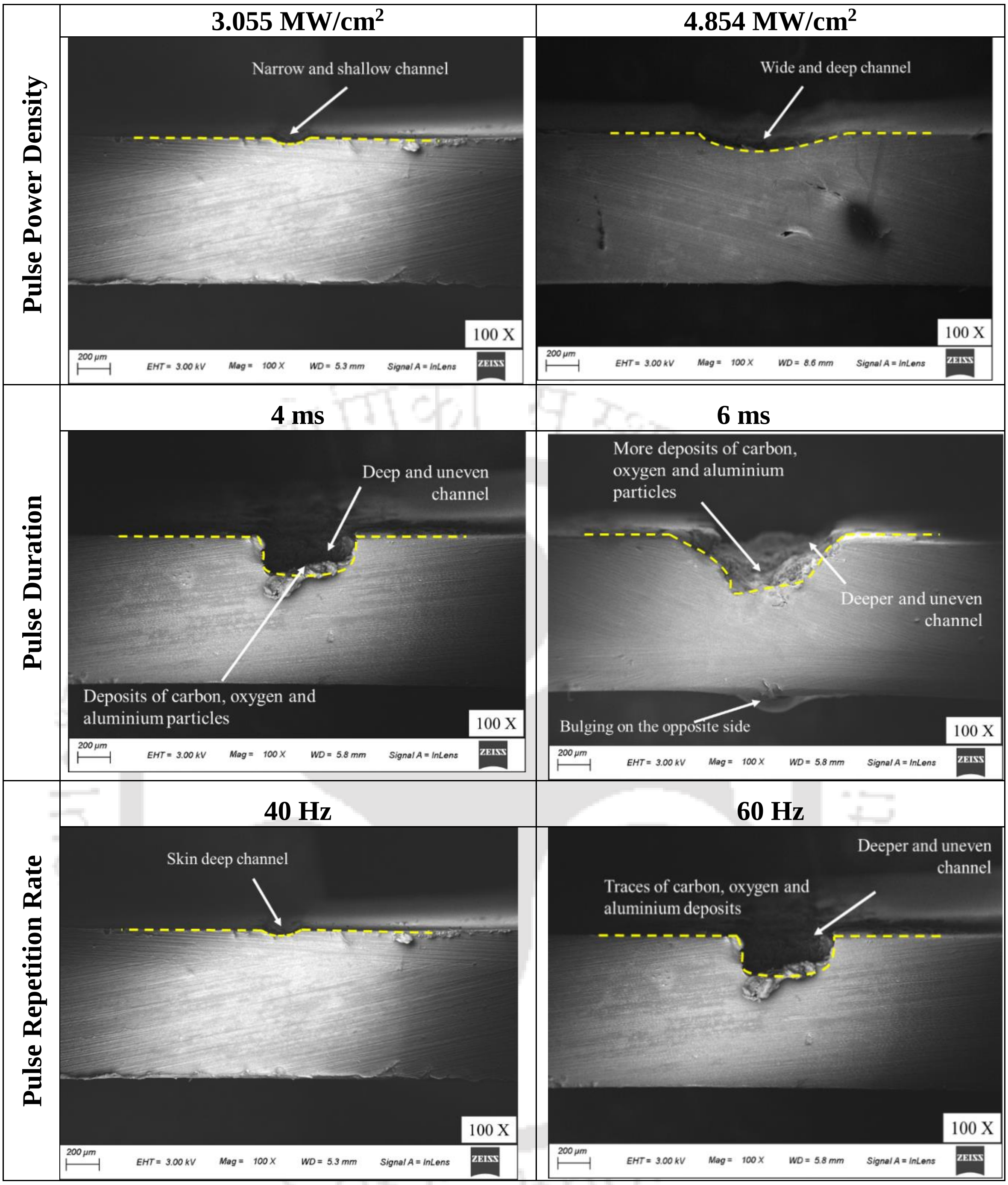

Figure 4.6 FESEM images of the effect of pulse power density, pulse duration and pulse repetition rate on channel depth

(B) Impact of scanning speed on channel formation

Figure 4.7 shows the effect of scanning speed on the channel geometry. As the scanning speed increases, the effect of plasma on the PC sheet decreases and almost diminishes as the scanning speed increases to a value of about 10 mm/s at low pulse power density.

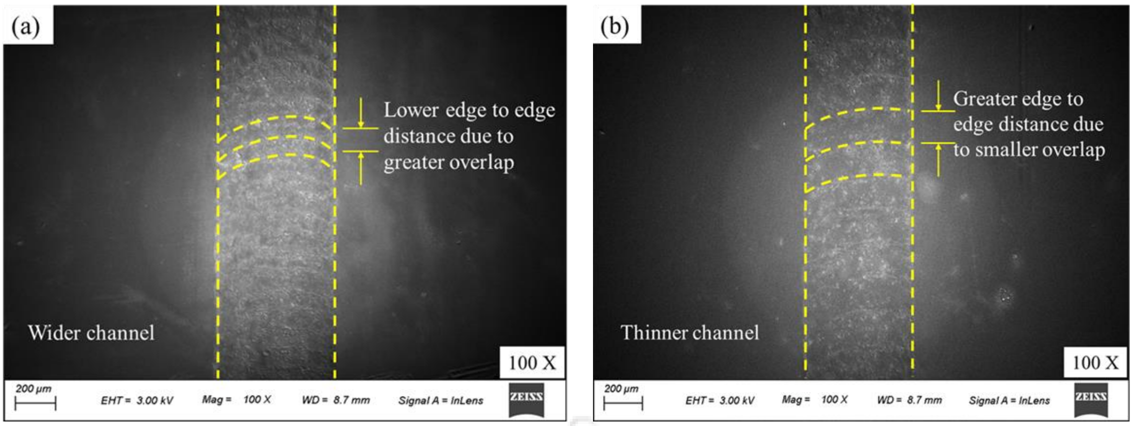

Figure 4.7 Effect of laser scanning speed on the width of the fabricated microchannel on PC at pulse duration 2 ms, repetition rate of 40 Hz, pulse power density of 6.112 MW/cm^2 and varying scanning speed of (a) 4 mm/s (b) 7 mm/s

The reason for such variation may be stated that as the scanning speed increases the time of interaction of the laser with the aluminium decreases. In other words, the laser energy per unit area decreases and as such, plasma generation decreases. Thus there is a little thermal effect on the rear side of the PC which results in reduced channel size. Also, the successive laser pulse moves to a distance from the former laser pulse. There will be less overlapping of the laser pulses and smaller heat affected zone at higher scanning speed. Therefore, the channel width, channel depth and channel roughness decrease with increase in scanning speed. The scanning speed not only affects the channel geometry and roughness, but also plays an important role in the formation of the channel. For a channel to be formed, the pulse overlap must be greater than zero. For pulse overlap less than zero, discrete crater formation will occur. The effect of these pulse overlap is called the jump effect. The distance between two laser pulses, i.e. overlap distance, D_L and the overlap percentage, O can be expressed by Eq. (3) and Eq. (4) respectively (Vora and Dahotre, 2015).

$$D_{\mathrm{L}} = \frac{v}{f} \tag{4.3}$$

$$O = \left(\frac{\omega - D_{\mathrm{L}}}{\omega} \right) \times 100\% \tag{4.4}$$

where, ω is the focussed beam diameter, D_L is the overlap distance, v is the scanning speed and f the pulse repetition rate.

In our present work, the focussed beam diameter, D is 200 µm. Figure 4.8 shows the jump effect at scanning speeds of 4 mm/s and 7 mm/s and a fixed repetition rate of 40 Hz. The overlap distance for scanning speed of 4 mm/s and 7 mm/s was found to be

100 µm and 175 µm respectively. Taken in order, the overlap percentage for the two mentioned cases are found to be 50% and 12.5%.

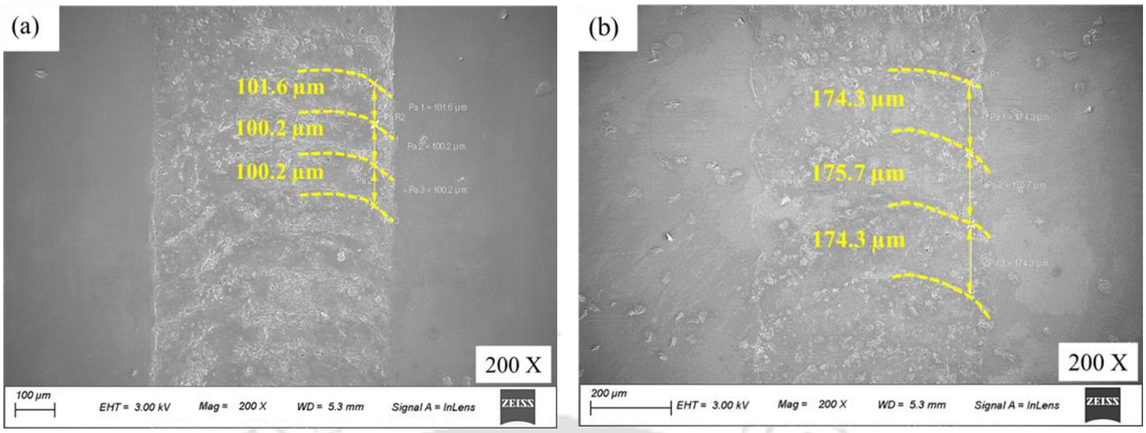

Figure 4.8 Jump effect at scanning speed of (a) 4 mm/s and (b) 7 mm/s at a repetition rate of 40 Hz

(C) Effect of number of scanning passes

As the number of scanning passes increases, the width and depth of the channel increase without increasing the roughness value. This is because a repeated number of passes will remove unwanted debris. It is because repeated number of passes results in removal of unwanted residue. This effect of the number of scanning passes on channel geometry is shown in figure 4.9. It is observed that the channel width and depth significantly increase with number of scanning passes, however on further increase in the number of passes beyond five to six; significant variation in the channel geometry was not observed. This may be due to the carbon deposited on the channel bed and also the increasing distance between the aluminium sheet and the PC channel bed. In addition, the carbon deposits on the channel can actually cause burning to the PC when the laser beam passes through it. Therefore, an acceptable number of passes is required to obtain a channel of the desired width and depth.

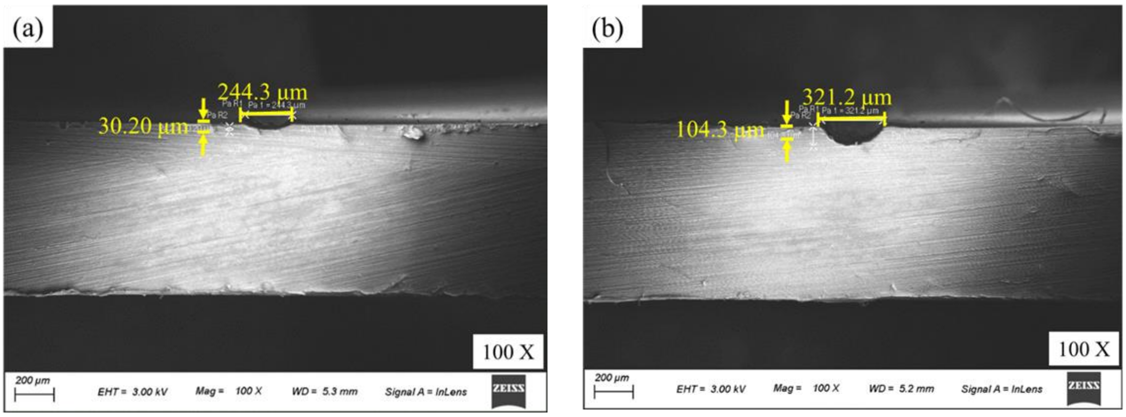

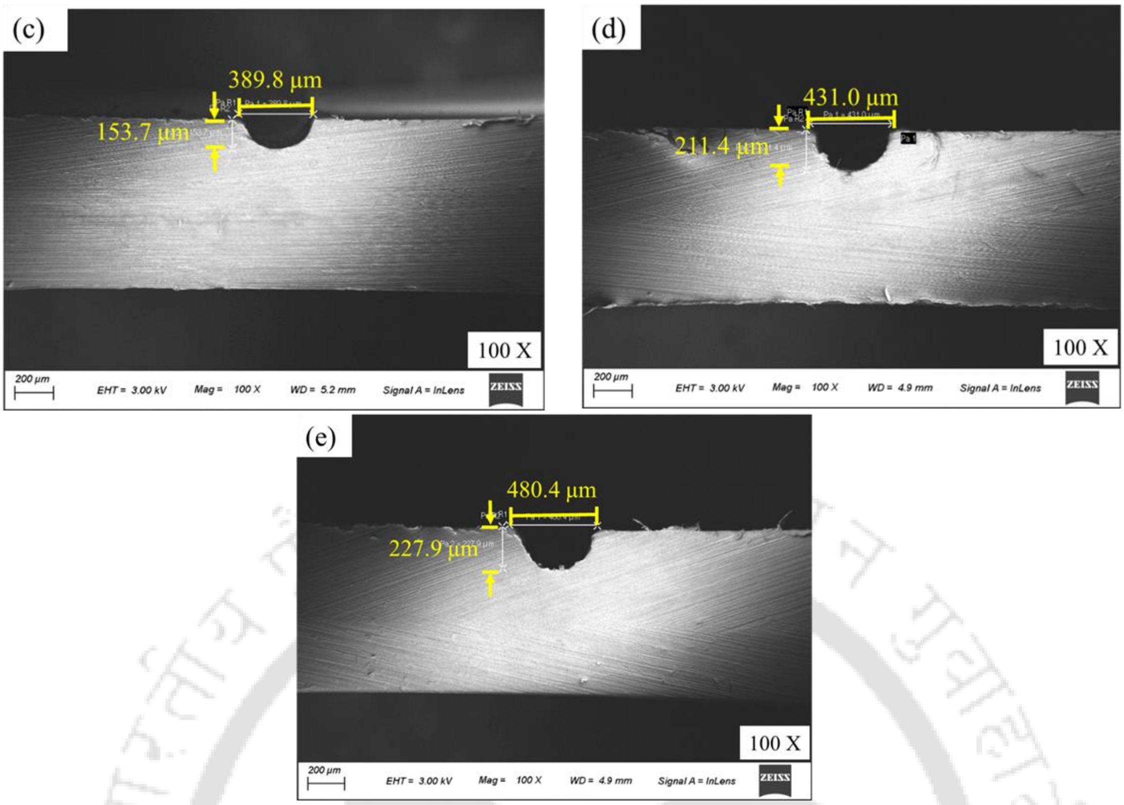

Figure 4.9 FESEM images showing the effect of number of laser scans (a) one pass, (b) double pass, (c) triple pass, (d) four passes and (e) five passes

Figure 4.10 shows a graphical representation of increase in width and depth with the increase in the number of passes. It can be noted that increase in both the channel width and channel depth follows the same trend with the increase in number of passes thereby maintaining a nearly constant aspect ratio for all the passes.

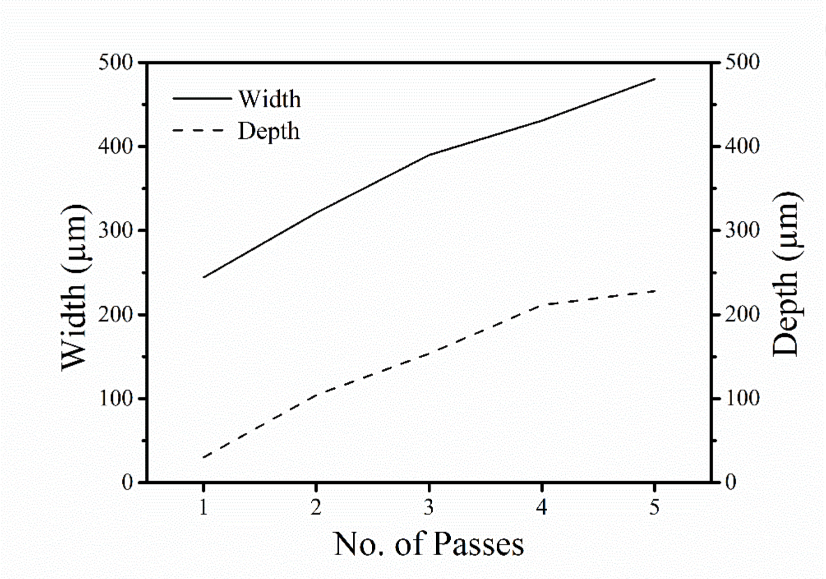

Figure 4.10 Variation of channel width and depth with number of passes

4.3.2 Statistical analysis

In the present work, to determine the significance of the factors on the responses viz. channel dimensions and channel roughness, Analysis of Variance (ANOVA) was performed. Second order mathematical relations among the input laser parameters, their interactions and the responses were also developed and confirmation experiments were performed to assess its prediction accuracy. Further, multiple objective (response) optimization of the input parameters for prediction of better quality channel geometry and channel roughness was carried out. The detail explanation of the analyses is presented in the subsequent sections.

(A) Analysis of Variance (ANOVA) for channel width

ANOVA analysis was performed to learn about the influence of input parameters on the channel width. The test for significance of the individual coefficients were obtained by ANOVA analysis. From the analysis it is observed that the linear parameters effective are repetition rate (f), pulse duration (t_{on}) and pulse power density (I_P). Also, among the square terms, repetition rate (f^2) and pulse duration (t_{on}^2) were found effective. For two-way interaction terms, pulse duration and pulse power density ($t_{on} \times I_P$) show significant effect on each other. The terms that are not significant were eliminated by backward elimination process in the ANOVA table. The linear parameter scanning speed has been eliminated from the table depicting its insignificant influence on the channel width. On the contrary, the other process parameters like repetition rate, pulse duration and pulse power density are found to be significant with P-*value* less than 0.05. The result of ANOVA for the response channel width is shown in table 4.3. The values of *adjusted* R^2 and *predicted* R^2 were computed and were observed that the *predicted* R^2 value of 0.8770 is in reasonable agreement with the *adjusted* R^2 value of 0.9013. Adequate precision ratio measures the signal to noise ratio. A ratio of 30.710 indicates an adequate signal and hence this model can be used to navigate the design space.

Table 4.3 Analysis of Variance of channel width

Source	DF	Adj SS	Adj MS	F-Value	P-Value
Model	6	40322020	6720337	53.31	0.000
Linear	3	38655317	12885106	102.22	0.000
Repetition rate	1	7627087	7627087	60.50	0.000
Pulse duration	1	10216854	10216854	81.05	0.000
Pulse power density	1	20811376	20811376	165.09	0.000

Square	2	1037823	518912	4.12	0.020
Repetition rate × Repetition rate	1	408345	408345	3.24	0.076
Pulse duration × Pulse duration	1	629478	629478	4.99	0.028
2-way interaction	1	628881	628881	4.99	0.029
Pulse duration × Pulse power density	1	628881	628881	4.99	0.029
Error	74	9328237	126057		
Total	80	49650257			

Determining the significance of the process parameters from ANOVA, the main effect plots for the channel width have been plotted as shown in figure 4.11. The plots show the effect of the pulse power density, pulse duration, pulse repetition rate and scanning speed on the channel width. The nearly horizontal line for scanning speed represents its insignificant effect on the channel width. While the other process parameters repetition rate, pulse duration and laser pulse power density shows its significant effect on channel width. True to form, the channel width increases with repetition rate, pulse duration and pulse power density. However, steeper slope for pulse power density shows its greater effect on channel width. Figure 4.12 shows the 3D contour plot which explains the combined effect of the pulse power density with the pulse duration and pulse repetition rate.

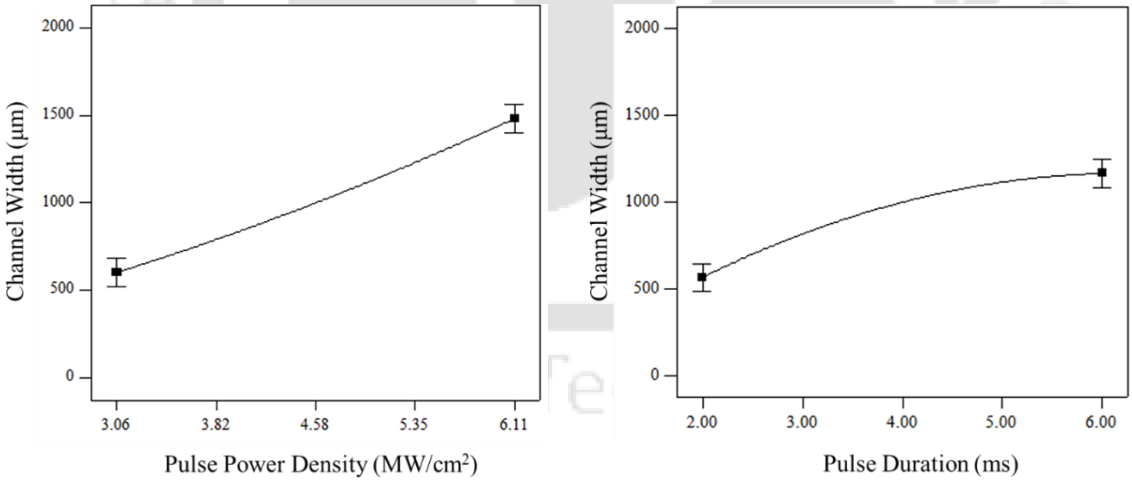

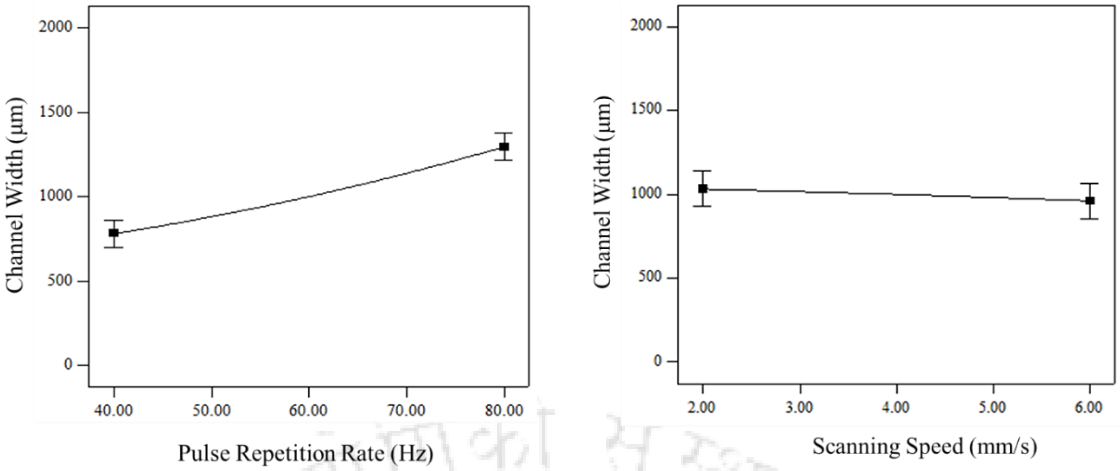

Figure 4.11 Main effect plot for channel width

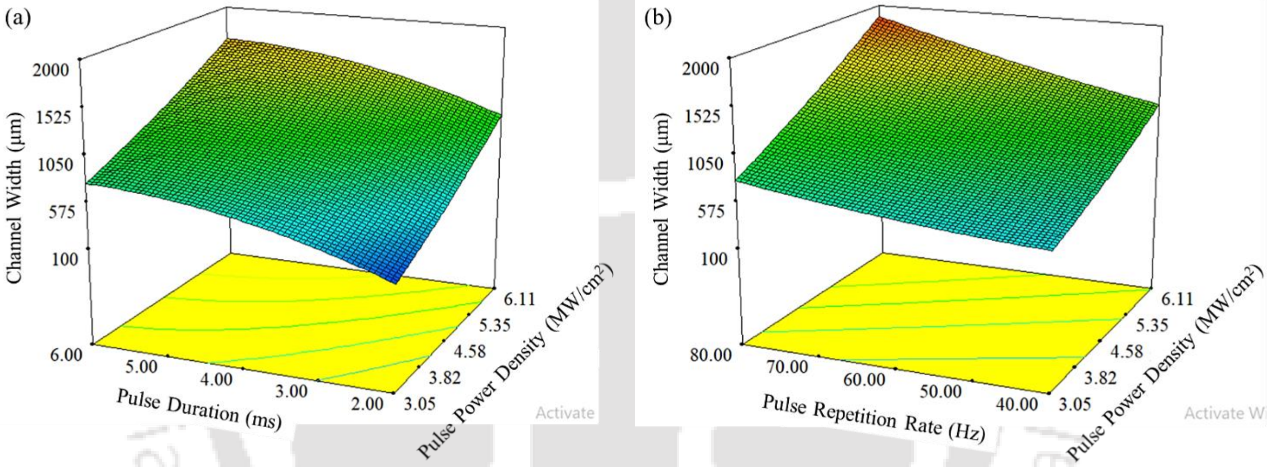

Figure 4.12 3D contour plot for channel width

(B) Analysis of Variance (ANOVA) for channel depth

ANOVA was also performed to study the effect of laser parameters on channel depth. It is observed from the analysis that the linear parameters having significant impact on channel depth are pulse repetition rate (f), pulse duration (t_{on}) and pulse power density (I_P). However, the linear term scanning speed was found to have negligible effect on the channel depth and hence was eliminated from the ANOVA table. Among the square terms, only repetition rate (f^2) was found to be effective. Whereas no two-way interaction term has significant effect on the channel depth. The ANOVA table for the response channel depth is shown in table 4.4. The values of *adjusted* R^2 and *predicted* R^2 were found to be 0.86 and 0.82 respectively. The *predicted* R^2 value was noted to be in reasonable agreement with the *adjusted* R^2 value. Further, the adequate precision ratio of

26.26 indicates an adequate signal and that the model can be used to navigate the design space.

Table 4.4 Analysis of Variance of channel depth

Source	DF	Adj SS	Adj MS	F-Value	P-Value
Model	4	13172842	3293210	50.64	0.000
Linear	3	12851303	4283768	65.87	0.000
Repetition rate	1	2014979	2014979	30.99	0.000
Pulse duration	1	3988556	3988556	61.34	0.000
Pulse power density	1	6847767	6847767	105.30	0.000
Square	1	321539	321539	4.94	0.029
Repetition rate × Repetition rate	1	321539	321539	4.94	0.029
Error	76	4942185	65029		
Total	80	18115027			

The main effect plot for channel depth is presented in figure 4.13. The horizontal line for scanning speed represents its insignificant effect on channel depth. The figure shows that with the increase in the significant parameters like repetition rate, pulse duration and pulse power density, the channel depth increases. The steeper slope for pulse power density shows its highest significance, followed by pulse duration and pulse repetition rate. The variation of the channel depth with the significant process parameters is also represented clearly by the 3D contour plots presented in figure 4.14.

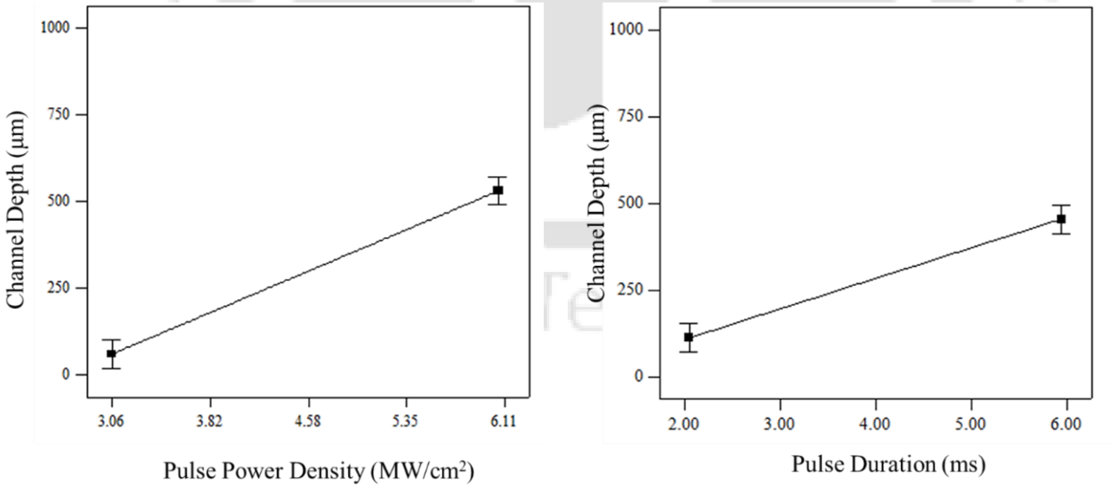

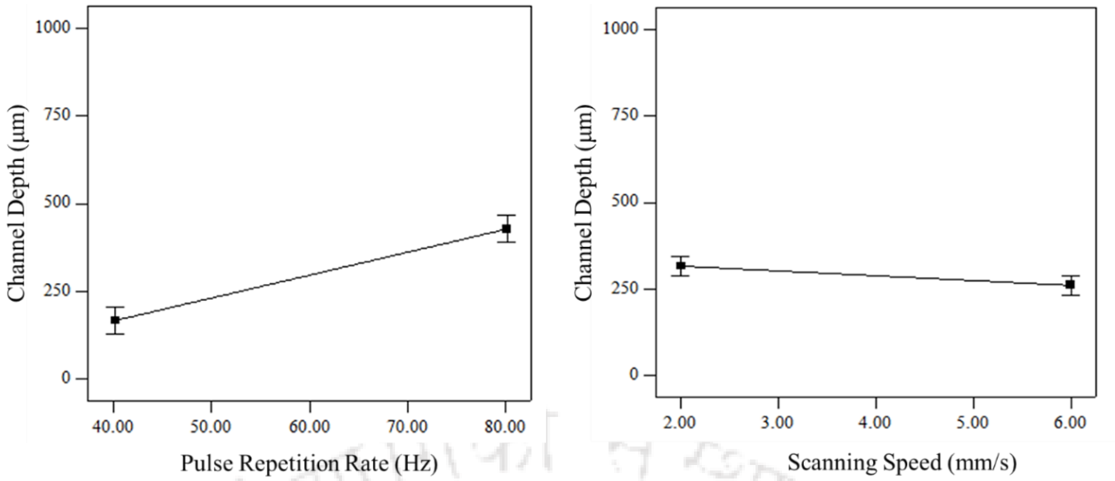

Figure 4.13 Main effect plot for channel depth

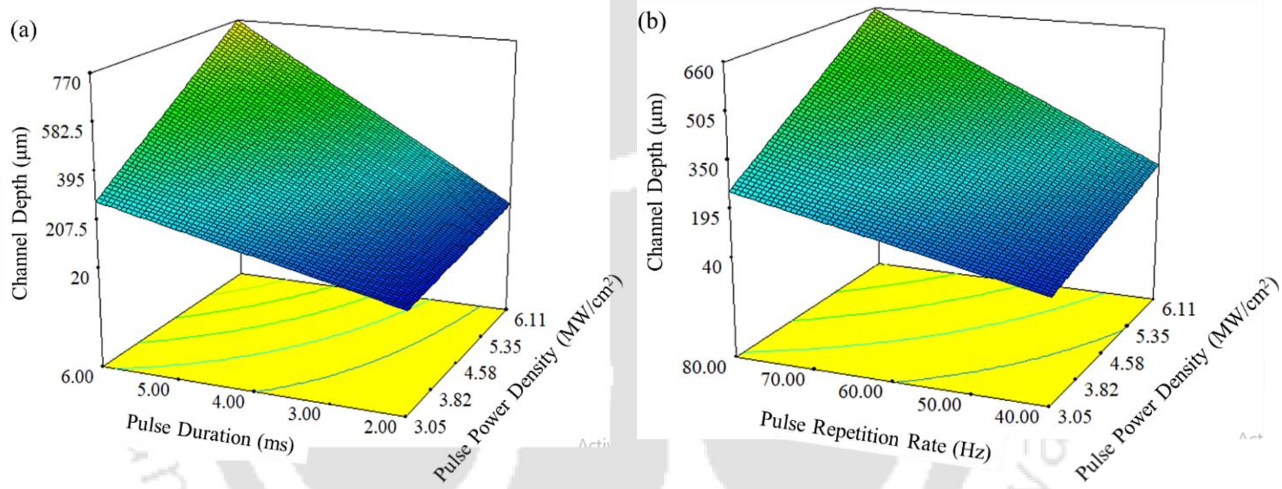

Figure 4.14 3D contour plot for channel depth

(C) Analysis of Variance (ANOVA) for channel roughness

Surface roughness (R) of the channel is also affected by the process parameters like repetition rate, pulse duration, scanning speed and pulse power density. However, the ANOVA for roughness shows that the effect of scanning speed is negligible compared to the linear parameters like pulse repetition rate (f), pulse duration (t_{on}) and pulse power density (I_P). The ANOVA table for roughness is as shown in table 4.5. The analysis shows that the linear process parameters like pulse power density (I_P), pulse repetition rate (f) and pulse duration (t_{on}) have significant effect on the roughness of the channel. The square terms repetition rate (f^2) and pulse duration (t_{on}^2) are also found to effect the channel roughness. Whereas for the two-way interaction terms, pulse duration and pulse power density ($t_{on}\times I_P$) show significant effect on each other. The values of *adjusted* R^2

and *predicted* R^2 were found to be 0.84 and 0.79 respectively. Hence, the *predicted* R^2 value is in reasonable agreement with the *adjusted* R^2 value. Further, adequate precision ratio of 24.3 indicates an adequate signal and hence this model can be used to navigate the design space.

Table 4.5 Analysis of Variance of channel roughness

Source	DF	Adj SS	Adj MS	F-Value	P-Value
Model	6	3862.43	643.74	47.13	0.000
Linear	3	3573.41	1191.14	87.21	0.000
Repetition rate	1	666.09	666.09	48.77	0.000
Pulse duration	1	1288.11	1288.11	94.31	0.000
Pulse power density	1	1619.21	1619.21	118.55	0.000
Square	2	174.74	87.37	6.40	0.003
Repetition rate × Repetition rate	1	103.22	103.22	7.56	0.008
Pulse duration × Pulse duration	1	71.52	71.52	5.24	0.025
2-way interaction	1	114.28	114.28	8.37	0.005
Pulse duration × Pulse power density	1	114.28	114.28	8.37	0.005
Error	74	1010.74	13.66		
Total	80	4873.16			

The main effect plot for roughness shown in figure 4.15 represents the effect of the process parameters and their significance. The effect of the scanning speed is however found to be quite considerable on the channel roughness compared to that on channel width and channel depth. Similarly, the pulse power density has the highest effect on roughness followed by pulse duration and repetition rate respectively. The 3D contour plots of channel roughness with reference to pulse power density and repetition rate; and pulse power density and pulse duration is shown in figure 4.16.

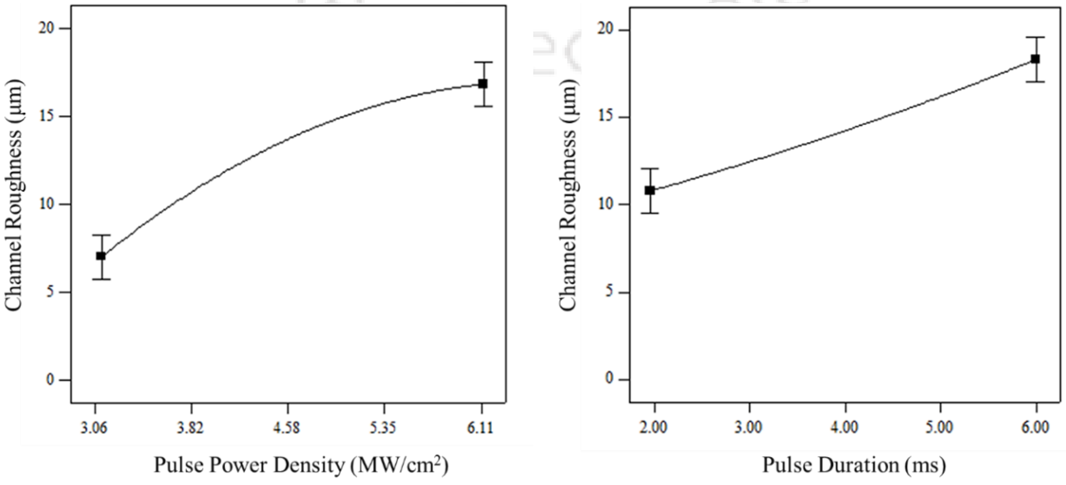

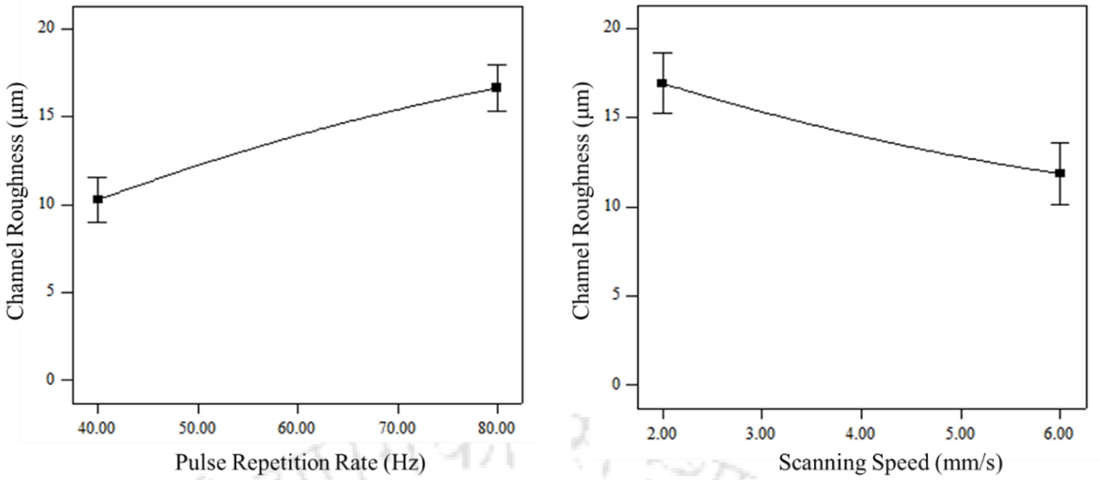

Figure 4.15 Main effect plot for channel roughness

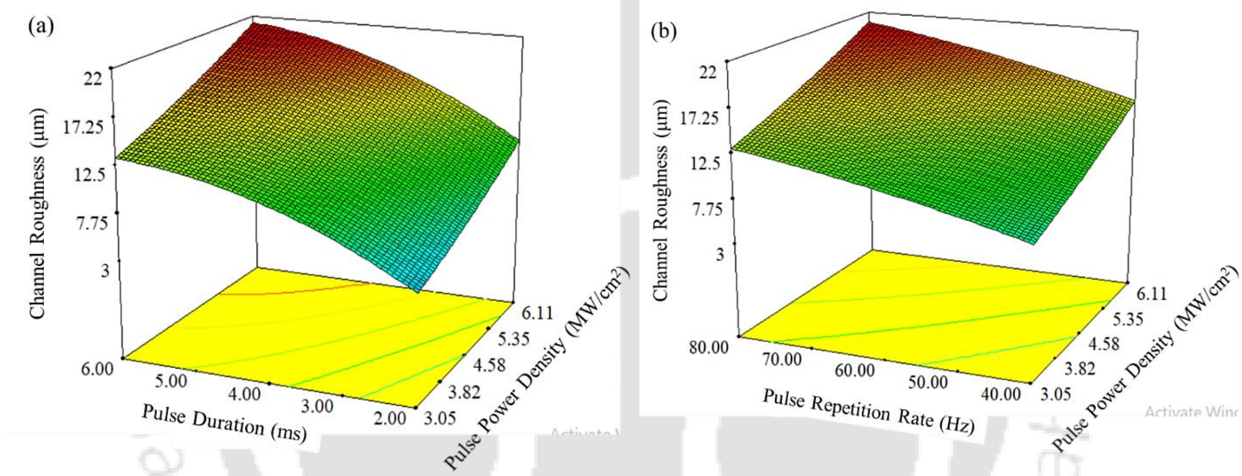

Figure 4.16 3D contour plot for channel roughness

(D) Regression model

In the present work, second order mathematical relations were developed between the input laser parameters viz. pulse power density (I_P), pulse duration (t_{on}), pulse repetition rate (*f*) and scanning speed (*v*), their interactions and the output responses like channel width (C_{width}), channel depth (C_{depth}) and channel roughness ($C_{roughness}$). These are as follows:

$$C_{width} = -5289 + 64.0\,f + 790\,t_{on} + 579.1\,I_P - 0.377\,f^2 - 46.8\,t_{on}^{\;2} - 43.2\,t_{on} \times I_P \quad (4.5)$$

$$C_{depth} = -2781 + 49.8\,f + 135.9\,t_{on} + 233\,I_P - 0.334\,f^2 \quad (4.6)$$

$$C_{roughness} = -61.22 + 0.894\,f + 9.10\,t_{on} + 5.914\,I_P - 0.00599\,f^2 - 0.498\,t_{on}^{\;2} - 0.583\,t_{on} \times I_P \quad (4.7)$$

The relations were modified by eliminating the non-significant terms by Backward Elimination Process. These equations can be used to predict the channel width, channel depth and the channel roughness value during the LIPAA process.

The correlation between actual and predicted values of the responses (C_{width}, C_{depth}, $C_{\mathrm{roughness}}$) are shown respectively in figure 4.17 (a), (b) and (c). It is observed that the developed model is acceptable and can be utilized to predict the responses with good accuracy.

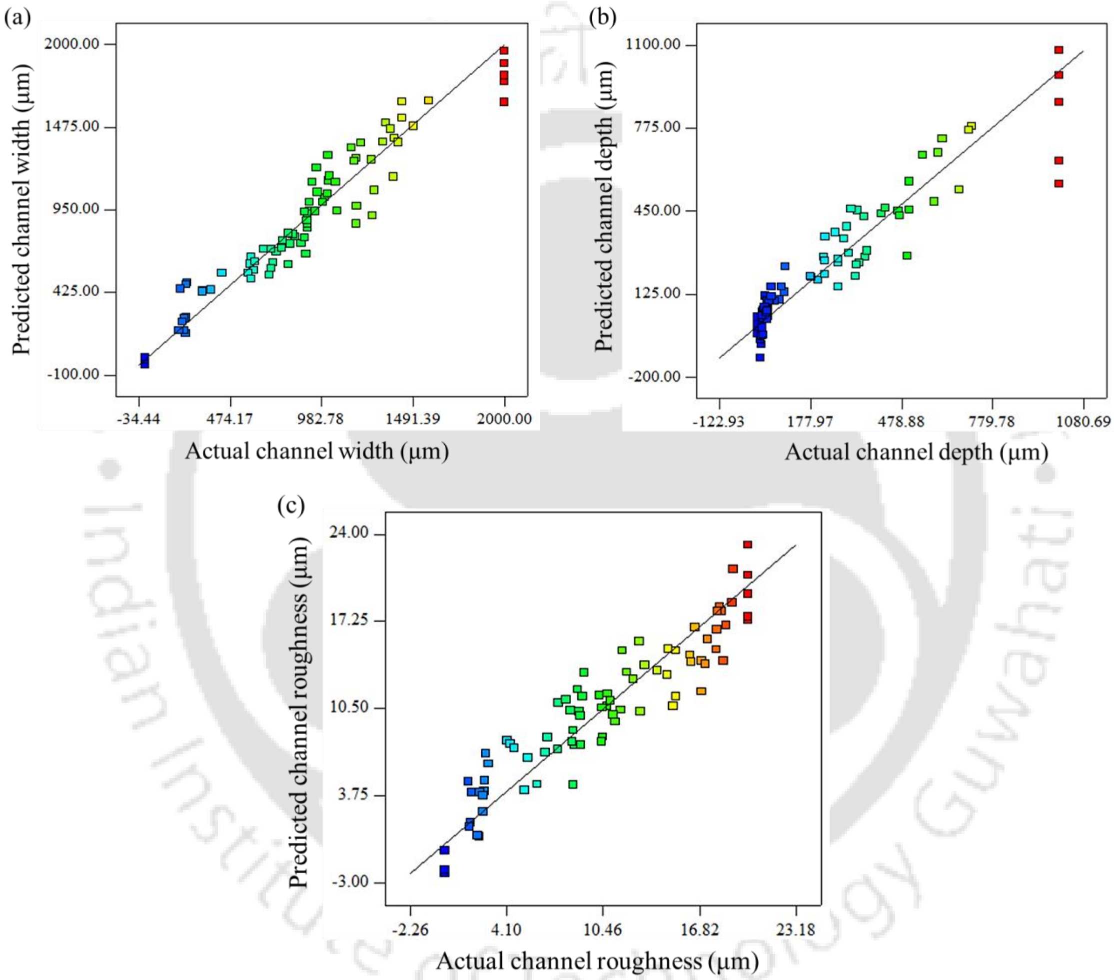

Figure 4.17 Plot of actual vs. predicted response, (a) channel width (b) channel depth (c) channel roughness

(E) Confirmation experiments and determination of optimal parameters

The developed mathematical equations can be used to predict the desired channel geometry and roughness for a chosen set of process conditions in this study. To keep the channel geometry within a definite limit and to minimize the roughness, an optimized set of the process parameters can be obtained. From the experimental results and analysis of the responses, the mathematical relations between the input process parameters and the responses were obtained as discussed. After the development of mathematical equations, confirmation experiments were performed to confirm the fairness of the mathematical model. The input process parameters for the confirmation tests were chosen randomly within the range of parameters used in the experimental study. The predicted as well as the experimental results are then determined and finally the percentage deviation is calculated. The entire confirmation tests are summarized in table 4.6.

Table 4.6 Confirmation experiments

Confirmation Experiment No.			1	2	3	4	5	6	Mean deviation
Input Parameters		Repetition rate	40	45	60	55	50	40	
		Pulse Duration	6	4	3	2.5	3.5	3.5	
		Pulse power density	3.43	4.202	3.055	3.819	4.584	4.202	
		Scanning Speed	7	10	5	4	8	4	
Responses	Channel Width	Experiment	710.83	882.62	501.98	578.91	1132.25	675.37	5.05%
		Predicted	822.7	946.075	516	572.575	1121.8	657.55	
		Deviation (%)	15.73	7.18	2.79	1.09	0.92	2.64	
	Channel Depth	Experiment	279.91	363.99	114.85	172.67	509.46	114.85	10.8%
		Predicted	293.45	306.8	124.7	177.9	418.25	131.8	
		Deviation (%)	4.83	15.71	8.57	3.03	17.9	14.76	
	Roughness	Experiment	9.135	9.02	6.245	6.14	12	6.66	6.2%
		Predicted	9.943	10.372	6.404	6.495	12.0195	6.989	
		Deviation (%)	8.84	14.98	2.54	5.78	0.16	4.94	

It was observed that the developed mathematical model was in good agreement with the experimental responses. The prediction deviation (absolute) for the responses channel width, channel depth and channel roughness are 5.05%, 10.8% and 6.2% respectively. Therefore, it can be said that the mathematical model can be applied to predict the desired channel geometry and roughness.

Based on the confidence gained from the confirmation experiments performed, multiple objective (response) optimization of the input parameters to predict a better quality channel geometry and channel roughness was carried out. The existence of a number of objectives, results in a set of optimized parameters thereby creating a conflict among the objectives. Hence, the multiple objective optimization was performed. With a target of 250 µm channel width, 150 µm channel depth and minimum roughness as per the requirement in microfluidic-based medical devices, the optimized value for repetition rate, pulse duration and pulse power density are found to be 40 Hz, 2 ms and 4.79 MW/cm^2.

4.4 Fabrication of closed microchannels using thermal bonding technique

After obtaining an optimized set of laser process parameters for microchannel fabrication, open microchannels were fabricated on PC sheet for applications in microfluidic devices. The microfluidic devices are a novel tool for basic biological and chemical analysis, by controlling fluids in microchannel networks, with which many key laboratory unit operations such as sample injection, separation, mixing, reaction and biochemical detection can be performed. However, open microchannels cannot meet this demand. Therefore, it is of great importance to produce a tightly closed, leak-proof microchannel.

Thermal bonding is one of the most widely employed techniques for obtaining a high quality bonding of the channels with uniform surface properties. It gives a quick and economical way of bonding a channel with better product quality. Figure 4.18 shows the conventional hot press machine used for thermal bonding.

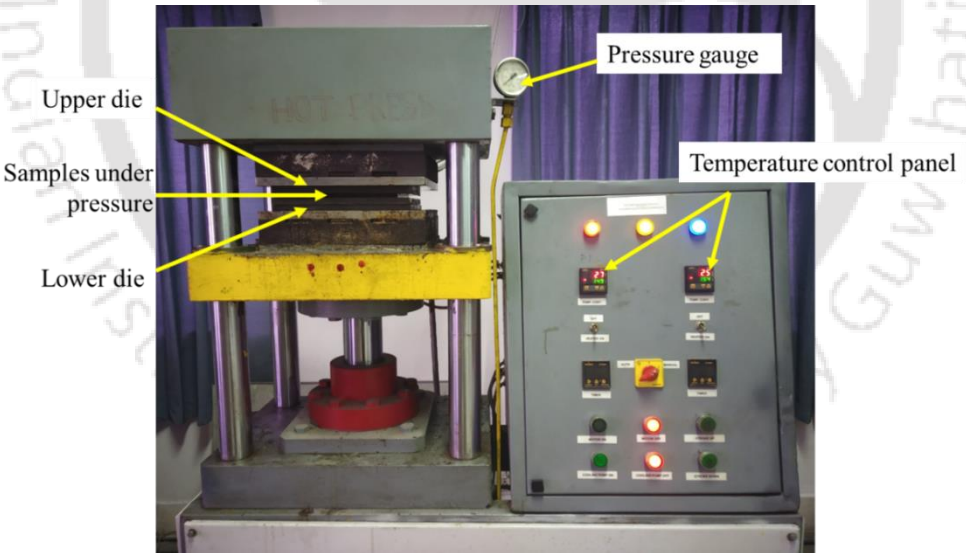

Figure 4.18 Setup of the conventional hot press

For the method of thermal bonding, the PC sheets with engraved micro-channels on it were first cleaned with acetone. Unprocessed PC sheets were then cut to the size of the sheets with micro-channel engraved on it. These unprocessed cut sheets served the purpose of cover substrate for the channels. The PC substrate having the channel and the PC cover substrate were then aligned one above the other. The aligned substrates were placed between the two dies of the hot press. Keeping into consideration the affecting parameters like bonding pressure, bonding temperature and contact time, the bonding pressure used was 2 MPa. The bonding temperature on both the dies was kept at a difference. The temperature of the metal die in contact with the microchannel engraved PC substrate was set below PC transition temperature (T_g -5°C), while the temperature of the metal die in contact with the PC cover substrate was set at the PC transition temperature (T_g). After the current temperature values of the dies reach their set values, the aligned substrates were kept in between the dies under pressure for an additional 20 minutes. The dies were then moved apart from each other and hence the sealed micro-channel was obtained. The cross section view of the sealed micro-channel is presented in figure 4.19.

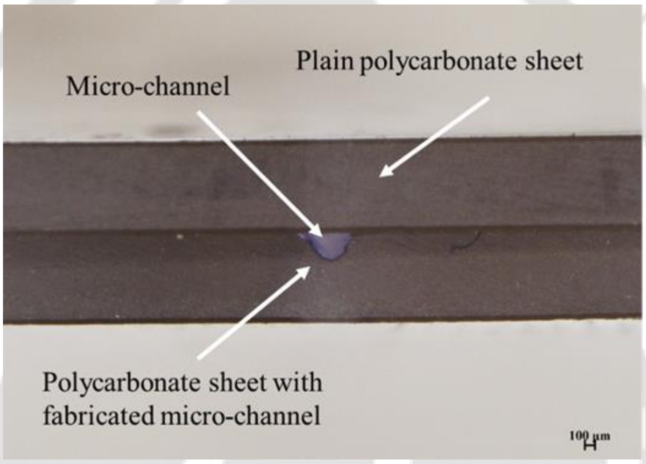

Figure 4.19 Cross section view of a thermally bonded micro-channel

4.4.1 Testing of fabricated closed microchannels for microfluidic application

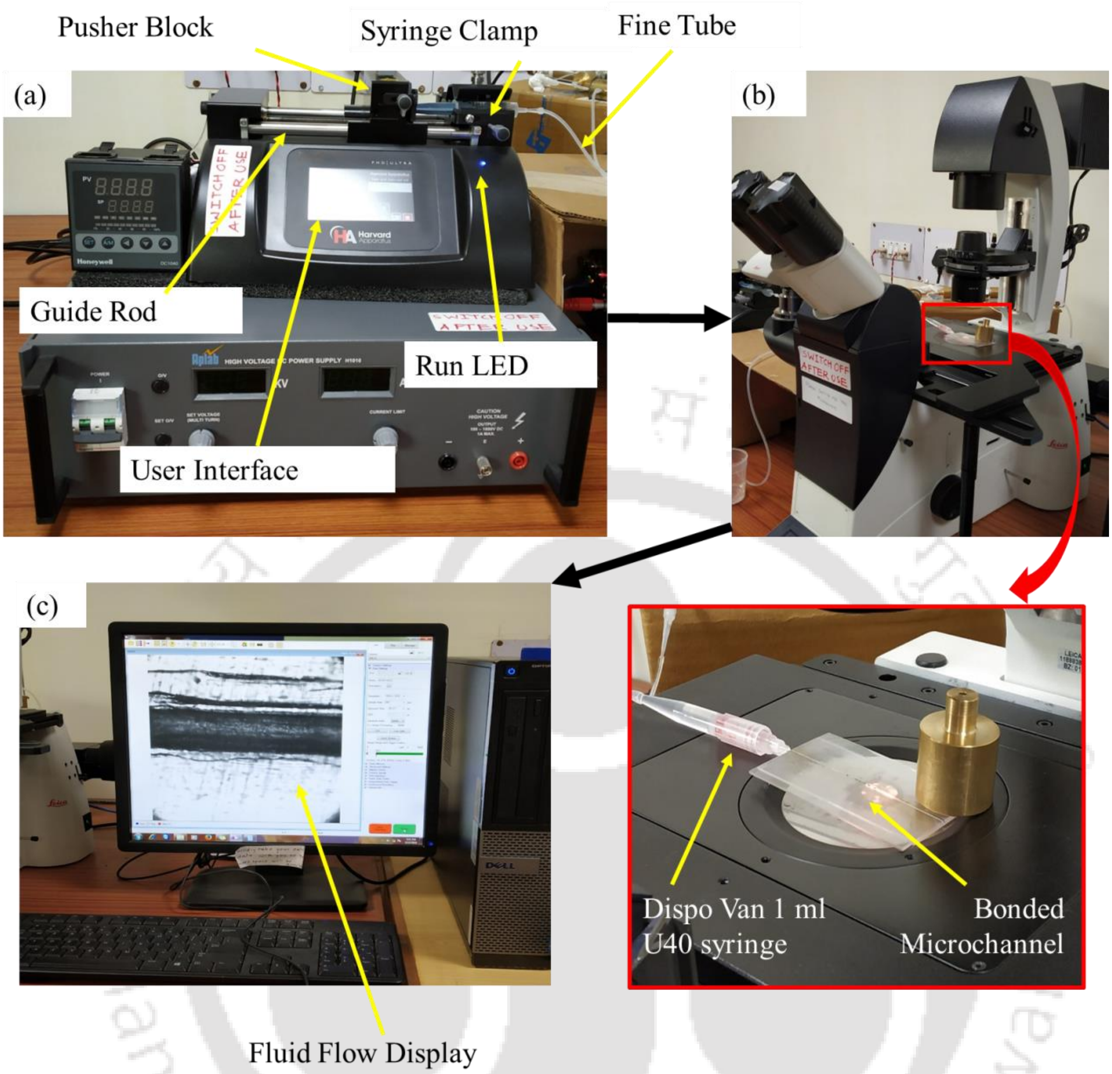

Figure 4.20 Setup for flow test (a) syringe micro-pump connected to (b) optical microscope to observe the fluid flow displayed in (c) the computer system attached.

After the formation of the bonded micro-channels, the bonded channels were put through a flow test to check its ability to be used as a microfluidic device. Figure 4.20 shows the complete set up of the flow test that includes a syringe micro-pump (PHD ULTRA™ syringe pump by HARVARD Apparatus) connected to an optical microscope (Leica DMI3000B Inverted Microscope with Fluorescence) to observe the fluid flow displayed in the computer system attached. The plunger end of the 1 ml U40 syringe was securely connected to the syringe micro-pump by a fine flexible tube and the needle of the syringe was connected to the bonded channel. The syringe was used to infuse the liquid into the bonded channel. The syringe and the bonded channel were placed on the stage of the optical microscope. Once the connections for the flow test were ready, the syringe pump was operated and the liquid medium (distilled water) started flowing through the fine flexible tube. The input flow rate of the liquid can be adjusted independently by the syringe pump. A constant flow rate of 800 µl/hr was maintained for the injection of the fluid into the channel. The flow through the channel was observed in the optical microscope and was recorded. Figure 4.21 shows the flow of the liquid medium through a clean and smooth micro-channel. It is observed that the flow was annular and there was no bubble formation in the fluid inside the micro-channel. Hence, the uniform flow of the fluid in the channel and the ideal properties of the PC for a microfluidic device marks its potentiality to be used as a microfluidic device.

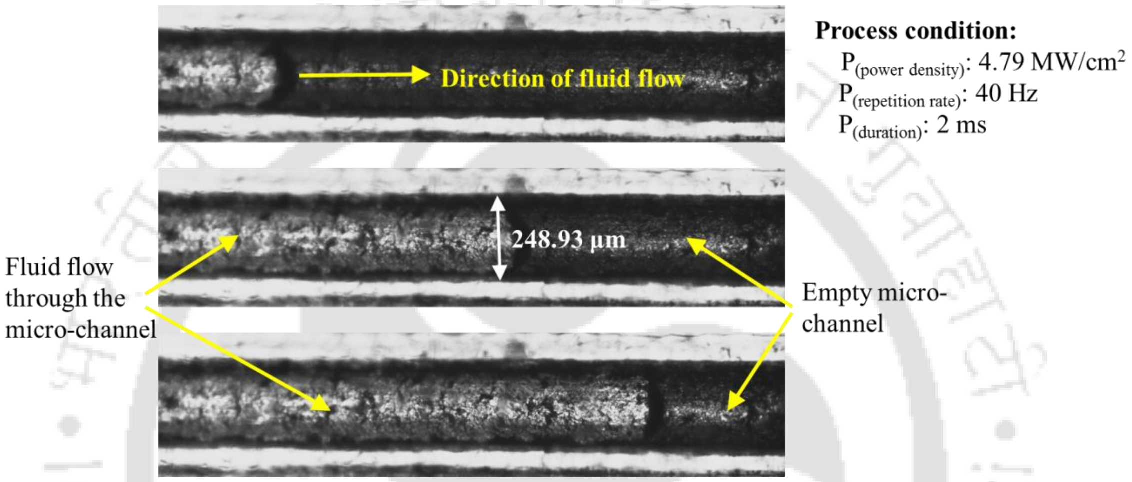

Figure 4.21 Flow through the micro-channel

4.5 Generation of various microchannel profiles using present setup and optimal parameters

Profiles of microchannels have a special impact on the flow resistance of the fluid passing through it. Correspondingly, the temperature distribution and velocity distribution in the microchannel heat sinks, electrofluidic devices etc. are also governed by the geometry of the microchannels (Guo *et al.*, 2013). As such, proper selection of the microchannel profile will help achieve the best performance of the microfluidics or microchannel based heat sinks.

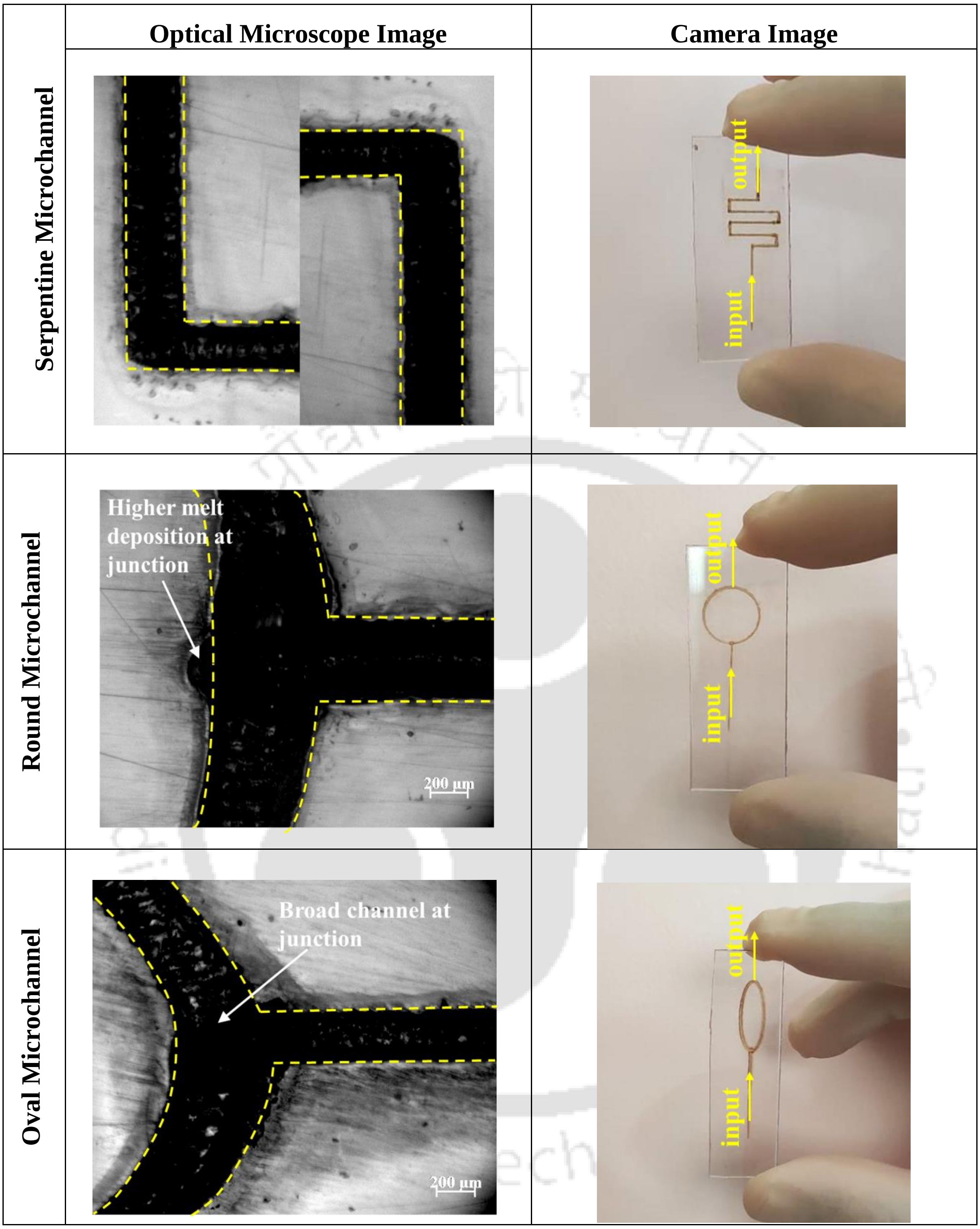

Figure 4.22 Serpentine, round and oval shaped microchannels fabricated on PC by LIPAA

After obtaining an optimized set of laser process parameters for microchannel fabrication, different profile viz. serpentine, round and oval shaped microchannels were also produced on PC using the LIPAA process. The microchannels were fabricated at 40 Hz pulse repetition rate, 4.79 MW/cm^2 pulse power density and 2 ms pulse duration.

Figure 4.22 shows the camera and the microscopic images of the serpentine shaped, round and oval shaped microchannels. It can be observed that the channels at the three-way junction (in round and oval microchannel), the channels become broad and higher melt deposition is found, which may be due to the higher laser irradiation on such region. The serpentine shaped channel has a total length of 50 mm, while the round shape channel is of 5 mm radius and the oval shape channel of 5 mm major radius and 2 mm minor radius. These channel profiles plays a crucial role in maintaining the flow stability of the fluid passing through channel based microfluidics or heat sinks. It controls the flow resistance which can greatly be optimized by channels of different configurations like serpentine, round and oval shaped microchannels. Further, temperature uniformity is an essential factor for achieving better performance in microchannel heat sinks and electrofluidic devices. Serpentine shape increases the channel length in a small region, whereas the round or oval shape divides the flow into two equal portion, thereby maintaining a uniform flow and temperature throughout the channel.

4.6 Summary

This chapter presented a comprehensive experimental study on microchannel fabrication on PC using the LIPAA process. Full factorial experiments were carried out by varying process parameters viz. pulse power density, pulse repetition rate and pulse duration at three levels. Total 81 experiments were conducted and the responses in terms of the channel geometry and the roughness were systematically measured and analyzed. The influence of varying the process parameters on the channel geometry and the roughness was studied. The role of scanning speed in the channel formation during laser processing is also being discussed. ANOVA was carried out to find the significance of the factors on the responses and second order mathematical relations among the input laser parameters, their interactions and the responses were developed. Further, the predictions by the models were verified by conducting confirmatory experiments. The important observations from the current experimental study can be summarized as follows:

- Low pulse duration of 2 ms along with either pulse power density of 3.055 MW/cm^2 or pulse repetition rate of 40 Hz results in the formation of no channels.
- The combination of high pulse power density of 6.112 MW/cm^2 and high pulse repetition rate of 80 Hz is detrimental to the output responses viz. channel width, channel depth and roughness of the process causing burning of the PC sheet.

- The increase in pulse power density, pulse duration and repetition rate results in the increase in the responses viz. channel width, channel depth and roughness. However, a decrease in the responses was observed with the increase in the scanning speed.
- The scanning speed not only affects the channel geometry and roughness but also plays an important role in the formation of channel. A channel is formed when the pulse overlap is greater than zero and discrete craters are formed when the pulse overlap is less than zero. For the beam diameter of 200 µm, the overlap distance for scanning speed of 4 mm/s and 7 mm/s was found to be 100 µm and 175 µm respectively which provide the overlap percentage of 50% and 12.5%. For channel formation, a maximum scanning speed of 4 mm/s (which corresponds to 50% overlap) can be preferred.
- Increase in the channel geometry without increase in the roughness can be achieved by subjecting the channel to multiple numbers of scans of the laser beam. Clean and uniform channels can be obtained at quite a low pulse power density (3.055 MW/cm^2) with moderate pulse duration of approximately 4 ms and pulse repetition rate of 40 Hz. Four to five number of scans of the laser beam at low pulse power density with moderate pulse duration can be employed to achieve the desired channel geometry with minimum roughness.
- Pulse power density has the highest significant effect on channel geometry and channel roughness, followed by pulse duration and repetition rate.
- For a width of 250 µm, depth of 150 µm and minimum roughness on a single pass, the optimized pulse repetition rate, pulse duration and pulse power density were found to be 40 Hz, 2 ms and 4.79 MW/cm^2.

By using the optimum process parameters, open channels were fabricated, which were then closed by using thermal bonding technique. The leak-proof bonded channels were thoroughly tested and the sustainability of the LIPAA process was verified. Also, different profiles viz. serpentine shaped, round and oval shaped microchannels were produced on PC using the LIPAA process. The sustainability of the LIPAA process of machining transparent material is thus proved in fabricating microchannels of different shapes.

Chapter 5

2D thermo-physical modelling and simulation on LIPAA of moving heat source for microchannel fabrication on polycarbonate

---

5.0 Scope

This chapter presents the development of a two-dimensional thermo-physical model of Laser-Induced Plasma Assisted Ablation (LIPAA) using the finite element method (FEM). Initially, the need to carry out the thermo-physical analysis is identified. The two-dimensional FEM model of the LIPAA process, considering its thermal characteristics, is presented in detail in terms of its geometric model, governing equation, boundary conditions, laser heat source model and solution methodology. Simulations are carried out within the effective range of process parameters viz. pulse power density, pulse repetition rate, pulse duration and scanning speed. A systematic investigation is performed to analyze the effect of these process parameters on the responses viz. channel width and channel depth. The predicted results from the model are then compared with the experimental results. Finally, conclusions and contributions are summarized.

5.1 The need

Microchannels have important applications in the optical and medical device industries. Such devices call for the use of materials with high transparency, high impact strength, high dimensional stability, high chemical stability and optical clarity. In view of that, polycarbonate's (PC's) inherent impact strength, dimensional stability and eco-friendly nature make it an ideal material in the medical device industry. Again, the high transmissivity of PC makes the laser based fabrication of microchannels a challenging task. The LIPAA process is capable of meeting this challenge and as a result LIPAA has been widely accepted for laser processing of transparent materials. However, sparse work on numerical research of the LIPAA process has been reported in the literature. A need was thus identified to carry out a numerical investigation to study the process of LIPAA on PC and prove itself to be an effective and powerful tool to achieve the real-time requirements of the LIPAA process.

5.2 Overview of two-dimensional LIPAA process model development

Figure 5.1 represents the current approach for the development of the process model of LIPAA using FEM. A 2D transient nonlinear FE model was developed in the first stage to determine the microchannel width and depth during the LIPAA process. The impact of the moving laser heat flux on the temperature generation along the scanning direction in the PC sheet has also been analyzed. In the second stage, microchannels were fabricated experimentally on PC by the LIPAA process using an Nd: YAG millisecond pulsed laser of wavelength 1.064 µm. The width and depth of the microchannel were then determined. In the third stage, the simulated results were compared with the experimental results. A systematic parametric analysis was performed based on the confidence gained from the validation of the simulated results. The influence of the parameters like pulse power density, pulse duration, and pulse repetition rate on the channel dimensions was studied.

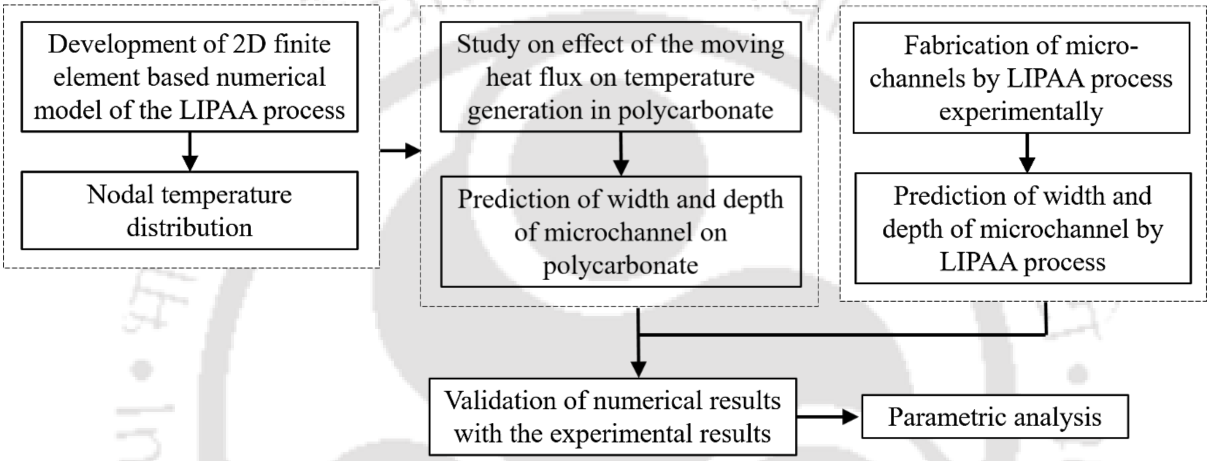

Figure 5.1 LIPAA process model development

In what follows, the thermo-physical model for the LIPAA process is presented in detail.

5.3 Thermo-physical modelling of LIPAA using Finite Element Method (FEM)

In the study, a two-dimensional nonlinear transient finite element model of Laser-Induced Plasma Assisted Ablation (LIPAA) of PC has been developed. A temperature profile is generated by solving the finite element model considering the temperature dependent material properties of the PC. The influence of the plasma and the input laser irradiance have been taken into consideration in the heat flux model of the simulation. The developed model is employed to study the effects of laser parameters on the channel dimensions during the LIPAA process. The model takes into account only the melting of the material. As mentioned in the previous chapter, ablation on both the PC sheet and the aluminium target is obtained in the LIPAA process. However, our present study is confined to the PC sheet only. The model is applied not only to analyze the effect of the parameters on LIPAA of PC, but also on the effect of the moving heat flux on the PC sheet.

5.3.1 Assumptions

In the present work, certain assumptions were made to make the model realistic. These are as follows:

- The heat source is assumed to be of Gaussian shape (Acherjee *et al.*, 2012). Considering Gaussian-shaped heat flux at the zone of irradiation will make the model conditions closer to the real LIPAA phenomenon.
- The thermal properties of the material are temperature dependent.
- The reflectivity of both the PC and aluminium is considered.
- Only the melting of the PC above its melting poit temperature is considered. The decomposition of the PC above its degradation temperature is neglected.
- The transparent material and metal target are isotropic and homogeneous in nature.
- The ambient temperature is 300 K.

5.3.2 Geometric model

In the LIPAA process, as shown in figure 5.2(a), the PC sheet is arranged above the aluminium sheet without the application of any external pressure. Gaussian heat flux is considered to be moving along a straight line at the interface of the two materials. A section ABCD on the x–z plane is considered at the zone of irradiation of the moving laser, representing the two-dimensional domain of the LIPAA process. However, for the numerical study, only an axisymmetric section of the PC from the two-dimensional domain is considered as represented in the figure. 5.2(b). It is because a 2D domain of the model consists of much fewer elements, which reduces the simulation time. Further, the temperature profile generated in the axial and longitudinal direction is sufficient to predict the channel width and channel depth in much less time.

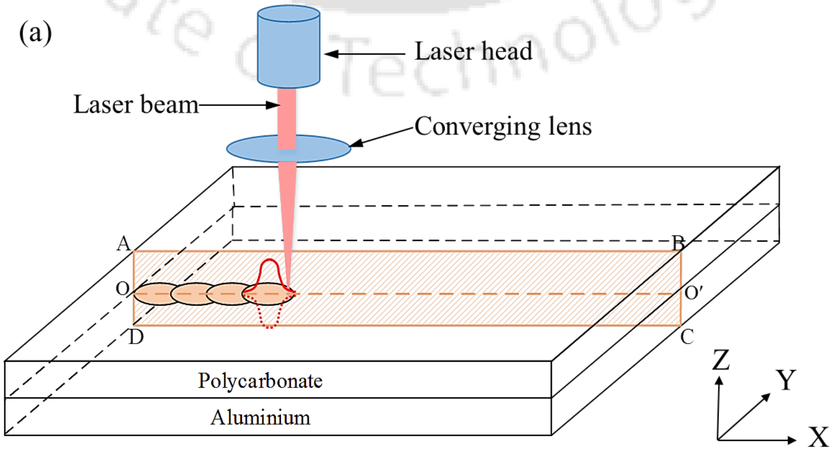

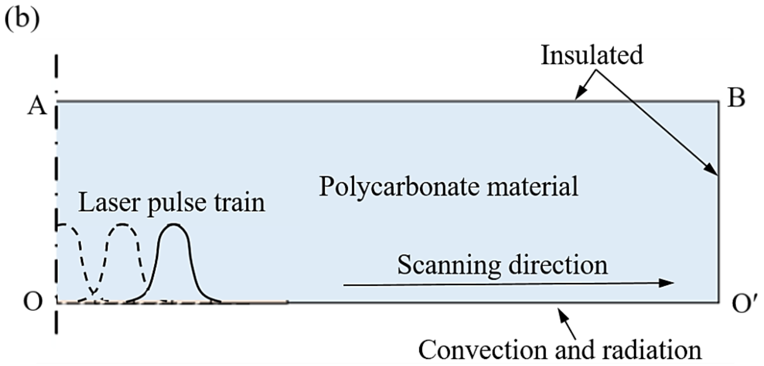

Figure 5.2 Geometric representation of the LIPAA model

In the present numerical model, geometric model of PC has been assigned with the essential material properties. The thermal properties of the PC are considered temperature dependent, as shown in table 5.1. Other thermal and physical properties of the PC and the aluminium were considered constant and are listed table 5.2.

Table 5.1 Temperature dependent properties of PC

Temperature (K)	**Conductivity (W/mK)**	**Specific Heat Capacity (J/kg K)**
323	0.204	1330
373	0.213	1370
423	0.213	1480
473	0.215	1500
523	0.226	1540
573	0.238	1550

Table 5.2 Thermal and physical properties of PC and aluminium (Acherjee *et al.*, 2012; Sharma *et al.*, 2019)

	Property	**Value**
Polycarbonate	Density (kg/m^3)	1200
	Emissivity	0.95
	Reflectivity	0.07
	Melting Point (K)	503
Aluminium	Reflectivity	0.96
	Density (kg/m^3)	2700

5.3.3 Thermal analysis

The two-dimensional non-linear transient heat conduction equation that governs the heat generation during the LIPAA process can be described as:

$$\frac{\partial}{\partial x}\left(k\frac{\partial T}{\partial x}\right)+\frac{\partial}{\partial z}\left(k\frac{\partial T}{\partial z}\right)=\rho c\frac{\partial T}{\partial t} \tag{5.1}$$

where x, y are the Cartesian coordinates, t is the time, k is the thermal conductivity of the material, ρ is the density, c is the specific heat of the material and T is the temperature.

The boundary conditions include the moving Gaussian heat flux, convection and radiation on the thermally affected boundary of the PC. The other two sides of the axisymmetric domain are taken to be insulated. The boundary conditions on the axisymmetric section of the PC have been represented in figure 5.3 (concerning figure 5.2(a)).

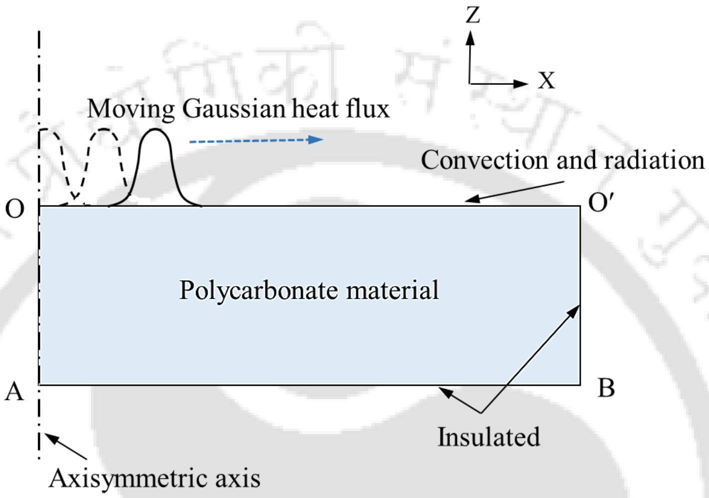

Figure 5.3 Boundary conditions for the numerical model

Mathematically, the boundary conditions can be expressed as:

$$k\frac{\partial T}{\partial x} = q \quad \textit{for pulse-on time} \tag{5.2}$$

$=0$ *for pulse-off time* and

$$k\frac{\partial T}{\partial x} + k\frac{\partial T}{\partial z} = -h(T_\mathrm{s} - T_\infty) - \varepsilon\sigma(T_\mathrm{s}^4 - T_\infty^4) \tag{5.3}$$

where q is the laser heat source, h is the convective heat transfer coefficient, T_s is the surface temperature, ε is the emissivity of the transparent material and σ is the Stefan Boltzmann constant (5.67×10^{-8} W/m^{2}K^4). By merging the convection and the radiation conditions, the final boundary condition can be expressed as (Acherjee *et al.*, 2012)

$$k\frac{\partial T}{\partial x} + k\frac{\partial T}{\partial z} = -h_\mathrm{r}(T_\mathrm{s} - T_\infty) \tag{5.4}$$

where h_r is the combined heat transfer coefficient. The combined heat transfer coefficient is given by

$$h_\mathrm{r} = h + \varepsilon\sigma(T_\mathrm{s} + T_\infty)(T_\mathrm{s}^2 + T_\infty^2) \tag{5.5}$$

Initially, i.e. at t = 0, the workpiece is considered to be at ambient temperature, T_∞ of 300 K i.e.

$$T(x,y,0)=T_\infty \tag{5.6}$$

5.3.4 Laser heat source

The heat source is considered taking into account the plasma power density besides the input laser intensity. Assuming that the laser intensity follows Gaussian distribution, the heat source, q can be expressed as

$$q=(1-R_a)\ I+q_1 \tag{5.7}$$

where R_a is the reflectivity of the metal target, I is the laser pulse intensity and q_1 is the plasma power density.

The Gaussian distribution of the laser pulse intensity is given by Sundqvist *et al.* (2017) as:

$$I=I_o \exp\left(-2\frac{x^2}{R^2}\right) \tag{5.8}$$

where I_o is the peak laser pulse intensity and R is the laser spot radius. The plasma power density can be estimated by using the following relation:

$$q_1=\frac{E_{\text{plasma}}}{t_{\text{on}}} \tag{5.9}$$

where E_{plasma} is the plasma energy density and t_{on} is the pulse duration.

5.4 Solution methodology

A two-dimensional nonlinear transient numerical model has been developed to compute the values of the channel width and channel depth, and to study the effect of the moving heat flux on the temperature generation. PC and aluminium were taken as the transparent and the metal target, respectively. In the present work, the focus was mainly on the PC sheet to determine the channel width and the channel depth. The thermal conductivity and specific heat of the PC sheet were considered to be temperature dependent while the density was kept constant. PC ablation is obtained on its rear surface with the help of plasma generated by laser irradiation with the aluminum metal target. However for the numerical study, the 'upside down' view of the PC is considered. Therefore, in the current study, the temperature profile is represented on the upper face of the PC.

5.4.1 Finite element formulation

In the present work, a two-dimensional nonlinear transient modeling and simulation of the LIPAA process for microchannel fabrication on transparent materials has been reported. Temperature is the only degree of freedom considered at each node. The temperature field variable with the element is interpolated by,

$$T = [N]\{T_e\} \tag{5.10}$$

and

$$\begin{aligned} T &= [B]\{T_e\} \\ &= \left[\frac{\partial}{\partial x} N\right]\{T_e\} \end{aligned} \tag{5.11}$$

where $[N]$ is the interpolation or shape function matrix, $\{T_e\}$ is the element nodal temperature matrix and $[B]$ is the general geometric matrix. Galerkin method is used to solve the above equations, and the resulting equations are expressed in the matrix form as

$$[C]\{T\} + [K_T]\{T\} = \{Q\} \tag{5.12}$$

where $[C]$ and $[K_T]$ are the global heat capacity matrix and global conductivity matrix respectively, which are given as

$$[C] = \int_V^0 \rho c [N][N]^T \, dV \tag{5.13}$$

$$[K_T] = \int_V^0 k [B][B]^T \, dV \tag{5.14}$$

and $\{Q\}$ is the heat flux vector.

The entire model was meshed into small elements to simplify the problem based on the finite element method. The element type chosen is thermal solid 35 with triangular-6 nodes. The entire geometry was coarse meshed and the mesh was further refined at the zone where heat flux was applied, as shown in figure 5.4.

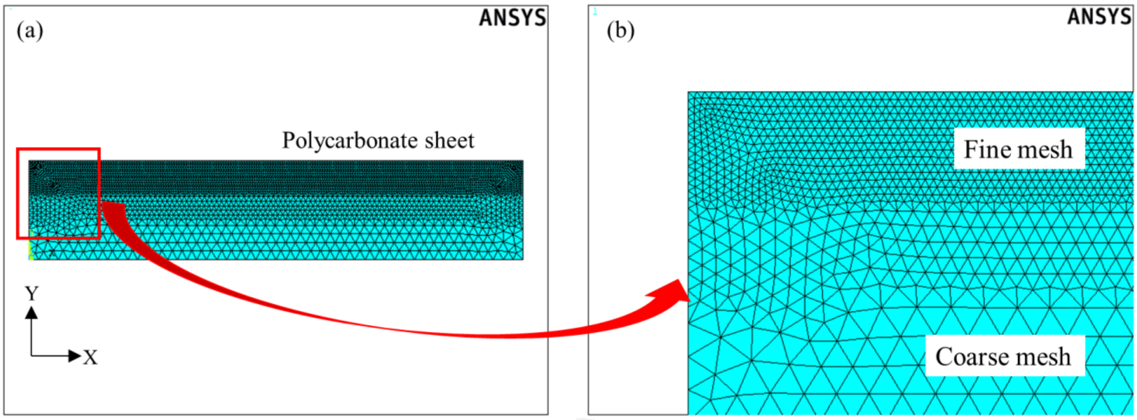

Figure 5.4 Meshed model of process continuum

Nd: YAG pulsed mode laser with focal spot radius (*R*) of 100 µm is considered. A set of complete 27 numerical simulations were carried out in this work. Based on the experiments performed, scanning speed was kept constant at 4 mm/s. At the same time, the other parameters such as pulse power density, pulse repetition rate and pulse duration are varied in a suitable range. The levels of the process parameters are shown in table 5.3.

Table 5.3 Process parameters and their levels

Parameters	Levels		
Pulse power density (MW/cm^2)	3.055	4.584	6.112
Pulse repetition rate (Hz)	40	60	80
Pulse duration (ms)	2	4	6

Experiments were also carried out using an Nd: YAG pulsed millisecond laser with a wavelength of 1064 nm for the fabrication of microchannels on PC as mentioned in the previous chapter. Successful fabrication of micro-channels on PC was obtained experimentally and consequently, the experimental results were used to validate the numerical data.

5.5 Results and discussion

By varying the process parameters listed in table 5.3, a full factorial nonlinear transient analysis of LIPAA has been carried out. 27 numerical simulations were performed to compute the channel width and the channel depth during LIPAA of PC, its dependence on the laser parameters and the effect of the moving heat flux on temperature generation. Figure 5.5 shows the 2D isothermal contours on PC along the scanning direction for the case of 3.055 MW/cm^2 pulse power density, 40 Hz pulse repetition rate, and 6 ms pulse duration at different times of 0.106 s, 0.506 s and 0.906 s, respectively.

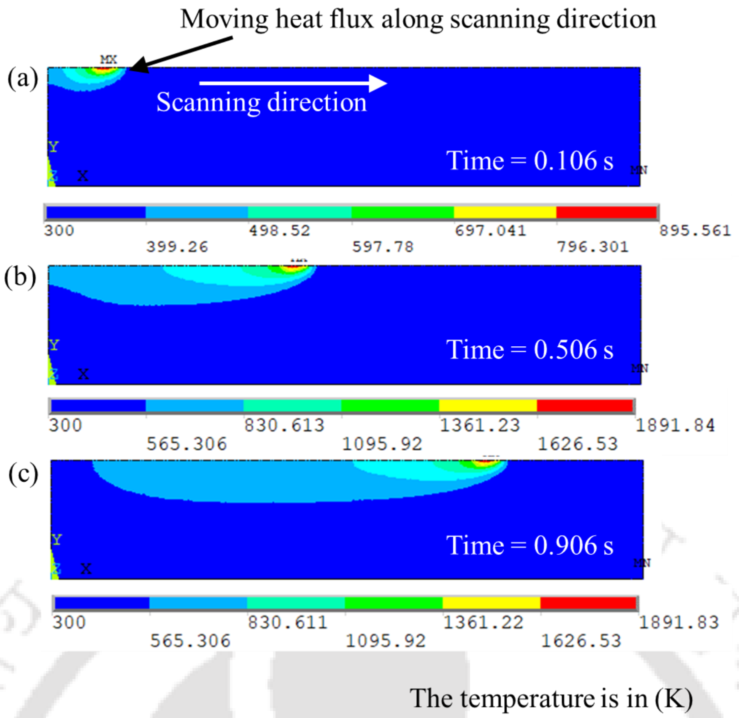

Figure 5.5 2D temperature distribution on PC at (a) 0.106 s, (b) 0.506 s, (c) 0.906 s along the scanning direction

From the above figure, it is observed that initially, there was an increase in the maximum temperature with increasing time. After a certain period, the maximum temperature attains a quasi-steady state and it is then that one can assure to have a channel of uniform width and depth. A maximum temperature of 895.56 K was observed at the plane of laser beam irradiation at 0.106 s. However, the maximum temperature increases to 1891.8 K as the time reaches 0.506 s and beyond. Considering a melting point temperature of 503 K for PC, the region exceeding the melting point temperature in the contours plot for the moving heat flux shows the molten zone of the PC sheet. As the laser source moves along, the melt pool moves along with the laser source, which results in the formation of a channel. Figure 5.6 shows the graphical visualization of the variation of maximum temperature as a function of time at various locations along the scanning direction.

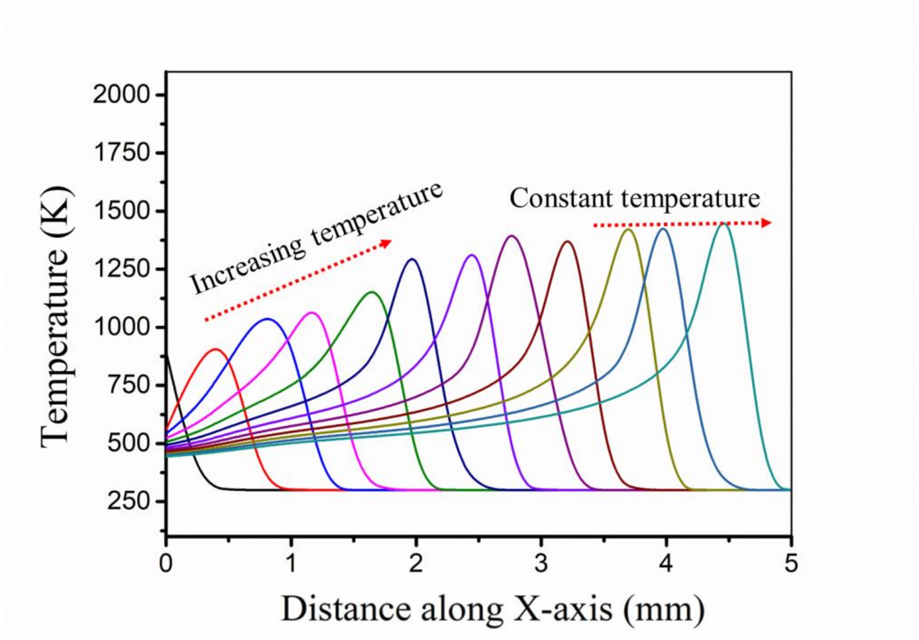

Figure 5.6 Temperature vs Distance plot along the scanning direction

The effect of the process parameters on the channel width and the channel depth has also been studied by using the developed model. The elements above the melting temperature of PC are considered to be removed during the LIPAA process, and accordingly, the channel dimensions were determined.

The complete set of numerical results are presented in table 5.4. The evaluation and characterization of the channels were carried out by using an optical microscope (Make: Carl Zeiss).

Table 5.4 L27 array and the channel dimensions

Frequency (Hz)	Pulse Duration (ms)	Current (A)	Channel Width (μm)	Channel Depth (μm)
40	2	40	*	*
40	2	60	*	*
40	2	80	246	13.16
40	4	40	310.2	25.19
40	4	60	357.69	33.67
40	4	80	468.16	51.29
40	6	40	379.58	46.34
40	6	60	410.34	59.42
40	6	80	469.27	71.63
60	2	40	264.9	9.67
60	2	60	305.94	15.46
60	2	80	349.81	29.61
60	4	40	399.76	14.32
60	4	60	457.64	21.51
60	4	80	502.37	33.24

60	6	40	411.68	19.57
60	6	60	486.08	25.66
60	6	80	524.49	39.36
80	2	40	356.32	18.08
80	2	60	384.12	24.81
80	2	80	425.91	36.44
80	4	40	411.36	26.99
80	4	60	487.14	41.22
80	4	80	531.22	49.23
80	6	40	442.19	36.11
80	6	60	509.47	44.98
80	6	80	561.33	56.78

* No ablation observed

5.5.1 Effect of pulse power density on channel dimension

The temperature variation along the x-direction and the z-direction at varying pulse power density is presented graphically in figure 5.7(a) and 5.7(b), respectively. It is observed from the graphs that the peak temperature increases with the increase in the pulse power density. However, for pulse power density values of 3.055 MW/cm^2 and 4.584 MW/cm^2, the peak temperature doesn't exceed the melting point temperature of the PC, thereby leading to no channel formation. Whereas for 6.112 MW/cm^2 power density, the peak temperature exceeds the melting point temperature and a channel of width 246.3 µm and depth 13.16 µm is formed. Similar observations were also observed from the experimental results.

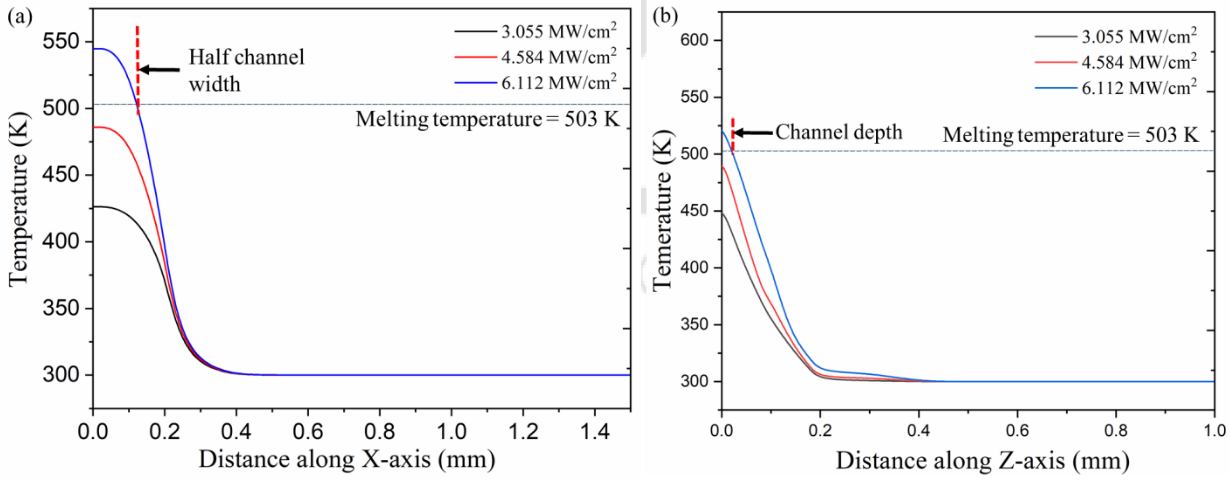

Figure 5.7 Temperature distribution along (a) X-axis and (b) Z-axis at varying pulse power density

The optical microscope images for the channels formed are shown in figure 5.8. It is witnessed that a well-defined channel is formed at a pulse power density of 6.112

MW/cm^2; however, a channel of nominal width and depth was developed at 4.854 MW/cm^2. From the comparison, it was found that the numerical model predicts channel width and channel depth with mean deviation of 1.9 % and 8.5 % respectively at varying pulse power density.

	3.055 MW/cm^2	**4.584 MW/cm^2**	**6.112 MW/cm^2**
Channel Width	No channel formation	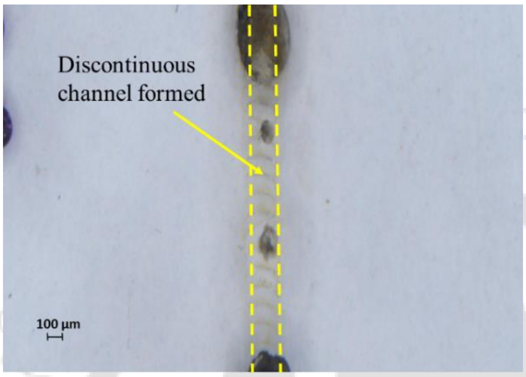 	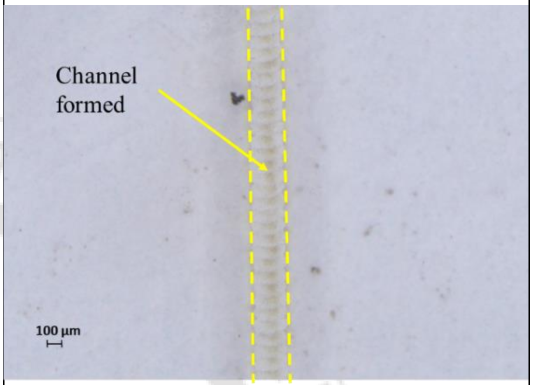
Channel Depth	No channel formation	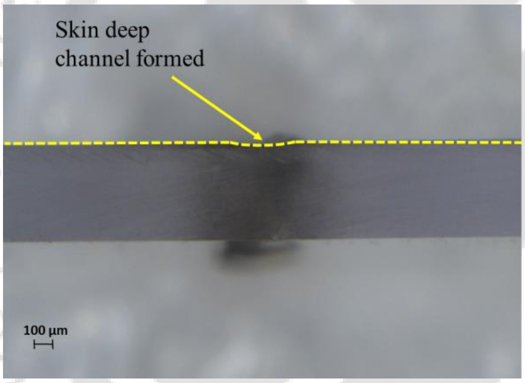 	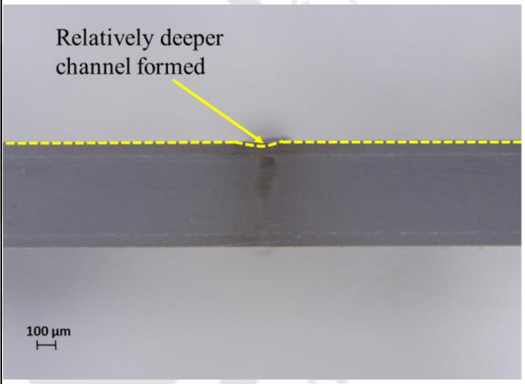

Figure 5.8 Optical microscope images of the channel width and channel depth formed at varying pulse power density

From the present investigation, it can be learnt that, increase in the pulse power density results in enhancement in channel dimensions, i.e. channel width and channel depth. It is because, when the pulse power density increases, it induces a higher population inversion, which gives greater stimulated emission. This enhanced stimulated emission leads to increased irradiation of photons on the aluminium sheet, thereby generating a higher density of electrons and ions. The increased density of the electrons and ions further interacts with the incoming laser beam, resulting in the generation of a radially expanded plasma. Thus, the plasma expands radially with the increase in pulse power density. The expanded plasma has a significant thermal effect on the PC, resulting in wider channel width and deeper channel depth.

5.5.2 Effect of pulse repetition rate on channel dimension

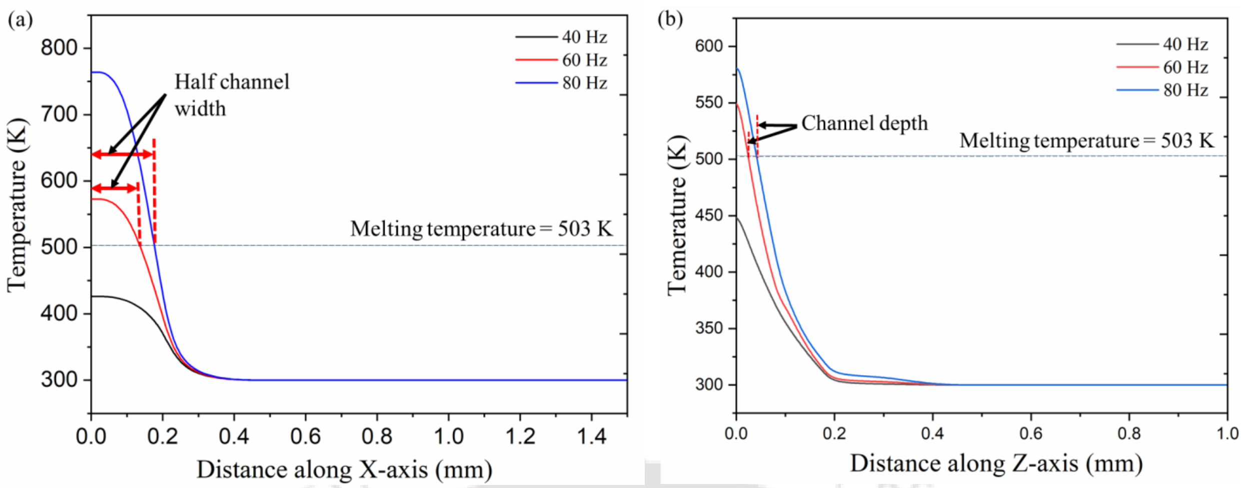

Figure 5.9 Temperature distribution along (a) X-axis and (b) Z-axis at varying pulse repetition rate

Figure 5.9(a) and 5.9(b) depicts the temperature variation at varying pulse repetition rate along the x-direction and the z-direction, respectively. It can be observed, increase in the pulse repetition rate increases the peak temperature. When the pulse repetition rate value is greater than or equal to 60 Hz, the peak temperature exceeds the melting point temperature of the PC, thereby leading to the channel formation. A channel of 264.9 µm width and 9.67 µm depth was noted to be formed at a pulse repetition rate of 60 Hz. For pulse repetition rate of 80 Hz, channel of 356.32 µm width and 18.08 µm depth was generated. However, when the pulse repetition rate is less than 60 Hz, the peak temperature does not exceed the melting point temperature of the PC and as such, no channel formation was obtained. The predicted numerical results were found to be in good agreement with the experimental results, as shown in figure 5.10. It is observed that well-defined channels can be generated at 60 Hz and 80 Hz pulse repetition rate values, while no channel formation was obtained at 40 Hz. On comparison, a mean deviation of 4.8 % for the channel width and 9.3 % for the channel depth were obtained from the numerical results at varying pulse repetition rate.

	40 Hz	60 Hz	80 Hz
Channel Width	No channel formation	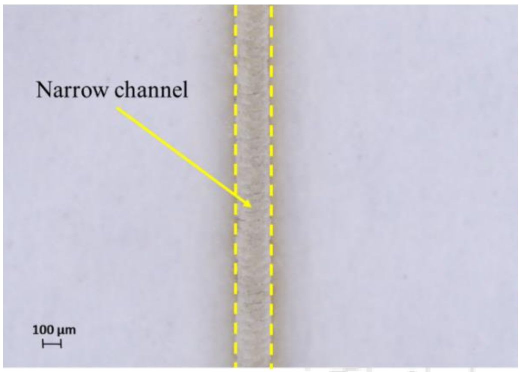 	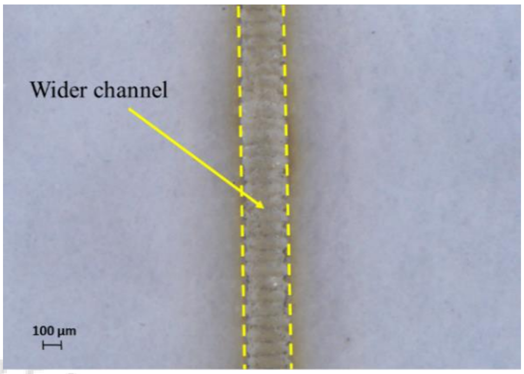
Channel Depth	No channel formation	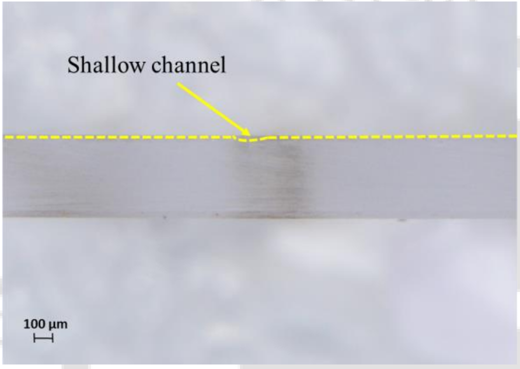 	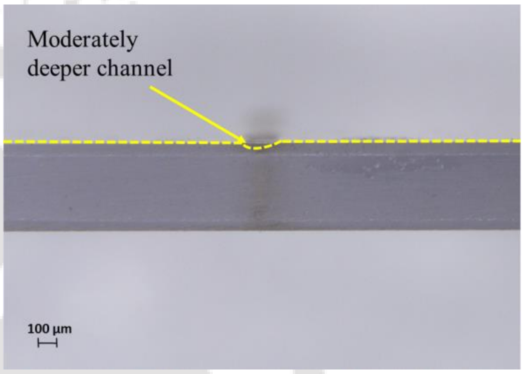

Figure 5.10 Optical microscope images of channel width and channel depth formed at varying pulse repetition rate

In general, it can be noted that increase in the pulse repetition rate results in increase in channel size, i.e. the channel width and channel depth. It may be due to the fact that, at a higher pulse repetition rate, the number of pulses per second interacting with the aluminium sheet increases. Additionally, the interaction of the vapour molecules formed from the previous pulses with the incoming laser beam also increases. Hence, the vaporization of aluminium sheet and ionization of vapour molecules will be amplified. This leads to the generation of an expanded plasma, which has a more significant thermal effect on the PC sheet, thereby producing channels of larger dimensions. However, at a low pulse repetition rate, the initial velocity of generated plasma is very low and does not have a significant effect on the PC sheet, resulting in formation of no channels.

5.5.3 Effect of pulse duration on channel dimension

The graphical presentation of the temperature variation along the x-direction and z-direction at varying pulse duration is shown respectively in figure 5.11(a) and 5.11(b).

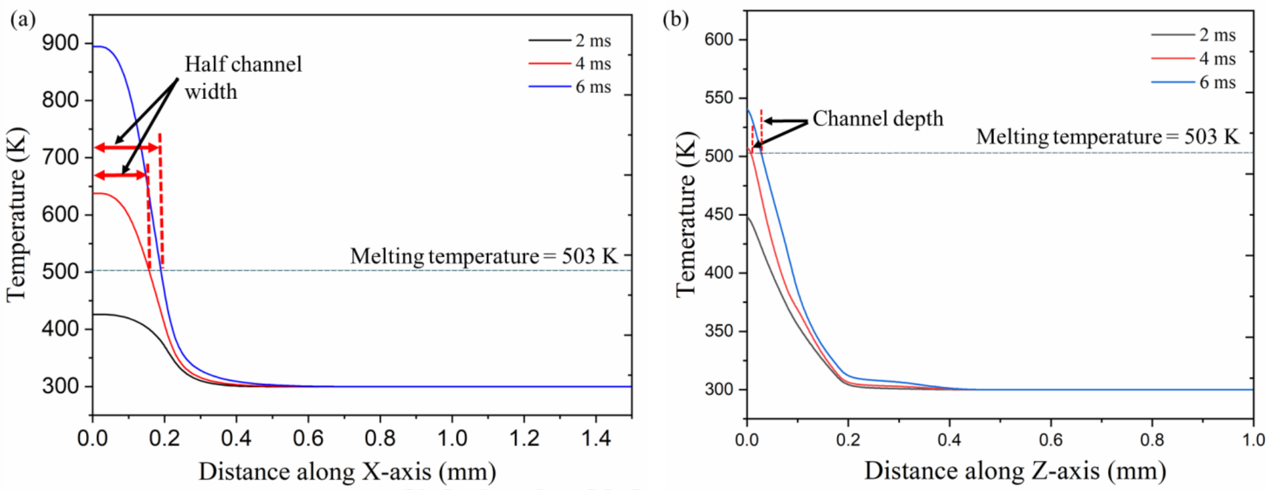

Figure 5.11 Temperature distribution along (a) X-axis and (b) Z-axis at varying pulse duration

It can be observed that, there is an increase in the peak temperature value with the rise in the pulse duration. For a pulse duration value of 4 ms and higher, the peak temperature exceeds the melting point temperature of the PC. As such microchannel is formed when the pulse duration is 4 ms or greater. A channel of 310.2 µm width and 25.19 µm depth was noted to be formed at a pulse duration of 4 ms, while at a pulse duration of 6 ms, channel of 379.58 µm width and 46.34 µm depth was generated. Nevertheless, for a pulse duration value of 2 ms, the peak temperature does not exceed the melting point temperature of the PC and consequently, no channel formation was noticed. The predicted numerical results are found to be in good agreement with the experimental results. The optical microscope images of the channels are as shown in figure 5.12. From the experimental studies, it can be observed that well-defined channels can be generated at pulse duration of 4 ms and 6 ms, while no channel formation was obtained at 2 ms. Comparing the numerical results with the experimental results at varying pulse duration, it was found that mean deviation of 6.35 % and 9.23 % were obtained, respectively for the channel width and channel depth.

	2 ms	**4 ms**	**6 ms**
Channel Width	No channel formation	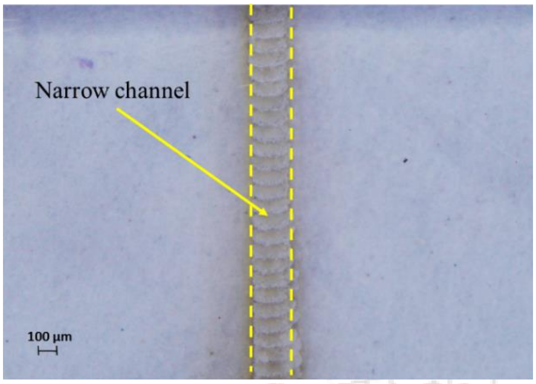	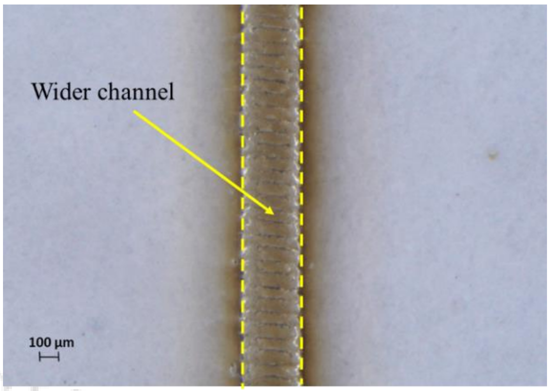
Channel Depth	No channel formation	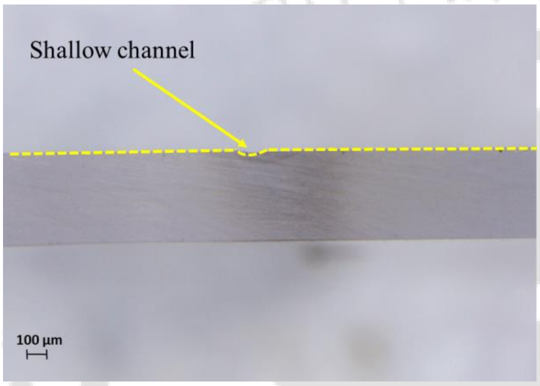	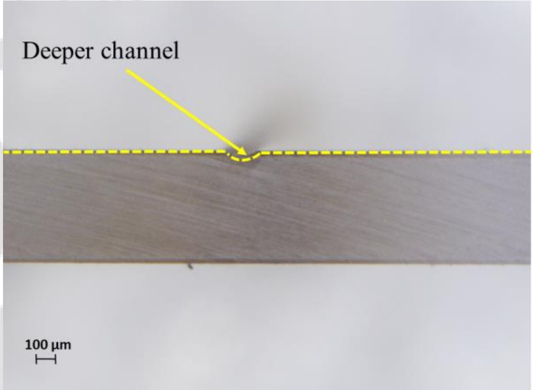

Figure 5.12 Optical microscope image for the channel width and channel depth formed at a varying pulse duration

Therefore, from the above discussion, it can be said that an increase in the channel width and the channel depth is attained with the increase in the pulse duration value. It is because, when the pulse duration value is low, the laser intensity may not be sufficient enough to ablate the PC substrate. The heat energy of the laser is not allowed to sink into the aluminium sheet. Hence, there will be no plasma formation, leading to no formation of channels. But increase in the pulse duration, provides longer interaction of laser beam with the metal, thus generating an expanded plasma. Higher pulse duration also results in higher pulse energy, as given by the relation:

$$t_{\mathrm{on}} = \frac{E}{P_{\mathrm{peak}}} \tag{5.15}$$

where t_{on} is the pulse duration, E is pulse energy, and P_{peak} is pulse peak power. The expanded plasma has more and longer thermal effect on PC, thereby increasing the channel width and channel depth.

5.6 Summary

In the present chapter, a thermo-physical numerical model of LIPAA, based on ablation of PC has been developed. The merit of the model lies in using moving Gaussian laser heat source to simulate the channel fabrication. Extensive numerical analysis was performed, taking into consideration the effect of plasma along with the effect of input laser irradiation. The channel dimensions, i.e., the width and the depth of the channel, were computed from the thermal distribution obtained from the numerical study. The computed results have been duly verified with our experimental results and found in good agreement. Based upon the full factorial analysis carried out using the numerical results of the model, the following conclusions have been brought:

- With the increase in pulse power density, an increase in the channel dimension was obtained. Also, it was observed that, below a specific value of the pulse power density, i.e., 4.584 MW/cm^2, no effect on the PC sheet was obtained, leading to no channel formation.
- An increase in the channel dimension is also obtained with an increase in the pulse repetition rate. It was witnessed that a well-defined channel formation is achieved for a pulse repetition rate of 60 Hz and more. However, at a pulse repetition rate of 20 Hz, there was no channel formation obtained.
- Again, an increase in the channel width and depth was seen with the rise in pulse duration. Likewise, pulse power density and pulse repetition rate, no effect on the PC sheet was obtained for a pulse duration value of 2 ms. While, at a pulse duration value of 4 ms and higher, well-defined channels were formed.
- The model was also utilized to analyze the effect of moving heat flux on the PC sheet along the scanning direction. It was observed that for the initial few distances, an increase in the peak temperature was obtained. However, after attaining a certain distance, the peak temperature reached a constant value and it is from this part, where one can assure to get a channel of uniform width and depth.

Overall, it can be concluded that the LIPAA process can be used to process transparent materials like PC, glass, etc. and that, the presented model can be effectively used to establish LIPAA in practice. Though the provided model proves itself to be an effective and powerful tool to achieve the real-time requirements of the LIPAA process, there are certain directions that are worth investigating. For instance, a three-dimensional model of the LIPAA process can be developed to have a more realistic approach.

Chapter 6

3D thermo-physical modelling and simulation on LIPAA for microchannel fabrication on polycarbonate with aluminium as metal target

---

6.0 Scope

This chapter reports a three-dimensional nonlinear transient modelling and simulation of the LIPAA process for microchannel fabrication on transparent materials. Primarily, the need to carry out the three-dimensional analysis has been identified. The merit of the approach of the current chapter lies in simulating simultaneous ablation of both transparent polycarbonate (PC) and aluminium metal target during the process. The effect of plasma energy besides input laser irradiation has also been considered to have a realistic approach to the process and consequently, ablation on rear side of PC is obtained. Spatial-temperature distribution along the traverse direction and direction perpendicular to it has been determined from the developed model. The spatial distribution lent a hand in predicting the width and depth of the microchannel. The predicted results from the model are then compared with the experimental results. Temporal-temperature distribution for pulse–on and pulse–off time was also explored. A channel index (CI) has also been estimated by calculating a ratio between the machining rate and the maximum permissible machining rate for microchannel fabrication. Finally, the conclusions and contributions are summarized.

6.1 The need

Transparent PC and its processing have become an important research area in optical, chemical, medical and display industries. They have a special mention in microfluidics (Pan *et al.*, 2017) and microfluidic-based devices like lab-on-a-chip (Trotta *et al.*, 2018), electrofluidic devices (Xu *et al.*, 2017), micro reactors (Suryawanshi *et al.*, 2018), etc. Fabrication of microfluidics on PC have been studied by various researchers by using different techniques like micro-milling (Chen *et al.*, 2014), compression moulding (Liu *et al.*, 2001), direct laser writing ablation (Qi *et al.*, 2009), LIPAA (Pan *et al.*, 2017), etc. Compared to the above mentioned techniques, LIPAA process has the capability to overcome the challenge of laser machining of transparent materials with long pulsed and long wavelength lasers. However, limited work in the simulation study of the LIPAA process has been reported. Very scant work has been reported on 3D numerical modelling and simulation of the LIPAA process. Therefore, it was thought to be worthy to develop a 3D numerical model of the LIPAA process, embracing the influence of the plasma together with the incoming laser beam on both the transparent material and the metal target. In the sections that follow, the details of development of numerical model, its validation with experimental results and the spatial and temporal thermo-physical analysis of the process are illustrated.

6.2 Present approach for the spatial and temporal analysis of LIPAA

Figure 6.1 represents the present approach for the spatial and temporal analysis of the LIPAA process. In this study, a 3D transient non-linear FE model has been developed for determining the microchannel width and depth and also the machining rate of the LIPAA process. Plasma energy in addition to the incoming laser beam intensity were considered in the heat flux model of the LIPAA process. Further, microchannels were fabricated experimentally on PC by the LIPAA process using a Nd: YAG millisecond pulsed laser of wavelength 1.064 µm. The width and depth of microchannel and the machining rate of the process were hence determined. The simulated results were then compared with the experimental results. Based on the confidence gained from the validation of the simulated results, further investigation on the numerical model was carried out. Spatial thermal analysis was carried out at different locations along the x and y direction. The temporal analysis was also studied for the pulse–on time (t_{on}) and pulse–off time (t_{off}). The influence of process parameters viz. pulse power density, pulse duration and pulse repetition rate on channel width, channel depth and machining rate of the process were studied by using the developed model.

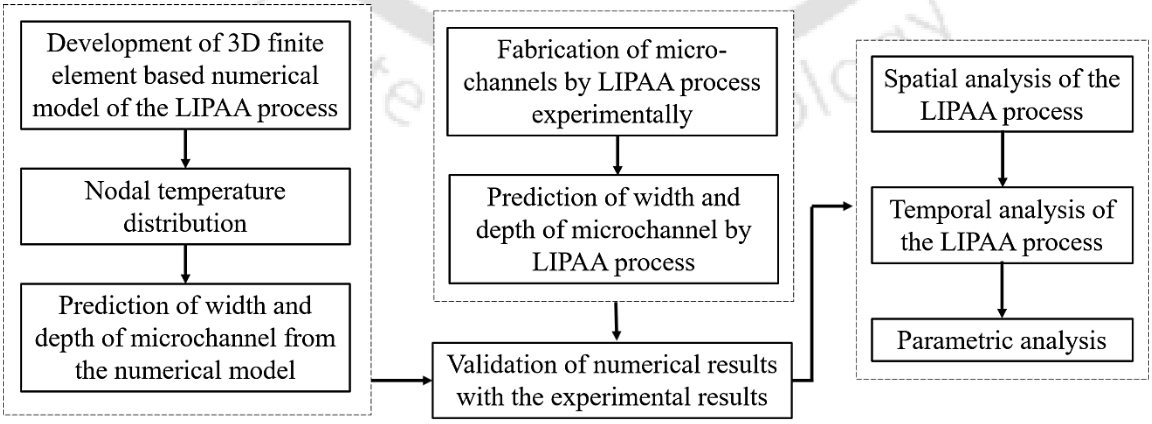

Figure 6.1 Approach of the present research work

In what follows, the thermo-physical model for the LIPAA process is presented in detail.

6.3 Three-dimensional thermo-physical modelling of LIPAA using Finite Element Method (FEM)

An investigation of the LIPAA process for microchannel fabrication on the rear side of PC taking aluminium as the target metal has been carried out numerically. The spatial and temporal-temperature distribution of the process is analysed considering the effect of the plasma energy besides the incoming laser heat flux. The spatial analysis leads the way of determining the microchannel width and depth and also, the machining rate of the LIPAA process, whilst, the temporal-temperature distribution provides information related to the effect of pulse–on time and pulse–off time on temperature distribution along the scanning direction.

6.3.1 Geometric modelling of process continuum

In the LIPAA process, the PC sheet is placed on aluminium sheet as presented in figure 6.2(a). Figure 6.2(b) represents the axisymmetric domain chosen for the numerical study of the LIPAA process that considers PC and aluminium sheet of 1 mm thickness and of 5 mm × 2 mm cross-sectional area each. The blue part represents the PC while the grey part represents the aluminium sheet. The geometric model of the domain was developed using the ANSYS Parametric Design Language (APDL) and is shown in figure 6.2(c).

(A) Assumptions

The development of the numerical model involves complex interactions between the laser beam, plasma and the workpiece. Hence, certain assumptions were made to simplify the model. These are:

- The laser heat source and the plasma energy density is assumed to be of Gaussian shape. Gaussian-shaped heat flux at the irradiation zone make the model conditions approach the actual LIPAA phenomenon.
- The thermal properties of the material are temperature dependent.
- The reflectivity of both the PC and aluminium is considered.
- Only the melting of the PC above its melting poit temperature is considered. The decomposition of the PC above its degradation temperature is neglected.
- The transparent material and metal target are isotropic and homogeneous in nature.
- The ambient temperature is 300 K.

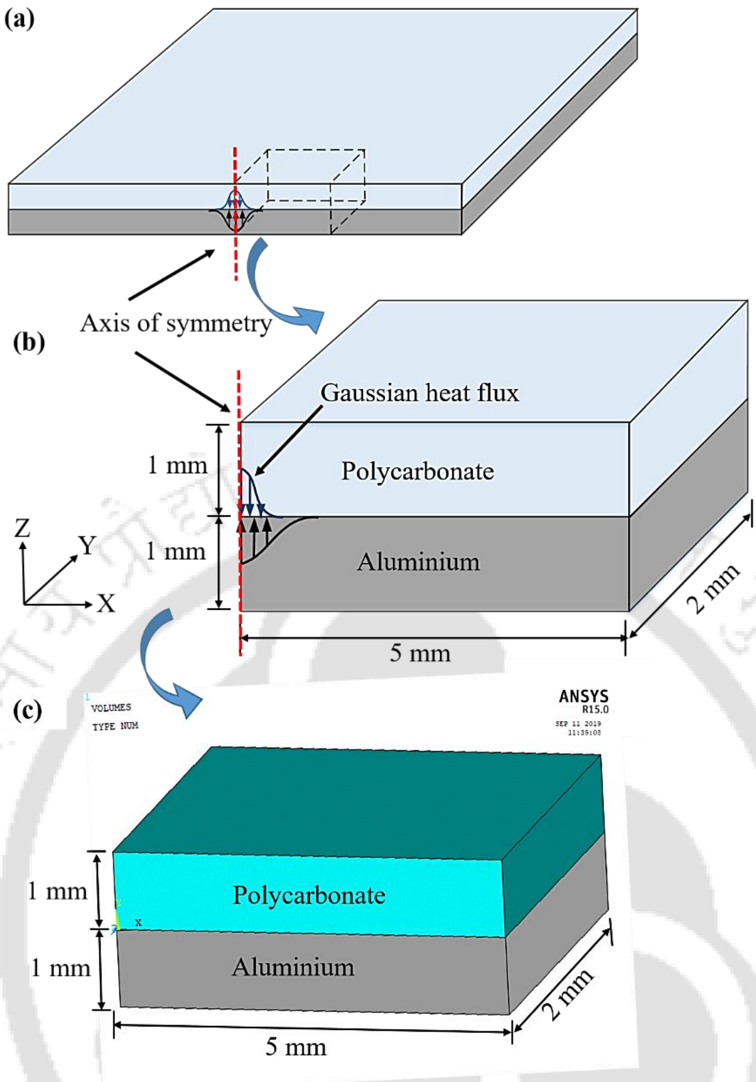

Figure 6.2 Schematic of (a) arrangement of PC and aluminium sheet, (b) domain for numerical study with symmetric conditions and (c) geometric model of the domain developed

6.3.2 Thermal modelling of LIPAA

In the present study, a finite element method based model of the LIPAA process has been developed to simulate the simultaneous ablation of both PC and aluminium sheet during the process. Temperature dependent properties of both the materials have been considered. By solving the model, a temperature profile was generated at the irradiated zone at the interface of the two materials. A comprehensive explanation of the thermal model is given in the subsequent sections.

(A) Governing equation and boundary conditions

The transient 3D heat conduction equation that determines the heat generation on the PC and the aluminium sheet during the LIPAA process is given by:

$$\rho c \frac{\partial T}{\partial t} = \frac{\partial}{\partial x}\left(k \frac{\partial T}{\partial x}\right) + \frac{\partial}{\partial y}\left(k \frac{\partial T}{\partial y}\right) + \frac{\partial}{\partial z}\left(k \frac{\partial T}{\partial z}\right) \tag{6.1}$$

where x, y, z are the Cartesian coordinates, t is the time, k is the thermal conductivity of the material, ρ is the density, c is the specific heat of the material and T is the temperature.

Initially at time, $t = 0$, the materials are treated to be at ambient temperature (T_∞) of 300 K, i.e.

$$T(x, y, z, 0) = T_\infty = 300\,\mathrm{K} \tag{6.2}$$

Boundary conditions applied to the model of the numerical study includes the laser and plasma heat flux, convection, radiation and insulation as presented in figure 6.3.

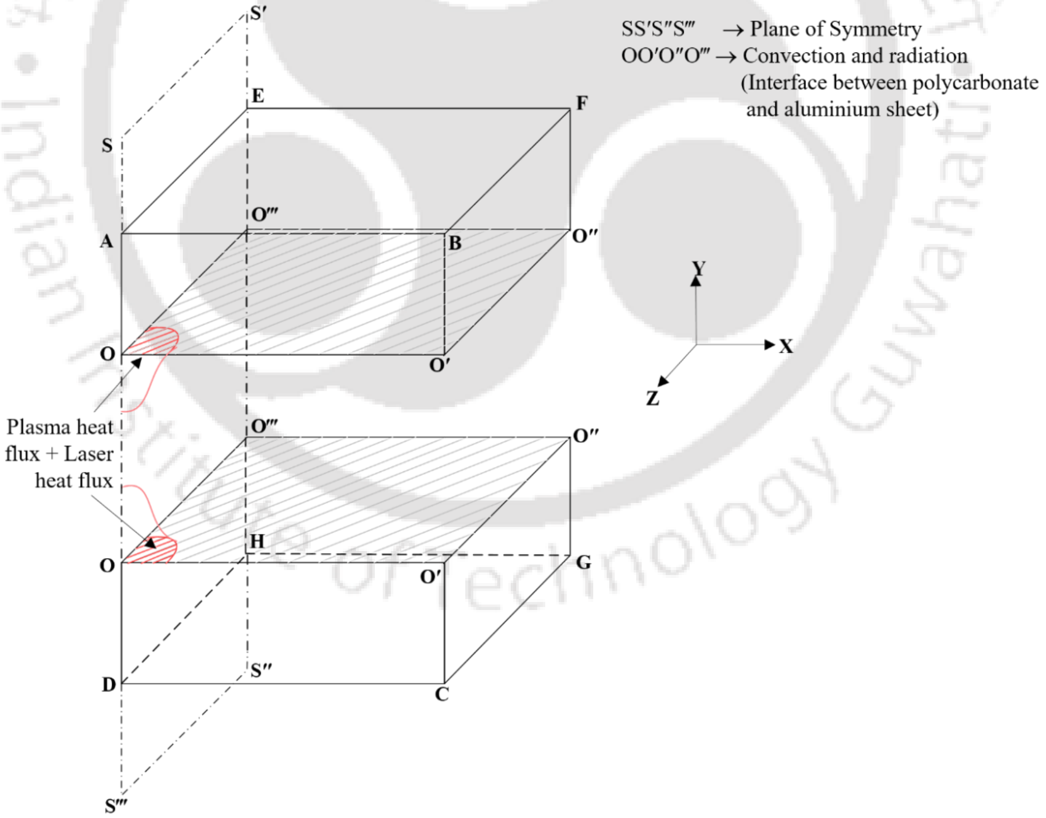

Figure 6.3 Boundary conditions and thermal load for numerical modelling

The laser heat flux and the plasma power density are assumed to be distributed at the zone of irradiation at the interface represented by OO′O″O‴. On the remaining part of the interface, convection and radiation have been considered as the boundary condition. Mathematically, these boundary conditions can be described as follows:

$$k\frac{\partial T}{\partial x} + k\frac{\partial T}{\partial z} = q \;\; \textit{for pulse-on time} \tag{6.3}$$

$$= 0 \;\; \textit{for pulse-off time} \text{ and}$$

$$k\frac{\partial T}{\partial x} + k\frac{\partial T}{\partial z} = -h\left(T_s - T_\infty\right) - \varepsilon\sigma\left(T_s^4 - T_\infty^4\right) \tag{6.4}$$

where q is the heat source, h is the convective heat transfer coefficient, T_s is the surface temperature, ε is the emissivity of the transparent material and σ is the Stefan Boltzmann constant (5.67×10^{-8} W/m^{2}K^4).

Integrating the boundary conditions of convection with that of radiation into a single condition, the combined boundary condition can be written as (Acherjee *et al.*, 2012):

$$k\frac{\partial T}{\partial x} + k\frac{\partial T}{\partial z} = -h_r\left(T_s - T_\infty\right) \tag{6.5}$$

where h_r is the combined heat transfer coefficient and h_r can be expressed as:

$$h_r = h + \varepsilon\sigma\left(T_s + T_\infty\right)\left(T_s^2 + T_\infty^2\right) \tag{6.6}$$

(B) Modelling of heat flux

In this study, Gaussian heat flux is considered for the numerical simulations based on the Beer-Lambert law. The Gaussian laser heat flux in addition to the plasma power density is considered in the laser heat flux model. In the model, the reflectivity and the absorption coefficient of the PC and the aluminium sheet were considered to take count of the power loss due to reflection at the materials and correspondingly, absorption on the aluminium sheet (Hussein *et al.*, 2017).

The Gaussian laser heat flux (q) can be expressed as:

$$q = \left(1 - R_a\right)I + q_1 \tag{6.7}$$

where R_a is the reflectivity of the metal target, I is the laser pulse intensity and q_1 is the plasma power density.

The laser pulse intensity (I) can be expressed as:

$$I = I_o \exp\left(-\frac{2\left(x^2 + z^2\right)}{R^2}\right) \tag{6.8}$$

where I_o is the peak laser pulse intensity and R is the laser spot radius. The peak laser pulse intensity (I_o) can be further computed by using:

$$I_o = (1 - R_t)\left(\frac{P_{peak}}{A}\right) \tag{6.9}$$

where R_t is the reflectivity of the transparent material and P_{peak} is the peak laser power. Since the plasma is thermally coupled with the laser beam, the *in situ* measurement of the plasma energy is difficult. However, as reported by Saxena *et al.* (2014), beyond the plasma generation threshold, a linear increase in the input laser irradiance leads to a linear increase in the energy transfer to the plasma. It is considered that the plasma generation threshold is obtained when the density of the electrons (N_e) reaches a value of about $10^{18}/\text{cm}^3$ (Dahotre and Harimkar, 2008). The plasma energy density can thus be estimated from the electron density by the following equation (Saxena *et al.*, 2014):

$$E_{plasma} = N_e\left(\frac{\Delta E}{2}\right) \tag{6.10}$$

The value of E_{plasma} has been determined to be 2.72×10^6 J/m^3, taking 34 eV as the ionisation energy (ΔE) for air. The plasma power density (q_1) can thus be estimated from the following expression:

$$q_1 = \frac{E_{plasma}}{t_{on}} \tag{6.11}$$

where t_{on} is the pulse duration.

6.3.3 Solution methodology

In the present work, a three-dimensional FEM based numerical model has been developed to analyse the spatial and the temporal temperature distribution during the LIPAA process. The coupled effect of the laser heat flux and the plasma power density has been considered in the heat flux model as it gives a more realistic approach to the process. Simultaneous ablation of both PC and aluminium metal target was obtained during the simulations of the LIPAA process. The focus was however mainly on the PC sheet and accordingly, the channel width and channel depth were predicted from analysis and were validated with experimental results.

(A) Finite element formulation

After formulating the problem in terms of governing equations and boundary conditions, finite element method (FEM) was used to solve the problem. FEM is a numerical technique to solve the engineering problems in which the unknown function is approximated by piecewise defined functions. In this technique, the worksheet is discretized into elements. The collection of elements is called finite element mesh. Each element has nodes which are used to represent values of the field variables (for example, temperature) over the element by an interpolation function. In thermal analysis, the field variable is temperature, which is approximated within the element using its nodal temperatures,

$$T = [N]\{T_{\mathrm{e}}\} \tag{6.12}$$

and

$$T = [B]\{T_e\} = \left[\frac{\partial}{\partial x} N\right]\{T_{\mathrm{e}}\} \tag{6.13}$$

where $[N]$ is the interpolation or shape function matrix, $\{T_{\mathrm{e}}\}$ is the element nodal temperature matrix and $[B]$ is the general geometric matrix. Galerkin method is used to solve the above equations, and the resulting equations are expressed in the matrix form as

$$[C]\{T\} + [K_{\mathrm{T}}]\{T\} = \{Q\} \tag{6.14}$$

where $[C]$ and $[K_{\mathrm{T}}]$ are the global heat capacity matrix and global conductivity matrix respectively, which are given as

$$[C] = \int_V^0 \rho c [N][N]^T \, dV \tag{6.15}$$

$$[K_{\mathrm{T}}] = \int_V^0 k [B][B]^T \, dV \tag{6.16}$$

and $\{Q\}$ is the heat flux vector.

(B) Mesh model and mesh sensitivity analysis

The process continuum was discretized with thermal solid 35 with triangular-6 nodes initially for the two dimensional geometrical model and later, with thermal solid 70 with brick-8 nodes for the three-dimensional geometrical model. The entire model was discretised into coarse mesh and the mesh was further refined at the zone of laser irradiation at the interface of the two materials as shown in figure 6.4.

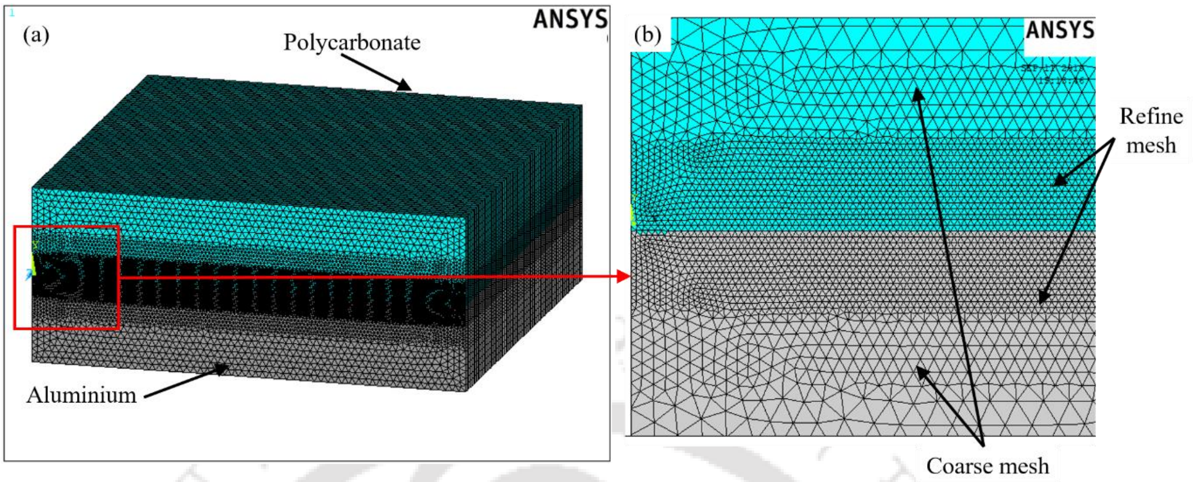

Figure 6.4 Meshed geometric model (a) 3D view and (b) 2D view

Both the PC and the aluminium were modelled using two different sets of nodes that correspond to two separate materials. A distinct interface of these materials has duly been defined. There was no external pressure applied on the top PC sheet during the experiments, therefore, in numerical simulations no pressure or contact resistance effect was considered at the interface of the two materials. Accordingly, the incoming laser heat flux was applied directly at the interface of the two materials. Mesh size is an important factor that needs to be controlled during the FE analysis. Larger mesh size leads to inconvergent simulation results, whereas smaller mesh size take long computational time. Thus, selection of an optimized mesh size is obtained by carrying out the mesh sensitivity analysis as shown in table 6.1. Mesh sensitive analysis was performed for the process condition of 3.06 MW/cm^2 pulse power density, 40 Hz pulse repetition rate and 2 ms pulse duration. From the mesh sensitive analysis, it was found that with a finer mesh size of 20 µm, the simulation gave the best results with computational time of 1.53 hours. The effect of a moving Gaussian heat flux was employed in the numerical model of the LIPAA process. The spatial and temporal thermo-physical investigation of the LIPAA process was carried out by implementing the laser heat source at the interface of the two materials and assuming an automatic time step increment. The spatial investigation lent a hand in predicting the width and depth of the microchannel. In the model, the material removal criterion to achieve ablation in aluminium and PC is such that, the material exceeding its melting point temperature is considered to be ablated or removed from the base material. However, the current study focuses upon the PC sheet for the determination of the channel width and the channel depth fabricated on its rear side. As such, melting point temperature of the PC sheet i.e. 503 K was taken into consideration to ablate the PC sheet. The temporal temperature distribution for pulse-on time (heating) and pulse-off time (cooling) were also explored. Figure 6.5 shows the outline of the developed numerical modelling approach for prediction of the dimensions of the microchannel and the machining rate during LIPAA process.

Table 6.1 Analysis of mesh sensitivity for refined mesh zone

Mesh Size (μm)	**Maximum Temperature (K)**	**Change in Temperature (ΔT)**	**CPU time (hours)**
35	666.7	-	0.23
30	672.9	6.2	0.43
25	674.4	1.5	0.72
20	**674.7**	**0.3**	**1.53**
15	676.5	1.8	3.17
10	677	0.5	4.69

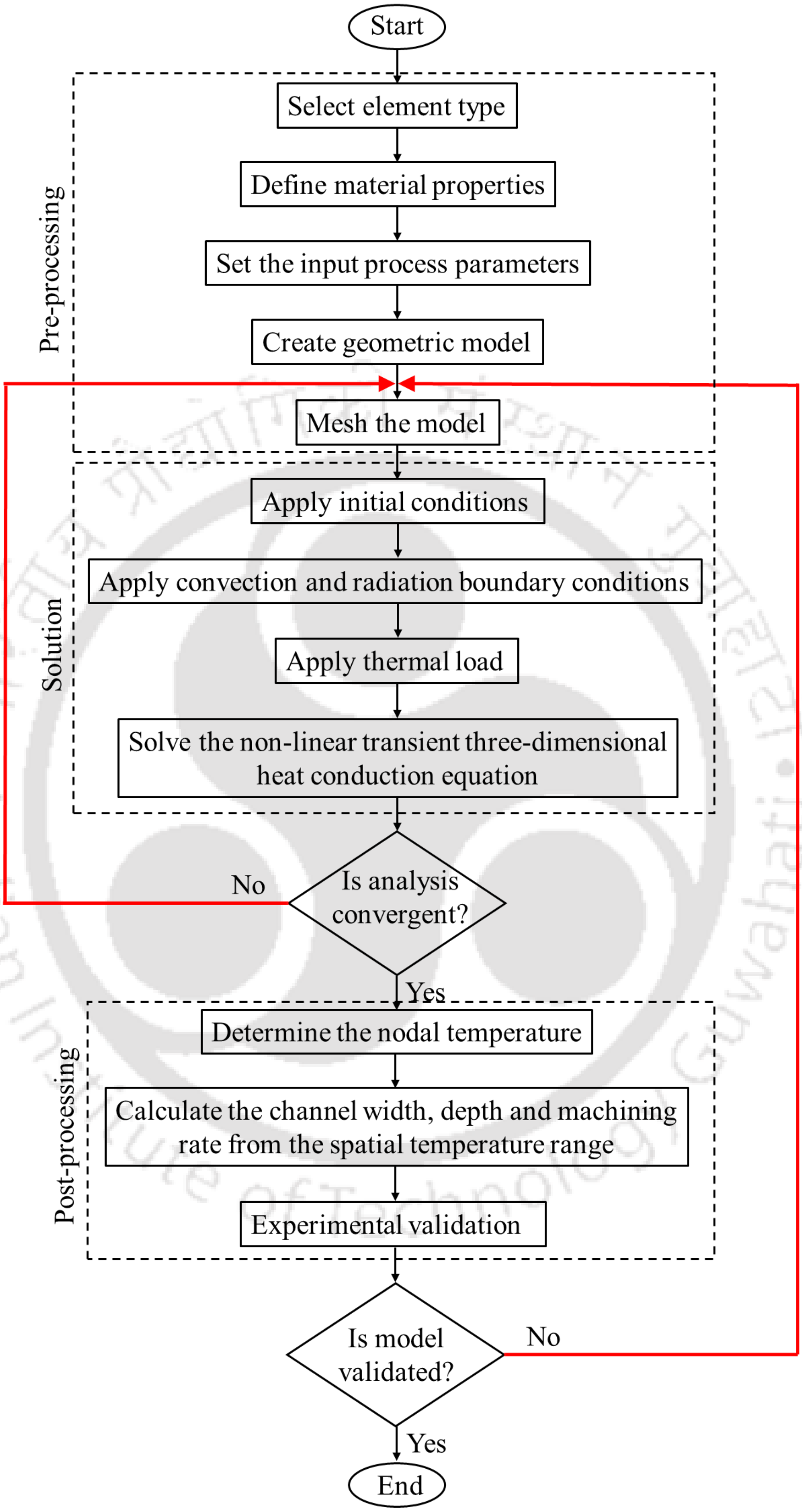

Figure 6.5 Outline of numerical modelling approach for predicting the width and depth of the microchannel and the machining rate of the LIPAA process

6.3.4 Material properties

The materials in the model were allotted the necessary material properties to outline the interface of the two materials (Hussein *et al.*, 2017). The thermal properties of the PC and the aluminium were considered to be temperature dependent. These properties of the materials are illustrated in figure 6.6(a) and 6.6(b) respectively (Luo and Zhao, 2018; Sedighi *et al.*, 2018). The other thermal and physical properties of the materials considered in the model are shown in table 6.2.

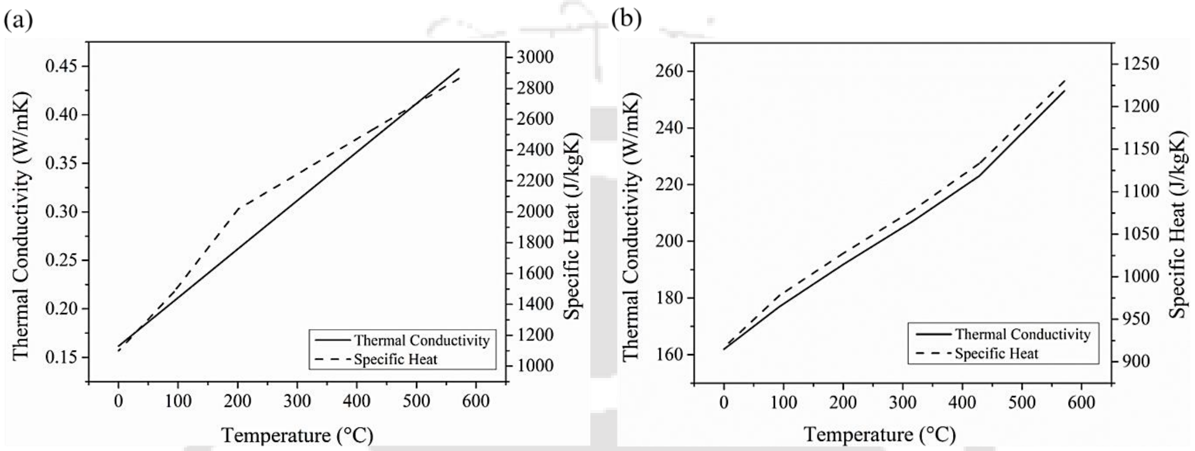

Figure 6.6 Temperature dependent properties of (a) PC and (b) aluminium

Table 6.2 Thermo-physical properties of PC and aluminium (Genna *et al.*, 2018; Chen *et al.*, 2016; Sedighi *et al.*, 2018; Jorik *et al.*, 2019)

	Property	**Value**
Polycarbonate	Density (kg/m^3)	1200
	Emissivity	0.95
	Reflectivity	0.07
	Glass transition temperature (K)	427
	Melting temperature (K)	503
Aluminium	Density (kg/m^3)	2700
	Reflectivity	0.96

6.4 Results and discussion

A numerical investigation was carried out for microchannel fabrication using the LIPAA process. In the analysis, parameters like pulse power density, pulse repetition rate and pulse duration were taken as the input laser parameters. Each of these laser parameters were varied at three distinct levels as presented in table 6.3. The levels of the laser parameters were kept within an appropriate range based on the introductory experiments carried out, while a constant value of 4 mm/s for the scanning speed was maintained.

Table 6.3 Laser process parameters

Laser Parameters	**Levels**		
Pulse power density (MW/cm^2)	3.06	4.6	6.1
Pulse duration (ms)	2	4	8
Pulse repetition rate (Hz)	40	60	80

In the beginning, the simulations were carried out with and without the consideration of the effect of the plasma. The results obtained for both the numerical conditions were compared with the experimental data as shown in figure 6.7. From the comparison, it was found that a mean deviation of 2.3% was obtained for the simulated results with the consideration of the plasma effect while a mean deviation of about 9.6% was obtained with no consideration for the plasma effect. Thus, the further investigation into the numerical study of the LIPAA process were carried out concerning the plasma effect in addition to the influence of the input laser heat flux. The transient temperature profile at the interface of PC and aluminium is shown in figure 6.8(a). The profile of the temperature shown is for the process condition of pulse power density 3.06 MW/cm^2, pulse repetition rate 60 Hz, pulse duration 2 ms and scanning speed 4 mm/s. Figure 6.8(b) and 6.8(c) represent the temperature contours at two different times viz. towards the end of pulse-on time i.e. 2 ms and end of pulse-off timei.e.16.7 ms respectively.

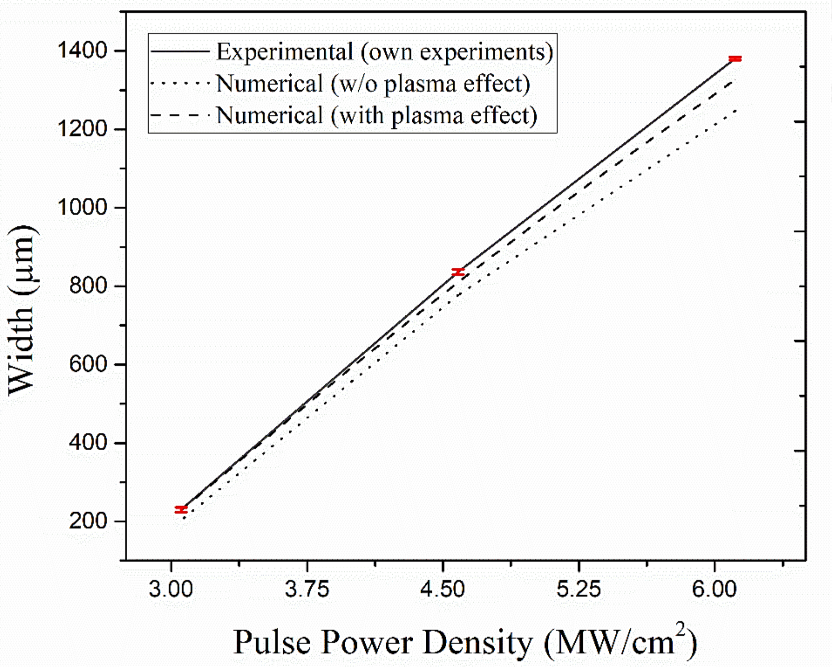

Figure 6.7 Comparison of the simulated results (with and without the influence of the plasma) with the experimental results

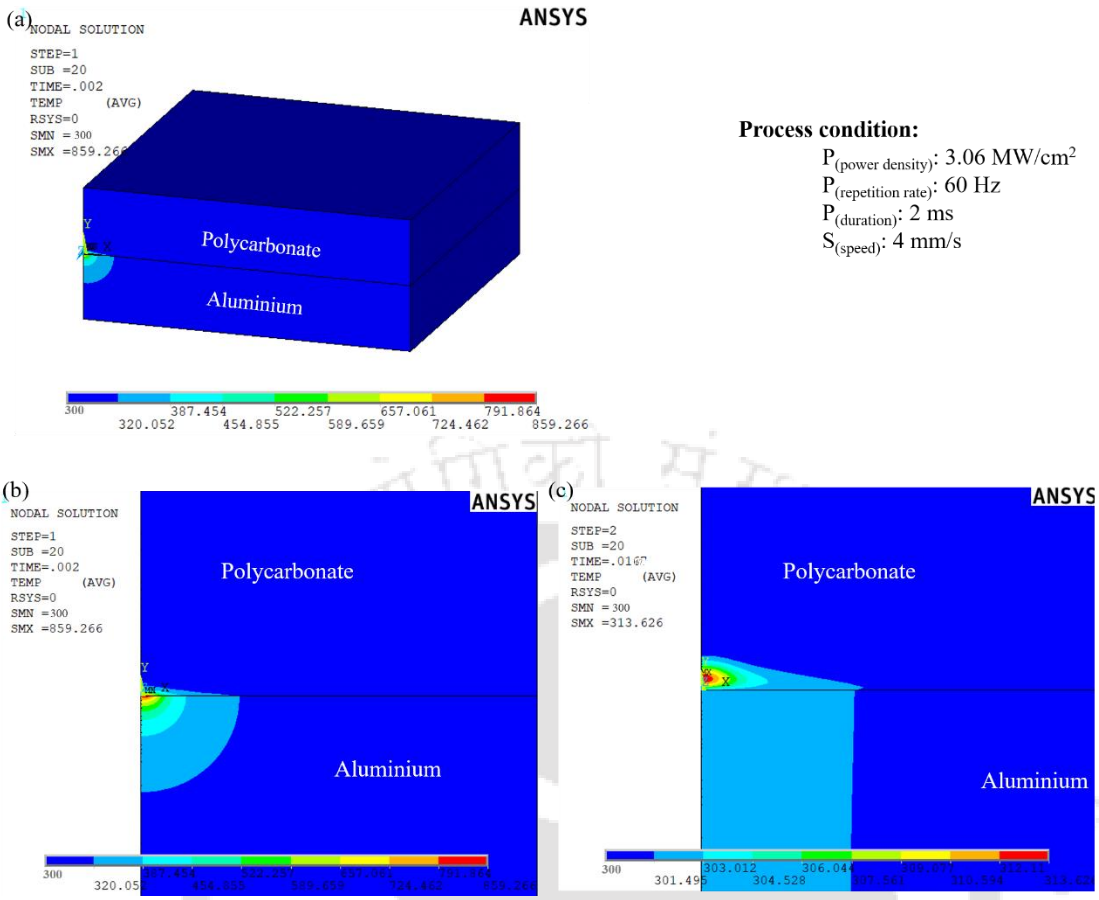

Process condition:

$P_{(\text{power density})}$: 3.06 MW/cm^2
$P_{(\text{repetition rate})}$: 60 Hz
$P_{(\text{duration})}$: 2 ms
$S_{(\text{speed})}$: 4 mm/s

Figure 6.8 (a) The 3D temperature profile on the PC and the aluminium sheet for the chosen set of experiment at (b) 2 ms and (c) 16.7 ms

As observed from the above figure, a temperature of maximum value 859 K is obtained at the end of pulse–on time (2 ms) and this maximum temperature lies within the metal target. While at the same point of time, a highest temperature of 819 K is attained at the interface of the two materials, which is lower than the maximum temperature attained within the metal target but surpasses the melting temperature of the PC (503 K). As a result, material removal on the rear side of the PC was noted. Also, it was observed, a very small region of the PC, neighbouring the ablated part surpasses the glass transition temperature of PC not exceeding the melting temperature. Such region of the PC transforms into a rubber like state, is not ejected and sooner or later, recovers its original form of state. Nevertheless, at the end of pulse-off time, i.e. 16.7 ms, the temperature at the irradiated zone comes closer to the initial surface temperature (300 K) of both the materials.

6.4.1 Validation with experimental data

Experiments were performed considering PC and aluminium sheet respectively as the transparent and the metal target, both of them were of 1 mm thickness. The PC sheet was cut into pieces of 100 mm × 30 mm and the aluminium sheet into pieces of 110 mm × 40 mm. Ablation on the PC by the LIPAA process was obtained using a Nd: YAG millisecond pulsed laser (Model: 500 W pulsed Nd: YAG CNC Laser, Make: Suresh Indu Lasers Pvt. Ltd) of 1.064 µm wavelength. To study the ablation process and the influence of the laser parameters on the responses like microchannel width, microchannel depth and machining rate, single pulse stoke of the laser beam was produced for each set of machining parameters. During the machining process, the pulse power density was varied in the range of 3.06–6.1 MW/cm^2, pulse repetition rate in the range 40–80 Hz and pulse duration in the range of 2–6 ms.

The fabricated microchannels were examined by using Field Emission Scanning Electron Microscope (FESEM) to analyse the microchannel width and depth. Measurement of the microchannel size was carried out done both on its rear surface and its cross-section as shown in figure 6.9. Machining rate of the process was calculated considering the values of width and depth of the microchannels. From the measurements, it was witnessed that the width and depth of the microchannels increases with the increase in the values of the laser parameters viz. pulse power density, pulse duration and pulse repetition rate.

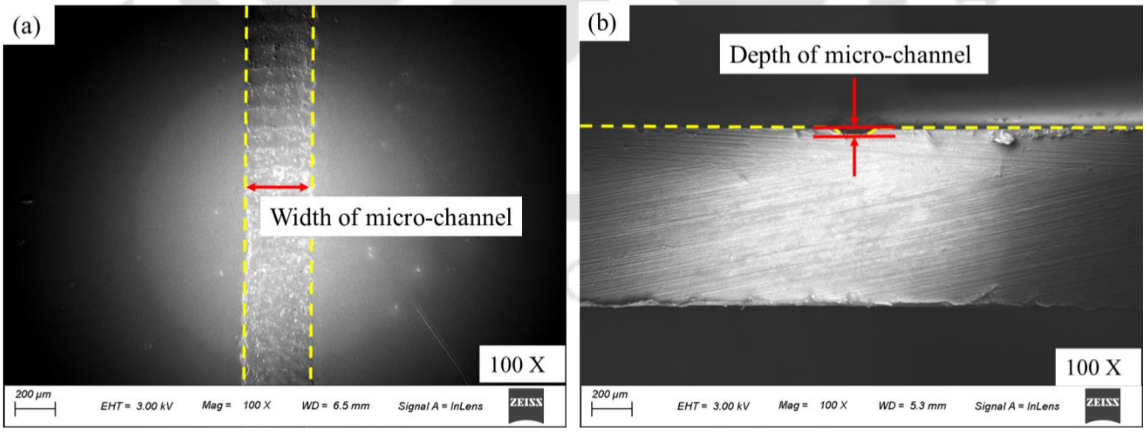

Figure 6.9 FESEM images of (a) top and (b) cross-section view of the microchannel

The experimental values of the width, depth and the machining rate were utilised for validating the developed FE model. The microchannel width, microchannel depth on the PC sheet and the machining rate of the process from the ANSYS simulations were compared with the experimental data. Both the simulated and the experimental outcomes were compared for varying pulse power density keeping the other parameters constant at 40 Hz pulse repetition rate, 4 ms pulse duration and 4 mm/s scanning speed. The simulation results were observed to be slightly lower than the experimental data. Such differences between the simulated and experimental results may be due the assumptions considered which differs the model from the real experimental environment. However, from the comparisons shown in figure 6.10, it can be said that the numerical results are in good agreement with experimental results with a mean deviation of 2.3% for channel width, 9.8% for channel depth and 10.5% for machining rate.

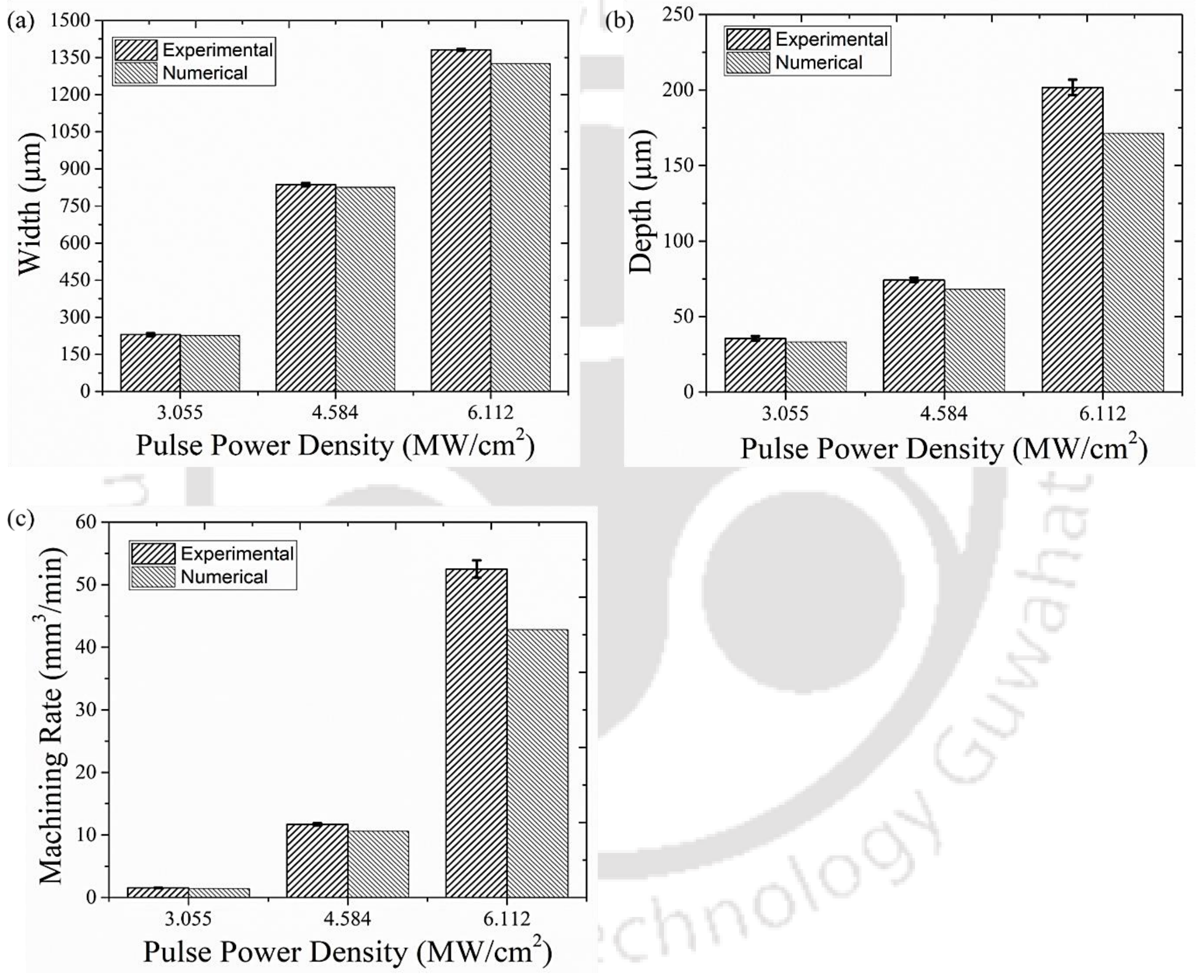

Figure 6.10 Comparison of numerical and experimental results for (a) width, (b) depth and (c) machining rate

6.4.2 Spatial and temporal investigation of LIPAA process

Based on the confidence gained from the validation of the simulated results, further investigation on the numerical model was carried out. Spatial thermal analysis was performed at various positions along the x-direction and the y-direction. The temporal analysis was also carried out in the course of the pulse-on time (heating) and pulse-off time (cooling).

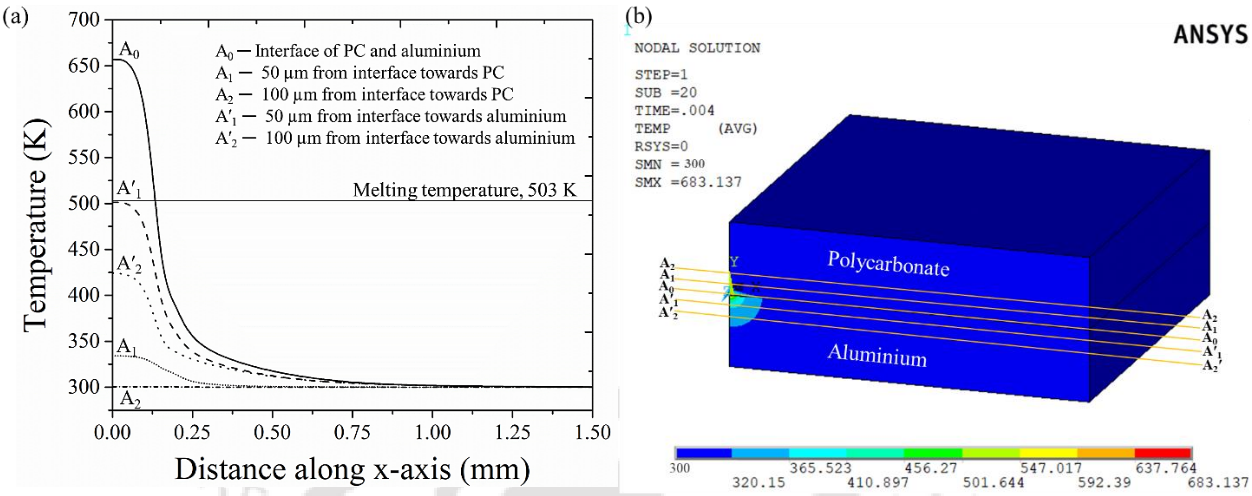

Process condition:

$P_{(power\ density)}$: 3.06 MW/cm^2
$P_{(repetition\ rate)}$: 40 Hz
$P_{(duration)}$: 4 ms
$S_{(speed)}$: 4 mm/s

Figure 6.11 (a) Temperature distribution and (b) Temperature contour of LIPAA process along x-direction for the chosen set of process condition

The spatial temperature contour along the x-direction at different distances from the interface of the two materials are shown in figure 6.11. The plot is shown for the process condition of pulse power density of 3.06 MW/cm^2, pulse repetition rate of 40 Hz, pulse duration of 4 ms and scanning speed of 4 mm/s. It is observed that, at A_1 and A'_1 i.e. at a distance of 50 µm from the interface towards the PC and the aluminium sheet respectively, the temperature at A'_1 is much higher than that at A_1. It may be due to the higher thermal conductivity of aluminium compared to the thermal conductivity of the PC. Thus, most of the laser heat is conducted into the aluminium sheet. Similar variance of the temperature was also observed for A_2 and A'_2 i.e. at a distance 100 µm on both sides from the interface. Further, it is observed that, at the end of pulse-on time (4 ms), a temperature of maximum value 657 K is obtained at $A_{0,}$ i.e., at the interface of the two materials. At the same time, a highest temperature of 683 K is generated within the aluminium sheet. But then again, the temperature at the interface is beyond the melting temperature of the PC and hence material removal is obtained. At 50 µm distance from the interface towards the PC, the maximum temperature attained was 334 K which is below the melting temperature of the PC. Thus, there was no material removal. Similar observations were also seen for 100 μm distance from the interface. The simulated results show good agreement with the FESEM image of the machined PC surface. The same can be observed from the experimentally fabricated microchannels, shown by the FESEM image in figure 6.12.

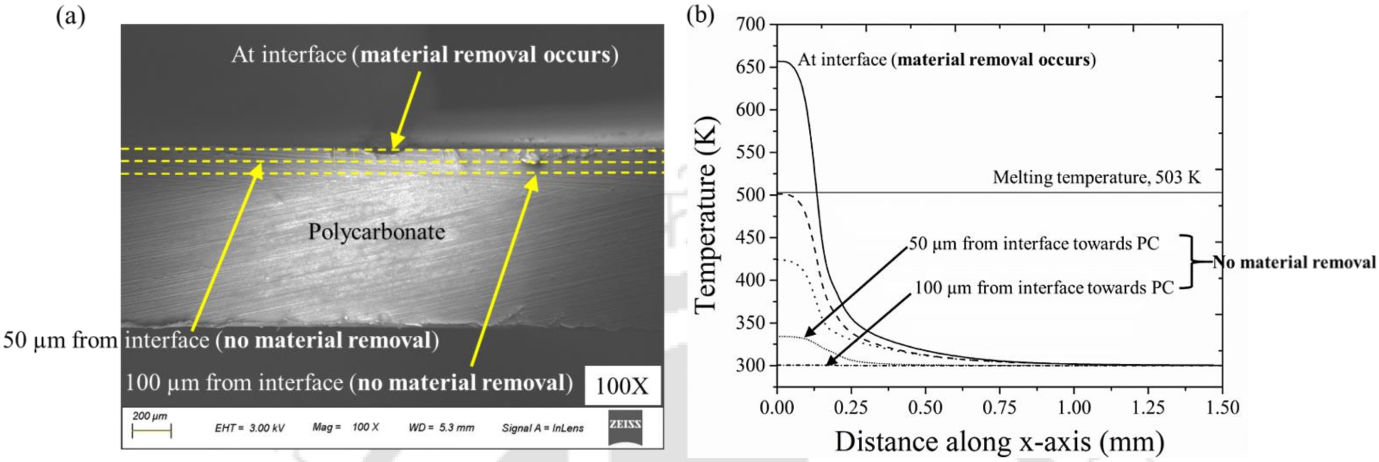

Figure 6.12 Comparison of temperature distribution and its effect on material removal (a) experimental results and (b) computational results

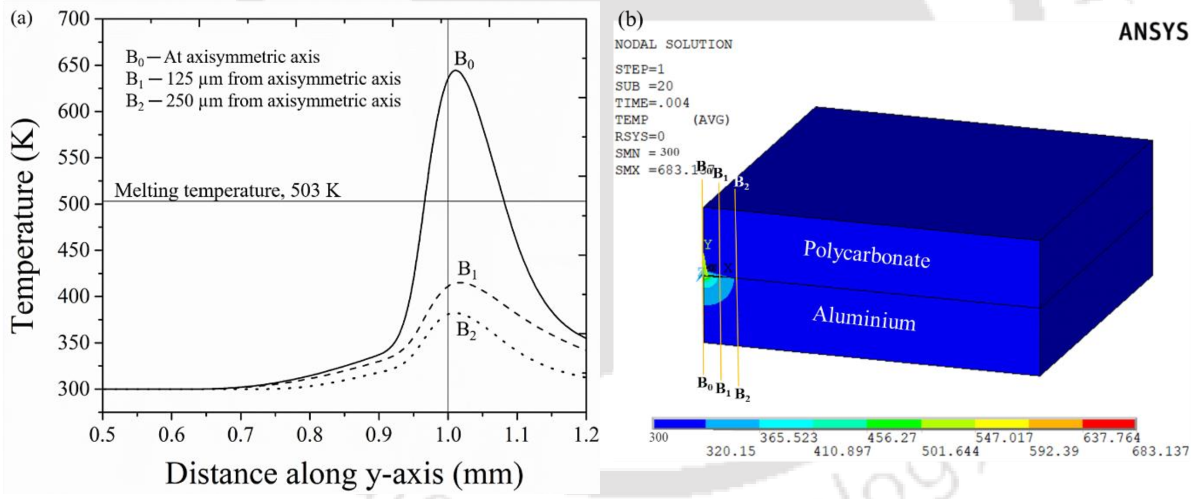

Process condition:

$P_{(power\ density)}$: 3.06 MW/cm2
$P_{(repetition\ rate)}$: 40 Hz
$P_{(duration)}$: 4 ms
$S_{(speed)}$: 4 mm/s

Figure 6.13 (a) Temperature distribution and (b) Temperature contour of LIPAA process along y-direction for the chosen set of process condition

The spatial temperature distribution in the y-direction on the X-Y plane is shown in figure 6.13. The distributions are shown at three different distances from the axisymmetric axis. It is observed that, a maximum temperature of 657 K is obtained at B_0 i.e. at the axisymmetric axis and lies at the interface of the PC and the aluminium sheet. The temperature at the interface of the axisymmetric axis is thus found to surpass the melting temperature of the PC and consequently, the material removal on PC sheet is achieved. Moving to a distance of 125 µm and 250 µm from the axisymmetric axis i.e. at B_1 and B_2, decrease in the temperature distribution was observed. The maximum temperature at B_1 and B_2 was less than the melting temperature of the PC and thus, no material removal was obtained. Identical observation was found from the experiments too, as shown by the FESEM image of the microchannel on PC for the same set of parameters in figure 6.14.

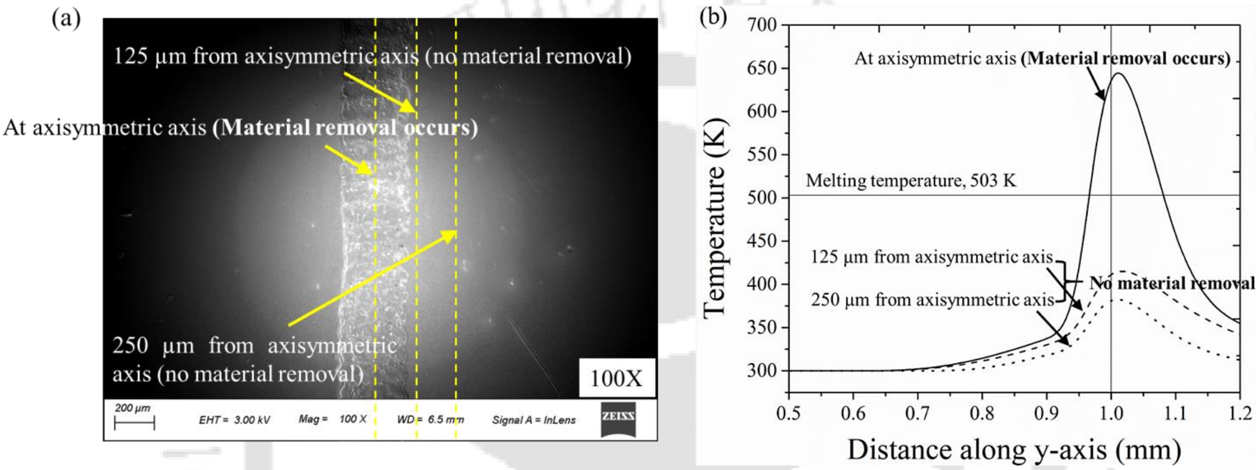

Figure 6.14 Comparison of temperature distribution and its effect on material removal (a) experimental results and (b) computational results

It can also be observed from figure 6.14 that, at equal distance from the interface towards both PC and aluminium, the temperature on the aluminium is higher than that on PC, resulting in a non-axisymmetric temperature contour (along the y-axis). It is because of the application of lower value of laser process parameters (3.06 MW/cm^2 pulse power density, 40 Hz pulse repetition rate and 4 ms pulse duration). At low value of laser parameters, plasma generation is less and thus, laser beam irradiation plays a significant role in temperature generation in both the materials. The PC being transmissible to the laser beam is subjected to very less thermal effect. Thus, it can be understood that, the aluminium metal target is more thermally affected and as such, at equal distance from the interface towards both PC and aluminium, the temperature on the aluminium is higher than that on PC, resulting in a non-axisymmetric temperature contour.

For the same set of process condition, the temporal investigation of the LIPAA process on PC was also carried out. The peak temperature during pulse–on time and pulse–off time of the process was obtained as a function of time as shown in figure 6.15.

As observed from the figure, the temperature rises at a high rate during pulse–on time and reaches to maximum value of 683 K at its end i.e. at 4 ms. The pulse–on time is also referred to as the heating time. However, the temperature after 4 ms starts decreasing at a slow rate and at the end of pulse–off time i.e. 25 ms, reaches a value very close to the initial temperature of the materials. The pulse–off time is hence, referred to as the cooling time. In a time period, the cooling time is thus found to be much longer than the heating time, thereby resulting in a slower cooling rate. But depending on the repetition rate and the scanning speed, the cooling period of the former laser pulse is overlapped with the heating time of the upcoming laser pulse, hence resulting in the formation of microchannels.

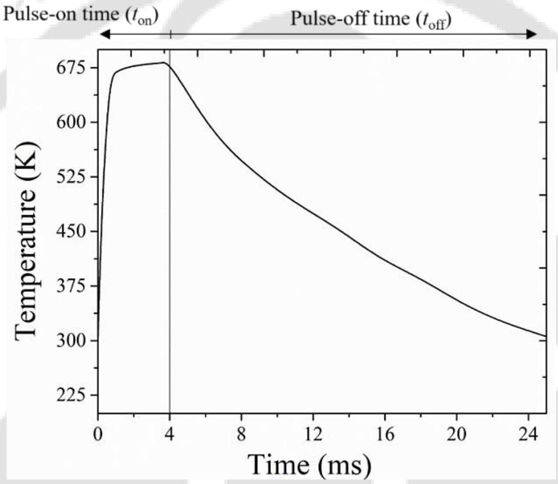

Figure 6.15 Time versus temperature for pulse-on time of 4 ms and pulse-off time of 21 ms

6.4.3 Influence of laser parameters on microchannel fabrication

A parametric analysis was performed to understand the contribution of the laser parameters such as pulse power density, pulse duration and pulse repetition rate on the responses such as microchannel width, microchannel depth and eventually the machining rate. Figure 6.16(a) and 6.16(b) shows the variation of temperature along the x-axis and y-axis at varying pulse power density. From the figures, it can be seen that as the pulse power density increases keeping the other parameters fixed at 60 Hz pulse repetition rate and 4 ms pulse duration, values of both the width and depth of the fabricated microchannel increase. And hence, an increase in the machining rate is also obtained. Similarly, the effect of the increase in the pulse duration on the width and depth of the microchannel is shown in figure 6.16(c) and 6.16(d). In this case, the pulse duration was increased from 2 ms to 6 ms while the other parameters were fixed at 60 Hz pulse repetition rate and 4.6 MW/cm^2 pulse power density. It is noticed that as the pulse duration is increased, a growth in the width and depth of the microchannel is achieved, thereby resulting in the increase of the machining rate too. The width and depth of the microchannel is also affected by the variation in pulse repetition rate, as shown in figure 6.16(e) and 6.16(f). On increasing the value of pulse repetition rate from 40 Hz to 80 Hz, keeping the other parameters fixed at 4 ms pulse duration and 4.6 MW/cm^2 pulse power density, there was a growth in the microchannel width and depth and as a result of which, increase in the machining rate was also obtained.

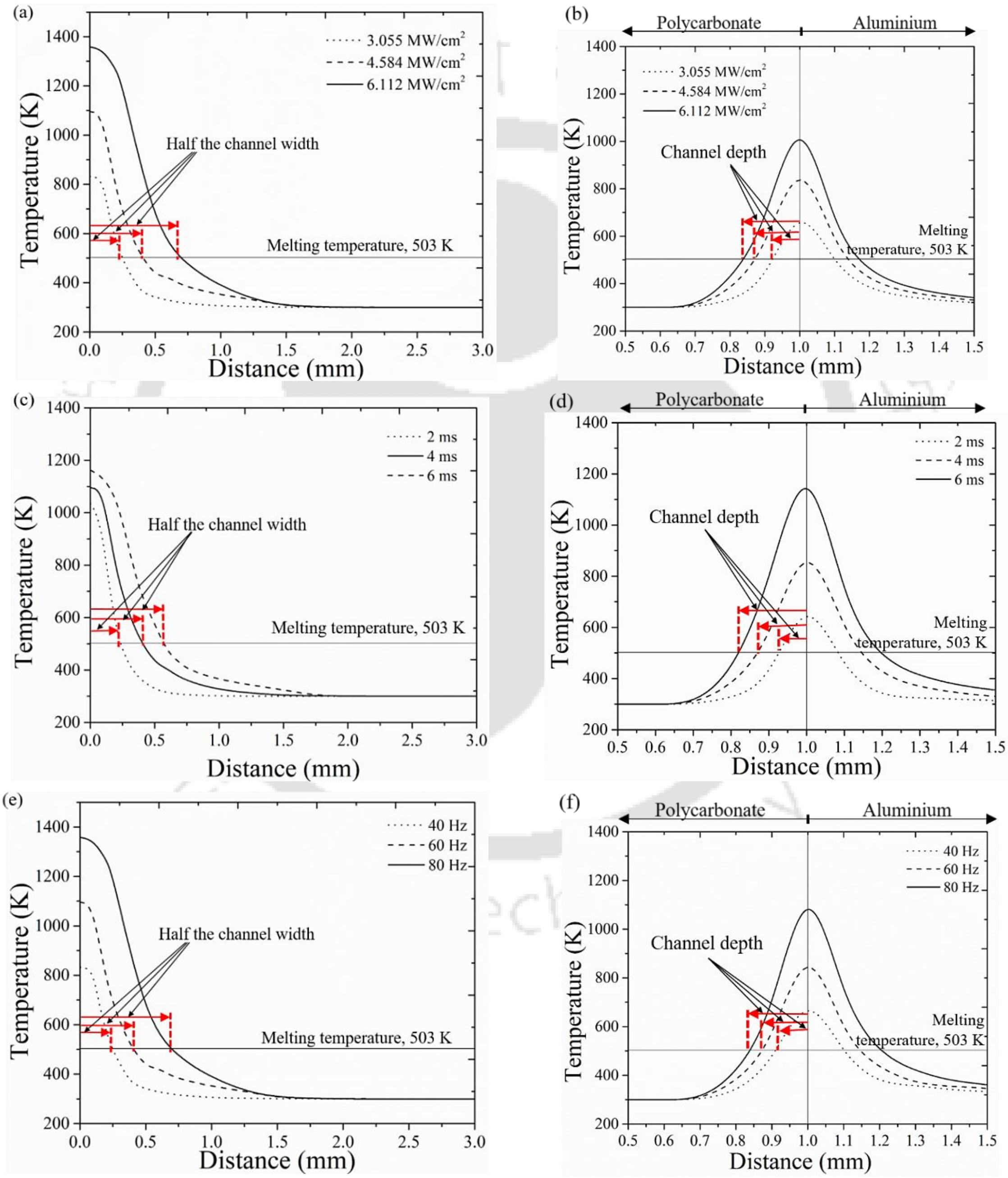

Figure 6.16 Influence of pulse power density, pulse repetition rate and pulse duration on microchannel width and depth

Overall, the graphs portray that, as the laser parameters are increased, an increase in the microchannel width and depth and the machining rate of the process is obtained. It is because; an enriched plasma is produced with the rise in the laser parameters. Correspondingly, the plasma attains a temperature of 2500 K to about 50000 K, with a pressure of approximately 500 MPa [27]. The plasma thus has a large influence on the rear side of the PC sheet. A temperature beyond the melting temperature of the PC will be produced on its surface, thus, resulting in an increased microchannel width and microchannel depth.

Again in figure 6.16(b), (d) and (f), it is observed that the temperature contours on PC and aluminium are nearly axisymmetric (i.e. at equal distance from the interface towards PC and aluminium, the temperature on both the material is nearly the same). The reason for such observation is that, the input laser process parameters applied are at comparatively higher levels. As the laser parameters are increased, there is an increase in the laser intensity resulting in dynamic interaction of the plasma with the laser irradiation. This causes a rapid expansion of the plasma. As such, at higher levels of laser parameters, the plasma plays a major role in temperature generation in both the materials. Again, we know that the thermal conductivity of PC being low (~0.4 W/mK) generates higher temperature near the irradiated zone with narrower temperature distribution. While thermal conductivity of aluminium being high (~250 W/mK), due to higher conduction of heat into the material, it results in less temperature generation near the irradiated zone with a much wider temperature distribution. It can thus be witnessed that, at higher value of laser parameters, the temperature at equal distance from the interface are more or less similar, thereby resulting in a near axisymmetric temperature contour. Moreover, it can also be witnessed that as we move away from the irradiated zone on both side of the interface, the temperature profile are not axisymmetric in nature.

The scanning speed during the simulation of the LIPAA process was however kept constant at a value of 4 mm/s to form the channel. It is known that for a channel to form, the overlap of the consecutive pulses must be larger than zero. The overlap distance and its percentage between two pulses is denoted by D_L and O and can be expressed as:

$$D_L = \frac{v}{f} \tag{6.17}$$

$$O = \left(\frac{\omega - D_L}{\omega} \right) \times 100\% \tag{6.18}$$

where v is the laser scanning speed, f if the repetition rate and w is the laser spot diameter. Scanning speed of 4 mm/s results in the minimum overlap of 50 % to a maximum value of 75 % for our selected levels of laser process parameters where pulse power density was varied from 3.06 MW/cm^2 to 6.1 MW/cm^2, pulse duration from 2 ms to 6 ms and pulse repetition rate from 40 Hz to 80 Hz. The focused beam diameter was considered to be 200 µm.

It is also found that the nature of change in both width and depth of the microchannel with the change in the laser process parameters is similar, maintaining a constant aspect ratio of the microchannel. Thus, it can be said that, a very narrow microchannel to a wide microchannel with a nearly constant aspect ratio can be obtained by the technique of LIPAA.

6.5 Estimation of channel index (CI) for microchannel fabrication during LIPAA using millisecond pulsed laser

Channels having width in the micron–scale (1-999 µm) are considered as microchannels. Further, it has been observed from the experiments that channels with channel depth exceeding a value of 250 µm starts showing deterioration and burning in the PC sample (which is of 1 mm thickness). Therefore, channel width of 999 µm and channel depth of 250 µm has been considered as standard dimensional limits for fabrication of microchannel and correspondingly, the maximum permissible machining rate for microchannel fabrication during LIPAA using millisecond pulsed laser has been determined. Mathematically, the machining rate can be calculated as (Dahotre *et al.*):

$$\begin{aligned} \mathit{Machining\ rate} &= \left(\mathit{Cross\ sectional\ area\ of\ microchannel}\right)\times\left(\mathit{Laser\ scanning\ speed}\right) \\ &= \left(\frac{\pi}{2}\times\left(\frac{1}{2}\mathit{Width}\right)\times \mathit{Depth}\right)\times\left(\mathit{Laser\ scanning\ speed}\right) \end{aligned} \tag{6.19}$$

Using equation (6.19), the maximum permissible machining rate is found to be 47.05 mm^3/min considering a channel width of 999 µm and a channel depth of 250 µm. The machining rates for each process set has also been calculated and compared with the maximum permissible machining rate to determine the channel index (CI) for microchannel fabrication during LIPAA using a millisecond pulsed laser. Mathematically, the CI can be expressed as:

$$CI = \frac{Machining\ rate}{Max^{m}\ permissible\ machining\ rate} \tag{6.20}$$

The machining rates and their corresponding CI are listed in table 6.4. In the present study, the maximum value of machining rate within the permissible limit was found to be 40.6 mm^3/min, resulting in a CI value of 0.86 for process set condition of 3.06 MW/cm^2 pulse power density, 60 Hz pulse repetition rate, 4 ms pulse duration and 4 mm/s scanning speed. It is observed that, when the machining rate is less than its maximum permissible machining rate value (47.05 mm^3/min) i.e. for CI < 1, the channels dimensions are within the acceptable dimensional limits for microchannel fabrication. However, if the machining rate is equal to or exceeds its maximum permissible rate i.e. for CI ≥ 1, the channel dimensions go beyond the acceptable dimensional limit and the PC sheet starts deteriorating and causes burning of the sample. Therefore, microchannel fabrication on PCs using LIPAA technology should avoid process conditions that lead to CI ≥ 1. Consequently, it can be said that CI can be used as an index in determining the permissible set of process conditions for fabrication of microchannel during LIPAA using a millisecond pulsed laser. The estimated CI value provides insightful information regarding the feasibility of microchannel formation on transparent PC sheet, without the material being damaged or burnt out.

Table 6.4 Machining rate during LIPAA and corresponding channel index (CI) for different set of process conditions

Pulse repetition rate (Hz)	Pulse duration (ms)	Pulse power density (MW/cm^2)	Machining rate (mm^3/min)	Channel index (CI)
40	2	4.584	0.51	0.010
40	4	3.055	1.55	0.033
60	2	6.112	7.56	0.161
80	4	3.055	11.85	0.252
80	2	4.584	18.19	0.387
40	6	4.584	38.19	0.812
60	**4**	**3.055**	**40.56**	**0.862**
60	6	3.055	48.79	1.038
80	6	3.055	72.16	1.535
80	4	4.584	78.94	1.679
80	6	4.584	120.24	2.55
60	6	6.112	211.60	4.502
80	6	6.112	376.8	8.017

∗ No ablation observed

Let us consider the case of successful application of microchannels in health biomarker such as glucose test trip. A width of at least 600 μm is recommended in the test strips to avoid fluctuations in electrode resistance and improve the accuracy of glucose measurements. The depth of the microchannel, on the other hand, varies depending on its width to maintain constant blood flow through the channel and achieve the same electrical resistance. In such glucose test strip cases, when width and depth are dependent on each other, the CI can be considered as a standard factor to represent a glucose test strip size. For example, two different strips, one of width 600 μm and depth 60 μm and the other of width 900 μm and depth 40 μm would have the same CI of 0.14. Thus, we can state that for a particular glucose measuring machine, glucose strip of 0.14 CI is required.

6.6 Summary

In this chapter, a 3D non-linear transient thermo-physical model of the LIPAA process has been developed. By using the developed model, spatial and temporal analysis of the process has been carried out. The salient features of the model can be summarized as follows:

- The developed 3D thermo–physical model of the LIPAA process incorporates the effect of the plasma power density in addition to the effect of incoming laser beam on both the transparent PC and the aluminium metal target.
- The model simulates the simultaneous ablation of both the PC and the aluminium sheet during the process, thereby providing a more realistic approach of modelling and simulation of LIPAA.
- Simulations were initially performed with and without the consideration of the effect of the plasma. The results of both the cases were compared with the experimental outcomes and the simulations considering the effect of plasma was found to have better correlation with a mean deviation of about 2.3%. As such, the numerical analysis of the LIPAA process was carried out with regard to the effect of the plasma.
- From the developed model, it has been found for lower value of laser process parameters that, at an equal distance from the interface towards the PC and the aluminium sheet, the temperature on the aluminium is comparatively larger than that on the PC. However, at higher value of laser process parameters, the temperature at equal distance from the interface towards the PC and the aluminium sheet is nearly the same.

- The spatial distribution helps in predicting the width and depth of the microchannel respectively. The spatial distribution along the x-direction at the interface provided half the value of the width of the fabricated microchannel while the depth was obtained from the distribution along the y-direction at the axisymmetric axis. The simulated results were found agreeing well with the experimental results with a mean deviation of 2.3% for channel width, 9.8% for channel depth and 10.5% for machining rate.
- From the temporal distribution of temperature, it has been found that the maximum temperature obtained in the simulation was within the aluminium sheet. The temperature at the interface was less than the maximum temperature obtained but surpasses the melting temperature of the PC and consequently, material removal on the PC sheet is achieved.
- The temporal investigation also indicated that the rate at which the temperature rises during pulse–on time (heating time) was higher than the rate at which temperature reduces during pulse–off time (cooling time).
- The maximum machining rate value within the permissible limit was found to be 40.6 mm^3/min for the process condition of 3.06 MW/cm^2 pulse power density, 60 Hz pulse repetition rate, 4 ms pulse duration and 4 mm/s scanning speed. The corresponding CI value of 0.86 can thus be considered as a limiting factor for fabrication of a channel within the micro-scale (1–999 μm).

Thus, it can be concluded that the developed 3D thermo–physical numerical model can be utilized to decide the accurate laser parameters for a given size of the microchannel without any burning effect of the PC material.

Chapter 7

Conclusions and future scope

7.0 Overview

The primary objective of the present research work is to enhance the product quality and process efficiency of transparent material processing by using the method of Laser-Induced Plasma Assisted Ablation (LIPAA). The work addressed a challenging task in laser processing of transparent polycarbonate (PC) due to its high transmissibility of laser in visible and near-infrared spectral range of electromagnetic spectrum. In addition, systematic work was carried out to fabricate clean microchannel on PC sheet. Further, numerical analysis of the process was performed to understand the underlying physics of the LIPAA process. The present research work was carried out in the following stages:

1) Feasibility study of laser processing of transparent PC using the LIPAA process by carrying out systematic experiments.
2) Experimental analysis on the effect of various metal target properties on microchannel fabrication during LIPAA and recommendation of the metal target leading to the highest microchannel aspect ratio for further study.
3) Investigation on the impact of the laser parameters on channel geometry (channel width and channel depth) and channel quality (channel roughness) and determination of optimal parameters for microchannel fabrication on PC using LIPAA. The fabricated open micro-channels were closed by using thermal bonding process. A fluid flow test was carried out on the closed microchannel and its potentiality to be used as a microfluidic device was proved.
4) Development of two-dimensional thermo-physical model on LIPAA for microchannel fabrication on PC using aluminium metal target.
5) Development of three-dimensional thermo-physical model on LIPAA for microchannel fabrication on PC using aluminium metal target.

Important observations and research contributions from the present work are summarized in the sections to follow.

7.1 Conclusions and research contributions

Literature reports both conventional and non-conventional techniques like micro wire moulding, compression moulding, chemical etching and laser processing for microchannel fabrication. Correspondingly, microchannels are prepared on a variety of materials like metals, polymers and ceramics. Laser processing has however proved its capability in fabricating clean and uniform channels. Moreover, transparent PCs are widely used in the biomedical as well as optics industry owing to their inherent good impact strength, dimensional stability, optical clarity and eco-friendly nature. As such, studies on laser processing of PCs are important for the practical implementation of the process. The present work contributes comprehensive experimental and numerical studies to assess the feasibility, product quality and process efficiency of transparent material processing by using the method of LIPAA. Based on the research gaps identified in the literature, the present research has been carried out. Specific contributions of the current work are documented below:

7.1.1 Microchannel fabrication using LIPAA and study on the influence of metal target properties

Current work demonstrated the successful fabrication of microchannels on transparent PC using LIPAA. Then, the channel geometry (channel width and channel depth) and channel roughness of the fabricated microchannels were measured and analysed. After successful fabrication of microchannels, the effect of the properties of metal target was also investigated. Three different metal targets viz. aluminium, copper and stainless steel have been utilized during the process. The important observations from the study can be summarized as follows:

- LIPAA can successfully fabricate high quality microchannels for various scientific and industrial applications.
- EDX analysis showed the presence of carbon, aluminium and oxygen deposits on the channel edge and channel bed. The deposits are temporary in nature and are easily removed, thereby having no specific influence of the deposits on the quality of the microchannel for bio-medical applications.
- An increase in the thermal conductivity of the metal targets results in the decrease in the dimension of the channels fabricated on the PC sheet, while an increased melted and vaporized volume is obtained in the metal target itself. However, this effect of the thermal conductivity is more distinctly visible on the channel width rather than on the channel depth.
- The time span for plasma generation and the distance of the generated plasma from the rear side of the PC sheet plays the major role in determining the channel width on considering the variation in thermal conductivity of the metal targets.

- Again, an increase in the dimension of the channels fabricated on the PC sheet was observed with the increase in the value of the specific heat of the metal target, whereas a decrease in the melted and vaporized volume in the metal target itself was obtained. On the other hand, this influence of the specific heat capacity is more prominent on the channel depth rather than on the channel width.
- The reflected laser beam that reaches the rear side of the PC sheet during the process plays the main role in determining the channel depth when the variation in specific heat capacity is considered.

Higher aspect ratio microchannels are fabricated with aluminium metal target compared to that fabricated with copper and stainless steel as metal target. As such, further investigation of our research has been performed considering aluminium as the metal target.

7.1.2 Parametric and statistical investigation into microchannel fabrication on PC and fabrication of thermally bonded micro-channels

Current work presents comprehensive experimental study on microchannel fabrication on PC using the LIPAA process. Full factorial experiments were carried out by varying process parameters viz. pulse power density, pulse repetition rate and pulse duration at three levels and the responses in terms of the channel geometry and the roughness were systematically measured and analyzed. The influence of varying the process parameters on the responses was studied. The role of scanning speed in the channel formation during laser processing is also being discussed. ANOVA was carried out to find the significance of the factors on the responses and second order mathematical relations among the input laser parameters, their interactions and the responses were developed. Further, the predictions by the models were verified by conducting confirmatory experiments. Following are the important conclusions drawn from the present study.

- Low pulse duration of 2 ms along with either pulse power density of 3.055 MW/cm^2 or pulse repetition rate of 40 Hz results in the formation of no channels.
- The combination of high pulse power density of 6.112 MW/cm^2 and high pulse repetition rate of 80 Hz is detrimental to the output responses viz. channel width, channel depth and roughness of the process causing burning of the PC sheet.
- The increase in pulse power density, pulse duration and repetition rate results in the increase in the responses viz. channel width, channel depth and roughness. However, a decrease in the responses was observed with the increase in the scanning speed.

- The scanning speed not only affects the channel geometry and roughness but also plays an important role in the formation of channel. A channel is formed when the pulse overlap is greater than zero and discrete craters are formed when the pulse overlap is less than zero. For the beam diameter of 200 µm, the overlap distance for scanning speed of 4 mm/s and 7 mm/s was found to be 100 µm and 175 µm respectively which provide the overlap percentage of 50% and 12.5%. For channel formation, a maximum scanning speed of 4 mm/s (which corresponds to 50% overlap) can be preferred.
- Increase in the channel geometry without increase in the roughness can be achieved by subjecting the channel to multiple numbers of scans of the laser beam. Clean and uniform channels can be obtained at quite a low pulse power density (3.055 MW/cm^2) with moderate pulse duration of approximately 4 ms and pulse repetition rate of 40 Hz. Four to five number of scans of the laser beam at low pulse power density with moderate pulse duration can be employed to achieve the desired channel geometry with minimum roughness.
- Pulse power density has the highest significant effect on channel geometry and channel roughness, followed by pulse duration and repetition rate.
- For a width of 250 µm, depth of 150 µm and minimum roughness on a single pass, the optimized pulse repetition rate, pulse duration and pulse power density were found to be 40 Hz, 2 ms and 4.79 MW/cm^2.

By using the optimum process parameters, open channels were fabricated, which were then closed by using thermal bonding technique. The leak-proof bonded channels were thoroughly tested and the sustainability of the LIPAA process was verified. Also, different profiles viz. serpentine shaped, round and oval shaped microchannels were produced on PC using the LIPAA process. The sustainability of the LIPAA process of machining transparent material is thus proved in fabricating microchannels of different shapes.

7.1.3 2D thermo-physical modelling and simulation on LIPAA for microchannel fabrication on PC with aluminium metal target

A 2D thermo-physical numerical model of LIPAA, based on ablation of PC has been developed. The merit of the model lies in using moving Gaussian laser heat source to simulate the channel fabrication with consideration of both the effect of plasma and input laser irradiation. The channel dimensions, i.e., width and depth of the channel, were computed from the thermal distribution obtained during the numerical study. The computed results have been duly verified with our experimental results and found in good agreement. Based upon the full factorial analysis carried out using the numerical results of the model, the following conclusions have been drawn:

- With the increase in pulse power density, an increase in the channel dimension was obtained. Also, it was observed that, below a specific value of the pulse power density, i.e., 4.584 MW/cm^2, no effect on the PC sheet was obtained, leading to no channel formation.
- An increase in the channel dimension is also obtained with an increase in the pulse repetition rate. It was witnessed that a well-defined channel formation is achieved for a pulse repetition rate of 60 Hz and more. However, at a pulse repetition rate of 20 Hz, there was no channel formation obtained.
- Again, an increase in the channel width and depth was seen with the rise in pulse duration. Likewise, pulse power density and pulse repetition rate, no effect on the PC sheet was obtained for a pulse duration value of 2 ms. While, at a pulse duration value of 4 ms and higher, well-defined channels were formed.
- The model was also utilized to analyze the effect of the moving heat flux on the PC sheet along the scanning direction. It was observed that for initial few distances, an increase in the peak temperature was obtained. However, after attaining a certain distance, the peak temperature reached a constant value and it is from this part, where one can assure to get a channel of uniform width and depth.

7.1.4 3D thermo-physical modelling and simulation on LIPAA for microchannel fabrication on PC with aluminium metal target

A 3D non-linear transient thermo-physical model of the LIPAA process has been developed to study the underlying physics of the process. On the basis of the model, spatial and temporal analysis of the process has been carried out. The salient features of the model are as follows:

- The developed model of the LIPAA process incorporates the effect of plasma in addition to the effect of incoming laser beam on both the transparent PC and the aluminium metal target.
- The model simulates the simultaneous ablation of both the PC and the aluminium sheet during the process, thereby giving a more realistic approach to the process.

- Simulations were initially performed with and without the consideration of the effect of the plasma. The results of both the cases were compared with the experimental outcomes and the later was found to have better correlation with a mean deviation of about 2.3%. As such, further numerical analysis of the LIPAA process was carried out with regard to the effect of the plasma.
- From the developed model, it has been found for lower value of laser process parameters that, at an equal distance from the interface towards the PC and the aluminium sheet, the temperature on the aluminium is comparatively larger than that on the PC. However, at higher value of laser process parameters, the temperature at equal distance from the interface towards the PC and the aluminium sheet is nearly the same.
- The spatial distribution helps in predicting the width and depth of the microchannel. The spatial distribution along the x-direction at the interface provided half the value of the width of the fabricated microchannel while the depth was obtained from the distribution along the y-direction at the axisymmetric axis. On validating the simulated results with the experimental results, a good correlation between them was found to exist with a mean deviation of 2.3% for channel width, 9.8% for channel depth and 10.5% for machining rate.
- From the temporal distribution, it has been found that the maximum temperature obtained in the simulation was within the aluminium sheet. The temperature at the interface was less than the maximum temperature obtained but surpasses the melting temperature of the PC and consequently, material removal on the PC sheet is achieved.
- The temporal investigation also indicated that the rate at which the temperature rises during pulse–on time (heating time) was higher than the rate at which temperature drops during pulse–off time (cooling time).
- The maximum machining rate value within the permissible limit was found to be 40.6 mm^3/min for the process condition of 3.06 MW/cm^2 pulse power density, 60 Hz pulse repetition rate, 4 ms pulse duration and 4 mm/s scanning speed. The corresponding channel index (CI) value of 0.86 can thus be considered as a limiting factor for fabrication of a channel within the micro-scale (1–999 μm).

7.2 Scope for future work

The present work can further be extended on the following fronts:

- The process of LIPAA can also be worked considering various types of media (such as water, oil, etc.) between transparent material and metal target both experimentally and numerically. It is because; addition of a medium in between the two materials will result in the generation of a shock wave, thereby affecting the mechanical properties of the materials. Thus, varying the media between the transparent material and the metal target, the effect of shock wave produced in the medium by the plasma can be analysed. Also, the variation in the shapes of plasma plume in various types of medium between the two materials and its effect in channel dimensions can be studied.
- The effect of varying distance between transparent material and metal target can also be analysed experimentally as well as numerically. The mechanism of LIPAA varies depending upon the distance between the metal target and the transparent material. Thus, it would be worth studying the effect of varying distance between the transparent material and the metal target on microchannel fabrication during LIPAA.
- The numerical work can further be developed for prediction of channel dimensions during multiple laser scanning pass. Prediction of channel dimensions for multiple laser scanning pass would be useful when channels of larger width and depth are to be produced. In such cases, prediction of safe number of laser passes for fabrication of microchannel with appropriate laser parameters from the numerical model will help in time saving, energy saving and also low wastage of material.
- The phase transformation during the LIPAA process can be made to incorporate in the numerical modelling work. It can be incorporated from the thermal history of the thermal model, followed by the determination of the temperature dependent phase fraction. Phase transformation plays an important role in the field of material science, as well as other physical and chemical phenomena. Thus, implementing phase transformation in the numerical work will make the model more realistic.

References

Acherjee, B., Kuar, A. S., Mitra, S., & Misra, D. (2012). Modeling and analysis of simultaneous laser transmission welding of polycarbonates using an FEM and RSM combined approach. *Optics & Laser Technology*, *44*(4), 995-1006.

Ahn, J., Ko, J., Lee, S., Yu, J., Kim, Y., & Jeon, N. L. (2018). Microfluidics in nanoparticle drug delivery; From synthesis to pre-clinical screening. *Advanced drug delivery reviews*, *128*, 29-53.

Ai, Y., Zheng, K., Shin, Y. C., & Wu, B. (2018). Analysis of weld geometry and liquid flow in laser transmission welding between polyethylene terephthalate (PET) and Ti6Al4V based on numerical simulation. *Optics & Laser Technology*, *103*, 99-108.

Azmir, M. A., & Ahsan, A. K. (2009). A study of abrasive water jet machining process on glass/epoxy composite laminate. *Journal of Materials Processing Technology*, *209*(20), 6168-6173.

Bejan, A., & Kraus, A. D. (Eds.). (2003). *Heat transfer handbook* (Vol. 1). John Wiley & Sons.

Benton, M., Hossan, M. R., Konari, P. R., & Gamagedara, S. (2019). Effect of process parameters and material properties on laser micromachining of microchannels. *Micromachines*, *10*(2), 123.

Bhandari, S., Murnal, M., Cao, J., & Ehmann, K. (2019). Comparative experimental investigation of micro-channel fabrication in Ti alloys by laser ablation and laser-induced plasma micro-machining. *Procedia Manufacturing*, *34*, 418-423.

Bogaerts, A., & Chen, Z. (2005). Effect of laser parameters on laser ablation and laser-induced plasma formation: A numerical modeling investigation. *Spectrochimica Acta Part B: Atomic Spectroscopy*, *60*(9-10), 1280-1307.

Böhme, R., Hirsch, D., & Zimmer, K. (2006). Laser etching of transparent materials at a backside surface adsorbed layer. *Applied surface science*, *252*(13), 4763-4767.

Böhme, R., & Zimmer, K. (2004). Low roughness laser etching of fused silica using an adsorbed layer. *Applied surface science*, 239(1), 109-116.

Bulgakova, N. M., Evtushenko, A. B., Shukhov, Y. G., Kudryashov, S. I., & Bulgakov, A. V. (2011). Role of laser-induced plasma in ultradeep drilling of materials by nanosecond laser pulses. *Applied Surface Science*, *257*(24), 10876-10882.

Bulushev, E., Bessmeltsev, V., Dostovalov, A., Goloshevsky, N., & Wolf, A. (2016). High-speed and crack-free direct-writing of microchannels on glass by an IR femtosecond laser. *Optics and Lasers in Engineering*, *79*, 39-47.

Campanella, B., Legnaioli, S., Pagnotta, S., Poggialini, F., & Palleschi, V. (2019). Shock waves in laser-induced plasmas. *Atoms*, *7*(2), 57.

Chang, T. L., Chen, Z. C., Lee, Y. W., Li, Y. H., & Wang, C. P. (2016). Ultrafast laser ablation of soda-lime glass for fabricating microfluidic pillar array channels. *Microelectronic Engineering*, *158*, 95-101.

Chen, J., Gu, C., Lin, H., & Chen, S. C. (2015). Soft mold-based hot embossing process for precision imprinting of optical components on non-planar surfaces. *Optics express*, *23*(16), 20977-20985.

Chen, X., & Liu, X. (1999). Short pulsed laser machining: How short is short enough? *Journal of laser applications*, *11*(6), 268-272.

Chen, P. C., Pan, C. W., Lee, W. C., & Li, K. M. (2014). Optimization of micromilling microchannels on a polycarbonate substrate. *International Journal of Precision Engineering and Manufacturing*, *15*(1), 149-154.

Chen, X., & Hu, Z. (2017). An effective method for fabricating microchannels on the polycarbonate (PC) substrate with CO laser. *International Journal of Advanced Manufacturing Technology*, *92*.

Chen, G., Gu, X., & Bi, J. (2016). Numerical analysis of thermal effect in aluminum alloy by repetition frequency pulsed laser. *Optik*, *127*(20), 10115-10121.

Cheng, C. W., Wang, S. Y., Chang, K. P., & Chen, J. K. (2016). Femtosecond laser ablation of copper at high laser fluence: Modeling and experimental comparison. *Applied Surface Science*, 361, 41-48.

Cheng, J., Perrie, W., Edwardson, S. P., Fearon, E., Dearden, G., & Watkins, K. G. (2009). Effects of laser operating parameters on metals micromachining with ultrafast lasers. *Applied surface science*, *256*(5), 1514-1520.

Chien, C. Y., & Gupta, M. C. (2005). Pulse width effect in ultrafast laser processing of materials. *Applied Physics A*, *81*(6), 1257-1263.

Daghighi, Y. (2015). Microfluidic technology and its biomedical applications. *Journal of Thermal Engineering*, *1*(7), 621-626.

Dahotre, N. B., & Harimkar, S. (2008). *Laser fabrication and machining of materials*. Springer Science & Business Media.

Darvishi, S., Cubaud, T., & Longtin, J. P. (2012). Ultrafast laser machining of tapered microchannels in glass and PDMS. *Optics and Lasers in Engineering*, *50*(2), 210-214.

Das, S., & Srivastava, V. C. (2016). Microfluidic-based photocatalytic microreactor for environmental application: a review of fabrication substrates and techniques, and operating parameters. *Photochemical & Photobiological Sciences*, *15*(6), 714-730.

Day, D., & Gu, M. (2005). Microchannel fabrication in PMMA based on localized heating by nanojoule high repetition rate femtosecond pulses. *Optics express*, *13*(16), 5939-5946.

Ding, X., Kawaguchi, Y., Sato, T., Narazaki, A., Kurosaki, R., & Niino, H. (2004). Micron-and submicron-sized surface patterning of silica glass by LIBWE method. *Journal of photochemistry and photobiology A: Chemistry*, 166(1-3), 129-133.

Dudala, S., Rao, L. T., Dubey, S. K., Javed, A., & Goel, S. (2020). Experimental characterization to fabricate CO2 laser ablated PMMA microchannel with homogeneous surface. *Materials Today: Proceedings*, *28*, 804-807.

Effati, E., & Pourabbas, B. (2018). New portable microchannel molding system based on micro-wire molding, droplet formation studies in circular cross-section microchannel. *Materials Today Communications*, *16*, 119-123.

Ehrhardt, M., Lorenz, P., Yunxiang, P., Bayer, L., Han, B., & Zimmer, K. (2017). Laser-induced back-side etching with liquid and the solid hydrocarbon absorber films of different thicknesses. *Applied Physics A*, *123*(4), 251.

Ehrhardt, M., Lorenz, P., & Zimmer, K. (2012). Surface modification by laser etching using a surface-adsorbed layer. *Thin solid films*, *520*(9), 3629-3633.

Fabbro, R., Fournier, J., Ballard, P., Devaux, D., & Virmont, J. (1990). Physical study of laser-produced plasma in confined geometry. *Journal of applied physics*, *68*(2), 775-784.

Fujii, T. (2002). PDMS-based microfluidic devices for biomedical applications. *Microelectronic Engineering*, *61*, 907-914.

Genna, S., Lambiase, F., & Leone, C. (2018). Effect of laser cleaning in Laser Assisted Joining of CFRP and PC sheets. *Composites Part B: Engineering*, *145*, 206-214.

Guan, Y., Sun, S., Zhao, G., & Luan, Y. (2005). Influence of material properties on the laser-forming process of sheet metals. *Journal of Materials Processing Technology*, *167*(1), 124-131.

Guo, X., Fan, Y., & Luo, L. (2013). Mixing performance assessment of a multi-channel mini heat exchanger reactor with arborescent distributor and collector. *Chemical engineering journal*, *227*, 116-127.

Hammadi, O. A. (2020). Using third-harmonic radiation of Nd: YAG laser to fabricate high-quality microchannels for biomedical applications. *Optik*, *208*, 164147.

Hanada, Y., Sugioka, K., Obata, K., Takase, H., Takai, H., Miyamoto, I., & Midorikawa, K. (2004, October). Micromachining of transparent materials by laser-induced plasma-assisted ablation (LIPAA). In *Fifth International Symposium on Laser Precision Microfabrication* (Vol. 5662, pp. 526-531). International Society for Optics and Photonics.

Hanada, Y., Sugioka, K., Gomi, Y., Yamaoka, H., Otsuki, O., Miyamoto, I., & Midorikawa, K. (2004). Development of practical system for laser-induced plasma-assisted ablation (LIPAA) for micromachining of glass materials. *Applied Physics A*, *79*(4), 1001-1003.

Hanada, Y., Sugioka, K., Miyamoto, I., & Midorikawa, K. (2005, April). LIPAA technique and its possible impact on microelectronics. In *Photon Processing in Microelectronics and Photonics IV* (Vol. 5713, pp. 445-455). International Society for Optics and Photonics.

Hanada, Y., Sugioka, K., & Midorikawa, K. (2006, June). Laser-induced plasma-assisted ablation (LIPAA): fundamental and industrial applications. In *High-Power Laser Ablation VI* (Vol. 6261, p. 626111). International Society for Optics and Photonics.

Hanada, Y., Sugioka, K., Obata, K., Garnov, S. V., Miyamoto, I., & Midorikawa, K. (2006). Transient electron excitation in laser-induced plasma-assisted ablation of transparent materials. *Journal of applied physics*, *99*(4), 043301.

Hnatovsky, C., Taylor, R. S., Simova, E., Rajeev, P. P., Rayner, D. M., Bhardwaj, V. R., & Corkum, P. B. (2006). Fabrication of microchannels in glass using focused femtosecond laser radiation and selective chemical etching. *Applied Physics A*, *84*(1), 47-61.

Hong, M., Sugioka, K., Wu, D. J., Wong, L. L., Lu, Y., Midorikawa, K., & Chong, T. C. (2001, October). Laser-induced-plasma-assisted ablation for glass microfabrication. In *Photonic Systems and Applications* (Vol. 4595, pp. 138-146). International Society for Optics and Photonics.

Hong, M. H., Sugioka, K., Wu, D. J., Chew, K. J., Lu, Y. F., Midorikawa, K., & Chong, T. C. (2003, February). Laser-induced plasma-assisted ablation and its applications. In *Third International Symposium on Laser Precision Microfabrication* (Vol. 4830, pp. 408-413). International Society for Optics and Photonics.

Hopp, B., Smausz, T., Vass, C., Szabó, G., Böhme, R., Hirsch, D., & Zimmer, K. (2009). Laser-induced backside dry and wet etching of transparent materials using solid and molten tin as absorbers. *Applied Physics A*, *94*(4), 899-904.

Hopp, B., Vass, C., & Smausz, T. (2007). Laser induced backside dry etching of transparent materials. *Applied surface science*, *253*(19), 7922-7925.

Hu, Z., Kovacevic, R., & Labudovic, M. (2002). Experimental and numerical modeling of buckling instability of laser sheet forming. *International Journal of Machine Tools and Manufacture*, *42*(13), 1427-1439.

Hussein, F. I., Salloomi, K. N., Akman, E., Hajim, K. I., & Demir, A. (2017). Finite element thermal analysis for PMMA/st. st. 304 laser direct joining. *Optics & Laser Technology*, *87*, 64-71.

Hwang, J., Cho, Y. H., Park, M. S., & Kim, B. H. (2019). Microchannel fabrication on glass materials for microfluidic devices. *International Journal of Precision Engineering and Manufacturing*, *20*(3), 479-495.

Jia, Y., Jiang, J., Ma, X., Li, Y., Huang, H., Cai, K., Cai, S. and Wu, Y. (2008). PDMS microchannel fabrication technique based on microwire-molding. *Chinese Science Bulletin*, *53*(24), 3928-3936.

Jiao, J., & Wang, X. (2008). A numerical simulation of machining glass by dual CO2-laser beams. *Optics & Laser Technology*, *40*(2), 297-301.

Jin, C. E., Lee, T. Y., Koo, B., Sung, H., Kim, S. H., & Shin, Y. (2018). Rapid virus diagnostic system using bio-optical sensor and microfluidic sample processing. *Sensors and Actuators B: Chemical*, *255*, 2399-2406.

Jorik, S., Lion, A., & Johlitz, M. (2019). Design of the novel tensile creep experimental setup, characterisation and description of the long-term creep performance of polycarbonate. *Polymer Testing*, *75*, 151-158.

Kanca, Y., Milner, P., Dini, D., & Amis, A. A. (2018). Tribological evaluation of biomedical polycarbonate urethanes against articular cartilage. *Journal of the mechanical behavior of biomedical materials*, *82*, 394-402.

Keidar, M., Boyd, I. D., Luke, J., & Phipps, C. (2004). Plasma generation and plume expansion for a transmission-mode microlaser ablation plasma thruster. *Journal of applied physics*, *96*(1), 49-56.

Kim, H. G., & Park, M. S. (2017). Circuit patterning using laser on transparent material. *Surface and Coatings Technology*, *315*, 377-384.

Kim, K. R., Kim, H. J., Choi, H. I., Shin, K. S., Cho, S. H., & Choi, B. D. (2015). Ultrafast laser microfabrication of a trapping device for colorectal cancer cells. *Microelectronic Engineering*, *140*, 1-5.

Kopitkovas, G., Lippert, T., Venturini, J., David, C., & Wokaun, A. (2007, April). Laser induced backside wet etching: mechanisms and fabrication of micro-optical elements. In *Journal of Physics: Conference Series* (Vol. 59, No. 1, p. 113). IOP Publishing.

Kumar, U., Panda, D., & Biswas, K. G. (2018). Non-lithographic copper-wire based fabrication of micro-fluidic reactors for biphasic flow applications. *Chemical Engineering Journal*, *344*, 221-227.

Laviano, F., Ghigo, G., Mezzetti, E., Hollmann, E., & Wördenweber, R. (2010). Control of the vortex flow in microchannel arrays produced in YBCO films by heavy-ion lithography. *Physica C: Superconductivity*, *470*(19), 844-847.

Lawrence, J. (2002). A comparative investigation of the efficacy of CO2 and high-power diode lasers for the forming of EN3 mild steel sheets. *Proceedings of the Institution of Mechanical Engineers, Part B: Journal of Engineering Manufacture*, *216*(11), 1481-1491.

Le Harzic, R., Breitling, D., Weikert, M., Sommer, S., Föhl, C., Valette, S., Donnet, C., Audouard, E. and Dausinger, F. (2005). Pulse width and energy influence on laser micromachining of metals in a range of 100 fs to 5 ps. *Applied Surface Science*, *249*(1-4), 322-331.

Lei, J. D., & Tong, A. J. (2005). Preparation of Zl-Phe-OH-NBD imprinted microchannel and its molecular recognition study. *Spectrochimica Acta Part A: Molecular and Biomolecular Spectroscopy*, *61*(6), 1029-1033.

Li, G., & Xu, S. (2015). Small diameter microchannel of PDMS and complex three-dimensional microchannel network. *Materials & Design*, *81*, 82-86.

Li, J.M., Liu, C., Dai, X.D., Chen, H.H., Liang, Y., Sun, H.L., Tian, H. and Ding, X.P. (2008). PMMA microfluidic devices with three-dimensional features for blood cell filtration. *Journal of Micromechanics and Microengineering*, *18*(9), 095021.

Li, L., Zhang, D. M., Li, Z. H., Tan, X. Y., & Fang, R. R. (2007). Metal absorptivity in femtosecond pulsed laser ablation. *Frontiers of Physics in China*, *2*(3), 322-326.

Li, Q., Grojo, D., Alloncle, A. P., & Delaporte, P. (2019). Dynamics of double-pulse laser printing of copper microstructures. *Applied Surface Science*, 471, 627-632.

Linsen, S., & Guoquan, S. (2012). Temperature field simulation of laser drilling in ANSYS. *cal*, *900*, 0-12.

Liu, Y., Ganser, D., Schneider, A., Liu, R., Grodzinski, P., & Kroutchinina, N. (2001). Microfabricated polycarbonate CE devices for DNA analysis. *Analytical Chemistry*, *73*(17), 4196-4201.

Lorenz, P., Zajadacz, J., Bayer, L., Ehrhardt, M., & Zimmer, K. (2015). Nanodrilling of fused silica using nanosecond laser radiation. *Applied Surface Science*, *351*, 935-945.

Lorenz, P., Ehrhardt, M., & Zimmer, K. (2012). Laser-induced front side and back side etching of fused silica with KrF and XeF excimer lasers using metallic absorber layers: A comparison. *Applied surface science*, *258*(24), 9742-9746.

Lorenz, P., Ehrhardt, M., & Zimmer, K. (2014). Structuring of glass fibre surfaces by laser-induced front side etching. *Applied Surface Science*, *302*, 52-57.

Luo, Z., & Zhao, Y. (2018). A survey of finite element analysis of temperature and thermal stress fields in powder bed fusion additive manufacturing. *Additive Manufacturing*, *21*, 318-332.

Majumdar, J. D., & Manna, I. (2003). Laser processing of materials. Sadhana, 28(3), 495-562.

McCann, R., Bagga, K., Duaux, G., Stalcup, A., Vázquez, M., & Brabazon, D. (2018). Taguchi method modelling of Nd: YAG laser ablation of microchannels on cyclic olefin polymer film. *Optics & Laser Technology*, *106*, 265-271.

McCann, R., Bagga, K., Groarke, R., Stalcup, A., Vázquez, M., & Brabazon, D. (2016). Microchannel fabrication on cyclic olefin polymer substrates via 1064 nm Nd: YAG laser ablation. *Applied Surface Science*, *387*, 603-608.

McUsic, A. C., Lamba, D. A., & Reh, T. A. (2012). Guiding the morphogenesis of dissociated newborn mouse retinal cells and hES cell-derived retinal cells by soft lithography-patterned microchannel PLGA scaffolds. *Biomaterials*, *33*(5), 1396-1405.

Meijer, J., Du, K., Gillner, A., Hoffmann, D., Kovalenko, V. S., Masuzawa, T., ... & Schulz, W. (2002). Laser machining by short and ultrashort pulses, state of the art and new opportunities in the age of the photons. *CIRP Annals*, *51*(2), 531-550.

Mishra, I., Lattanzi, A. M., LaMarche, C. Q., Morris, A. B., & Hrenya, C. M. (2019). Experimental validation of indirect conduction theory and effect of particle roughness on wall-to-particle heat transfer. *AIChE Journal*, *65*(10), e16703.

Mohammed, M. K., Umer, U., & Al-Ahmari, A. (2019). Optimization of Nd: YAG laser for microchannels fabrication in alumina ceramic. *Journal of Manufacturing Processes*, *41*, 148-158.

Moradi, M., Moghadam, M.K., Shamsborhan, M., Beiranvand, Z.M., Rasouli, A., Vahdati, M., Bakhtiari, A. and Bodaghi, M. (2021). Simulation, statistical modeling, and optimization of CO2 laser cutting process of polycarbonate sheets. *Optik*, *225*, 164932.

Negarestani, R., & Li, L. (2012). Laser machining of fibre-reinforced polymeric composite materials. In *Machining Technology for Composite Materials* (pp. 288-308). Woodhead Publishing.

Nguyen, T., Jung, S. H., Lee, M. S., Park, T. E., Ahn, S. K., & Kang, J. H. (2019). Robust chemical bonding of PMMA microfluidic devices to porous PETE membranes for reliable cytotoxicity testing of drugs. *Lab on a Chip*, *19*(21), 3706-3713.

Niino, H., Kawaguchi, Y., Sato, T., Narazaki, A., Gumpenberger, T., & Kurosaki, R. (2006). Surface micro-structuring of silica glass by laser-induced backside wet etching with ns-pulsed UV laser at a high repetition rate. *J. Laser Micro/Nanoeng*, *1*(1), 39-43.

Pallav, K., & Ehmann, K. F. (2010, February). Feasibility of laser induced plasma micro-machining (LIP-MM). In *International Precision Assembly Seminar* (pp. 73-80). Springer, Berlin, Heidelberg.

Pallav, K., Saxena, I., & Ehmann, K. F. (2014). Comparative assessment of the laser-induced plasma micromachining and the ultrashort pulsed laser ablation processes. *Journal of Micro and Nano-Manufacturing*, *2*(3), 031001.

Pan, C., Chen, K., Liu, B., Ren, L., Wang, J., Hu, Q., Liang, L., Zhou, J. and Jiang, L. (2017). Fabrication of micro-texture channel on glass by laser-induced plasma-assisted ablation and chemical corrosion for microfluidic devices. *Journal of Materials Processing Technology*, *240*, 314-323.

Paul, S., Kudryashov, S. I., Lyon, K., & Allen, S. D. (2007). Nanosecond-laser plasma-assisted ultradeep microdrilling of optically opaque and transparent solids. *Journal of applied physics*, *101*(4), 043106.

Pimpin, A., & Srituravanich, W. (2012). Review on micro-and nanolithography techniques and their applications. *Engineering Journal*, *16*(1), 37-56.

Prakash, S., & Kumar, S. (2015a). Fabrication of microchannels on transparent PMMA using CO 2 Laser (10.6 μm) for microfluidic applications: An experimental investigation. *International Journal of Precision Engineering and Manufacturing*, *16*(2), 361-366.

Prakash, S., & Kumar, S. (2015b). Fabrication of microchannels: A review. *Proceedings of the Institution of Mechanical Engineers, Part B: Journal of Engineering Manufacture*, *229*(8), 1273-1288.

Prakash, S., & Kumar, S. (2017). Fabrication of rectangular cross-sectional microchannels on PMMA with a CO2 laser and underwater fabricated copper mask. *Optics & Laser Technology*, *94*, 180-192.

Qi, H., Chen, T., Yao, L., & Zuo, T. (2009). Micromachining of microchannel on the polycarbonate substrate with CO2 laser direct-writing ablation. *Optics and Lasers in Engineering*, *47*(5), 594-598.

RAČIUKAITIS, G., Brikas, M., Gecys, P., Voisiat, B., & Gedvilas, M. (2009). Use of high repetition rate and high power lasers in microfabrication: How to keep the efficiency high?. *JLMN Journal of Laser Micro/Nanoengineering*, *4*(3), 186-191.

Rahman, T.U., Rehman, Z.U., Ullah, S., Qayyum, H., Shafique, B., Ali, R., Liaqat, U., Dogar, A.H. and Qayyum, A. (2019). Laser-induced plasma-assisted ablation (LIPAA) of glass: Effects of the laser fluence on plasma parameters and crater morphology. *Optics & Laser Technology*, *120*, 105768.

Rahman, T.U., Qayyum, H., Amin, U., Ullah, S., Rehman, Z.U., Dogar, A.H., Rafique, M. and Qayyum, A. (2021). The role of sacrificial target material in micromachining of glass using laser-induced plasma-assisted ablation (LIPAA). *Radiation Effects and Defects in Solids*, 1-11.

Rajendran, S., Keidar, M., Boyd, I. D., Jones, C. H., & Mork, B. (2007). Modeling of The Plasma Formation Due to Laser Irradience During Directed-Energy Testing. International Foundation for Telemetering.

Rodriguez, I., Spicar-Mihalic, P., Kuyper, C. L., Fiorini, G. S., & Chiu, D. T. (2003). Rapid prototyping of glass microchannels. *Analytica Chimica Acta*, *496*(1-2), 205-215.

Roy, S., Yue, C. Y., Wang, Z. Y., & Anand, L. (2012). Thermal bonding of microfluidic devices: Factors that affect interfacial strength of similar and dissimilar cyclic olefin copolymers. *Sensors and Actuators B: Chemical*, *161*(1), 1067-1073.

Salama, A., Li, L., Mativenga, P., & Sabli, A. (2016). High-power picosecond laser drilling/machining of carbon fibre-reinforced polymer (CFRP) composites. *Applied Physics A*, *122*(2), 73.

Samant, A. N., & Dahotre, N. B. (2008). Computational predictions in single-dimensional laser machining of alumina. *International Journal of Machine Tools and Manufacture*, *48*(12-13), 1345-1353.

Sanjay, S. T., Zhou, W., Dou, M., Tavakoli, H., Ma, L., Xu, F., & Li, X. (2018). Recent advances of controlled drug delivery using microfluidic platforms. *Advanced drug delivery reviews*, *128*, 3-28.

Saxena, I., Ehmann, K., & Cao, J. (2014). Laser-induced plasma in aqueous media: numerical simulation and experimental validation of spatial and temporal profiles. *Applied optics*, *53*(35), 8283-8294.

Schille, J., Ebert, R., Loeschner, U., Scully, P., Goddard, N., & Exner, H. (2010, February). High repetition rate femtosecond laser processing of metals. In *Frontiers in Ultrafast Optics: Biomedical, Scientific, and Industrial Applications X* (Vol. 7589, p. 758915). International Society for Optics and Photonics.

Schnell, G., Duenow, U., & Seitz, H. (2020). Effect of laser pulse overlap and scanning line overlap on femtosecond laser-structured Ti6Al4V surfaces. *Materials*, *13*(4), 969.

Sedighi, M., Afshari, D., & Nazari, F. (2018). Investigation of the effect of sheet thickness on residual stresses in resistance spot welding of aluminum sheets. *Proceedings of the Institution of Mechanical Engineers, Part C: Journal of Mechanical Engineering Science*, *232*(4), 621-638.

Sharma, P., Dubey, A. K., & Pandey, A. K. (2014). Numerical study of temperature and stress fields in laser cutting of aluminium alloy sheet. *Procedia Materials Science*, *5*, 1887-1896.

Sharma, S., Mandal, V., Ramakrishna, S. A., & Ramkumar, J. (2019). Numerical simulation of melt pool oscillations and protuberance in pulsed laser micro melting of SS304 for surface texturing applications. *Journal of Manufacturing Processes*, *39*, 282-294.

Shi, H., Nie, K., Dong, B., Long, M., Xu, H., & Liu, Z. (2019). Recent progress of microfluidic reactors for biomedical applications. *Chemical Engineering Journal*, *361*, 635-650.

Shirzadfar, H., & Khanahmadi, M. (2018). Review on structure, function and applications of microfluidic systems. *International Journal of Biosensors & Bioelectronics*, *4*(6), 263-265.

Shkuratova, V., Rymkevich, V., Kostyuk, G., & Sergeev, M. (2018). Laser-induced microplasma as effective tool for phase elements fabrication on amorphous and crystalline materials. *Journal of Laser Micro Nanoengineering*, *13*(3), 211-215.

Sia, S. K., & Whitesides, G. M. (2003). Microfluidic devices fabricated in poly (dimethylsiloxane) for biological studies. *Electrophoresis*, *24*(21), 3563-3576.

Singh, S. S., Baruah, P. K., Khare, A., & Joshi, S. N. (2018). Incubation studies and the threshold for surface damage and cavity formation in the processing of polycarbonate by Nd: YAG laser. *Optics & Laser Technology*, *108*, 592-601.

Singh, S. S., Khare, A., & Joshi, S. N. (2020). Fabrication of microchannel on polycarbonate below the laser ablation threshold by repeated scan via the second harmonic of Q-switched Nd: YAG laser. *Journal of Manufacturing Processes*, *55*, 359-372.

Stevens, T., & Baelmans, M. (2008). Optimal pressure drop ratio for micro recuperators in small sized gas turbines. *Applied Thermal Engineering*, *28*(17-18), 2353-2359.

Sugioka, K., Midorikawa, K., Yamaoka, H., Gomi, Y., Otsuki, M., Hong, M.H., Wu, D.J., Wong, L.L. and Chong, T.C. (2004, July). Glass microprocessing by laser-induced plasma-assisted ablation: fundamental to industrial applications. In *Nonresonant Laser-Matter Interaction (NLMI-11)* (Vol. 5506, pp. 1-10). International Society for Optics and Photonics.

Sundqvist, J., Kaplan, A. F. H., Shachaf, L., & Kong, C. (2017). Analytical heat conduction modelling for shaped laser beams. *Journal of Materials Processing Technology*, *247*, 48-54.

Suryawanshi, P. L., Gumfekar, S. P., Bhanvase, B. A., Sonawane, S. H., & Pimplapure, M. S. (2018). A review on microreactors: Reactor fabrication, design, and cutting-edge applications. *Chemical Engineering Science*, *189*, 431-448.

Tadamalle, A. P., Reddy, Y. P., Ramjee, E., & Reddy, V. (2014). Evaluation of Nd: YAG laser welding efficiencies for 304L stainless steel. *Procedia materials science*, *6*, 1731-1739.

Tan, B., Dalili, A., & Venkatakrishnan, K. (2009). High repetition rate femtosecond laser nano-machining of thin films. *Applied Physics A*, *95*(2), 537-545.

Tani, G., Orazi, L., Fortunato, A., & Cuccolini, G. (2008). Laser ablation of metals: a 3D process simulation for industrial applications. *Journal of manufacturing science and engineering*, *130*(3), 031111.

Temiz, Y., Lovchik, R. D., Kaigala, G. V., & Delamarche, E. (2015). Lab-on-a-chip devices: How to close and plug the lab?. *Microelectronic Engineering*, *132*, 156-175.

Trotta, G., Volpe, A., Ancona, A., & Fassi, I. (2018). Flexible micro manufacturing platform for the fabrication of PMMA microfluidic devices. *Journal of Manufacturing Processes*, *35*, 107-117.

Tsvetkov, M.Y., Yusupov, V.I., Minaev, N.V., Akovantseva, A.A., Timashev, P.S., Golant, K.M., Chichkov, B.N. and Bagratashvili, V.N., (2017). On the mechanisms of single-pulse laser-induced backside wet etching. *Optics & Laser Technology*, *88*, 17-23.

Umer, U., Mohammed, M. K., & Al-Ahmari, A. (2017). Multi-response optimization of machining parameters in micro milling of alumina ceramics using Nd: YAG laser. *Measurement*, *95*, 181-192.

Vass, C., Hopp, B., Smausz, T., & Ignácz, F. (2004). Experiments and numerical calculations for the interpretation of the backside wet etching of fused silica. *Thin Solid Films*, *453*, 121-126.

Vass, C., Kiss, B., Flender, R., Felhazi, Z., Lorenz, P., Erhardt, M., & Zimmer, K. (2015). Comparative study on grating fabrication in transparent materials by TWIN-

LIBWE and ultrashort pulsed ablation techniques. *Journal of Laser Micro Nanoengineering*, *10*(1), 38-42.

Vora, H. D., Santhanakrishnan, S., Harimkar, S. P., Boetcher, S. K., & Dahotre, N. B. (2013). One-dimensional multipulse laser machining of structural alumina: evolution of surface topography. *The International Journal of Advanced Manufacturing Technology*, *68*(1), 69-83.

Vora, H. D., & Dahotre, N. B. (2015). Surface topography in three-dimensional laser machining of structural alumina. *Journal of Manufacturing Processes*, *19*, 49-58.

Wang, S., Wang, X., Wang, L., Pu, Q., Du, W., & Guo, G. (2018). Plasma-assisted alignment in the fabrication of microchannel-array-based in-tube solid-phase microextraction microchips packed with TiO2 nanoparticles for phosphopeptide analysis. *Analytica chimica acta*, *1018*, 70-77.

Wegeng, R. S., Pederson, L. R., TeGrotenhuis, W. E., & Whyatt, G. A. (2001). Compact fuel processors for fuel cell powered automobiles based on microchannel technology. *Fuel Cells Bulletin*, *3*(28), 8-13.

Wei, X., Joshi, Y., & Patterson, M. K. (2007). Experimental and numerical study of a stacked microchannel heat sink for liquid cooling of microelectronic devices. *Journal of Heat Transfer, 129(10)*, 1432-1444.

Wu, T., Ke, C., & Wang, Y. (2019). Fabrication of trapezoidal cross-sectional microchannels on PMMA with a multi-pass translational method by CO2 laser. *Optik*, *183*, 953-961.

Xie, X., Huang, X., Jiang, W., Wei, X., Hu, W., & Ren, Q. (2017). Three dimensional material removal model of laser-induced backside wet etching of sapphire substrate with CuSO4 solutions. *Optics & Laser Technology*, *89*, 59-68.

Xing, Y., Zhang, K., Huang, P., Liu, L., & Wu, Z. (2020). Assessment machining of micro-channel textures on PCD by laser-induced plasma and ultra-short pulsed laser ablation. *Optics & Laser Technology*, *125*, 106057.

Xu, J., Locascio, L., Gaitan, M., & Lee, C. S. (2000). Room-temperature imprinting method for plastic microchannel fabrication. *Analytical Chemistry*, *72*(8), 1930-1933.

Xu, S., Liu, B., Pan, C., Ren, L., Tang, B., Hu, Q., & Jiang, L. (2017). Ultrafast fabrication of micro-channels and graphite patterns on glass by nanosecond laser-induced plasma-assisted ablation (LIPAA) for electrofluidic devices. *Journal of Materials Processing Technology*, *247*, 204-213.

Yang, J., Sun, S., Brandt, M., & Yan, W. (2010). Experimental investigation and 3D finite element prediction of the heat affected zone during laser assisted machining of Ti6Al4V alloy. *Journal of Materials Processing Technology*, *210*(15), 2215-2222.

Yao, P., Schneider, G. J., & Prather, D. W. (2005). Three-dimensional lithographical fabrication of microchannels. *Journal of microelectromechanical systems*, *14*(4), 799-805.

Yih, J., & Wang, H. (2020). Experimental characterization of thermal-hydraulic performance of a microchannel heat exchanger for waste heat recovery. *Energy Conversion and Management*, *204*, 112309.

Zakoldaev, R., Sergeev, M., Kostyuk, G., & Veiko, V. (2015). Laser-induced Black-body Heating (LIBBH) as a Method for Glass Surface Modification. *Journal of Laser Micro/Nanoengineering*, *10*(1).

Zhai, H., Li, J., Chen, Z., Su, Z., Liu, Z., & Yu, X. (2014). A glass/PDMS electrophoresis microchip embedded with molecular imprinting SPE monolith for contactless conductivity detection. *Microchemical Journal*, *114*, 223-228.

Zhang, J., Sugioka, K., & Midorikawa, K. (1998). Laser-induced plasma-assisted ablation of fused quartz using the fourth harmonic of a Nd+: YAG laser. *Applied Physics A*, *67*(5), 545-549.

Zhang, J., Sugioka, K., & Midorikawa, K. (1999, July). Micromachining of glass materials by laser-induced plasma-assisted ablation (LIPAA) using a conventional nanosecond laser. In *Laser Applications in Microelectronic and Optoelectronic Manufacturing IV* (Vol. 3618, pp. 363-369). International Society for Optics and Photonics.

Zhang, L., Wang, W., Ju, X. J., Xie, R., Liu, Z., & Chu, L. Y. (2015). Fabrication of glass-based microfluidic devices with dry film photoresists as pattern transfer masks for wet etching. *RSC Advances*, *5*(8), 5638-5646.

Zhao, X., & Shin, Y. C. (2013). Ablation dynamics of silicon by femtosecond laser and the role of early plasma. *Journal of Manufacturing Science and Engineering*, *135*(6).

Zhao, P. C., Shen, Y. F., Huang, G. Q., & Zheng, Q. X. (2018). Numerical simulation of friction stir butt-welding of 6061 aluminum alloy. *Transactions of Nonferrous Metals Society of China*, *28*(6), 1216-1225.

Zhou, W., Deng, W., Lu, L., Zhang, J., Qin, L., Ma, S., & Tang, Y. (2014). Laser micro-milling of microchannel on copper sheet as catalyst support used in microreactor for hydrogen production. *International journal of hydrogen energy*, *39*(10), 4884-4894.

Zimmer, K., & Böhme, R. (2008). Laser-induced backside wet etching of transparent materials with organic and metallic absorbers. *Laser Chemistry, 2008*.

Zou, M., Cai, S., Zhao, Z., Chen, L., Zhao, Y., Fan, X., & Chen, S. (2015). A novel polydimethylsiloxane microfluidic viscometer fabricated using microwire-molding. *Review of Scientific Instruments*, *86*(10), 104302.

Appendix 1.1

Permissions for figure 1.1 (a) (only first page of the license agreement)

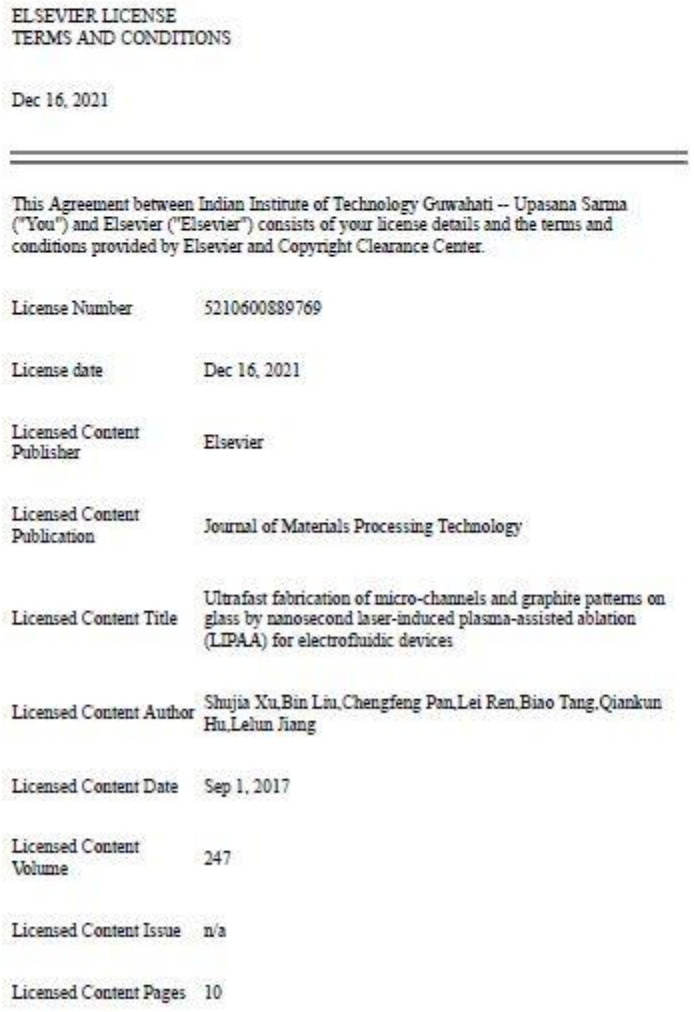

ELSEVIER LICENSE
TERMS AND CONDITIONS

Dec 16, 2021

This Agreement between Indian Institute of Technology Guwahati -- Upasana Sarma ("You") and Elsevier ("Elsevier") consists of your license details and the terms and conditions provided by Elsevier and Copyright Clearance Center.

License Number	5210600889769
License date	Dec 16, 2021
Licensed Content Publisher	Elsevier
Licensed Content Publication	Journal of Materials Processing Technology
Licensed Content Title	Ultrafast fabrication of micro-channels and graphite patterns on glass by nanosecond laser-induced plasma-assisted ablation (LIPAA) for electrofluidic devices
Licensed Content Author	Shujia Xu,Bin Liu,Chengfeng Pan,Lei Ren,Biao Tang,Qiankun Hu,Lelun Jiang
Licensed Content Date	Sep 1, 2017
Licensed Content Volume	247
Licensed Content Issue	n/a
Licensed Content Pages	10

Appendix 1.2

Permissions for figure 1.1 (b) (only first page of the license agreement)

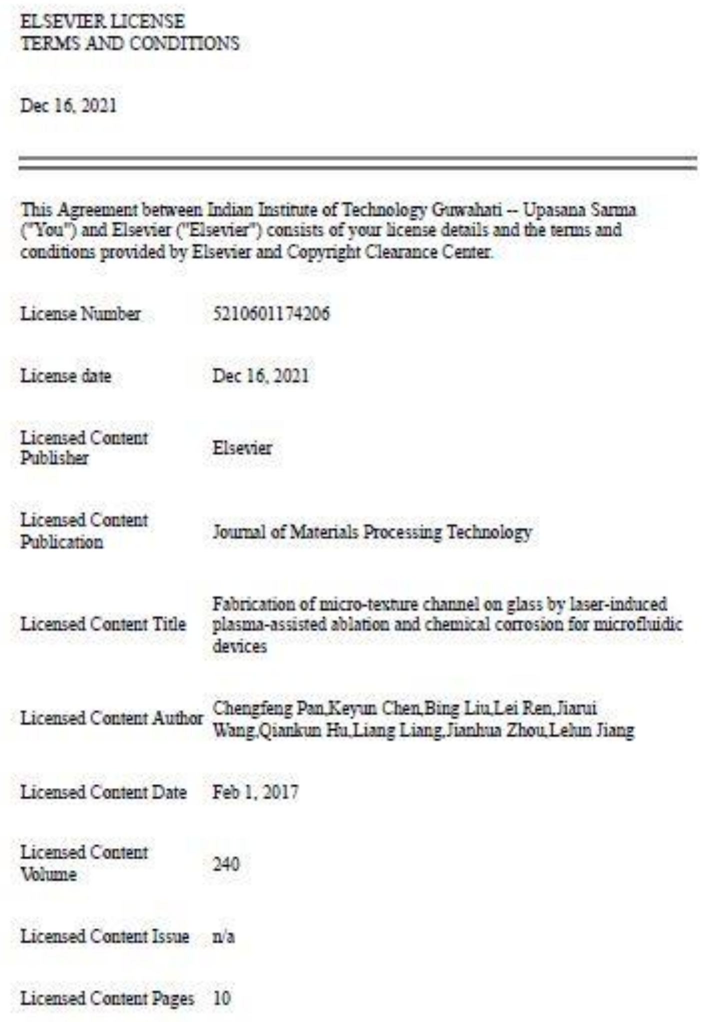

ELSEVIER LICENSE
TERMS AND CONDITIONS

Dec 16, 2021

This Agreement between Indian Institute of Technology Guwahati -- Upasana Sarma ("You") and Elsevier ("Elsevier") consists of your license details and the terms and conditions provided by Elsevier and Copyright Clearance Center.

License Number	5210601174206
License date	Dec 16, 2021
Licensed Content Publisher	Elsevier
Licensed Content Publication	Journal of Materials Processing Technology
Licensed Content Title	Fabrication of micro-texture channel on glass by laser-induced plasma-assisted ablation and chemical corrosion for microfluidic devices
Licensed Content Author	Chengfeng Pan,Keyun Chen,Bing Liu,Lei Ren,Jiarui Wang,Qiankun Hu,Liang Liang,Jianhua Zhou,Lelun Jiang
Licensed Content Date	Feb 1, 2017
Licensed Content Volume	240
Licensed Content Issue	n/a
Licensed Content Pages	10

Appendix 2.1

Permissions for figure 2.6 (a) (only first page of the license agreement)

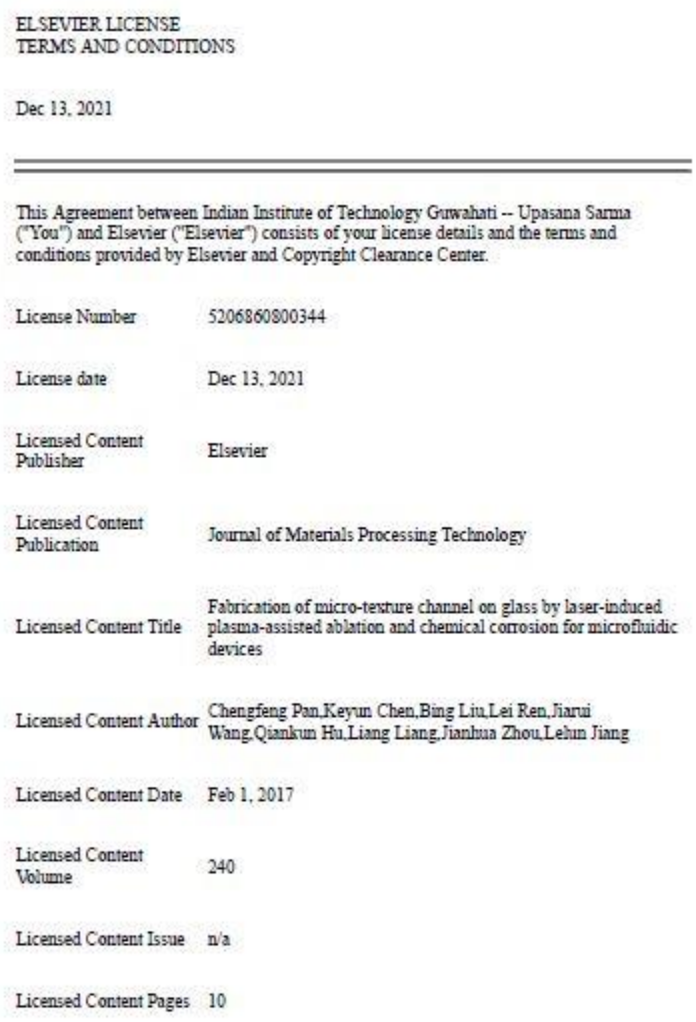

ELSEVIER LICENSE
TERMS AND CONDITIONS

Dec 13, 2021

This Agreement between Indian Institute of Technology Guwahati -- Upasana Sarma ("You") and Elsevier ("Elsevier") consists of your license details and the terms and conditions provided by Elsevier and Copyright Clearance Center.

License Number	5206860800344
License date	Dec 13, 2021
Licensed Content Publisher	Elsevier
Licensed Content Publication	Journal of Materials Processing Technology
Licensed Content Title	Fabrication of micro-texture channel on glass by laser-induced plasma-assisted ablation and chemical corrosion for microfluidic devices
Licensed Content Author	Chengfeng Pan,Keyun Chen,Bing Liu,Lei Ren,Jiarui Wang,Qiankun Hu,Liang Liang,Jianhua Zhou,Lelun Jiang
Licensed Content Date	Feb 1, 2017
Licensed Content Volume	240
Licensed Content Issue	n/a
Licensed Content Pages	10

Appendix 2.2

Permissions for figure 2.6 (b) (only first page of the license agreement)

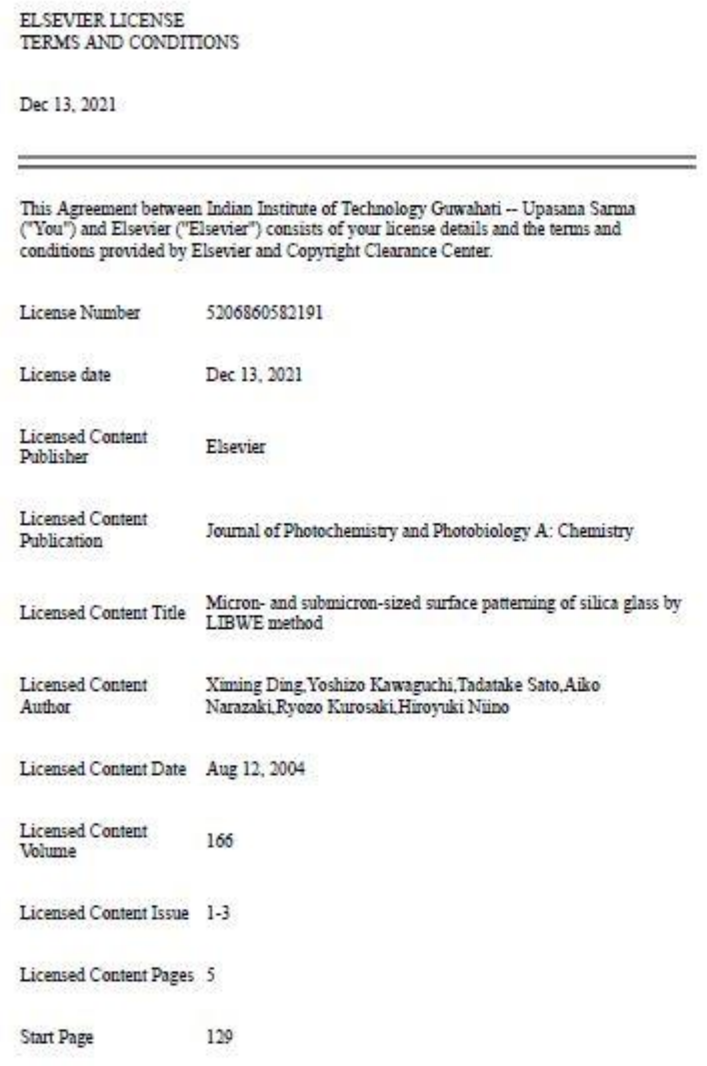

ELSEVIER LICENSE
TERMS AND CONDITIONS

Dec 13, 2021

This Agreement between Indian Institute of Technology Guwahati -- Upasana Sarma ("You") and Elsevier ("Elsevier") consists of your license details and the terms and conditions provided by Elsevier and Copyright Clearance Center.

License Number	5206860582191
License date	Dec 13, 2021
Licensed Content Publisher	Elsevier
Licensed Content Publication	Journal of Photochemistry and Photobiology A: Chemistry
Licensed Content Title	Micron- and submicron-sized surface patterning of silica glass by LIBWE method
Licensed Content Author	Ximing Ding,Yoshizo Kawaguchi,Tadatake Sato,Aiko Narazaki,Ryozo Kurosaki,Hiroyuki Niino
Licensed Content Date	Aug 12, 2004
Licensed Content Volume	166
Licensed Content Issue	1-3
Licensed Content Pages	5
Start Page	129

Appendix 2.3

Permissions for figure 2.6 (c) (only first page of the license agreement)

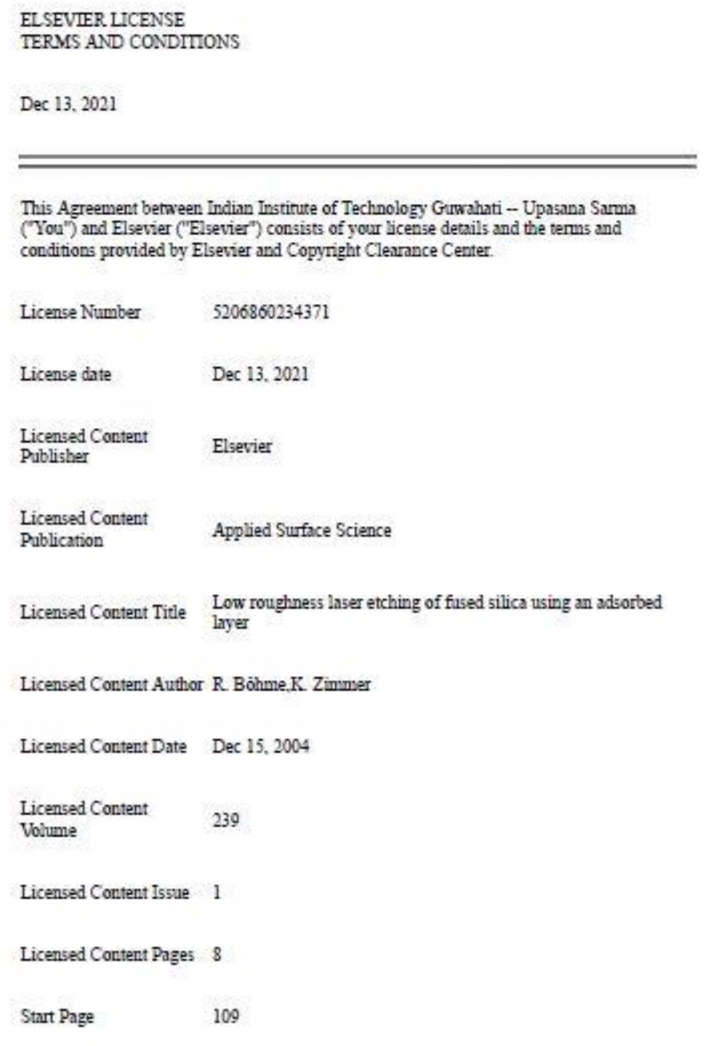

ELSEVIER LICENSE
TERMS AND CONDITIONS

Dec 13, 2021

This Agreement between Indian Institute of Technology Guwahati -- Upasana Sarma ("You") and Elsevier ("Elsevier") consists of your license details and the terms and conditions provided by Elsevier and Copyright Clearance Center.

License Number	5206860234371
License date	Dec 13, 2021
Licensed Content Publisher	Elsevier
Licensed Content Publication	Applied Surface Science
Licensed Content Title	Low roughness laser etching of fused silica using an adsorbed layer
Licensed Content Author	R. Böhme,K. Zimmer
Licensed Content Date	Dec 15, 2004
Licensed Content Volume	239
Licensed Content Issue	1
Licensed Content Pages	8
Start Page	109

Appendix 3.1

Laser machine specifications

Model: 500 W pulsed Nd: YAG CNC Laser

Make: Suresh Indu Lasers Pvt. Ltd.

A) Laser Source

Laser Type Pulsed : Nd: YAG
Wavelength : 1.06 μm
Average power : 500 W
Peak Power : 9 kW
Pulse Energy : 0.1 - 100 J
Pulse width : 0.5 – 20 mS
Pulse Frequency : 1 – 500 Hz
Beam Quality : 25 mm mrad
Input Power : 18 kW

B) Beam Delivery & Focusing Optics System

- 45-degree beam bender with beam expander and collimator.
- Beam focusing assembly, gas flow system with pressure attachment
- Beam focus spot radius is 100 microns.
- Dummy beam for evaluation, before processing the actual component.
- Protective cover for laser head and optical assembly.
- Auto focus head.

C) CNC Table

In this system the laser head is placed above the CNC table to process the material. Here, the laser head is stationary and the CNC table (worktable) is movable. The axis motion is through the ball screw with servo motor. The position and the feed is displayed continuously on the console. The whole system has resolution & positional accuracy of ± 0.1 mm through digital drive & control system with provision for PC interface. The laser parameters should be individually measurable & controllable.

X stroke : 500 mm max
Y stroke : 500 mm max

D) Laser Safety

The safety provisions are provided which full proof and fail-safe type for the safety of the personnel and the machine. It complies with all the relevant international norms and guidelines for the safety of the personnel and laser equipment. The safety feature included are as follows:

- Laser beam path should be completely covered and shielded between the laser unit and the work piece surface.
- Suitable interlocking arrangement should exist against faulty sequence of operation, sudden power failure and fluctuations in the voltage beyond permissible ranges.
- Protection against over travel of moving machine sub-assemblies and sub-systems.
- Provision of an emergency stop.
- Machine should not start automatically on resumption of power supply without ensuring safety stapes.
- Protection against overload
- Minimum accidental protection

E) Gas Assist System

Gas assist system is a standard feature for the system. The system enables the user to mix gases and use for specific application or directly use individual gas as needed. The system also consists of nozzles that will supply pressure regulated gas to the point of laser machining. The system supports the use of inert gases, nitrogen, oxygen, compressed air, etc. during the specific processes.

F) Chiller System

The chiller system utilized is a water chiller system. It cools the external optical parts like the laser source and the integrated electrical cabinet. It also controls an eventual leak through rotameter. Chiller specifications are as follows:

- Cooling Capacity: 17 kW
- Water to Water Heat exchanger,
- Includes water tank with on loop chiller.
- Pump for the input.
- Treated water with circulating pump on the laser side

Appendix 3.2

Specification of high precision non-contact computerized surface profilometer

Make	Tylor Hobson
Precision	1 mega pixel
Lens magnification	20×
Field of view	0.825mm*0.825mm
Focal distance	4.7mm
Power supply	220V AC supply

Appendix 3.3

Specification of Gemini Field Emission Scanning Electron Microscope (FESEM)

Make	Zeiss
Model	Gemini 300
Accelerating voltage	0.02 to 30 kV
Resolution	0.8 nm at 15 kV; 1.4 nm at 1 kV
Magnification	20,00,000×

Appendix 3.4

Experimental results for microchannel fabrication on polycarbonate with copper as metal target

PRR−Pulse repetition rate, **PD**− Pulse duration, **SS** −Scanning speed, **PPD**−Pulse power density

Sl. No.	PRR (Hz)	PD (ms)	PPD (MW/cm^2)	Experimental	
				Mean Width (µm)	**Mean Depth (µm)**
1	40	2	3.055	0	0
2	40	4	5.483	802.5	43.92
3	40	6	6.112	931.4	259.4
4	60	2	3.055	191.21	0
5	60	4	5.483	806.2	156.09
6	60	6	6.112	1203.5	524.9
7	80	2	5.483	812.6	51.9
8	80	4	6.112	1597.1	523.11
9	80	6	3.055	821.8	249.8
10	40	2	6.112	315.9	13.1
11	80	6	6.112	2000	1000
12	40	6	5.483	851.9	154.6
13	60	2	5.483	554.7	18.36
14	60	4	6.112	1164.2	204.9
15	60	6	3.055	760.03	194
16	80	2	6.112	1114.31	64.33
17	80	4	3.055	661.12	189.4
18	80	6	5.483	1259.4	519.7
19	80	4	5.483	906.3	225.9
20	60	6	5.483	898.3	526.11
21	60	4	3.055	541.7	41.27
22	40	4	3.055	232.14	19.22
23	40	4	6.112	1014.23	51.61
24	40	6	3.055	706.7	34.9
25	40	2	5.483	206.85	9.86
26	60	2	6.112	967.45	31.01
27	80	2	3.055	267.1	11.3

Appendix 3.5

Experimental results for microchannel fabrication on polycarbonate with stainless steel as metal target

PRR−Pulse repetition rate, **PD**− Pulse duration, **SS** −Scanning speed, **PPD**−Pulse power density

Sl. No.	**PRR (Hz)**	**PD (ms)**	**PPD (MW/cm^2)**	**Experimental**	
				Mean Width (µm)	**Mean Depth (µm)**
1	40	2	3.055	0	0
2	40	4	5.483	1274.67	65.94
3	40	6	6.112	1465.3	301.7
4	60	2	3.055	266.17	0
5	60	4	5.483	1215.3	267.8
6	60	6	6.112	1586.01	698.6
7	80	2	5.483	1254.3	75.3
8	80	4	6.112	2000	695.31
9	80	6	3.055	1131.4	368.1
10	40	2	6.112	791.3	11.88
11	80	6	6.112	2000	1000
12	40	6	5.483	1116.3	203.1
13	60	2	5.483	714.36	19.51
14	60	4	6.112	1511.4	289.13
15	60	6	3.055	1237.33	324
16	80	2	6.112	1512	81.9
17	80	4	3.055	1014.67	259.16
18	80	6	5.483	1506.1	554.9
19	80	4	5.483	1341.2	364.3
20	60	6	5.483	1361.4	641.7
21	60	4	3.055	948.7	144.6
22	40	4	3.055	367.83	33.47
23	40	4	6.112	1462.17	115.52
24	40	6	3.055	914.62	48.33
25	40	2	5.483	253.6	11.9
26	60	2	6.112	1124.3	35.61
27	80	2	3.055	544.2	16.41

Appendix 6.1

Machining rates and their corresponding channel index (CI) for different set of process conditions during LIPAA with aluminium metal target

PRR−Pulse repetition rate, **PD**− Pulse duration, **SS** −Scanning speed, **PPD**−Pulse power density

PRR (Hz)	**PD (ms)**	**PPD (MW/cm^2)**	**Machining rate (mm^3/min)**	$CI = \frac{Machining\ rate}{Max^m\ permissible\ machining\ rate}$
40	2	3.055	0	0
60	2	3.055	0	0
40	2	4.584	0.516	0.010
80	2	3.055	1.090	0.023
40	2	6.112	1.320	0.028
40	4	3.055	1.513	0.032
60	2	4.584	2.126	0.045
60	2	6.112	7.568	0.161
40	6	3.055	9.711	0.206
40	4	4.584	11.694	0.248
80	4	3.055	11.854	0.252
80	2	6.112	12.204	0.259
80	2	4.584	18.198	0.387
40	6	4.584	38.199	0.812
60	**4**	**3.055**	**40.560**	**0.862**
60	6	3.055	48.798	1.038
60	4	4.584	52.269	1.112
40	4	6.112	52.464	1.116
80	6	3.055	72.167	1.535
60	4	6.112	73.908	1.572
80	4	4.584	78.947	1.679
40	6	6.112	86.840	1.847
80	6	4.584	120.243	2.558
60	6	4.584	129.346	2.752
60	6	6.112	211.608	4.502
80	4	6.112	376.8	8.017
80	6	6.112	376.8	8.017